Supported by 日本財団 THE NIPPON FOUNDATION

日中笹川医学奨学金制度
第４５期＜学位取得コース＞

中　間　報　告　書

2024 年 4 月～2025 年 3 月

公益財団法人　日中医学協会

目 次

日中笹川医学奨学金制度<学位取得コース>中間評価書
【課程博士:指導教官用】

第45期　　研究者番号:　G4501

氏名	袁 野	YUAN YE	性別	F	生年月日	1996/7/19
中国所属機関(役職)	遵義医科大学附属医院神経内科(住院医師)					
日本研究先(指導教官)	筑波大学医学医療系神経内科学分野(斉木 臣二　教授)					
研究テーマ	オートファジーによる加齢調節機構について					
専攻種別	論文博士	□	課程博士	☑		

研究者評価(指導教官記入欄)

成績状況	優・良・可・不可から選択してください⇒	可	取得単位数	
	学業成績係数=		取得すべき単位総数	
学生本人が行った研究の概要	1. 日本語、英語の学習 2. 細胞生物学、生化学を中心とした生命科学の学習 3. 細胞生物学的実験(免疫細胞染色、細胞内小器官の分画法)、生化学的実験(DNAシークエンス、ウェスタンブロッティング)の習得 上記の習得のためのトレーニングを行うと共に、各種化合物の生物学的意義についての実験を行った。 (2025年4月1日入学のための筑波大学大学院博士課程の試験に合格した)			
総合評価	【良かった点】 2024年10月以降、学習・実験の速度が上昇したこと。			
	【改善すべき点】 英語、日本語でのコミュニケーション能力。基礎生物学の知識・理解、実験技術の背景にある基礎生物学的な論理の理解			
	【今後の展望】 細胞生物学・生化学の基礎知識を身につけることができ、目の前で実施している実験の論理を理解し、的確な実験の調整を行うという、研究者として当然の姿勢を身につけられるかが最重要である。			
学位取得見込	多くの改善を行えば、見込みはある。			
評価者(指導教官記名)	斉木臣二	作成日:	2025年　3　月　7　日	

日中笹川医学奨学金制度<学位取得コース>中間報告書
【研究者用】

Supported by 日本財団 THE NIPPON FOUNDATION

第45期　　研究者番号：G4501　　作成日：2025年3月10日

氏名	袁 野	YUAN YE	性別	F	生年月日	1996/7/19
中国所属機関(役職)	遵義医科大学附属医院神経内科（住院医師）					
日本研究先（指導教官）	筑波大学医学医療系神経内科学分野（斉木 臣二　教授）					
研究テーマ(日文)	アルベンダゾール誘導体のオートファジー促進活性の評価					
Research theme	Evaluation of Autophagy-Enhancing Activity of Albendazole Derivatives					
専攻種別	論文博士	□	課程博士	☑		

1．研究概要(1)

1)目的(Goal):
Parkinson's disease (PD), the second most prevalent progressive neurodegenerative disorder after Alzheimer's disease, is characterized by dopamine depletion due to the loss of dopaminergic neurons in the substantia nigra pars compacta.The aggregation and deposition of the αSyn protein, also known as Lewy bodies, within dopaminergic neurons in the substantia nigra play a critical role in the etiology of PD (Spillantini et al.,1997; Postuma et al., 2015). Impaired autophagy has been implicated as a key pathological feature of PD, contributing to the accumulation of toxic protein aggregates and neuronal loss. Consequently, the enhancement of autophagy has emerged as a promising therapeutic strategy for PD and other neurodegenerative diseases. Recent studies have identified albendazole (ALB), a benzimidazole-based anthelmintic drug, as a potential autophagy activator with neuroprotective properties (Date et al., 2024). Given the structural similarity between Albendazole (ALB) and other benzimidazole derivatives, it is essential to explore whether chemical modifications can enhance its autophagy-inducing potency. This study systematically compares the autophagy-enhancing effects of ALB and its derivatives to identify structural modifications that maximize autophagy induction. These findings may contribute to the development of novel autophagy-targeting therapeutic candidates for Parkinson's disease (PD).

2)戦略(Approach)
To evaluate the autophagy-enhancing effects of ALB and its structural derivatives, we conducted a comparative analysis of their ability to induce LC3B-II accumulation in SH-SY5Y neuronal cells. SH-SY5Y cells were treated with ALB and its derivatives, including mebendazole (MEB), 2-(4-Thiazolyl) benzimidazole (2,4-TB), fenbendazole (FEN), flubendazole (FLU), and triclabendazole (TCB), at a final concentration of 10 μM for 7 hours, with DMSO-treated cells serving as the vehicle control. Following treatment, LC3B-II protein levels were assessed using Western blot analysis, with β-actin as a loading control. The relative expression of LC3B-II was quantified using densitometric analysis, and values were normalized to β-actin to allow for comparative evaluation of autophagy activation across treatment groups. Statistical significance was determined using one-way ANOVA, followed by Dunnett comparison test, with $p < 0.05$ considered statistically significant.

3)材料と方法(Materials and methods)
(1) Cell Culture and Drug Treatment
SH-SY5Y neuronal cells were used as a model system due to their neuronal origin and widespread use in neurodegenerative disease research.SH-SY5Y neuronal Cells were treated with albendazole (ALB) and its structural derivatives, including mebendazole (MEB), 2-(4-Thiazolyl)benzimidazole (2,4-TB), fenbendazole (FEN), flubendazole (FLU), and triclabendazole (TCB), at a final concentration of 10 μM for 7 hours, with DMSO-treated cells serving as the vehicle control.
(2) Protein Extraction and Western Blot Analysis
Following treatment, protein concentration was measured using a BCA assay, and equal amounts of total protein were loaded onto 4-20% SDS-PAGE Midi gel. Proteins were subsequently transferred onto PVDF membranes and blocked with 5% non-fat milk in TBST for 30 minutes. Primary antibody incubation was performed overnight at 4° C, using LC3B for autophagy assessment. Membranes were then incubated with HRP-conjugated secondary antibodies for 1 hour at room temperature. Protein bands were visualized using enhanced chemiluminescence (ECL) detection and quantified by densitometric analysis.
(3) Data Quantification and Statistical Analysis
Densitometric quantification of LC3B-II levels was performed using Image J, with values normalized to β-actin for comparative analysis. Statistical comparisons were conducted using one-way ANOVA followed by Dunnett test, with $p < 0.05$ considered statistically significant.

1．研究概要(2)．
4)実験結果(Results)．
Result 1: Western blot analysis assessed LC3 protein expression in SH-SY5Y cells treated with albendazole (ALB) and its derivatives, using DMSO-treated cells as the control. β -actin served as a loading control. ALB treatment significantly increased LC3B-II accumulation, confirming its role as an autophagy inducer. In contrast, its derivatives—Mebendazole (MEB), 2-(4-Thiazolyl)benzimidazole (2,4-TB), Fenbendazole (FEN), Flubendazole (FLU), and Triclabendazole (TCB)—exhibited varying levels of LC3B-II expression. The control group showed the lowest LC3B-II levels, reflecting basal autophagy activity.
Result 2: Densitometric quantification of LC3B-II levels results confirmed that only ALB treatment led to a statistically significant increase in LC3B-II expression compared to the control group ($p < 0.05$). In contrast, treatment with the structural derivatives (MEB, 2,4-TB, FEN, FLU, and TCB) did not result in a significant change ($p > 0.05$, ns). These results suggest that chemical modifications in ALB derivatives may diminish their ability to enhance autophagy.

5)考察(Discussion)
This study aimed to evaluate whether albendazole (ALB) and its derivatives could enhance autophagy induction.Our findings confirm that ALB significantly increases LC3B-II levels, whereas its structural derivatives fail to elicit a comparable response, suggesting that specific chemical modifications may attenuate its autophagy-enhancing effects.
Several factors may contribute to these differences:
First, differences in intracellular localization could play a crucial role. ALB has been reported to accumulate in lysosomes, where it facilitates autophagy activation by enhancing lysosomal clustering (Date et al., 2024). However, structural modifications in its derivatives may alter lysosomal targeting or retention, thereby reducing their efficacy in triggering autophagy. Second, variability in metabolic stability and bioavailability could influence drug activity. Structural modifications may impact drug solubility, stability, or cellular uptake, leading to lower intracellular drug concentrations and potentially diminishing their ability to enhance autophagy. Lastly, divergence in autophagy activation mechanisms may explain the observed differences. While ALB is proposed to activate autophagy through mTOR inhibition or lysosomal enhancement, its derivatives may not engage the same molecular targets or exhibit differential regulatory effects on autophagic pathways (Date et al., 2024).
Taken together, these findings suggest that while ALB effectively induces autophagy, its structural modifications may compromise its activity, highlighting the need for further structure-activity relationship (SAR) studies to optimize benzimidazole-based compounds for potential therapeutic applications in Parkinson's disease and other neurodegenerative disorders.

6)参考文献(References)．
1. Date, Y., Sasazawa, Y., Kitagawa, M., Gejima, K., Suzuki, A., Saya, H., Kida, Y., Imoto, M., Itakura, E., Hattori, N., & Saiki, S. (2024). Novel autophagy inducers by accelerating lysosomal clustering against Parkinson's disease. eLife, 13, e98649. [DOI: 10.7554/eLife.98649], [PMID: 38899618].
2. Spillantini, M. G., Schmidt, M. L., Lee, V. M. Y., Trojanowski, J. Q., Jakes, R., & Goedert, M. (1997). Alpha-synuclein in Lewy bodies. Nature, 388, 839-840. [DOI: 10.1038/42166], [PMID: 9278044].
3. Postuma, R. B., Berg, D., Stern, M., Poewe, W., Olanow, C. W., Oertel, W., Obeso, J., Marek, K., Litvan, I., Lang, A. E., Halliday, G., Goetz, C. G., Gasser, T., Dubois, B., Chan, P., Bloem, B. R., Adler, C. H., & Deuschl, G. (2015). MDS clinical diagnostic criteria for Parkinson's disease. Movement Disorders, 30, 1591-1601. [DOI: 10.1002/mds.26424], [PMID: 26474316].

2. 執筆論文 Publication of thesis ※記載した論文を添付してください。Attach all of the papers listed below.

論文名 1 Title						
掲載誌名 Published journal						
	年 月	巻(号)	頁 ～ 頁	言語 Language		
第1著者名 First author		第2著者名 Second author		第3著者名 Third author		
その他著者名 Other authors						
論文名 2 Title						
掲載誌名 Published journal						
	年 月	巻(号)	頁 ～ 頁	言語 Language		
第1著者名 First author		第2著者名 Second author		第3著者名 Third author		
その他著者名 Other authors						
論文名 3 Title						
掲載誌名 Published journal						
	年 月	巻(号)	頁 ～ 頁	言語 Language		
第1著者名 First author		第2著者名 Second author		第3著者名 Third author		
その他著者名 Other authors						
論文名 4 Title						
掲載誌名 Published journal						
	年 月	巻(号)	頁 ～ 頁	言語 Language		
第1著者名 First author		第2著者名 Second author		第3著者名 Third author		
その他著者名 Other authors						
論文名 5 Title						
掲載誌名 Published journal						
	年 月	巻(号)	頁 ～ 頁	言語 Language		
第1著者名 First author		第2著者名 Second author		第3著者名 Third author		
その他著者名 Other authors						

3. 学会発表　Conference presentation　※筆頭演者として総会・国際学会を含む主な学会で発表したものを記載してください。

※Describe your presentation as the principal presenter in major academic meetings including general meetings or international meetings.

学会名 Conference							
演　題 Topic							
開催日 date	年　　月　　日		開催地 venue				
形式　method	□　口頭発表　Oral	□　ポスター発表　Poster	言語　Language	□　日本語	□　英語	□　中国語	
共同演者名 Co-presenter							
学会名 Conference							
演　題 Topic							
開催日 date	年　　月　　日		開催地 venue				
形式　method	□　口頭発表　Oral	□　ポスター発表　Poster	言語　Language	□　日本語	□　英語	□　中国語	
共同演者名 Co-presenter							
学会名 Conference							
演　題 Topic							
開催日 date	年　　月　　日		開催地 venue				
形式　method	□　口頭発表　Oral	□　ポスター発表　Poster	言語　Language	□　日本語	□　英語	□　中国語	
共同演者名 Co-presenter							
学会名 Conference							
演　題 Topic							
開催日 date	年　　月　　日		開催地 venue				
形式　method	□　口頭発表　Oral	□　ポスター発表　Poster	言語　Language	□　日本語	□　英語	□　中国語	
共同演者名 Co-presenter							

4. 受賞（研究業績）　Award (Research achievement)

名　称 Award name				
	国名 Country		受賞年 Year of award	年　　月
名　称 Award name				
	国名 Country		受賞年 Year of award	年　　月

5. 本研究テーマに関わる他の研究助成金受給 Other research grants concerned with your resarch them

受給実績 Receipt record	☐ 有　☐ 無
助成機関名称 Funding agency	
助成金名称 Grant name	
受給期間 Supported period	年　月 ～　年　月
受給額 Amount received	円
受給実績 Receipt record	☐ 有　☐ 無
助成機関名称 Funding agency	
助成金名称 Grant name	
受給期間 Supported period	年　月 ～　年　月
受給額 Amount received	円

6. 他の奨学金受給 Another awarded scholarship

受給実績 Receipt record	☐ 有　☐ 無
助成機関名称 Funding agency	
奨学金名称 Scholarship name	
受給期間 Supported period	年　月 ～　年　月
受給額 Amount received	円

7. 研究活動に関する報道発表 Press release concerned with your research activities

※記載した記事を添付してください。Attach a copy of the article described below

報道発表 Press release	☐ 有　☐ 無	発表年月日 Date of release	
発表機関 Released medium			
発表形式 Release method	・新聞　・雑誌　・Web site　・記者発表　・その他(　　)		
発表タイトル Released title			

8. 本研究テーマに関する特許出願予定 Patent application concerned with your research theme

出願予定 Scheduled	☐ 有　☐ 無	出願国 Application	
出願内容(概要) Application contents			

9. その他 Others

Under the guidance of my supervisor Professor Saiki, I successfully passed the PhD entrance exam at my university within five months of enrollment. Over the next three months, I also mastered several essential experimental techniques, including Western blotting, gene knockout, and viral transfection. Additionally, I have obtained some preliminary results in the project “Evaluation of Autophagy-Enhancing Activity of Albendazole Derivatives.”
I sincerely hope to continue my PhD research under Professor Saiki’s supervision. As a formal PhD student,I aim to improve my scientific English and write a review paper based on my literature reading, including papers published by my supervisor and cutting-edge advancements in this field. Furthermore,I will conduct experiments more rigorously, and strive to discover new findings during the PhD period and publish articles. I also plan to apply for JST SPRING funding in our university around June this year.

指導責任者(記名)　斉木 臣二

日中笹川医学奨学金制度<学位取得コース>中間評価書
【課程博士:指導教官用】

Supported by 日本財団 THE NIPPON FOUNDATION

第45期　　研究者番号:　G4502

氏名	穆姬莎 阿布力米提	MUYASHA ABULIMITI	性別	F	生年月日	1990/4/5
中国所属機関(役職)	中国医学科学院腫瘤医院深圳医院放射線治療科(主治医師)					
日本研究先(指導教官)	筑波大学医学医療系放射線腫瘍学(櫻井 英幸　教授)					
研究テーマ	難治性膠芽腫に対する相乗的併用療法のためのスマートナノファイバーメッシュの開発と検証					
専攻種別	論文博士	□	課程博士	☑		

研究者評価(指導教官記入欄)

成績状況	優・良・可・不可から選択してください⇒	優	取得単位数	19
	学業成績係数=		取得すべき単位総数	30
学生本人が行った研究の概要	1)難治性で知られる膠芽腫に対する新規治療法として、放射線との併用を念頭に置いたナノファイバーメッシュ(NFM)の開発に関わる研究を遂行している。具体的には、膠芽腫に対して標準的に使用される抗がん剤テモゾロミド(TMZ)と分子標的薬の1つであるHsp90阻害剤Pimitespib (TAS-116)を含有させたNFMによる放射線治療効果の向上を目指すものである。これまでに、TMZとTAS-116単剤での細胞毒性評価及び放射線増感効果について検討し、NFM合成に適した濃度検討を進めている。来年度早々に、2剤含有NFMを物質・材料研究機構との共同研究にて合成し、細胞および担がんマウスを用いた有効性および安全性評価を進める予定である。 2)研究テーマであるBNCTの研究動向を把握する目的で、2023年12月31日以前に報告されたBNCTに関する論文及び総説に対して計量書誌学的および視覚化分析を行い、研究トレンドとホットスポットを明らかにし、Frontiers in Oncology誌に投稿し、2024年12月に受理された。本研究へのAbulimiti氏の貢献は大きく、Yuyang Cong氏とのDouble first論文となっている。			
総合評価	【良かった点】 研究及び実験に対して真摯かつ貪欲であり、日々クリーンベンチに向かいながら、本研究室に来て初めて学んだ細胞培養及び放射線照射実験に関して、既に実験手技としては成熟してる。実験前に実験計画書を綿密に作成することで、実験時の誤り及び無駄を省き、また実験結果についても理解が十分ではないと判断すれば、すぐに指導教員に相談し、次の実験につなげるプロセスも問題ない。また、外部研究者との積極的なコラボレーションも行なっており、知見を広げるための活動にも余念がない。 【改善すべき点】 実験を推し進めることに重点を置きすぎ、実験室の整備や管理に対する貢献が不十分なことが散見された。具体的には、使用した実験機材の補充、ピペットなどの器具の定期メンテナンス等をより積極的に行うように心がけて欲しい。 【今後の展望】 既に薬剤単独及び放射線との併用効果についてはほぼ検討が済んでおり、NFMの合成から細胞及び担がんマウスを用いた有効性・安全性評価へと進む段階まで到達している。2025年度内に本実験を完了させ、論文投稿まで進める可能性は非常に高いと考えており、学位取得に向けて順調に進めていると判断する。			
学位取得見込	上述したように、研究は順調に進んでおり、期限内に十分学位を取得できると考える。			
評価者(指導教官記名)	櫻井英幸、松本孔貴	作成日:	2025年　2　月　28　日	

日中笹川医学奨学金制度<学位取得コース>中間報告書
【研究者用】

Supported by 日本財団 THE NIPPON FOUNDATION

第45期　　研究者番号：G4502　　作成日：2025年3月10日

氏名	穆婭莎 阿布力米提	MUYASHA ABULIMITI	性別	F	生年月日	1990/4/5
中国所属機関(役職)	中国医学科学院腫瘤医院深圳医院放射線治療科（主治医師）					
日本研究先（指導教官）	筑波大学医学医療系放射線腫瘍学（櫻井 英幸　教授）					
研究テーマ(日文)	難治性膠芽腫に対する相乗的併用療法のためのスマートナノファイバーメッシュの開発と検証					
Research theme	Development and verification of smart Nanofiber mesh for synergistic combination therapy against refractory glioblastoma					
専攻種別	論文博士	□	課程博士	☑		

1．研究概要（1）

1）目的（Goal）：The objective of this study is to develop a new sustained-release drug delivery system, PCL-Nanofiber mesh, for local brain implantation to improve GBM treatment efficacy, reduce side effects, and prevent recurrence.

2）戦略（Approach）：
To achieve the goal of developing a sustained-release drug delivery system for GBM treatment, we employed a multidisciplinary approach integrating biomaterials engineering, cell biology, and radiation oncology. Initially, the in vitro efficacy of TMZ, TAS116, and radiotherapy was assessed using U87MG glioblastoma cells through a series of assays. Subsequently, a PCL-nanofiber mesh was designed as a localized drug delivery platform to enable the sustained release of TMZ and TAS116, aiming to enhance treatment efficacy while minimizing systemic side effects..

3）材料と方法（Materials and methods）

Cell culture and drugs. A human cell line derived from GBM multiforme U87MG cells was purchased from the RIKEN BioResource Research Center. Cells were maintained in Eagle's minimum essential medium (E-MEM; Sigma-Aldrich, Tokyo, Japan) supplemented with 10% fetal bovine serum (FBS) and antibiotics (100 U/mL penicillin and 100 mg/mL streptomycin; Sigma-Aldrich) in a 5% CO2 incubator at 37 ° C for further experiments. The TAS116 was obtained from Sigma-Aldrich Japan (Tokyo, Japan). TMZ was purchased from Tokyo Chemical Industry Co., Ltd. (Tokyo, J)

Colony formation assay. Cell survival curves were determined by colony formation assay. Cells were seeded in 6 cm dishes or T25 flasks, incubated in a 5% CO2 incubator at 37 ° C for 48 h, and treated with drugs or irradiated with X-rays. After drug treatment or irradiation, cells were washed with PBS, separated from the dishes by 0.02% trypsin processing, diluted with a fresh medium, counted, and diluted. Cell suspensions expected to produce approximately 100 surviving cells were seeded into six cm culture dishes in triplicate and cultured for 14 days. Subsequently, the cells were fixed and stained with 10% formalin solution and 1% methylene blue solution (20% MtOH). The number of colonies was counted, with colonies consisting of 50 or more as significant colonies, and this was plotted as the cell survival rate to produce a cell survival curve.

Irradiation and radiosensitization of drugs. T98G cell suspensions containing 2.5 × 105/5 mL were added to T25 flasks and incubated for 48 h. Cultured T98G cells were treated with different concentrations of 17AAG (100 nM, 200 nM) or TMZ (150 μM, 500 μM) solutions for 24 h. Irradiation time was adjusted so that samples containing each concentration of 17AAG were irradiated at 0.8, 1.5, 2, 4, and 6 Gy, respectively. Samples containing TMZ were irradiated at doses of 0.8, 1.5, 3, and 6 Gy. A colony formation assay was conducted immediately after irradiation, and survival curves were obtained based on the survival rate with different irradiation and drug combinations. In this experiment, the sensitizing effect of TMZ and 17AAG drugs on radiation was determined by the sensitizer enhancement ratios (SERs). The SER is the ratio of the irradiation dose required to achieve a specific biological effect when irradiated alone and the irradiation dose required to achieve the same biological effect when irradiation is combined with the application of a radiosensitizer (such as drugs) [1]; after the application of a radiosensitizer, the irradiation dose can be reduced to achieve a specific biological effect when irradiated alone. SER > 1 indicates that the drug has a radiosensitization effect, and higher values suggest a more
substantial sensitization effect. SER = DO/DC (for a certain survival)

1．研究概要（2）

4）実験結果（Results）

1. The growth characteristics, radiation response, and drug sensitivity of U-87MG cells were analyzed. The cell growth curve indicated a doubling time of 24 hours. When exposed to X-ray radiation, the IC_{10} dose was determined to be 3.5 Gy, demonstrating the cells' sensitivity to radiation. The cytotoxicity assay of temozolomide (TMZ) revealed an IC_{50} value of 138.1 μM, indicating the concentration required to reduce cell viability by half. Furthermore, the combination of X-ray and TMZ treatment resulted in a lower survival fraction compared to radiation alone, suggesting a synergistic effect between the two treatments. Higher concentrations of TMZ further enhanced the cytotoxic effect, leading to greater tumor cell death.

2. The Radio sensitization of TMZ:

By interpolating the radiation dose corresponding to 50% cell survival, we determined that the 50% survival dose for X-ray alone was 1.922 Gy. Combined with 50 μM, 100 μM, and 130 μM TMZ, the corresponding doses were 1.724 Gy, 0.9476 Gy, and 0.6138 Gy, respectively. The calculated sensitizer enhancement ratios (SER) were 1.11, 2.03, and 3.13, respectively, indicating that TMZ exhibited significant radiosensitizing effects. increasing TMZ concentration improves its effectiveness in sensitizing glioblastoma cells to radiation therapy.

5）考察（Discussion）

Our research aims to develop a more effective and long-lasting treatment strategy by combining nanofiber mesh loaded with TAS116 and TMZ with radiotherapy. The initial phase of our study focused on investigating the synergistic effects of TMZ and TAS116, as well as their radiosensitizing effects when combined with X-ray irradiation.

In the previous year, our team began by characterizing the growth properties of U87MG glioblastoma cells. Subsequently, we irradiated the cells with X-rays and observed an exponential decline in tumor cell survival as radiation doses increased. We then evaluated the cytotoxic effects of TMZ and TAS116 on U87MG cells, determining their IC50 values. Further experiments combining different concentrations of these drugs with radiation revealed a dose-dependent increase in tumor cell killing, demonstrating enhanced cytotoxicity with increasing drug and radiation doses.

Moving forward, we will further explore the synergistic effects of TAS116 and TMZ, employing a PCL-nanofiber mesh as a localized drug delivery platform to achieve sustained release of these agents, aiming to optimize GBM treatment outcomes.

6）参考文献（References）

1. Navarra G, Pagano C, Pacelli R, Crescenzi E, Longobardi E, Gazzerro P, Fiore D, Pastorino O, Pentimalli F, Laezza C, Bifulco M. N6-Isopentenyladenosine Enhances the Radiosensitivity of Glioblastoma Cells by Inhibiting the Homologous Recombination Repair Protein RAD51 Expression. Front Oncol. 2020 Jan 14;9:1498. doi: 10.3389/fonc.2019.01498. PMID: 31993371; PMCID: PMC6971108.

2. 執筆論文　Publication of thesis　※記載した論文を添付してください。Attach all of the papers listed below.

論文名 1 Title	Proton beam therapy in a patient with secondary glioblastoma (32 years after postoperative irradiation of medulloblastoma): case report and literature review				
掲載誌名 Published journal	Radiation Oncology				
	2024 年 10 月	19 巻（号）	136 頁 ～ 144 頁	言語 Language	English
第1著者名 First author	Bai Jiwei1	第2著者名 Second author	Muyasha Abulimiti (co-first author)	第3著者名 Third author	Jin Yonglong
その他著者名 Other authors	Wang Jie5, Zhang Shuyan6, Liu Chao6, Wang Zishen5, Wang Wei7, Li Yinuo8, Wang Weiwei6, Yang Lu6 , Shosei Shimizu6, 8*				
論文名 2 Title	Current research trends and hotspots of boron neutron capture therapy: a bibliometric and visualization analysis				
掲載誌名 Published journal	Frontier in Oncology				
	2024 年 12 月	14 巻（号）	1 頁 ～ 18 頁	言語 Language	English
第1著者名 First author	Yuyang Cong	第2著者名 Second author	Muyasha Abulimiti	第3著者名 Third author	Yoshitaka Matsumoto
その他著者名 Other authors	Jing Jin				
論文名 3 Title					
掲載誌名 Published journal					
	年 月	巻（号）	頁 ～ 頁	言語 Language	
第1著者名 First author		第2著者名 Second author		第3著者名 Third author	
その他著者名 Other authors					
論文名 4 Title					
掲載誌名 Published journal					
	年 月	巻（号）	頁 ～ 頁	言語 Language	
第1著者名 First author		第2著者名 Second author		第3著者名 Third author	
その他著者名 Other authors					
論文名 5 Title					
掲載誌名 Published journal					
	年 月	巻（号）	頁 ～ 頁	言語 Language	
第1著者名 First author		第2著者名 Second author		第3著者名 Third author	
その他著者名 Other authors					

3. 学会発表 Conference presentation ※筆頭演者として総会・国際学会を含む主な学会で発表したものを記載してください。

※Describe your presentation as the principal presenter in major academic meetings including general meetings or international meetings.

学会名 Conference	2024 American Society for Radiation Oncology(ASTRO) Annual Meeting			
演 題 Topic	Exploration of Flap-Protected Hypofractionated Radiotherapy in Patients with Locally Advanced Autologous Reconstructive Breast Cancer			
開催日 date	2024 年 9 月 30 日	開催地 venue	Washington USA	
形式 method	☐ 口頭発表 Oral ☑ ポスター発表 Poste	言語 Language	☐ 日本語 ☑ 英語 ☐ 中国語	
共同演者名 Co-presenter				
学会名 Conference	第4回 日本量子医科学会 学術大会			
演 題 Topic	Current research trends and hotspots of boron neutron capture therapy: a bibliometric and visualization analysis			
開催日 date	2024 年 12 月 6 日	開催地 venue	国立研究開発法人量子科学技術研究開発機構 千葉市	
形式 method	☐ 口頭発表 Oral ☑ ポスター発表 Poste	言語 Language	☐ 日本語 ☑ 英語 ☐ 中国語	
共同演者名 Co-presenter				
学会名 Conference	JST-SPRING/BOOS 2024年度研究発表会			
演 題 Topic	The smart nanofiber system with locally sustained drug release enabled synergistic combination therapy for glioblastoma			
開催日 date	2024 年 12 月 5 日	開催地 venue	くば国際会議場（エポカルつくば）	
形式 method	☐ 口頭発表 Oral ☑ ポスター発表 Poste	言語 Language	☐ 日本語 ☑ 英語 ☐ 中国語	
共同演者名 Co-presenter				
学会名 Conference				
演 題 Topic				
開催日 date	年 月 日	開催地 venue		
形式 method	☐ 口頭発表 Oral ☐ ポスター発表 Poste	言語 Language	☐ 日本語 ☐ 英語 ☐ 中国語	
共同演者名 Co-presenter				

4. 受賞（研究業績）Award (Research achievement)

名 称 Award name				
	国名 Country name		受賞年 Year of	年 月
名 称 Award name				
	国名 Country name		受賞年 Year of	年 月

研究者番号：G4502

5．本研究テーマに関わる他の研究助成金受給 Other research grants concerned with your resarch t

受給実績 Receipt record	□ 有　□ 無
助成機関名称 Funding agency	
助成金名称 Grant name	
受給期間 Supported period	年　月 ～　年　月
受給額 Amount received	円
受給実績 Receipt record	□ 有　□ 無
助成機関名称 Funding agency	
助成金名称 Grant name	
受給期間 Supported period	年　月 ～　年　月
受給額 Amount received	円

6．他の奨学金受給 Another awarded scholarship

受給実績 Receipt record	■ 有　□ 無
助成機関名称 Funding agency	Japan Science and Technology Agency (JST)
奨学金名称 Scholarship name	JST-SPRING
受給期間 Supported period	2024 年 4 月 ～ 2028 年 4 月
受給額 Amount received	180,000 円

7．研究活動に関する報道発表 Press release concerned with your research activities

※記載した記事を添付してください。 Attach a copy of the article described below

報道発表 Press release	□ 有　□ 無	発表年月日 Date of release	
発表機関 Released medium			
発表形式 Release method	・新聞　・雑誌　・Web site　・記者発表　・その他（　）		
発表タイトル Released title			

8．本研究テーマに関する特許出願予定 Patent application concerned with your research theme

出願予定 Scheduled	□ 有　□ 無	出願国 Application	
出願内容（概要） Application contents			

9．その他 Others

指導責任者（記名） 福可美等

Jiwei *et al. Radiation Oncology* (2024) 19:136
https://doi.org/10.1186/s13014-024-02515-5

Radiation Oncology

CASE REPORT Open Access

Proton beam therapy in a patient with secondary glioblastoma (32 years after postoperative irradiation of medulloblastoma): case report and literature review

Bai Jiwei[1†], Muyasha Abulimiti[2†], Jin Yonglong[3,4], Wang Jie[5], Zhang Shuyan[6], Liu Chao[6], Wang Zishen[5], Wang Wei[7], Li Yinuo[8], Wang Weiwei[6], Yang Lu[6] and Shosei Shimizu[6,8*]

Abstract

Objective This report details the experience of a patient who developed a second primary glioblastoma (GB), offering insights into the treatment process and reviewing relevant literature.

Case presentation A male patient, who was diagnosed with medulloblastoma at age 9, received treatment with cobalt-60 craniospinal irradiation (CSI) (36 Gy/20 fractions) and a tumor bed boost (total of 56 Gy). After 32 years, at age 41, an MRI revealed a space-occupying mass in the left cerebellar hemisphere. Surgical resection was performed, and postoperative pathology confirmed a diagnosis of radiation-induced glioblastoma (RIGB). Given the history of irradiation and the current tolerability of brainstem doses, proton beam therapy (PBT) combined with Temozolomide (75 mg/m^2) was chosen. The treatment plan included 60 Gy on the gross tumor bed and 54 Gy on the clinical target volume, delivered in 30 fractions. The patient underwent regular follow-up and achieved a complete response.

Clinical discussion For childhood cancer survivors, the development of a second primary tumor significantly impacts prognosis. RIGB is a rare form of secondary tumor with distinct molecular characteristics compared to primary GB and recurrent secondary GB. Molecular markers such as IDH and MGMT status can help differentiate between primary GB, recurrent secondary GB, and radiation-induced secondary GB in patients with a history of prior radiation therapy. Surgical resection remains a primary treatment option, while PBT is preferred for postoperative treatment due to its superior protection of normal tissues and the ability to deliver high-dose irradiation.

Conclusion RIGB is a rare second primary tumor that requires strategic molecular profiling and individualized management. Proton beam therapy provides effective high-dose irradiation in the postoperative phase and is the preferred treatment option for such cases.

†Bai Jiwei and Muyasha Abulimiti are co-first authors.

*Correspondence:
Shosei Shimizu
23s.showsay.shimizu@gmail.com

Full list of author information is available at the end of the article

Keywords Medulloblastoma, Second primary tumor, Radiation-induced glioblastoma, Proton beam radiotherapy

Introduction

Historically, the priority for treating medulloblastoma (MB) in children has been avoidance of undue side effects while achieving tumor control. As diagnostic and therapeutic techniques for such tumors increasingly have become more standardized, particularly through molecular subgroup stratification and multidisciplinary regimens (i.e., surgery, chemotherapy, and radiotherapy), the potential for survival or cure has significantly improved. At the same time, there has been an upturn in subsequent occurrences of second primary tumors (SPTs) [1]. The International Agency for Research on Cancer (IARC) [2] has defined in which a patient harbors two or more primary tumors simultaneously or successively. Initially diagnosed tumors are considered primary lesions, whereas those arising later are designated SPTs. Central nervous system (CNS) is the most frequent site for SPT emergence, followed by endocrine and hematologic systems [3]. However, there is less data on glioblastoma (GB) as a SPT and its preferred mode of therapy after treatment of MB.

The purpose of this article was to share our experience with a patient who developed a second primary GB. The latter occurred 32 years after previously administered craniospinal irradiation (CSI) for MB as a child. We intended to provide insights into the treatment process and review relevant publications in the literature.

Case presentation

In February 1991, our male patient (then 9 years old) presented with complaints of dizziness, vomiting, and loss of balance for 6 months. His condition had worsened recently, during the past month. Imaging studies disclosed a cerebellar tumor (30×25×25 mm) that was surgically removed on February 11, 1991. The pathology report confirmed MB, so cobalt-60 CSI (36 Gy/20 fractions) was delivered postoperatively, with a tumor bed boost (total of 56 Gy). He was monitored regularly thereafter, undergoing annual brain magnetic resonance imaging (MRI), but no chemotherapy was given.

In March 2023 (32 years later), a space-occupying mass of left cerebellar hemisphere was detected by MRI. By June 25, 2023, loss of balance and difficulty walking had developed. A subsequent brain MRI again showed a mass of left cerebellar hemisphere, roughly 50.3×47×51.1 mm in size (Fig. 1A). On July 6, 2023, left cerebellar hemispheric resection was performed using the prior incision line at left cerebellopontine angle. The tumor within was soft and richly vascularized, with no clearly demarcated borders. Once separated along its apparent boundaries, it measured approximately 50×50×45 mm. The brainstem was well protected, as were various cranial nerves (ipsilateral posterior group, facial, auditory, trigeminal, abducens) and other structures. Postsurgical recovery was event-free.

Representative histologic preparations revealed a high-grade and diffusely infiltrating neuroepithelial tumor of left cerebellum. For the most part, this lesion was densely cellular, demonstrating marked pleomorphism and tumor giant cells in conjunction with microvascular proliferation and fenestrated necrosis. Its immunohistochemical and morphologic features were compatible with radiation-induced glioblastoma (RIGB), World Health Organization (WHO) Grade IV. Results of immunostaining are provided in Table 1, and additional evidence to support a diagnosis of RIGB is offered in Table 2.

Proton beam radiotherapy (PBT)

At this juncture, the patient was a 41-year-old man scoring 90 by Kanefsky Performance Scale. His medical history and past treatment did not preclude reirradiating the same area. Based on current and previous ranges of irradiation and the dosing tolerability of brainstem, proton beam therapy (PBT) was selected, hoping to minimize brainstem and spinal cord exposure. The patient received treatment on August 7, 2023, 1 month after surgery. We defined postoperative tumor bed area and contrast-enhanced volume in T1 fat-saturated contrast-enhanced MRI scan as gross tumor volume (GTVtb), adding a 5-mm clinical target volume (CTV) margin. Treatment planning relied on a RayStation platform (RaySearch Laboratories, Stockholm, Sweden) for inversely planned intensity-controlled (raster-scanned) proton delivery using two horizontal beams. GTVtb and CTV doses were 60 Gy and 54 Gy, respectively in 30 fractions each (Fig. 2). Maximum doses (Dmax values) to spinal cord and brain were 43.5 Gy and 53.5 Gy, respectively. Mean doses (Dmean values) to left and right hippocampus were 33 Gy and 0.95 Gy, respectively. Temozolomide (TMZ, 75 mg/m^2) was administered on days of radiotherapy, followed by postradiotherapy TMZ maintenance (200 mg/m^2 daily) for 5 days and cyclic dosing (every 28 days) for 6 months.

During the 32-year course of patient monitoring, multiple meningiomas had also arisen as SPTs, the first diagnosed in December 2008. One was removed in March 2009, but several non-resected meningiomas were under continued observation. To date, there is no evidence of recurrence or size increases, indicating stable disease. Likewise, MRI views of tumor bed remain devoid of high signal intensity nearly 1 year after completing radiotherapy. Aside from mild dizziness, the patient has

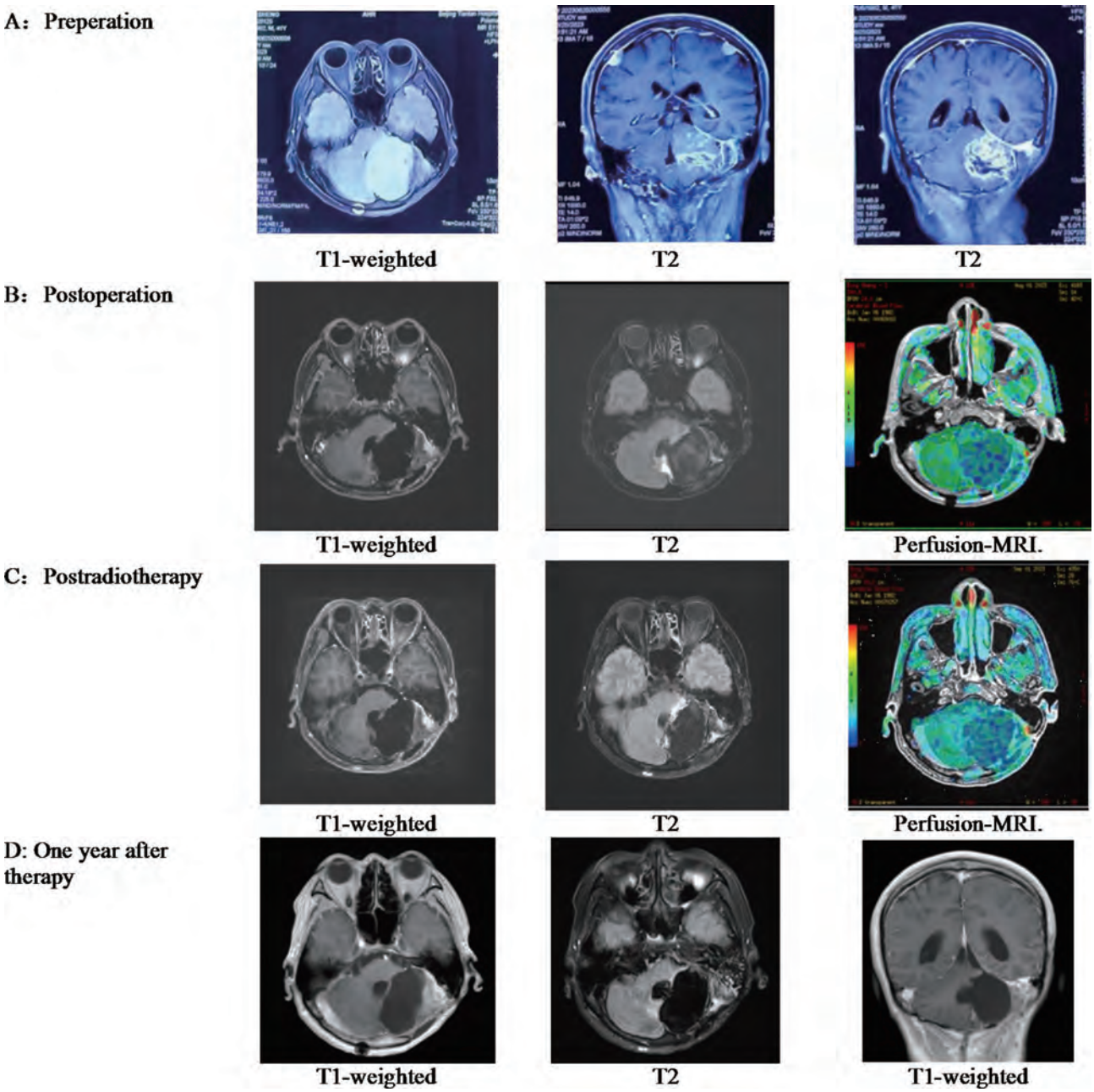

Fig. 1 Magnetic resonance imaging studies of 41-year-old male patient: **(A)** space-occupying mass of left cerebellar hemisphere (50.3 × 47 × 51.1 mm); **(B)** striated circumferential enhancement of tumor bed 1 month after surgery and 3D-arterial spin labeling (ASL) sequence showing localized, string-like, slightly hyperperfused operative margins; **(C)** less margin enhancement at operative site, compared with pretreatment baseline, but no real hyperperfusion of operative margins in 3D-ASL sequence; and **(D)** high intensity signal absent from tumor bed, 1 year after radiotherapy

experienced no other discomfort. A chronologic overview of the key medical events elaborated is included as Fig. 3.

Discussion

Herein, we have chronicled the medical course a childhood cancer survivor, including 32 years of follow-up after surgery and radiotherapy for MB and similar treatment imposed by a rare RIGB of later adult life. In this instance, PBT afforded access to high-dose, second-phase postoperative radiotherapy.

Second primary tumors (SPTs)

For survivors of childhood cancer, the cumulative incidence of SPTs arising within 30 years after initial tumor diagnoses ranges from 3 to 10% [3]. This is roughly 3–6 times higher than comparable rates in the general population. The most common SPTs encountered are breast

Table 1 Immunohistochemical features of primary and secondary glioblastoma

Tumor marker	Secondary GB [4]	Primary GB [5]	Present case
GFAP	**Positive (GFAP+)**	**Positive (GFAP+)**	**Positive (GFAP+)**
Olig-2	Positive (Olig-2+)	Positive (Olig-2+)	Positive (Olig-2+)
IDH1 R132H	Positive (IDH1 R132H+)	Negative (IDH1 R132H-)	**Negative (IDH1 R132H-)**
IDH2 R172K	Positive (IDH2 R172K+)	Negative (IDH2 R172K-)	**Negative (IDH2 R172K-)**
ATRX	Negative (ATRX-)	Positive/Negative (varies)	Negative (ATRX-)
p53	Positive (p53+)	Negative (p53-)	**Negative (p53-)**
Ki-67	Approximately 30%	Typically high (varies)	Approximately 30%
Synaptophysin	Positive (Syn+)	Positive/Negative (varies)	**Weak Positive (Syn weak +)**
H3K27M	Negative (H3K27M-)	Negative (H3K27M-)	Negative (H3K27M-)
H3K27me3	Typically retained	Typically retained	**Partial expression missing**
EZH2	Positive (EZH2+)	Variable (EZH2+)	**Negative (EZH2-)**
MTAP	Negative (MTAP-)	Negative (MTAP-)	Negative (MTAP-)
SOX11	Positive (SOX11+)	Variable (Positive/Negative)	Positive (SOX11+)
MSH6	Positive (MSH6+)	Positive (MSH6+)	Positive (MSH6+)
MSH2	Positive (MSH2+)	Positive (MSH2+)	Positive (MSH2+)
MLH1	Positive (MLH1+)	Positive (MLH1+)	Positive (MLH1+)
PMS2	Positive (PMS2+)	Positive (PMS2+)	Positive (PMS2+)
MGMT promoter methylation	**Methylated**	**Variable (methylated/non-methylated)**	**Methylated**
IDH1/IDH2	Mutant	Wild type	Wild type
1p/19q deletion	No deletion	No deletion	No deletion
EGFR amplification	No amplification	Often amplified	No amplification
CDKN2A deletion	Common (pure deletion)	Common	Pure deletion
CDKN2B deletion	Common (pure deletion)	Common	Pure deletion

Table 2 Differing profiles of secondary GB (recurrent vs. radiation induced)

Characteristic	Recurrent secondary GB [6]	Radiation-induced secondary GB
Etiology	Progression from low-grade or intermediate-grade glioma	Development after radiotherapy for other conditions (e.g., leukemia, brain tumor)
IDH mutation	Common (especially IDH1 R132H mutation)	Rare
TP53 mutation	Common	Possible, but less frequent
ATRX inactivation	Common	Possible
MGMT promoter methylation	Common	Possible
TERT promoter mutation	Rare	Possible
1p/19q co-deletion	Rare	Rare
Typical patient age	Usually younger patients	Usually older patients
Medical history	History of low-grade or intermediate-grade glioma	History of radiotherapy for other tumors or diseases
Other chromosomal abnormalities	Common specific chromosomal mutation patterns	May have more heterogeneous chromosomal mutations and structural variations

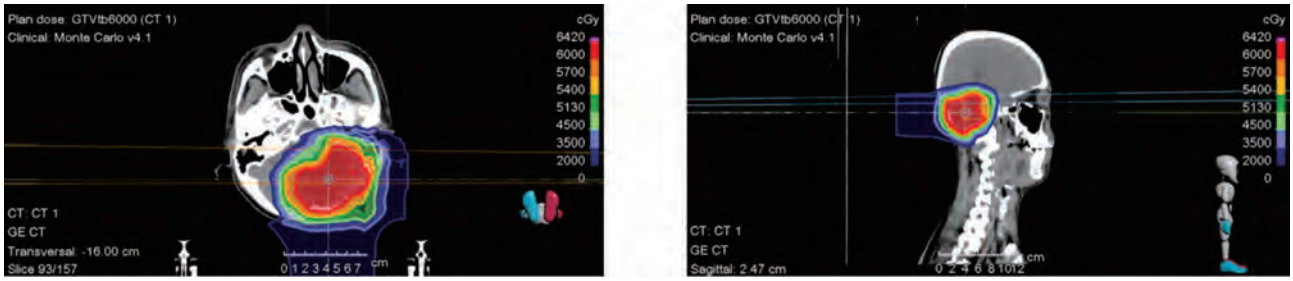

Fig. 2 Postoperative proton beam therapy plan (gross tumor volume [GTVtb] in red; clinical target volume [CTV] in dark green)

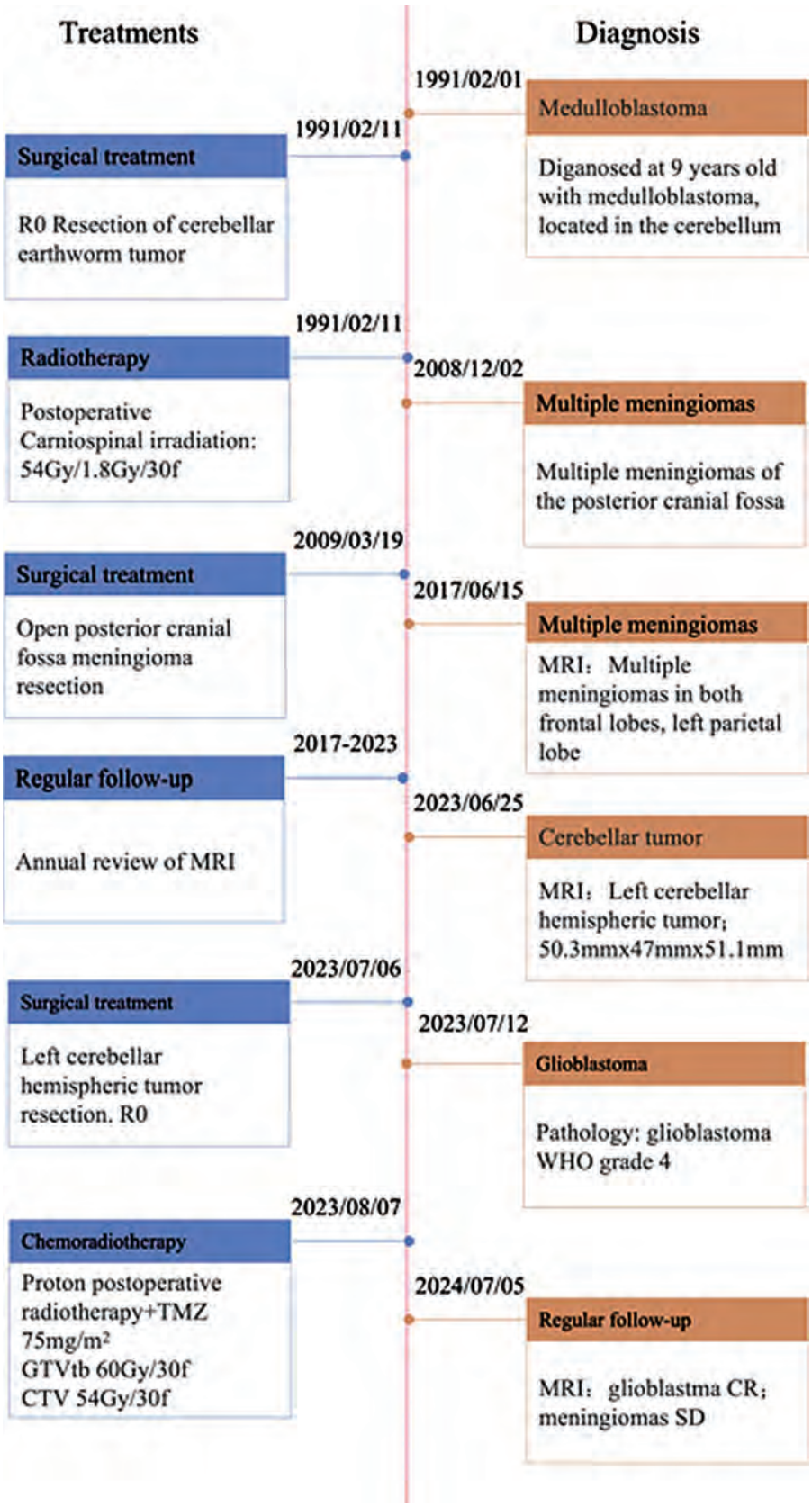

Fig. 3 Timeline of events during 32-year patient surveillance period

cancer for female survivors, ranging from 12 to 20%; thyroid cancer, estimated at 2–7%; and skin cancer, exceeding general population risk by 2–6 times [7, 8]. GB is a relatively rare SPT as such, but it is a recognized risk, particularly for recipients of cranial radiotherapy. More so than chemotherapy, irradiation is usually associated with a higher incidence of SPT (9.5% vs. 2.4%) [3], given its capacity to alter DNA methylation and methyltransferase activity and its deregulation of mRNA.

MB is a common childhood tumor, the overall survival of which has improved through combined use of radiotherapy, chemotherapy, and surgery. Current survival rates are ~80–85% for standard risk groups and ~65–70% for high-risk groups. However, long-term toxic effects (especially SPTs) are increasing as a result. In the aftermath of MB, CNS is reportedly the most common site of SPTs (63/146, 43.2%), followed by endocrine and hematologic systems. Similar outcomes have been documented during the Childhood Cancer Survivor Study and its British counterpart probe, likely due to whole brain and spinal axis targeting during CSI [7, 9]. The unique physical properties entailed have broadened the usage of PBT in treating childhood cancer. Proton doses are characterized by abrupt surges in energy release, called Bragg peaks. Such rapid dosing decays reduce radiation to nearby healthy tissues by a factor of 2–3. However, monitoring of treated patients for potential SPTs is a long-term proposition, and available research on SPT incidence by mode of MB treatment (proton vs. photon therapy) is currently lacking.

Raymond [10] has generated estimates of secondary cancer incidence using a model derived from Publication No. 60 of the International Commission on Radiologic Protection. Compared with intensity-modulated or conventional X-ray plans, proton beams lowered the expected incidence of radiation-induced secondary cancers after MB treatment by a factor of 8–15. An analysis of the SEER database from mid-2000s forward, ostensibly marked by greater PBT use, has also confirmed fewer SPTs as late effects [3]; and in another assessment according to treatment time frames (1973–1995 vs. 1995–2014), the SPT rate proved higher during earlier years (1973–1995) of more limited PBT use [11]. Matched adult populations ($n=558$ each) receiving proton or photon therapy have been followed as well (median interval: proton group, 6.7 years; photon group, 6.0 years) [12], recording SPT rates of 5.2% and 7.5%, respectively. Above findings imply a lower incidence of SPT after PBT of childhood MB. On the other hand, most present-day survivors of pediatric tumors have received photon therapy over a decade ago, so longer follow-up periods may be needed to ascertain SPT incidence in relation to PBT.

Radiation-induced second primary glioblastoma (RIGB)

Classification of a second primary GB as radiation induced (rather than recurrent second primary) [13–15] is based on the following criteria: (1) tumor situated within the irradiated field; (2) sufficient latency between irradiation and tumor occurrence; (3) histological type different from that of original neoplasm; and (4) no pathology, such as Von Recklinghausen disease, favoring tumor development. The most common malignancies associated with RIGB are nasopharyngeal carcinoma (37%), primary intracranial germinoma (21%), and MB (16%) [16]. At 9 years of age, our patient with MB received postoperative CSI only. In analyzing 2771 patients with MB from the SEER-18 database, there were 146 patients (5.27%) who developed SPTs at 15 years. Rates of SPTs after radiotherapy only, radio- and chemotherapy, and chemotherapy only were 9.5%, 4.3%, and 2.4%, respectively [3]. Several studies have shown a 14-year mean latency between radiotherapy and diagnosis of RIGB, unlike the 32-year span in our patient that surpassed most previously published intervals [11, 14]. It is a widely held concept that the younger a patient is at primary treatment, the greater the risk of RIGB will be. Younger onset may therefore render patients especially vulnerable to radiation-induced gliomagenesis in later years due to an abundance of neurogenic stem cells and increased growth factor activity [17].

RIGB is a relatively rare SPT, with a molecular profile that distinguishes it from primary GB and recurrent secondary GB. Clinicians focus more on recurrent secondary GB, tending to overlook the specific and individualized treatment of RIGB. *IDH* mutation is a critical marker in glioma classification that helps differentiate recurrent and radiation-induced forms of secondary GB (Tables 1 and 2). *IDH* mutations are largely features of less ominous tumors (WHO grade II-III), whereas the *IDH* wild type primarily reflects aggressive disease (WHO grade IV), signaling a worse prognosis. In 2021, the latest WHO revision of GB grading was substantial, stipulating that only *IDH* wild-type lesions warrant a GB diagnosis [5]. Still, there are perhaps some GBs with *IDH* mutations. The latter have chiefly presented as secondary GBs, morphologically similar to primary GB but imparting a more favorable prognosis [18]. In patients with *IDH*-mutant GBs, median OS may be ~31 months, as opposed to 15 months for those with *IDH*-wildtype GBs [18, 19].

Among 39 patients with secondary GBs, the *IDH* mutation rate was found to be 60%, and the O6-methylguanine-DNA methyltransferase (MGMT) promoter methylation rate was 68.8% [20]. MGMT is a direct DNA repair enzyme that eliminates the TMZ-produced genotoxic O6-methylguanine adduct in a single-step process. Because this restores the genomic integrity of tumors,

MGMT promoter methylation denotes a better prognosis. An earlier meta-analysis has determined a median OS (mOS) of 10 months in patients with RIGBs [Peter Y. M]. Across the spectrum of grade IV GBs, survival in patients with RIGBs (mOS, 4.8 months) was shorter than in instances of *de novo* GB (mOS, 19.2 months; $p<0.001$). These findings may be explained by the fact patients with *IDH* wild type were involved, and there was a lower percentage of MGMT promoter methylation [14]. Our patient with WHO grade IV GB exhibited both *IDH* mutation and MGMT promoter methylation, thus suggesting TMZ sensitivity and a better prognosis than anticipated for primary or recurrent secondary GB of *IDH* wild type.

RIGB treatment

Currently, there is no consensus on oncologic treatment in instances of RIGB. Studies have concluded that patients with secondary GBs experience significantly longer survival times if repeat resection is elected, instead of foregone [20]. Patients with good KPS scores and proper suitability for surgery should subsequently consider second-phase resection as a primary treatment option, although decisions on postoperative adjuvant therapy are comparatively more difficult. Physicians must weigh the perceived benefit of reirradiation against the risk of related brain damage.

In the past, the conventional dose limit for partial brain radiotherapy has been 60 Gy. Some sources have challenged this view, suggesting that reirradiated brain tissue may tolerate a fractionated (2 Gy/fr) cumulative normalized total dose of 100 Gy before necrosis ensues [13]. Paulino et al. have noted that among patients with radiotherapy-induced high-grade gliomas, those who received reirradiation of 50 Gy (35/85, 41%) displayed a 2-year overall survival (OS) rate of 21%. This was significantly better than the 3% rate recorded at 2 years in the absence of reirradiation [21]. Similarly, a meta-analysis has found that reirradiation (mean dose, 48 Gy) conferred a better 2-year OS rate (24%) than the rate achieved (9%) through different treatment. Upon examining factors linked to survival in the setting of grade III-IV RIGB, multimodality combination therapy (including radiotherapy) was identified as an independent prognostic factor ($p=0.002$) [16]. These observations suggest that in some patients with radiation-induced gliomas, a therapeutic strategy of reirradiation may serve to prolong disease control. However, the tolerance threshold is changing due to advances in radiotherapy technology, such as PBT. These improvements stand to mitigate the risk of late radiation effects. Despite a scarcity of data on PBT use for reirradiation of RIGB, we are encouraged by its successful application in patients with recurrent gliomas or other brain tumors. Scartoni et al. [22] have investigated 33 patients who completed questionnaires before starting PBT, on last day of treatment, and at every follow-up visit until disease progression. It appears that PBT is safe and well tolerated, ensuring stable quality-of-life parameters for the duration.

The Proton Collaborative Group (PCG) has examined 45 patients from 12 PBT centers in the United States, all receiving photon radiotherapy initially at doses of 60 Gy. The median time between original diagnosis and recurrence was only 20 months, and the median total reirradiation dose was 46.2 Gy (range, 25–60 Gy), with a median of 2.2 Gy per fraction. Of these 45 patients, 40 (88.9%) had received an equivalent dose in 2 Gy fractions (EQD2) of >39 Gy. All patients had GB as their primary diagnosis. Median progression-free survival (PFS) time was 13.9 months, and median OS was 14.2 months. In terms of side effects, a total of five patients experienced grade 3 toxicity. One showed acute toxicity (ataxia), whereas late toxicity (neuropathy, cognitive disturbance, optic nerve disorder, or seizure) surfaced in the other four. No acute or delayed grade 4 or 5 toxicities were observed.

During a similar multicenter study, patients with GB were reirradiated at high dose, without serious side effects over a year's time, highlighting the utility of PBT for this purpose [23]. Another 20 patients who received proton reirradiation for recurrent gliomas also registered acceptable outcomes after high-dose radiotherapy. The mean initial dose was 59.4 Gy, and the mean reirradiation dose after a median of 15.3 months (range, 5.3-152.6 months) was 54 Gy [24]. Several earlier investigations have further reinforced the prospect of high-dose irradiation enabled by PBT.

When irradiating our patient (32 years after initial radiotherapy), we used a standard postoperative dose of 60 Gy, delivering a low dose to brainstem and hippocampus. The Dmax of brain scan was 53.5 Gy, the Dmean of left hippocampus was 33 Gy, and the Dmean of right hippocampus was 0.95 Gy. Although the prognosis of a grade IV RIGB is poor, lessening our concerns over later clinically significant necrosis, it is important for physicians to optimally protect a patient's cognitive function. The incidence of radiation necrosis typically peaks around 1–3 years after radiotherapy [25]. At 1 year after reirradiation, no signs of tumor recurrence or radiation necrosis have been detected as yet.

In summary, RIGB is a rare SPT determined by strategic molecular profiling and requiring individualized management. PBT is the preferred postoperative treatment.

Abbreviations

SPT	Second primary tumors
IARC	International Agency for Research on Cancer
CNS	Central Nervous System
CSI	Craniospinal Irradiation
MRI	Magnetic Resonance Imaging
CPA	Cerebellopontine Angle region

IHC	Immunohistochemistry
RIGB	Radiation-induced Glioblastoma
NPC	Nasopharyngeal Cancer
NOS	Not Otherwise Specified
WHO	World Health Organization
KPS	Karnofsky Performance Status
OS	Overall Survival
PFS	Progression-free Survival
PCG	Proton Collaborative Group
PBT	Proton beam therapy

Author contributions
Bai Jiwei and Shousei Shimizu contributed to formulating the surgical and radiotherapy treatment programs. Data collection and the first draft of the manuscript were written by MA. All authors provided comments on previous versions of the manuscript. Wang Jie, Zhang Shuyan, Liu Chao, and Wang Zishen contributed to the diagnosis and radiotherapy treatment. All authors read and approved the final manuscript.

Funding
Not applicable.

Data availability
No datasets were generated or analysed during the current study.

Declarations

Consent for publication
Written informed consent for publication was obtained from all participants.

Competing interests
The authors declare no competing interests.

Author details
[1]Department of Neurosurgery, Beijing Tiantan Hospital, Capital Medical University, Beijing 100050, China
[2]Department of Radiation Oncology, Graduate School of Comprehensive Human Sciences, University of Tsukuba, Tsukuba 305-8575, Japan
[3]Department of Radiotherapy, The Affiliated Hospital of Qingdao University, Qingdao, China
[4]School of Public Health, Qingdao University, Qingdao 266071, China
[5]Department of Radiotherapy Physics and Technology, Hebei Yizhou Cancer Hospital, Zhuozhou 072750, China
[6]Department of Pediatric Radiation Therapy Center/Pediatric Proton Beam Therapy Center, Hebei Yizhou Cancer Hospital, Zhuozhou 072750, China
[7]Department of Radiology, Hebei Yizhou Cancer Hospital, Zhuozhou 072750, China
[8]Department of Radiotherapy, University of Tsukuba Hospital, Tsukuba 305-8576, Japan

Received: 17 July 2024 / Accepted: 1 September 2024
Published online: 05 October 2024

References

1. Turcotte LM, Neglia JP, Reulen RC, et al. Risk, risk factors, and surveillance of subsequent malignant neoplasms in survivors of childhood cancer: a review. J Clin Oncol. 2018;36:2145.
2. Report WG. International rules for multiple primary cancers (ICD-0 third edition). Eur J cancer Prevention: Official J Eur Cancer Prev Organisation (ECP). 2005;14:307–8.
3. Nantavithya C, Paulino AC, Liao K, et al. Development of second primary tumors and outcomes in medulloblastoma by treatment modality: a surveillance, epidemiology, and end results analysis. Pediatr Blood Cancer. 2020;67:e28373.
4. Ohgaki H, Kleihues P. The definition of primary and secondary glioblastoma. Clin Cancer Res. 2013;19:764–72.
5. Mahajan S, Suri V, Sahu S, et al. World Health Organization Classification of Tumors of the central nervous system 5th Edition (WHO CNS5): what's new? Indian J Pathol Microbiol. 2022;65:S5–13.
6. Kleihues P, Ohgaki H. Primary and secondary glioblastomas: from concept to clinical diagnosis. Neurooncology. 1999;1:44–51.
7. Reulen RC, Frobisher C, Winter DL, et al. Long-term risks of subsequent primary neoplasms among survivors of childhood cancer. JAMA. 2011;305:2311–9.
8. Turcotte LM, Whitton JA, Friedman DL, et al. Risk of subsequent neoplasms during the fifth and sixth decades of life in the childhood cancer survivor study cohort. J Clin Oncol. 2015;33:3568.
9. Turcotte LM, Liu Q, Yasui Y, et al. Temporal trends in treatment and subsequent neoplasm risk among 5-year survivors of childhood cancer, 1970–2015. JAMA. 2017;317:814–24.
10. Miralbell R, Lomax A, Cella L, Schneider U. Potential reduction of the incidence of radiation-induced second cancers by using proton beams in the treatment of pediatric tumors. Int J Radiation Oncology* Biology* Phys. 2002;54:824–9.
11. Nantavithya C, Paulino AC, Liao K, et al. Observed-to-expected incidence ratios of second malignant neoplasms after radiation therapy for medulloblastoma: a Surveillance, Epidemiology, and end results analysis. Cancer. 2021;127:2368–75.
12. Chung CS, Yock TI, Nelson K, et al. Incidence of second malignancies among patients treated with proton versus photon radiation. Int J Radiation Oncology* Biology* Phys. 2013;87:46–52.
13. Salvati M, Artico M, Caruso R, et al. A report on radiation-induced gliomas. Cancer. 1991;67:392–7.
14. Woo PY, Lee JW, Lam SW, et al. Radiotherapy-induced glioblastoma: distinct differences in overall survival, tumor location, pMGMT methylation and primary tumor epidemiology in Hong Kong Chinese patients. Br J Neurosurg. 2024;38:385–92.
15. Cahan WG, Woodard HQ, Higinbotham NL, et al. Sarcoma arising in irradiated bone: report of eleven cases. Cancer: Interdisciplinary Int J Am Cancer Soc. 1998;82:8–34.
16. Yamanaka R, Hayano A, Kanayama T. Radiation-induced gliomas: a comprehensive review and meta-analysis. Neurosurg Rev. 2018;41:719–31.
17. Tubiana M. Can we reduce the incidence of second primary malignancies occurring after radiotherapy? A critical review. Radiother Oncol. 2009;91:4–15.
18. Juratli TA, Kirsch M, Geiger K, et al. The prognostic value of IDH mutations and MGMT promoter status in secondary high-grade gliomas. J Neurooncol. 2012;110:325–33.
19. Yan H, Parsons DW, Jin G, et al. IDH1 and IDH2 mutations in gliomas. N Engl J Med. 2009;360:765–73.
20. Hamisch C, Ruge M, Kellermann S, et al. Impact of treatment on survival of patients with secondary glioblastoma. J Neurooncol. 2017;133:309–13.
21. Paulino AC, Mai WY, Chintagumpala M, et al. Radiation-induced malignant gliomas: is there a role for reirradiation? Int J Radiation Oncology* Biology* Phys. 2008;71:1381–7.
22. Scartoni D, Amelio D, Palumbo P, et al. Proton therapy re-irradiation preserves health-related quality of life in large recurrent glioblastoma. J Cancer Res Clin Oncol. 2020;146:1615–22.
23. Saeed AM, Khairnar R, Sharma AM, et al. Clinical outcomes in patients with recurrent glioblastoma treated with proton beam therapy reirradiation: analysis of the multi-institutional Proton Collaborative Group Registry. Adv Radiation Oncol. 2020;5:978–83.
24. Galle JO, McDonald MW, Simoneaux V, Buchsbaum JC. Reirradiation with Proton Therapy for Recurrent Gliomas. Int J Part Therapy. 2015;2:11–8.
25. Strenger V, Lackner H, Mayer R, Sminia P, Sovinz P, Mokry M, Pilhatsch A, Benesch M, Schwinger W, Seidel M, Sperl D, Schmidt S, Urban C. Incidence and clinical course of radionecrosis in children with brain tumors. A 20-year longitudinal observational study. Strahlenther Onkol. 2013;189(9):759–64.

Publisher's note

frontiers | Frontiers in Oncology

TYPE Systematic Review
PUBLISHED 12 December 2024
DOI 10.3389/fonc.2024.1507157

OPEN ACCESS

EDITED BY
Francesca Ballarini,
University of Pavia, Italy

REVIEWED BY
Elvira V. Grigorieva,
Institute of Molecular Biology and Biophysics FRC FTM, Russia
Jiejian Chen,
Guangzhou First People's Hospital, China
Naoki Komatsu,
Kyoto University, Japan

*CORRESPONDENCE
Jing Jin
jingjin1025@163.com
Yoshitaka Matsumoto
ymatsumoto@pmrc.tsukuba.ac.jp

RECEIVED 07 October 2024
ACCEPTED 25 November 2024
PUBLISHED 12 December 2024

CITATION
Cong Y, Abulimiti M, Matsumoto Y and Jin J (2024) Current research trends and hotspots of boron neutron capture therapy: a bibliometric and visualization analysis. *Front. Oncol.* 14:1507157. doi: 10.3389/fonc.2024.1507157

Current research trends and hotspots of boron neutron capture therapy: a bibliometric and visualization analysis

Yuyang Cong[1], Muyasha Abulimiti[2], Yoshitaka Matsumoto[2*] and Jing Jin[1,3*]

[1]Department of Radiation Oncology, National Cancer Center/National Clinical Research Center for Cancer/Cancer Hospital & Shenzhen Hospital, Chinese Academy of Medical Sciences and Peking Union Medical College, Shenzhen, China, [2]Department of Radiation Oncology, Faculty of Medicine, University of Tsukuba, Tsukuba, Ibaraki, Japan, [3]Department of Radiation Oncology, National Cancer Center/National Clinical Research Center for Cancer/Cancer Hospital, Chinese Academy of Medical Sciences and Peking Union Medical College, Beijing, China

Purpose: This study aimed to describe the trends, current hotspots, and future directions in boron neutron capture therapy (BNCT) through a bibliometric analysis.

Methods: Articles related to BNCT published before 2023-12-31 were retrieved from the Web of Science Core Collection database. VOSviewer, R, and CiteSpace were used for bibliometric analysis and visualization.

Results: A total of 3347 related publications from 1975 to 2023 were retrieved. Since a burst of published documents in 1992, the past three decades have witnessed continuous investigations into BNCT-related studies. Japan was the most productive country (794, 23.72%), followed by the USA (792, 23.66%), while the latter had the most citations. Kyoto University was the most influential institution. Ono K was the most prolific author, and *Applied Radiation and Isotopes* was the most popular journal. Ono K was the author that had the most total citations, followed by Barth RF. "Carborane", "boronophenylalanine", "glioblastoma", "sodium borocaptate", "cancer" and "drug delivery" were the most frequent keywords. The article "Dendrimers and dendritic polymers in drug delivery" had the most citations, whereas "Boron delivery agents for neutron capture therapy of cancer" had the highest outbreak value.

Conclusion: Over the past three decades, research on BNCT has expanded significantly, with the development of novel boron carriers with improved medicinal characteristics being the most extensively investigated area. Future research will likely focus on the validation and modification of current BNCT treatment modalities using conventional boron agents in brain tumors, accelerator-based neutron sources and the application of BNCT in more clinical scenarios.

KEYWORDS

boron neutron capture therapy, bibliometric analysis, research trends, VOSviewer, CiteSpace

1 Introduction

Cancer remains one of the most devastating diseases affecting humans. In 2022, it was responsible for approximately one in six deaths globally, with an estimated 9.7 million fatalities (1). A major hinderance to the definitive cure of cancer is the therapeutic ratio, which has yet to increase owing to the inherent limitations of current treatment modalities. With respect to oncological surgery, the established principle of securing wide resection margins undoubtedly improved patient outcomes; however, a few residual tumor cells beyond the resection margins can lead to recurrence and metastasis (2). Systemic therapies can effectively eliminate disseminated malignant cells, but their side effects are common and sometimes lethal (3, 4). In the field of radiation therapy (RT), considerable effort has been devoted to the precise delivery of planned ionization radiation to the designed target volume and nowhere else (5, 6). Nonetheless, unintended doses to adjacent vulnerable organs at risk (OARs) limit its application to post-RT recurrences or tumors in critical locations.

Boron neutron capture therapy (BNCT), in contrast, is a unique two-step radiotherapy featuring unprecedented precision (Figure 1). In the first step, the nonradioactive isotope boron-10 (10B)-containing agent is administered and enriched in tumor cells. Second, with the selectively accumulated 10B, slow "thermal" neutrons radiated to the target volume induce neutron capture and decay reactions within a cell range (7). In this double-targeted manner, tumor cells, even those entangled with normal cells, receive a relatively high dose of irradiation and are thus susceptible to physical and biological destruction. Sparing nonmalignant components when killing tumors at a cellular resolution is a characteristic of BNCT that makes it a promising remedy for traditionally difficult-to-treat tumors.

Bibliometrics, first debuted in 1987, is a powerful tool for analyzing publication characteristics, canonical articles, and research trends in a specific field (8). By collecting most, if not all, related publications and utilizing statistical algorithms, bibliometric analysis could provide objective and comprehensive insights into the research area compared with conventional reviews that are dependent on the authors' viewpoint. However, this useful tool has not been applied to BNCT research. Therefore, we conducted this study to fill this gap, aiming at describing the entire body of knowledge and helping researchers interested in BNCT grasp the whole picture of the past, the present and the possible future.

2 Methods

2.1 Data acquisition

The following query line was used to retrieve publications from the Web of Science core collection (WoSCC): TS= (boron neutron capture therapy) AND LA= (English) AND DT= (Article OR Review). Related articles and reviews in English published before 2023-12-31 were collected. The search results were exported in plaintext format. Two authors independently conducted the literature screening, data retrieval and analysis to reduce bias in the results. The workflow is shown in Figure 2.

2.2 Bibliometrics and visualization analysis

VOSviewer 1.6.20), R (4.4.1), and CiteSpace (6.3. R1) were used in this study. VOSviewer was used to analyze the statistical characteristics of countries, institutions, journals, authors and keywords. CiteSpace was used to identify bursts of keywords and citations. Bibliometrix, a built-in R package, was used for data visualization (9).

3 Results

3.1 Publication characteristics

In total, 3347 publications related to BNCT were retrieved from the WoSCC (see Table 1). The annual publication numbers from 1975 to 2023 are shown in Figure 3A. We observed a surge of publications in 1992, followed by a 2.73% average annual growth

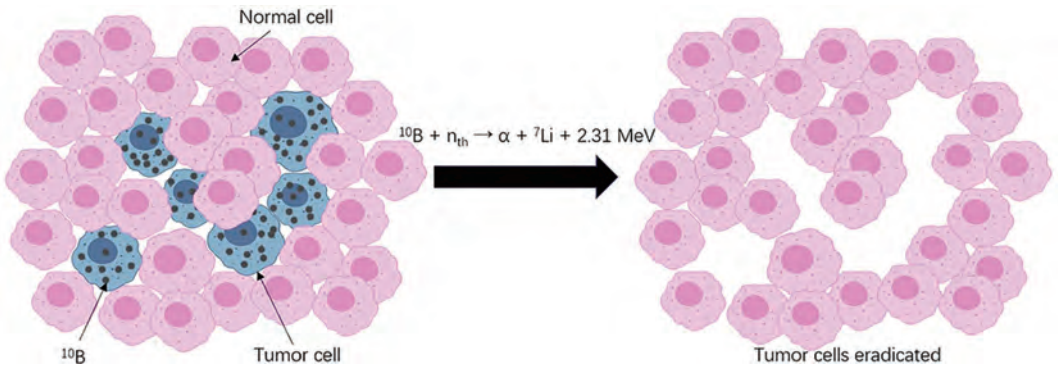

FIGURE 1
Ideal instance of BNCT.

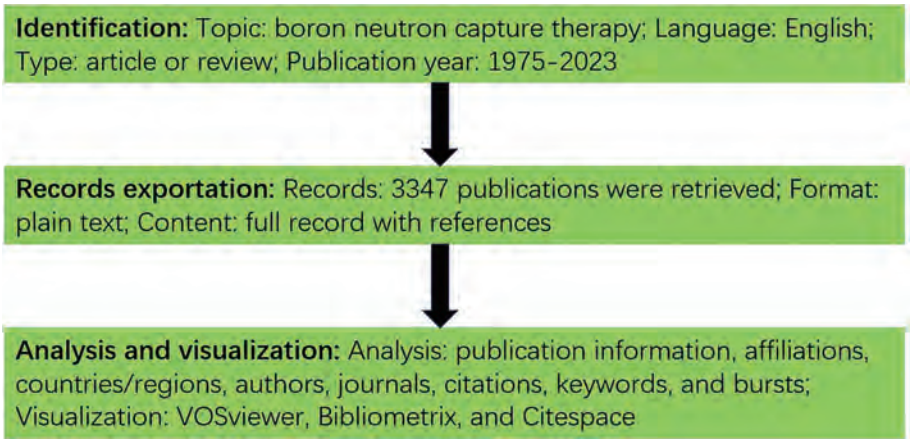

FIGURE 2
Research process of this study.

TABLE 1 Main information of the BNCT papers included in this study.

Description	Results
INFORMATION	
Timespan	1975-2023
Sources	688
Documents	3347
Annual growth rate	2.73%
Average citation per document	24.95
References	61368
DOCUMENT CONTENTS	
Keywords Plus (ID)	4290
Author's Keywords	5181
AUTHORS	
Authors	10318
Authors of single-authored documents	105
AUTHOR'S COLLABORATION	
Single authored documents	141
Coauthors per document	6.42
International coauthorships	22.47%
DOCUMENT TYPES	
Article	2614
Article; book chapter	34
Article; early access	9
Article; proceeding papers	446
Article; retracted publication	1
Review	240
Review; book chapter	2

rate, indicating that the attention attracted to BNCT research steadily increased. The year that had the most publications was 2023 (220, 6.57%). The total number of published articles steadily and rapidly increased from 1975 to 2023 (Figure 3B). From 1992 to 2021, the annual total number of citations was greater (Figure 3C), and the annual h index was 15 or greater, while it declined afterward (Figure 3D).

3.2 Countries/regions and institutions

A total of 79 counties/regions have contributed to research related to BNCT. The 38 countries/regions with more than 10 publications are shown in Figure 4A. The overlay network analysis of coauthorship reflects the number of publications by circle size and the average commencement year of study by color. In this two-dimensional diagram, strongly related nodes are located close to each other while weakly related nodes are located far away from each other. The link strength (LS) between nodes reflects the cooperation between countries, and the total link strength (TLS) is the sum of the LSs of a certain node. The USA had the strongest global cooperation (TLS=383) and cooperated the most with Argentina (LS=49). The top ten countries/regions with the highest number of publications and total citations are presented in Table 2. Japan had the most publications (794, 23.72%), followed by the USA (792, 23.66%) and Russia (274, 8.19%). Notably, the USA had the highest number of citations, followed by Japan. Figure 4B shows the geographic distribution of BNCT publications and cooperation strengths.

In total, 2234 organizations have participated in BNCT research. Figure 4C shows 148 institutions with more than 10 publications. Kyoto University had the most cooperative relationships (TLS=624). The top 10 most productive institutions are listed in Table 3. Kyoto University was the most productive (355, 10.61%), followed by the Russian Academy of Sciences (186, 5.56%) and Ohio State University (138, 4.12%). Ohio State University had the highest number of total citations (7873). Figure 4C shows that in the past 30 years, the Massachusetts

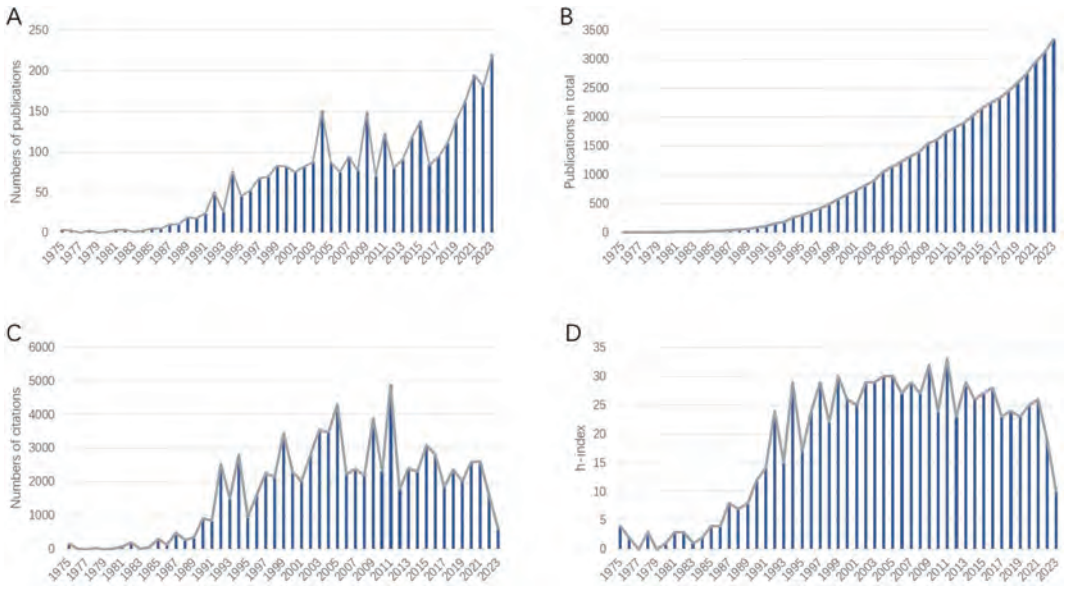

FIGURE 3
(A) Annual publications related to BNCT research. **(B)** Cumulative publications related to BNCT research. **(C)** Annual citations of the publications related to BNCT research. **(D)** Annual h-index of BNCT publications.

Institute of Technology (MIT), Brookhaven National Laboratory, and Ohio State University conducted BNCT research earlier, whereas Kyoto University, the Russian Academy of Sciences and the University of Tsukuba commenced later.

3.3 Authors

A total of 8,574 authors have contributed to publications on BNCT. The top 10 authors with the most publications are shown in Table 4. Ono K had the highest efficiency (191, 5.71%), followed by Suzuki M (187, 5.59%) and Sakurai Y (163, 4.87%). Ono K had the highest total number of citations, whereas Barth RF had the highest h-index. Figure 4D shows a map of overlay network analysis among 236 researchers of 10 articles or more. Ono K cooperated the most with the others (TLS=1314). Figure 4E shows the correlations among the five most prolific authors, institutions, and countries that have contributed to BNCT research from 1975 to 2023 via a Sankey diagram (10).

3.4 Journals

A total of 687 journals have published articles related to BNCT. The top 10 journals in terms of BNCT publications are listed in Table 5, along with their publication counts, total citations, average citations, impact factor (IF) and Journal Citation Reports (JCR) quantile rankings. *Applied Radiation and Isotopes* had the most publications, followed by *Medical Physics and Nuclear Instruments and Methods in Physics Research Section A. Applied Radiation and Isotopes* had the highest total number of citations (5116), whereas the *Journal of Neuro-Oncology* had the highest average number of citations (50.49). The *International Journal of Radiation Oncology Biology Physics* had the highest IF (6.4), followed by *Physics in Medicine & Biology* (3.3) and the *Journal of Neuro-Oncology* (3.2). Most journals were classified as Q2 and above (90%) by JCR ranking quantiles. Journal directions included nuclear medicine, radiotherapy, oncology, and clinical neurology. A map of the cocitation network analysis is shown in Figure 5A. The top 3 cocited journals were *Applied Radiation and Isotopes* (4627), the *Journal of the American Chemical Society* (3286), and the *International Journal of Radiation Oncology, Biology, Physics* (3086).

3.5 Citation and cocitation analysis

Citation analysis is a valuable way to evaluate the most cited articles, and the number of citations can reflect the impact of an article in a particular field of research. The most cited articles by year in the realm of BNCT from 1975 to 2023 are listed in Supplementary Table 1. Among the 47 publications, 20 appeared in journals focused on organic and inorganic chemistry, 15 in journals dedicated to oncology and radiotherapy research, 7 in journals related to medicinal studies, and 5 in journals covering physics. Additionally, 30 of the 47 studies concentrated on the synthesis and properties of new boron-containing compounds, 10 on BNCT for cancer treatment, 5 on dosimetry, and 2 on the biological effects. In Supplementary Table 2, we summarize the 100 most cited articles in this field. The article "Dendrimers and Dendritic Polymers in Drug Delivery", published in Drug Discovery Today in 2005, has received the highest citation count (1158).

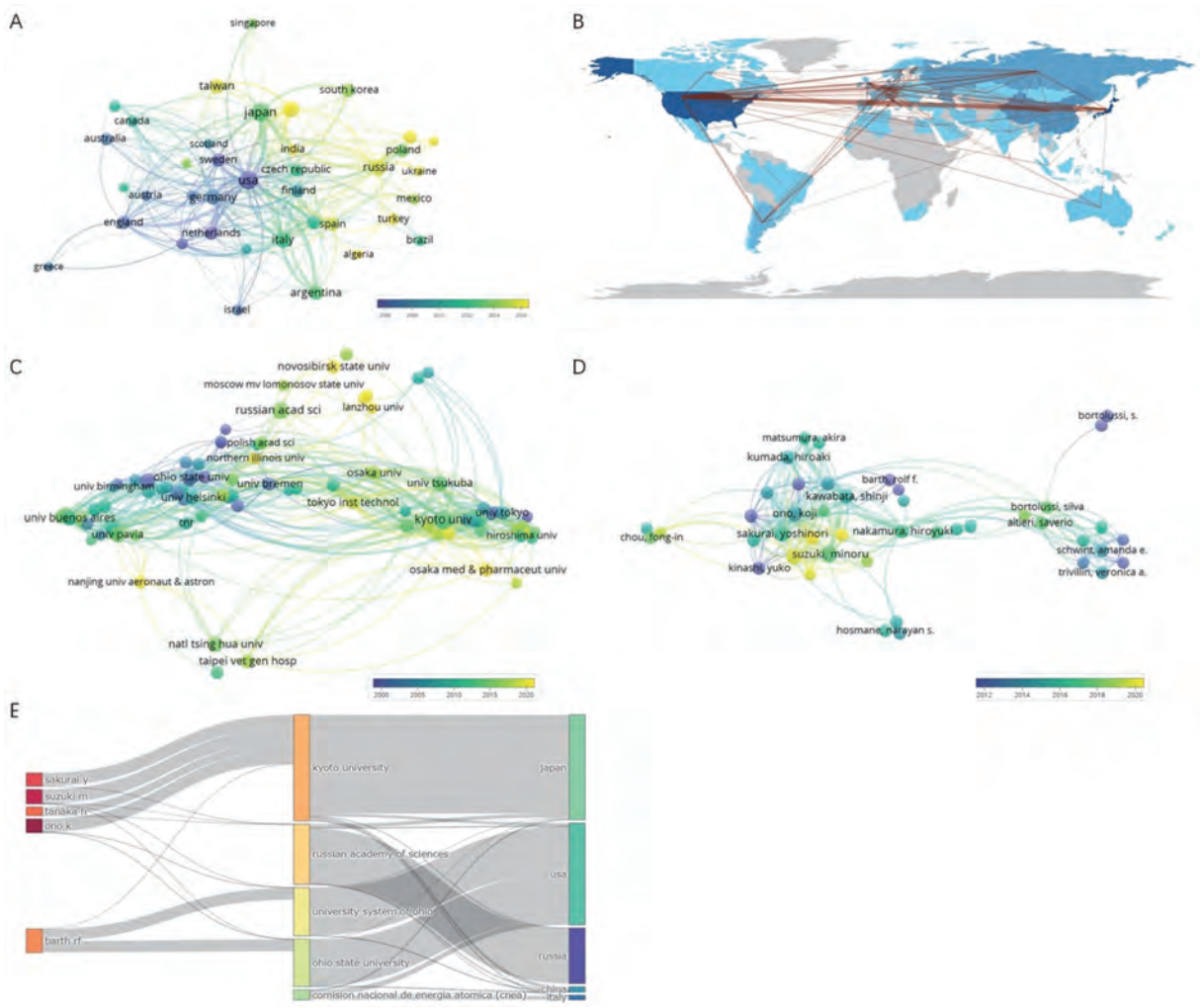

FIGURE 4
(A) Coauthorship overlay of countries/regions. **(B)** Geographic distribution of BNCT publications and cooperation strengths. **(C)** Coauthorship overlay of institutions. **(D)** Coauthorship overlay of authors. **(E)** Three fields plot of authors, affiliations and countries/regions.

TABLE 2 The top 10 most productive countries/regions regarding BNCT from 1975 to 2023.

Rank	Country/Region	Publication	Fraction	Total citations
1	Japan	794	23.72%	17094
2	USA	792	23.66%	31414
3	Russia	274	8.19%	4769
4	Italy	265	7.91%	5466
5	Mainland China	251	7.50%	5287
6	Germany	209	6.24%	6082
7	Argentina	149	4.45%	2215
8	Taiwan	116	3.47%	1385
9	England	105	3.14%	3164
10	Sweden	101	3.02%	2989

TABLE 3 The top 10 most productive institutions regarding BNCT research from 1975 to 2023.

Rank	Institution	Publication	Fraction	Total citations	TLS
1	Kyoto University	355	10.61%	7482	624
2	Russian academy of sciences	186	5.56%	3211	137
3	Ohio State University	138	4.12%	7873	109
4	University of Tsukuba	106	3.17%	1878	164
5	National Tsing Hua University	98	2.93%	1175	126
6	Brookhaven National Laboratory	96	2.87%	4636	106
7	Università di Pavia	90	2.69%	1519	190
8	Massachusetts Institute of Technology	74	2.21%	3460	128
9	Osaka Medical and Pharmaceutical University	73	2.18%	2519	176
10	Osaka University	70	2.09%	1823	118

TABLE 4 The top 10 most productive authors in BNCT research from 1975 to 2023.

Rank	Author	Publication	Fraction	Total citations	h-index	Start year
1	Ono, K	191	5.71%	5295	41	1996
2	Suzuki, M	187	5.59%	4047	33	1997
3	Sakurai, Y	163	4.87%	3235	30	1997
4	Tanaka, H	113	3.38%	1370	32	2009
5	Masunaga, S	87	2.60%	1888	25	1993
6	Coderre, J	78	2.33%	4497	37	1987
7	Nakamura, H	69	2.06%	1733	25	1993
8	Kawabata, S	68	2.03%	2377	27	2003
9	Kumada, H	68	2.03%	1414	22	2002
10	Barth, R	65	1.94%	4926	45	1984

TABLE 5 The top 10 most productive journals regarding BNCT research from 1992 to 2023.

Rank	Journal	Publications	Total citations	Average citations	IF	JCR
1	Applied Radiation and Isotopes	363	5116	14.09	1.6	Q2
2	Medical Physics	101	1954	19.35	3.2	Q1
3	Nuclear Instruments and Methods in Physics Research Section A	82	879	10.72	1.5	Q2
4	Radiation Research	73	2530	34.66	2.5	Q2
5	Radiation Protection Dosimetry	72	539	7.49	0.8	Q4
6	International Journal of Radiation Oncology Biology Physics	66	2756	41.76	6.4	Q1
7	Physics in Medicine & Biology	59	1494	25.32	3.3	Q1
8	Journal of Neuro-Oncology	55	2777	50.49	3.2	Q2
9	Nuclear Instruments and Methods in Physics Research Section B	46	741	16.11	1.2	Q1
10	Journal of Organometallic Chemistry	45	1150	25.56	2.1	Q2

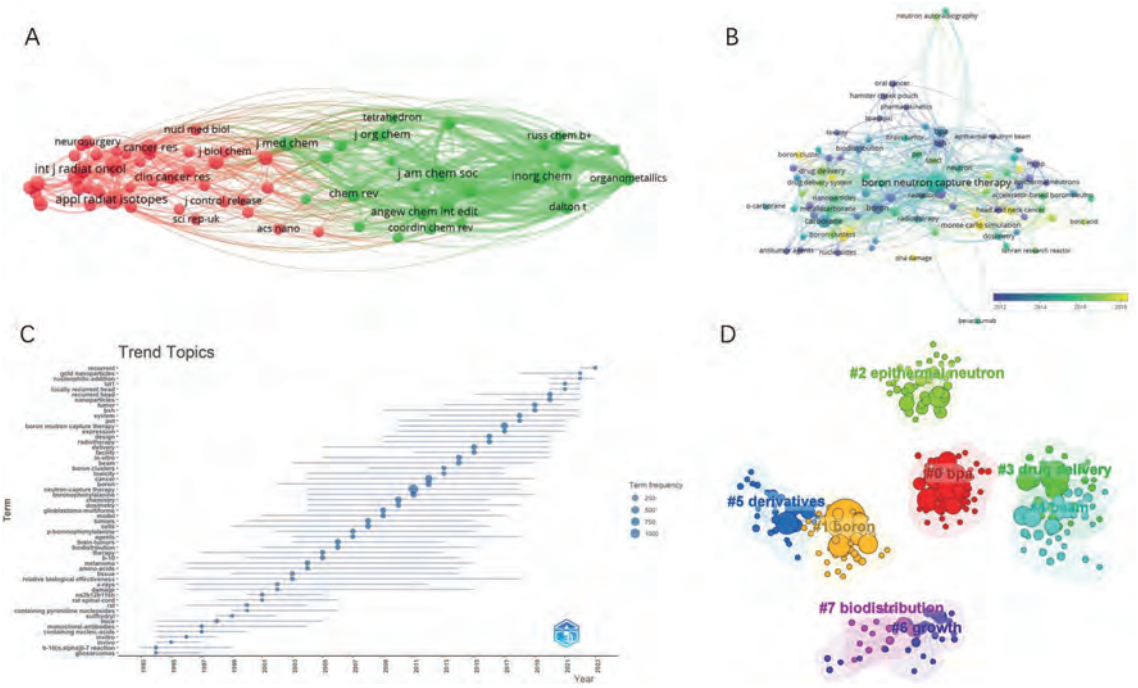

FIGURE 5
(A) Cocitation network map of journals. **(B)** Keyword co-occurrence network diagram of BNCT. **(C)** The trending topics. **(D)** Eight representative clusters of keyword clusters from 2019 to 2023.

3.6 Keywords

In total, 5181 keywords were proposed by the authors. A map of the overlay network analysis of keywords is shown in Figure 5B. The top 10 most common keywords were "BNCT", "carborane", "boronophenylalanine (BPA)", "boron", "glioblastoma (GBM)", "sodium borocaptate (BSH)", "cancer", "drug delivery", "neutron capture therapy", and "Monte Carlo". The terms marked in dark blue represent an average publication year of 2008 or earlier, whereas those in bright yellow represent 2016 or later. "BSH", "GBM", and "radiation" were previously the main topics. The keywords "Monte Carlo simulation", "accelerator-based neutron source", "cytotoxicity", "drug delivery", "head and neck cancer", and "boron cluster" appeared relatively late. A similar trend is shown in Figure 5C.

To obtain the latest research hotspots of BNCT research, we analyzed the clustering of keywords within 5 years. Eight major clusters are shown in Figure 5D with their sizes and silhouette values in Supplementary Table 3. On the basis of clustering vocabulary analysis, the latest BNCT studies have focused on BPA administration, sources of neutrons, synthesis of novel boron-containing agents, their biodistribution, and the influence on tumor growth in animal models.

3.7 Citation bursts

The top 25 keywords with citation bursts are shown in Figure 6A. The red lines reflect the burst duration. The keywords "mouse" (1990-2000) and "malignant melanoma" (1990-2000) drew considerable attention at the end of the 20th century, whereas "glioma" (1996-2005), "glioblastoma multiforme" (1999-2004), "brain tumors" (2000-2008), and "BSH synonyms" (1993-2005) suggested a surge of publications related to the clinical outcomes of BNCT in the treatment of brain tumors using BSH as a boron carrier. In the second decade of the 21st century, "recurrent head" (2013-2023), "drug delivery" (2015-2021), "nanoparticles" (2017-2023), and "Monte Carlo simulation" (2017-2023) have attracted extensive attention. The top 25 references with burst citations are shown in Figure 6B. The article "Boron delivery agents for neutron capture therapy of cancer" published by RF Barth et al. in Cancer Communications had the strongest outbreak, and the burst is still ongoing. The review "The Chemistry of Neutron Capture Therapy" by Soloway AH et al. had the second highest burst strength.

3.8 Trends of contribution

The production of top 5 countries, authors, affiliations, and journals over time is shown in Figure 7, respectively. As demonstrated in Figure 7A, the cumulate contribution of Japan surpassed that of USA in 2015, while China's production exceeded Italy's in 2021. In the last five years, the most prolific authors are Suzuki M, Tanaka H, and Sakurai Y from Japan, while Kyoto University and Russian academy of sciences are the most active institutions worldwide (Figures 7B, C). Top five journals of BNCT

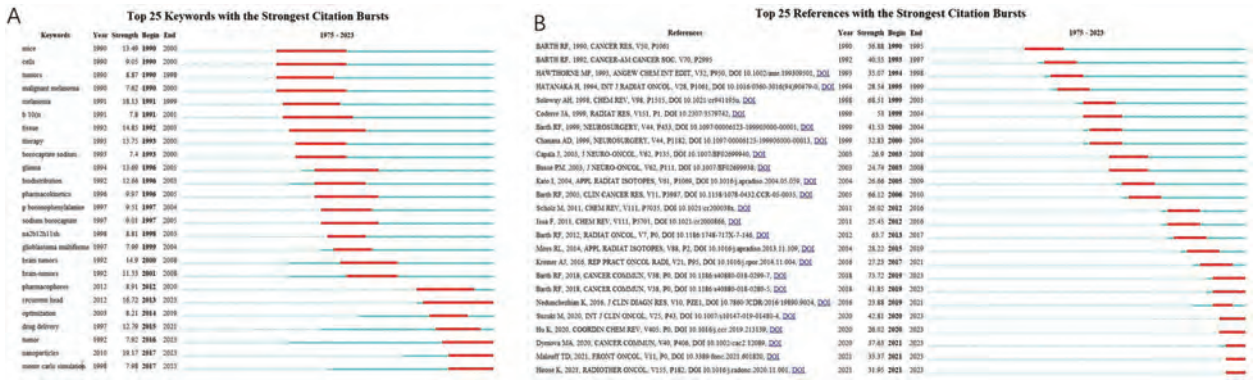

FIGURE 6
(A) The top 25 keywords and **(B)** references with the strongest citation bursts.

research are shown in Figure 7D. From late 2000s, the journal *Applied Radiation and Isotopes* has been the leading source of BNCT related articles.

4 Discussion

4.1 Trends in the development of BNCT-related research

To date, this is the first study to offer a comprehensive bibliometric analysis of BNCT-related publications in the WOSCC from 1975 to 2023. The findings show a consistent increase in scientific output in this field. The peak number of citations and the highest H-index occurred in 2011. Japan, China, and Russia are the top three most productive countries in the recent five years. The decrease in citations and the h-index since 2022 may be attributed to the proximity to the end of the collection period.

4.2 Contributions by countries, institutions, authors, and journals

We conducted this bibliometric analysis in the field of BNCT to objectively identify the most influential countries, institutions, authors, and journals. Japan has emerged as a major contributor with the highest number of publications, whereas the USA has led in citations and international collaboration. Notably, three of the

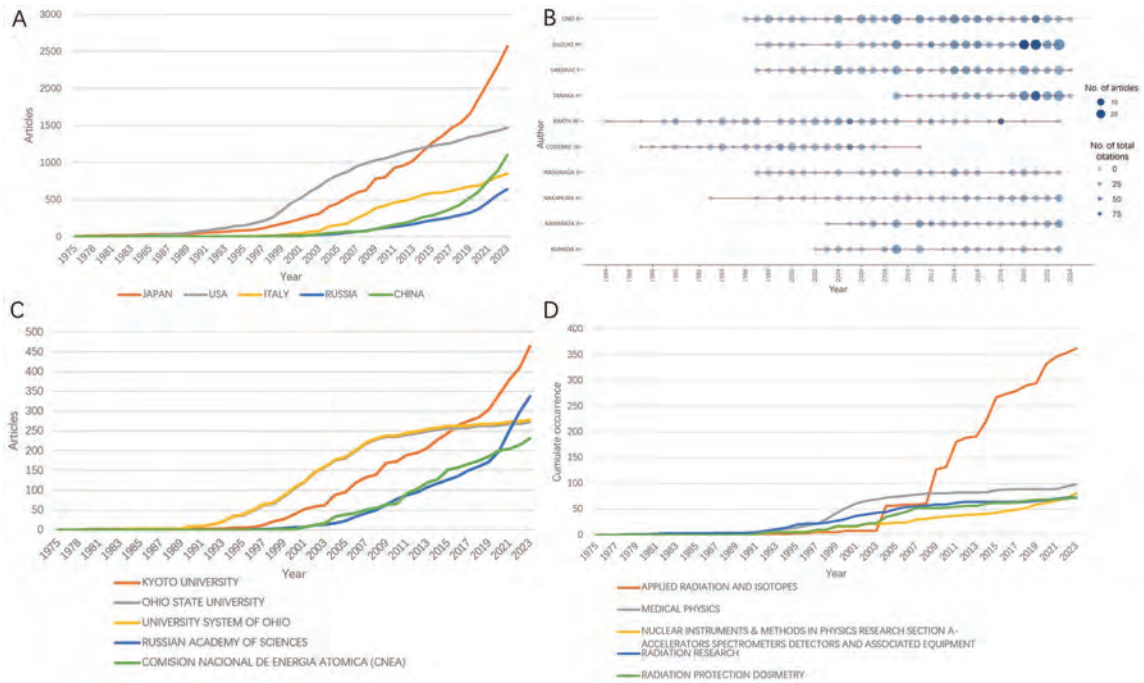

FIGURE 7
The production of top 5 **(A)** countries, **(B)** authors, **(C)** affiliations, and **(D)** journals over time.

top ten institutions and eight of the top ten most productive authors are Japanese. Kyoto University was the most influential institution, and Ono K was the most prolific author over the past 30 years. The journal *Applied Radiation and Isotopes* had the most publications and total citations. Additionally, our results indicated that the *Journal of Neuro-Oncology* had the highest number of citations per publication in this field, suggesting that clinical applications of BNCT for GBMs continue to attract the attention of physicians and researchers.

4.3 Research hotspots and frontiers

To find research hotspots and leading edges in the field of BNCT, we conducted an analysis of citations, cocitations, and keywords. To our knowledge, this study is the only bibliometric analysis of this topic, with several meaningful conclusions. First, the synthesis of novel boron-containing agents is a constant hotspot, varying from boronic acid derivatives lacking selectivity to boron clusters such as carboranes and then to modern boron carriers with targeting capacity. Antibody conjugates and nanoparticles are becoming more attractive to researchers. Our keyword analysis results indicate that researchers have paid increasing attention to "accelerator-based neutron source", "cytotoxicity", "drug delivery", "head and neck cancer", and "boron cluster", with the aim of improving the neuron source, boron delivery and number of types of cancer to treat with BNCT. In contrast, previous studies focused more on BSH and GBMs. Third, the burst analysis of keywords and citations revealed "brain tumors", "nanoparticles", and "Monte Carlo simulation", suggesting that they are milestones in the development of BNCT research. Finally, with the addition of cutting-edge publications, we sense prelusive therapeutic advancements using novel boron agents, with applications unrestricted to small animals in the near future.

4.3.1 Development of neutron sources

Ideal neutrons for BNCT should be radiated at high flux rates, designated energy levels and targeted volumes without unwanted heavy particles. Although the characteristics and purity of the neutrons were subpar with respect to modern standards, experimental nuclear reactors provided the first thermal neutrons that contributed to the proof of concept of BNCT. One decade after World War II, Farr LE and Sweet WH used the Massachusetts Institute of Technology nuclear reactor (MITR) as neutron sources (11). In the 1960s, Hatanaka initiated clinical trials on brain malignancies via the Hitachi Training Reactor and the Musashi Institute of Technology reactor (12). As mentioned above, the results of these trials were far from fruitful. The slow neutrons had a critical disadvantage. Owing to their low energy level, thermal neutrons can only pass through an average of 2 cm in the tissue before they lose the capacity to induce a nuclear reaction. This resulted in intracranial tumor patients often needing debulking resection and the surgical cavity being left open when receiving the external beam, which might have led to brain necrosis by increasing the boron concentration at exposed incisions (13). In addition, the short path length of thermal neutrons has limited the noninvasive application of BNCT to melanomas and other superficial neoplasms.

Reactors remained the mainstream neutron source until the early 21st century as the physical characterization of their neutrons improved. The epithermal neutrons from MITR II and Brookhaven Medical Research Reactor (BMRR) with modified beam parameters came into clinical use for melanoma and GBM patients in the 1990s (14, 15). The relatively high-energy epithermal neutrons (0.5 eV < E_n < 10 keV) from reactors had better penetration of approximately 6 cm beneath the tissue surface, comparing to 2 cm for thermal (E_n < 0.5 eV) neutrons, which significantly increased the body volume in reach and made craniotomy unnecessary (14, 16). However, several limitations of reactor-based BNCT exist. First, the rareness of a nuclear reactor is a major impediment to BNCT research. The technical requirements and financial burdens of building and maintaining a nuclear reactor dwarf the benefits of this promising solution as definitive precision medicine. In addition, the reactors need to be shared with basic physics researchers and shut down for maintenance for one third of a whole year (17). Finally, nuclear accidents are always a concern.

Alternative neutron sources have been under development since the 1980s (18). Accelerators at that time for physical research had a neutron density far less than the requirement of BNCT, which is more than 1×10^{11} to 10^{12} (n/cm^2·s) (19). In recent years, accelerator-based (AB) systems have provided comparable intensities of epithermal neutrons with the whole system in a compact form suitable for in-hospital installation (20). In short, protons are accelerated by cyclotrons (21) or linear accelerators (22) to hit the target metal materials, such as lithium (23) or beryllium (24). Nuclear reactions, e.g., ^{7}Li(p, n)^{7}Be or ^{9}Be(p, n)^{9}B, occur, and then, epithermal neutrons are emitted from the target. By 2023, AB-BNCT has become standard clinical therapy covered by medical insurance in 5 hospitals in Japan (25). Currently, several clinical studies in China (26) and Korea (27) in which several manufacturers use accelerator-based neutron sources (ABNSs) are in progress. The clinical application of ABNS in the new era warrants further investigation.

4.3.2 Development of boron delivery agents

The development of boron carriers has spanned over 70 years and remains critical to the success of BNCT. The general requirements for boron agents include low systemic toxicity, high selectivity, and durable persistence in tumors during BNCT (28). The challenge lies in achieving at least 20 μg/g ^{10}B in tumors for effective radiation, while less than one-third of the boron is present in blood or normal tissue. Advances in synthetic techniques and biological targeting have led to the emergence of several promising boron delivery strategies.

The first boron carrier used in early BNCT studies was borax. In Farr's procedure, sodium tetraborate was infused intravenously, followed by 30 min of irradiation of given neutron counts at the skin surface, and a few derivatives of it were used in subsequent trials (11, 29). These first-generation compounds have poor selectivity, a low tumor tissue ratio, short persistence in brain tumors and high systemic toxicity (29). BSH (30) and BPA (31) are second-

generation boron agents that are more selective and have been widely used in clinical trials. BSH is a polyhedral borane anion commonly used in Japanese clinical trials. The EORTC 11961 study revealed that the tumor-to-brain ratio of BSH was greater than 40 in GBM patients (32). BPA is a hydrophobic dihydroxyboryl derivative of phenylalanine that can be actively transported into cells via the L-amino acid transport system and is upregulated in most tumors (33). The safety of intravenous administration of BSH and BPA has been clinically tested in Japan, the USA, Europe, and Argentina (34), although neither meets all of the requirements. The main limitations of BSH are its lack of receptor-mediated tumor selectivity, low tumor-to-blood ratio, and significant side effects during treatment (35). While some researchers have addressed this by conjugating BSH with specific ligands (36, 37), its high cost remains a barrier to its use as an ideal boron carrier. The low boron content of BPA requires high doses, increasing treatment costs and straining liver and kidney metabolism. Its poor solubility and instability lead to a reduced boron concentration at the tumor site (38), whereas its short retention time, possibly influenced by LAT1's anti-transport mechanism, further limits its effectiveness.

The next generation of boron compounds features the conjugation of boron agents to tumor-targeting molecules to achieve the selective accumulation of boron in tumors. The targeting relies on the binding of linked ligands to corresponding receptors that are overexpressed by tumor cells. These novel boron agents generally consist of a stable boron cluster or moiety of high boron concentration and tumor-targeting molecules linked together. Amino acids, peptides, carbohydrates, nucleosides, antibodies, and nanoparticles as targeting or carrier moieties have attracted considerable attention.

Low-molecular-weight agents as targeting moieties. In addition to BPA, boronated amino acids, along with their derivatives, have been widely investigated. These include natural amino acids and unnatural cyclic amino acids (39, 40). However, none of these compounds possess better *in vitro* characteristics than BPA derivatives do (35). Peptide ligands have been demonstrated through the functionalization of carriers with high affinity and selectivity (41). Michiue et al. reported that when connected to arginine repeats, BSH has increased intracellular accumulation in both the cytoplasm and nucleus (42). *In vivo* positron emission tomography (PET) confirmed the selective retention of BSH-3R in tumor tissue. Nagasawa et al. developed and evaluated a novel boron carrier by conjugating BSH to cell-membrane penetrating peptides (CPPs) (43). Compared with BSH, the CPP-conjugated form presented a greater intracellular concentration and better eradication of T98G cells when exposed to neutrons. Barth's group proposed a strategy to target vascular endothelial growth factor receptor (VEGFR) and epidermal growth factor receptor (EGFR), which are often overexpressed in tumors (44, 45). However, indirect tumoricidal activity via ischemic necrosis and the expression of EGFR on normal glial cells have limited their success.

Cancer cells have an increased rate of glucose uptake and glycolysis, known as the Warburg effect (46), which renders carbohydrates an ideal ligand for boron conjugates. Aoki et al. synthesized highly hydrophilic 2-borylsugars that were actively transported into cancer cells by glucose transporter 1 (GLUT1). Then, 2-borylsugar is phosphorylated and stored intracellularly, as confirmed by *in vitro* assays (47). Ekholm et al. developed 6-O-carboranylmethyl glycoconjugates with high affinities for GLUT1 (48). Compared with second-generation boron agents, this compound has a 40-fold greater boron delivery capacity. Tsurubuchi et al. reported the synthesis of an α-D-mannopyranoside derivative named MMT1242 with prolonged intracellular retention compared with that of BPA (49). Notably, both mannose receptors (MRs) and GLUT1 mediate the uptake of MMT1242. Given that MRs are upregulated on the cell membranes of tumors and correlate with tumorigenesis (50), mannose conjugates hold potential for improving the therapeutic effects of BNCT. In summary, despite their high water solubility and rapid clearance from metabolically active tumor cells, leading to poor intracellular boron retention, these studies underscore the potential of carbohydrate-based boron carriers. Their enhanced uptake, high tumor affinity, and growth inhibition offer valuable insights for developing new boron agents for BNCT.

Other small molecules, such as nucleosides, porphyrins, folic acid (FA), hyaluronic acid (HA), and COX-2 substrates, have also been widely investigated in recent years. Thymidine kinase 1 (TK1) is highly expressed in the cytosol of proliferating tumor cells (51). To target TK1, Barth et al. synthesized a 3-carboranyl thymidine analog (3CTA), N5–2OH, with high tumor-to-brain and tumor-to-blood ratios (52). *In vivo* studies demonstrated a significantly prolonged mean survival time (MST) in rats bearing RG2 gliomas, whereas validation of N5–2OH in an F98 glioma model revealed minimal MST improvement (53). The underlying cause of this phenomenon needs further investigation. FA receptors are highly expressed in tumor cell lines and are correlated with a metastatic tendency (54, 55). In 2020, Nakagawa's group synthesized several hydrophilic FA derivatives with IC_{50} values of less than 3 mM in the U87 MG glioma cell line (56). The HA receptor CD44 is upregulated in cancers of numerous origins (57). In 2008, Crescenzi's group designed an HA-conjugated carborane, named HapACB, with high affinity for CD44 *in vitro* (58). COX-2 is highly expressed in oral squamous carcinoma cells (59). Boronated COX-2 inhibitors demonstrated great radiosensitization capacity in CAL27 cells by suppressing the PI3K/Akt and MAPK signaling pathways (60). The conjugation of boron-enriched moieties with well-validated targeting molecules might be a productive avenue in the future.

High-molecular-weight agents as targeting moieties. Monoclonal antibodies possess unparalleled targeting selectivity, and antibody-based therapies are achieving significant clinical success across various cancers (61). With respect to BNCT, the first antibody-assisted localization was achieved by conjugating benzenediazonium ions to antibodies against carcinoembryonic antigen (CEA) in 1984 (62). This conjugate contained 30 boron atoms per IgG molecule and demonstrated a high degree of selective accumulation in CEA-positive human colonic carcinomas grown in hamsters. Recently, EGFR and CD133 have been investigated as targets for antibody conjugates. Barth and colleagues developed dendrimers with high boron concentrations linked to cetuximab, a widely used monoclonal antibody that targets EGFR (63); or to

L8A4, which targets $EGFR_{vIII}$ (64); or to EGF (45) *per se*. These EGFR-binding boron agents demonstrated significant tumoricidal effects in a rat model bearing F98 gliomas transfected with the corresponding genes (63–66). Nakase's group also targeted EGFR via the conjugation of dodecaborate to cetuximab through the Z33 peptide (67). EGFR-expressing cells internalize the conjugates via the macropinocytotic pathway, but further validation of BNCT therapeutics involving this compound is necessary. Sun's group reported that with CD133 on SU2 glioma cells targeted by boron –antibody conjugates, the elongation of experimental mouse survival time was remarkable (68). To date, the key challenges of antibody-based boron delivery strategies include (1) coping with variable expression of the target across tumors (2); elucidating the mechanisms for entering cancerous cells; and (3) achieving uniform boron distribution or selective enrichment within critical compartments of the tumor.

As the burst analysis indicated, extensive investigations have recently been conducted on the use of nanocarriers for boron delivery. Nanoparticles are materials with specialized functions formed by atoms or molecules at the nanoscale. Recent progress in materials chemistry, biology, and related areas has rapidly advanced the use of nanoparticles in fields such as industry and medicine (69, 70). These nanoparticle-based systems have demonstrated numerous advantages in drug delivery, *e.g.*, high stability, water solubility, tumor accumulation, and low preparation requirements (71), due to the selective accumulation of nanoparticles in tumors, known as the enhanced permeability and retention (EPR) effect (72). Additionally, nanocarriers can easily deliver other therapeutic agents alongside boron compounds to tumors. As a result, nanostructures have emerged as a focus of BNCT research.

Polymers represent a prominent class of nanocarriers that have been extensively studied in recent years, such as dendrimers (73) and polymer micelles (74), which have the ability to extend drug retention in tumors and enhance the hydrophilicity of drugs. The boron-containing compounds are either conjugated to or encapsulated by the polymers. In 2012, Sumitani et al. reported significant suppression of colon-26 tumor (CT26) growth in mice treated with carboranes embedded by their poly(ethylene glycol)-block-poly(lactide) copolymer (PEG-b-PLA) (75). Five years later, Makino and coworkers reported that poly(L-lactide-co-glycolide) (PLLGA)-encapsulated carboranes maintained a tumor-to-blood ratio of boron concentration over 5 for more than 8 hours after administration (76). In 2019, Chen's group developed a polymer-based tumor-targeting boron delivery system, named iRGD-PEG-PCCL-B (77). When wrapped by this polymer, BSH had six times higher uptake by A549 cells than its original form. In addition, iRGD-PEG-PCCL-B could simultaneously pack the BSH with doxorubicin, enabling highly targeted BNCT combined with chemotherapy for synergistic tumor suppression. A year later, Nomoto and colleagues prepared a novel polyvinyl alcohol-BPA complex that demonstrated improved uptake mediated by LAT1, prolonged cellular retention, and substantial CT26 growth suppression with high biocompatibility (78). In 2023, Dai et al. synthesized novel BPA-containing polydopamine (B-PDA) nanoparticles that had significant glioma ablation capacity in mice exposed to neutron radiation, with a tumor-to-brain ratio of 6.83 ± 1.75 (79). Overall, the use of polymers as boron carriers has provided substantial preclinical evidence, demonstrating their potential as promising candidates for further investigations.

Liposomes and inorganic boron-containing nanoparticles have undergone extensive investigation, as examined in two recent reviews (80, 81). These inorganic nanoparticles can be classified into boron nitride (82, 83) (BN) nanotubes (84–86), boron-doped carbon dots (87), magnetic nanomaterials (88, 89), gold nanoparticles (90, 91), and mesoporous silica nanoparticles (92, 93), although a more detailed review is beyond the scope of this study. Owing to their high biocompatibility, low systemic toxicity, improved physiochemical stability, controlled release and EPR effect, the majority of these multifunctional nanocomposites demonstrated improved selectivity for tumor cells and increased boron uptake in both *in vivo* and *in vitro* experiments through ligand conjugations, surface modifications or structural alterations, rendering these categories of nanocarriers promising blueprints for innovative boron delivery materials.

4.3.3 Enhanced imaging and dosimetry

Traditional imaging techniques have offered limited insight into the distribution of boron compounds and the dose delivered to tissues. To analyze the boron concentration, various methods are available, including colorimetry, prompt γ-ray analysis (PGRA), inductively coupled plasma atomic emission spectrometry (ICP –AES), direct-current plasma atomic emission spectroscopy (DCP-AES), inductively coupled plasma–mass spectrometry (ICP-MS), quantitative neutron capture radiography (QNCR), electron energy loss spectroscopy (EELS), flow injection combined with ESI-MS/MS (FI/ESI-MS/MS), sputter-initiated resonance ionization microprobe (SIRIMP), laser atomization resonance ionization microprobe (LARIMP), secondary ion mass spectrometry (SIMS), single-photon emission computed tomography (SPECT), PET, nuclear magnetic resonance (NMR), and magnetic resonance imaging (MRI). All of the current boron drugs and their imaging techniques are presented in Table 6.

Currently, not all of these technologies are utilized in clinical settings. Many remain at the cellular level or in research stages, such as QNCR and SIRIMP, whereas newer methods such as nano-SIMS require additional development before clinical use. Presently, four primary methods are employed in clinical practice, all of which are based on modern imaging techniques: positron emission tomography (PET) and magnetic resonance imaging (MRI) provide enhanced visualization of the boron distribution and tumor response. Additionally, advanced dosimetry tools now enable precise measurement of radiation doses, ensuring accurate treatment planning.

4.3.4 Clinical advances

Early clinical trials had mixed results due to technology and compound limitations. More recent clinical trials have demonstrated promising results, particularly with new boron compounds and improved neutron sources. Trials are exploring the effectiveness of BNCT for various cancers, including those

TABLE 6 List of current boron drugs and imaging techniques.

Boron Agent	Technique	Invasion	Years	Disadvantages	Used in Clinic
BSSB	11B-NMR	No	1988	Requires high-field NMR equipment; limited clinical use due to cost and availability.	No
BSH	DCP-AES (94)	Yes	1991	Less commonly used than ICP–AES; potential matrix effects.	No
BSH	PGRA (95)	Yes	1995	Limited to quantification; Unsatisfactory accuracy.	No
BSSB	SIRIMP (96)	Yes	1997	Limited to research applications; may not be widely accessible.	No
BSSB	LARIMP (96)	Yes	1997	High cost and complexity; requires precise calibration and sample preparation.	No
BSH	10B-NMR	No	2001	High cost and specialized equipment required; less common in clinical practice.	No
BSH	EELS (97)	Yes	2003	Requires specialized equipment; sample must be electron-transparent.	No
BSH, BPA	QNCR (98)	Yes	2005	Limited availability; primarily used in research settings.	No
BSH	FI/ESI-MS/MS (99)	Yes	2005	Complex and costly; requires expertise in mass spectrometry.	No
BSH, BPA	ICP–AES (100, 101)	Yes	2006	Requires sample preparation; may have interference from other elements.	No
cis-ABCPC, 10BPA, 11BSH	SIMS (102, 103)	Yes	2013 2002	High resolution but require extensive sample preparation; limited to research use.	No
BSH, BPA	laser-SIMS (104)	Yes	2008	Requires sophisticated equipment; not widely used in clinical settings.	No
BPA	nano-SIMS (105)	Yes	2019	Extremely high cost; complex data analysis and sample preparation.	No
BPA	ICP-MS (106)	Yes	2015	High cost; requires skilled operators and extensive sample preparation.	No
BPA	SPECT (107)	No	2000	Lower spatial resolution compared to other imaging techniques; radiation exposure.	Yes
10BPA	18F-BPA PET (108)	No	2018	High cost; requires radiopharmaceutical production and specialized equipment.	Yes
carborane	MRI (109)	No	2000	May require contrast agents; lower resolution for boron-specific imaging compared to other techniques.	Yes
BPA	MRI (110)	No	2005	Limited specificity for boron without specialized contrast agents; resolution may vary.	Yes

BSSB, Cs4B24H22S2; BSH, Borocaptate sodium; BPA, boronophenylalanine; cis-ABCPC, 1-amino-3-borono-cyclopentane carboxylic acid; NMR, nuclear magnetic resonance; DCP-AES, direct-current plasma atomic emission spectroscopy; PGRA, prompt γ-ray analysis; SIRIMP, sputter-initiated resonance ionization microprobe; LARIMP, laser atomization resonance ionization microprobe; EELS, electron energy loss spectroscopy; QNCR, quantitative neutron capture radiography; FI/ESI-MS/MS, the flow injection technique combined with ESI-MS/MS; ICP–MS, inductively coupled plasma–mass spectrometry; SPECT, single-photon emission computed tomography; PET, positron emission tomography; MRI, magnetic resonance imaging.

resistant to conventional therapies. The evidence suggests better outcomes and fewer side effects in some cases.

Glioblastoma multiforme: The use of BNCT for treating brain gliomas can be traced back to 1951-1961 (111). During this period, Brookhaven National Laboratory conducted a clinical trial using 10B-enriched borax and recruited 28 patients with brain cancers, including GBM and other types of gliomas. However, these trials failed because the first generation of boron drugs could damage normal tissue and be cleared from tumor cells too quickly, resulting in insufficient boron concentrations in tumors. With the subsequent development of borocaptate sodium (BSH) and boronophenylalanine (BPA) compounds, a series of clinical findings emerged after the 1990s. Five trials conducted in Japan from 1998 to 2007 (112), 1998 to 2008 (113), 1999 to 2002 (114), and 2002 to 2007 (115) reported median survival times (MSTs) of 25.7 months, 19.5 months, 23.2 months, and 10.8 months, respectively. These trials involved 15, 23, 9, and 21 patients with brain cancer, and they used various medication regimens and radiation doses. This series of studies revealed that BNCT combined with X-ray and temozolomide could prolong the median survival time of patients with GBM. In the past 20 years, with the development of new boron drugs and advancements in dosimetry, seven clinical studies on GBM have been registered with the JRCT and NCT. A summary of the results is shown in Table 7. Two studies have reported preliminary results, namely, BNCT with temozolomide (TMZ) for GBM, with an MST of 15.6 months in patients with newly diagnosed GBM and 8.6 months in patients with recurrent GBM, with the remaining studies ongoing. Other studies are in the recruiting stage, and it is worthwhile to follow the results of these studies to better guide BNCT in treating GBM.

Head and neck cancers: BNCT has been used for various head and neck cancers, including squamous cell carcinoma (SCC). It provides a viable alternative to conventional therapies, especially for patients who have not responded well to traditional treatments or those with recurrent head and neck cancer (HNC). In the past 20 years, approximately 10 clinical trials have investigated BNCT for HNC. The earliest trial, EORTC 11011 (NCT00062348) (121), began in Essen, Germany, in 2003 and involved six patients with advanced SCC of the head and neck. These patients received an

injection of either BPA or BSH, and the researchers assessed the distribution of boron-10 (B10) in both tumor and normal tissues. The mucosa and skin were identified as the most critical organs at risk.

Between 2010 and 2015, researchers in Taiwan conducted studies involving 17 patients who underwent BNCT with BPA at a dose of 400 mg/kg, delivering a prescribed dose of 12–35 Gy. Among these patients, six achieved a complete response, and six achieved a partial response, resulting in a 2-year overall survival (OS) rate of 47%. This study demonstrated that fractionated BNCT, administered at 30-day intervals with adaptive planning, is both effective and safe (122). Another study at the same center

TABLE 7 List of Registered Clinical Studies of BNCT for the Treatment of Tumors in the Last 20 Years.

Number	Locations	Phase	Case	Study Status	Cancer Type	Interventions	Start Date	Completion Date	Results
NCT05737212 (116)	Korea	I/II	39	Recruiting	Brain and CNST Tumors	BNCT	2022/12/5	2024/12/1	Not reported.
NCT00974987 (117)	Japan	II	32	Completed	Brain and CNS Tumors	BNCT+XRT+TMZ	2009/9/1	2016/2/29	MST: 15.6 m
NCT01233492 (118)	United Kingdom	I	36	Terminated	Brain and CNS Tumors	BNCT+ mannitol	2007/10/1	2013/9/1	Not reported.
jRCT2032230554 (119)	Japan	I	18	Recruiting	Brain and CNS Tumors	BNCT+TMZ	2023/12/7	NA	Not reported.
jRCTs051180218 (120)	Japan	II	4	Recruiting	Brain and CNS Tumors	BNCT+TMZ	2019/3/27	2020/2/18	MST 8.5 m
NCT00062348 (121)	Germany	I	27	Completed	HNC	BNCT	2003/6/5	2012/1/20	Tumor/blood 1.2 ± 0.4. 1.4 ± 0.5 for skin
NCT01173172 (122)	Taiwan	I/II	17	Completed	HNC	BNCT	2010/7/1	2015/3/7	RR 71% 2yOS 47%
NCT02004795 (123)	Taiwan	I/II	28	Unknown	HNC	BNCT + IG-IMRT	2013/11/1	2018/11/1	Not reported.
NCT00114790 (124)	Finland	I/II	17	Completed	HNC	BNCT	2005/6/17	2013/5/6	RR 83%, MDOR 12.1 m
NCT05883007 (125)	Japan	I	30	Unknown	HNC	BNCT	2020/6/1	2024/5/31	Not reported.
jRCT2080224571 (126)	Japan	II	21	Completed	HNC	BNCT	2019/2/22	2021/1/25	3 m RR: 71.4%; 2y OS rate: 58% (rSCC12); 100% (r/la-nSCC13)
jRCTs051180160 (127)	Japan	II	7	Completed	HNC	BNCT	2019/3/25	2022/1/11	RR: 85.7%
jRCTs031180302 (128)	Japan	II	14	Completed	HNC	BNCT with PETCT	2019/3/15	2022/4/1	SUVmax = 4.5 +- 1.1/3.4 +- 0.8 T/N ratio = 3.6 +- 0.8/1.9 +- 0.6
UMIN000044118 (129)	Japan	II	120	Recruiting	HNC	BNCT	2021/5/10	NA	Not reported.
ChiCTR2200066473 (130)	China	II	6	Recruiting	HNC	BNCT	2022/09/19	2024/12/31	Not reported.
NCT02759536 (131)	China	I/II	30	Unknown	Melanoma	BNCT and IHNI-based BNCT	2013/7/1	NA	Not reported.

(Continued)

TABLE 7 Continued

Number	Locations	Phase	Case	Study Status	Cancer Type	Interventions	Start Date	Completion Date	Results
NCT00085059 (132)	Germany	II	4	Terminated	Melanoma	BNCT	2004/4/1	2012/7/18	None
NCT04293289 (133)	Japan	I	10	Completed	Melanoma Angiosarcoma	BNCT	2019/11/19	2022/12/31	Not reported.
NCT05601232 (134)	Japan	II	10	Recruiting	Angiosarcoma	BNCT	2022/11/1	2025/4/30	Not reported.

CNS, central nervous system MST, median survival time; TMZ, temozolomide; XRT, X-ray radiotherapy; IG-IMRT, image-guided intensity-modulated radiation therapy; RR, response rate; HNC, head and neck cancer; r/lHNC, recurrent/locally head and neck cancer; OS, overall survival; r/la-nSCC, recurrent/locally advanced nonsquamous cell carcinoma; a/rHNC, advanced/recurrent head and neck cancer; T/N ratio target/background ratio; IHNI, In-hospital Neutron Irradiator; MDOR, median duration of response; N, not available.

(NCT02004795) (135) focused on combining BNCT with image-guided intensity-modulated radiotherapy (IG-IMRT). The trial involved nine participants, and the combined BNCT+IMRT plan showed a significantly better conformity index for gross tumor volume (GTV) than did the BNCT-alone plan (P = 0.003). This improvement was particularly notable for tumors larger than 100 cm^3, indicating that combining BNCT with IG-IMRT enhances homogeneity and conformity in treating larger tumors. This study aimed to enroll 28 patients, and the final survival-related results are anticipated.

A phase I/II trial (NCT00114790) from Finland involved 12 patients with locally advanced (rT3, rT4, or rN2) head and neck cancer that had recurred and was inoperable (124). This study revealed that 83% of patients responded positively to treatment, and 17% experienced tumor growth stabilization for 5.5 to 7.6 months. The median duration of response was 12.1 months, highlighting the effectiveness and favorable safety profile of BNCT for treating inoperable, locally advanced head and neck carcinomas, including those with recurrence at previously irradiated sites.

In Japan, BNCT research for HNC has also been substantial. Over the past 20 years, five trials have been registered. Hirose et al. conducted a trial (jRCT2080224571) using BNCT with a cyclotron-based epithermal neutron source (C-BENS). The study included 21 patients, with eight recurrent SCC (rSCC) and 13 non-SCC (r/la-nSCC) cases. The response rates were 42.9% at one month, 57.1% at two months, and 71.4% at three months (126). The two-year OS rates were 58% for the rSCC group and 100% for the non-SCC group. Additionally, two small-sample phase II studies initiated in 2019 have yet to publish any results. By 2023, two other trials (UMIN000044118 and ChiCTR2200066473) established by Japanese and Chinese researchers were registered for HNC and BNCT. The Japanese study is expected to include 120 patients with SCC of the head and neck, providing valuable insights from larger clinical research outcomes.

Melanoma: Boron–Neutron capture therapy (BNCT) has demonstrated efficacy in treating melanoma, particularly in advanced stages. Research suggests that BNCT is effective in reducing tumor size and controlling metastases. Since 2013, five studies have investigated BNCT for skin tumors, but only one study has published results. A phase I/II trial conducted by Kamitani (136) (jRCTs061180066) and completed in June 2020 included three patients with recurrent skin malignancies who had not undergone surgical treatment. The patients were intravenously administered the BPA-F complex (200 mg/kg body weight) for 2.5 to 3 hours before irradiation. The results revealed a 100% tumor control rate (CR+PR) with no adverse effects exceeding Grade 3. These findings indicate the effectiveness of BNCT against recurrent skin cancers and malignancies. However, the study included only three patients. The largest ongoing study is being conducted by researchers from Xiangya Third Hospital in China. This study aimed to enroll 30 patients, use 350 mg/kg BPA and deliver 20.0 Gy of radiation biological effectiveness (RBE). The results of this study are anticipated and may provide further insights into the efficacy of BNCT for the treatment of melanoma.

In addition to the tumors mentioned above, BNCT has also been investigated in other cancers, such as liver cancer, sarcoma, angiosarcoma, and refractory breast cancer, demonstrating objective efficacy. For example, a phase I/II clinical study published in 2015 (137) reported the treatment of malignant peripheral nerve sheath tumors (MPNSTs) with 500 mg/kg of boronophenylalanine (BPA) and 24.3 Gy-Eq, resulting in a two-year stable disease (SD) period. Other nonregistered studies are not discussed here.

4.4 Future research trends

Although BNCT was theoretically established more than 80 years ago, its clinical development has been limited by neutron source technology. Recent advancements in accelerator-driven neutron sources have revitalized BNCT, enabling practical applications. On the basis of the analysis of recent keyword clusters, future research will likely focus on several key areas: enhancing targeting and specificity through new boron carriers that selectively accumulate in tumors, improving molecular targeting strategies, and developing more accurate assays for boron uptake. Additionally, synergistic approaches that combine BNCT with other therapies, such as immunotherapy and advanced delivery systems using nanoparticles, will be explored to improve treatment efficacy. Establishing standardized radiation dose guidelines through clinical trials is essential for diverse cancer types, alongside efforts to increase international collaboration and innovation in neutron source development to increase the accessibility and cost effectiveness of BNCT.

4.5 Advantages and limitations

The primary strength of our research lies in the comprehensive analysis of global publications on BNCT from a scientific literature perspective. However, there are several limitations. First, the papers in this study were exclusively sourced from WOSCC, which may have resulted in some omissions in the literature, especially considering the long-time frame. Second, since our findings were primarily based on common bibliometric indicators, we may have overlooked important metrics, potentially missing valuable insights. Third, as the BNCT field is rapidly advancing, the most recent publications were not included in our analysis; these publications will be incorporated in future studies. Fourth, the retrieval strategy focused solely on publications written in English, potentially introducing selection bias by excluding studies in other languages. Finally, owing to the large sample size, our findings provide a general overview of the BNCT field, but some potentially valuable research directions may have been overlooked.

5 Conclusion

To summarize, we conducted a bibliometric analysis using VOSviewer, R, and CiteSpace to outline the current research situation and development trend of BNCT. This article demonstrates the characteristics of the publications; identifies the most influential countries, institutions, authors, journals, and articles; and analyzes the bursts of keywords and references. In addition, we also discussed the research hotspots and trends of BNCT. At present, basic and preclinical research on novel boron agents, as well as the clinical application of BNCT in brain tumors, head and neck malignancies and melanomas, are current research hotspots. Future research trends will include improving the treatment regimen, examining the application of accelerator-based neutron sources, refining the dosimetry, and exploring the fitness of BNCT in other clinical settings, such as multiple liver or lung metastases. In addition, the synergistic effects and cost effectiveness of BNCT are largely unstudied. Finally, the pursuit of a better boron delivery solution is still far from complete.

Data availability statement

The original contributions presented in the study are included in the article/Supplementary Material. Further inquiries can be directed to the corresponding authors.

Author contributions

YC: Conceptualization, Data curation, Formal analysis, Methodology, Visualization, Writing – original draft, Investigation, Validation, Writing – review & editing. MA: Data curation, Formal analysis, Writing – original draft, Validation. YM: Writing – review & editing, Supervision. JJ: Funding acquisition, Writing – review & editing, Project administration, Supervision.

Funding

The author(s) declare financial support was received for the research, authorship, and/or publication of this article. This project was supported by Sanming Project of Medicine in Shenzhen (No. SZSM202211030), Shenzhen Key Medical Discipline Construction Fund (No. SZXK013), Shenzhen High-level Hospital Construction Fund, and Shenzhen Clinical Research Center for Cancer (No. (2021)287). All from the Shenzhen government for the research, authorship, and/or publication of this article.

Conflict of interest

The authors declare that the research was conducted in the absence of any commercial or financial relationships that could be construed as a potential conflict of interest.

Generative AI statement

The author(s) declare that no Generative AI was used in the creation of this manuscript.

Publisher's note

Supplementary material

The Supplementary Material for this article can be found online at: https://www.frontiersin.org/articles/10.3389/fonc.2024.1507157/full#supplementary-material

References

1. Bray F, Laversanne M, Sung H, Ferlay J, Siegel RL, Soerjomataram I, et al. Global cancer statistics 2022: globocan estimates of incidence and mortality worldwide for 36 cancers in 185 countries. *CA Cancer J Clin*. (2024) 74:229–63. doi: 10.3322/caac.21834

2. Seyfried TN, Huysentruyt LC. On the origin of cancer metastasis. *Crit Rev Oncog*. (2013) 18:43–73. doi: 10.1615/critrevoncog.v18.i1-2.40

3. Love RR, Leventhal H, Easterling DV, Nerenz DR. Side effects and emotional distress during cancer chemotherapy. *Cancer*. (1989) 63:604–12. doi: 10.1002/1097-0142(19890201)63:3<604::AID-CNCR2820630334>3.0.CO;2-2

4. Kroschinsky F, Stolzel F, von Bonin S, Beutel G, Kochanek M, Kiehl M, et al. New drugs, new toxicities: severe side effects of modern targeted and

immunotherapy of cancer and their management. *Crit Care*. (2017) 21:89. doi: 10.1186/s13054-017-1678-1

5. Connell PP, Hellman S. Advances in radiotherapy and implications for the next century: A historical perspective. *Cancer Res*. (2009) 69:383–92. doi: 10.1158/0008-5472.CAN-07-6871

6. Frazier RC, Vicini FA, Sharpe MB, Yan D, Fayad J, Baglan KL, et al. Impact of breathing motion on whole breast radiotherapy: A dosimetric analysis using active breathing control. *Int J Radiat Oncol Biol Phys*. (2004) 58:1041–7. doi: 10.1016/j.ijrobp.2003.07.005

7. Taylor HJ, Goldhaber M. Detection of nuclear disintegration in a photographic emulsion. *Nature*. (1935) 135:341–. doi: 10.1038/135341a0

8. Garfield E. 100 citation classics from the journal of the American medical association. *JAMA*. (1987) 257:52–9. doi: 10.1001/jama.1987.03390010056028

9. Aria M, Cuccurullo C. Bibliometrix: an R-tool for comprehensive science mapping analysis. *J Informetrics*. (2017) 11:959–75. doi: 10.1016/j.joi.2017.08.007

10. Riehmann P, Hanfler M, Fröhlich B. Interactive sankey diagrams. *IEEE Symposium on Information Visualization (InfoVis 05)*; Minneapolis. Hoboken, New Jersey, USA: John Wiley & Sons (2005). p. 233–40.

11. Farr LE. Neutron capture therapy with boron in the treatment of glioblastoma multiforme. *Am J Roentgenol Radium Ther Nucl Med*. (1954) 71:279–93.

12. Nakagawa Y, Pooh K, Kobayashi T, Kageji T, Uyama S, Matsumura A, et al. Clinical review of the Japanese experience with boron neutron capture therapy and a proposed strategy using epithermal neutron beams. *J Neurooncol*. (2003) 62:87–99. doi: 10.1007/bf02699936

13. Sweet WH. Practical problems of the past in the use of Boron: Slow neutron capture therapy in the treatment of glioblastoma multiforme. *The first international symposium on neutron capture therapy*. United States: International Atomic Energy Agency (IAEA) (1982).

14. Busse PM, Harling OK, Palmer MR, Kiger WS 3rd, Kaplan J, Kaplan I, et al. A critical examination of the results from the Harvard-mit nct program phase I clinical trial of neutron capture therapy for intracranial disease. *J Neurooncol*. (2003) 62:111–21. doi: 10.1007/bf02699938

15. Chadha M, Capala J, Coderre JA, Elowitz EH, Iwai J, Joel DD, et al. Boron neutron-capture therapy (Bnct) for glioblastoma multiforme (Gbm) using the epithermal neutron beam at the Brookhaven national laboratory. *Int J Radiat Oncol Biol Phys*. (1998) 40:829–34. doi: 10.1016/s0360-3016(97)00891-2

16. Pignol JP, Paquis P, Breteau N, Chauvel P, Sauerwein W, Group EBS. Boron Neutron Capture Enhancement of Fast Neutron for Nonremoved Glioblastomas: Rationale of a Clinical Trial. In: Wiegel T, Hinkelbein W, Brock M, Hoell T, editors. *Controversies in Neuro-Oncology: 3rd International Symposium on Special Aspects of Radiotherapy, Berlin, April/May 1998*, vol. 33. Basel, Switzerland: S. Karger AG (1999).

17. Suzuki M. Boron neutron capture therapy (Bnct): A unique role in radiotherapy with a view to entering the accelerator-based bnct era. *Int J Clin Oncol*. (2020) 25:43–50. doi: 10.1007/s10147-019-01480-4

18. Blue TE, Yanch JC. Accelerator-based epithermal neutron sources for boron neutron capture therapy of brain tumors. *J Neurooncol*. (2003) 62:19–31. doi: 10.1007/bf02699931

19. Amin Shokr AA, Auterinen C, Binney I, Blaumann S, Blue H, Burian T, et al. *Current Status of Neutron Capture Therapy*. Vienna: INTERNATIONAL ATOMIC ENERGY AGENCY (2001).

20. Kumada H, Sakae T, Sakurai H. Current development status of accelerator-based neutron source for boron neutron capture therapy. *EPJ Techn Instrument*. (2023) 10:18. doi: 10.1140/epjti/s40485-023-00105-5

21. Tanaka H, Sakurai Y, Suzuki M, Masunaga S, Kinashi Y, Kashino G, et al. Characteristics comparison between a cyclotron-based neutron source and kur-hwnif for boron neutron capture therapy. *Nucl Instruments Methods Phys Res Section B: Beam Interact Mater Atoms*. (2009) 267:1970–7. doi: 10.1016/j.nimb.2009.03.095

22. Nakamura S, Igaki H, Ito M, Imamichi S, Kashihara T, Okamoto H, et al. Neutron flux evaluation model provided in the accelerator-based boron neutron capture therapy system employing a solid-state lithium target. *Sci Rep*. (2021) 11:8090. doi: 10.1038/s41598-021-87627-8

23. Horiike H, Murata I, Iida T, Yoshihashi S, Hoashi E, Kato I, et al. Liquid li based neutron source for bnct and science application. *Appl Radiat Isotopes*. (2015) 106:92–4. doi: 10.1016/j.apradiso.2015.07.026

24. Kumada H, Kurihara T, Yoshioka M, Kobayashi H, Matsumoto H, Sugano T, et al. Development of beryllium-based neutron target system with three-layer structure for accelerator-based neutron source for boron neutron capture therapy. *Appl Radiat Isotopes*. (2015) 106:78–83. doi: 10.1016/j.apradiso.2015.07.033

25. Matsumura A, Asano T, Hirose K, Igaki H, Kawabata S, Kumada H. Initiatives toward clinical boron neutron capture therapy in Japan. *Cancer Biother Radiopharm*. (2023) 38:201–7. doi: 10.1089/cbr.2022.0056

26. Zhang Z, Chong Y, Liu Y, Pan J, Huang C, Sun Q, et al. A review of planned, ongoing clinical studies and recent development of bnct in mainland of China. *Cancers (Basel)*. (2023) 15:16. doi: 10.3390/cancers15164060

27. Bae Y-s, Kim D-S, Seo HJ, Han J-U, Yoon HJ, Hwang JJ, et al. Advances of linac-based boron neutron capture therapy in Korea. *AAPPS Bull*. (2022) 32:34. doi: 10.1007/s43673-022-00063-2

28. Barth RF, Coderre JA, Vicente MG, Blue TE. Boron neutron capture therapy of cancer: current status and future prospects. *Clin Cancer Res*. (2005) 11:3987–4002. doi: 10.1158/1078-0432.Ccr-05-0035

29. Goodwin JT, Farr LE, Sweet WH, Robertson JS. Pathological study of eight patients with glioblastoma multiforme treated by neutron-capture therapy using boron 10. *Cancer*. (1955) 8:601–15. doi: 10.1002/1097-0142(1955)8:3<601::aid-cncr2820080326>3.0.co;2-r

30. Soloway AH, Hatanaka H, Davis MA. Penetration of brain and brain tumor. Vii. Tumor-binding sulfhydryl boron compounds. *J Medicinal Chem*. (1967) 10:714–7. doi: 10.1021/jm00316a042

31. Snyder H, Reedy AJ, Lennarz WJ. Synthesis of aromatic boronic acids. Aldehydo boronic acids and a boronic acid analog of tyrosine1. *J Am Chem Soc*. (1958) 80:835–8. doi: 10.1021/ja01537a021

32. Hideghéty K, Sauerwein W, Wittig A, Götz C, Paquis P, Grochulla F, et al. Tissue uptake of bsh in patients with glioblastoma in the eortc 11961 phase I bnct trial. *J neuro-oncol*. (2003) 62:145–56. doi: 10.1007/BF02699941

33. Wittig A, Sauerwein WA, Coderre JA. Mechanisms of transport of P-borono-phenylalanine through the cell membrane *in vitro*. *Radiat Res*. (2000) 153:173–80. doi: 10.1667/0033-7587(2000)153[0173:motpb]2.0.co;2

34. Barth RF, Vicente MG, Harling OK, Kiger WS 3rd, Riley KJ, Binns PJ, et al. Current status of boron neutron capture therapy of high grade gliomas and recurrent head and neck cancer. *Radiat Oncol*. (2012) 7:146. doi: 10.1186/1748-717x-7-146

35. Barth RF, Mi P, Yang W. Boron delivery agents for neutron capture therapy of cancer. *Cancer Commun (Lond)*. (2018) 38:35. doi: 10.1186/s40880-018-0299-7

36. Kalot G, Godard A, Busser B, Pliquett J, Broekgaarden M, Motto-Ros V, et al. Aza-bodipy: A new vector for enhanced theranostic boron neutron capture therapy applications. *Cells*. (2020) 9:1953. doi: 10.3390/cells9091953

37. Lamba M, Goswami A, Bandyopadhyay A. A periodic development of bpa and bsh based derivatives in boron neutron capture therapy (Bnct). *Chem Commun*. (2021) 57:827–39. doi: 10.1039/D0CC06557A

38. Watanabe T, Hattori Y, Ohta Y, Ishimura M, Nakagawa Y, Sanada Y, et al. Comparison of the pharmacokinetics between L-bpa and L-fbpa using the same administration dose and protocol: A validation study for the theranostic approach using [18 F]-L-fbpa positron emission tomography in boron neutron capture therapy. *BMC Cancer*. (2016) 16:1–10. doi: 10.1186/s12885-016-2913-x

39. Kabalka G, Wu Z, Yao ML. Synthesis of a series of boronated unnatural cyclic amino acids as potential boron neutron capture therapy agents. *Appl Organometal Chem*. (2008) 22:516–22. doi: 10.1002/aoc.1435

40. Semioshkin A, Nizhnik E, Godovikov I, Starikova Z, Bregadze V. Reactions of oxonium derivatives of [B12h12]2– with amines: synthesis and structure of novel B12-based ammonium salts and amino acids. *J Organometal Chem*. (2007) 692:4020–8. doi: 10.1016/j.jorganchem.2007.06.001

41. Mäde V, Els-Heindl S, Beck-Sickinger AG. Automated solid-phase peptide synthesis to obtain therapeutic peptides. *Beilstein J Organ Chem*. (2014) 10:1197–212. doi: 10.3762/bjoc.10.118

42. Iguchi Y, Michiue H, Kitamatsu M, Hayashi Y, Takenaka F, Nishiki T-i, et al. Tumor-specific delivery of bsh-3r for boron neutron capture therapy and positron emission tomography imaging in a mouse brain tumor model. *Biomaterials*. (2015) 56:10–7. doi: 10.1016/j.biomaterials.2015.03.061

43. Isono A, Tsuji M, Sanada Y, Matsushita A, Masunaga S, Hirayama T, et al. Design, synthesis, and evaluation of lipopeptide conjugates of mercaptoundecahydrododecaborate for boron neutron capture therapy. *ChemMedChem*. (2019) 14:823–32. doi: 10.1002/cmdc.201800793

44. Backer MV, Gaynutdinov TI, Patel V, Bandyopadhyaya AK, Thirumamagal BTS, Tjarks W, et al. Vascular endothelial growth factor selectively targets boronated dendrimers to tumor vasculature. *Mol Cancer Ther*. (2005) 4:1423–9. doi: 10.1158/1535-7163.Mct-05-0161

45. Yang W, Barth RF, Wu G, Huo T, Tjarks W, Ciesielski M, et al. Convection enhanced delivery of boronated egf as a molecular targeting agent for neutron capture therapy of brain tumors. *J Neuro-Oncol*. (2009) 95:355–65. doi: 10.1007/s11060-009-9945-x

46. Koppenol WH, Bounds PL, Dang CV. Otto Warburg's contributions to current concepts of cancer metabolism. *Nat Rev Cancer*. (2011) 11:325–37. doi: 10.1038/nrc3038

47. Itoh T, Tamura K, Ueda H, Tanaka T, Sato K, Kuroda R, et al. Design and synthesis of boron containing monosaccharides by the hydroboration of D-glucal for use in boron neutron capture therapy (Bnct). *Bioorgan Medicinal Chem*. (2018) 26:5922–33. doi: 10.1016/j.bmc.2018.10.041

48. Matović J, Järvinen J, Bland HC, Sokka IK, Imlimthan S, Ferrando RM, et al. Addressing the biochemical foundations of a glucose-based "Trojan horse"-strategy to boron neutron capture therapy: from chemical synthesis to *in vitro* assessment. *Mol Pharma*. (2020) 17:3885–99. doi: 10.1021/acs.molpharmaceut.0c00630

49. Tsurubuchi T, Shirakawa M, Kurosawa W, Matsumoto K, Ubagai R, Umishio H, et al. Evaluation of a novel boron-containing A-D-mannopyranoside for bnct. *Cells*. (2020) 9:1277. doi: 10.3390/cells9051277

50. Xiong M, Lei Q, You X, Gao T, Song X, Xia Y, et al. Mannosylated liposomes improve therapeutic effects of paclitaxel in colon cancer models. *J Microencapsul*. (2017) 34:513–21. doi: 10.1080/02652048.2017.1339739

51. Arnér ESJ, Eriksson S. Mammalian deoxyribonucleoside kinases. *Pharmacol Ther*. (1995) 67:155–86. doi: 10.1016/0163-7258(95)00015-9

52. Tjarks W, Tiwari R, Byun Y, Narayanasamy S, Barth RF. Carboranyl thymidine analogues for neutron capture therapy. *Chem Commun*. (2007) 47:4978–91. doi: 10.1039/b707257k

53. Barth RF, Yang W, Nakkula RJ, Byun Y, Tjarks W, Chu Wu L, et al. Evaluation of tk1 targeting carboranyl thymidine analogs as potential delivery agents for neutron capture therapy of brain tumors. *Appl Radiat Isotopes*. (2015) 106:251–5. doi: 10.1016/j.apradiso.2015.06.031

54. Parker N, Turk MJ, Westrick E, Lewis JD, Low PS, Leamon CP. Folate receptor expression in carcinomas and normal tissues determined by a quantitative radioligand binding assay. *Anal Biochem*. (2005) 338:284–93. doi: 10.1016/j.ab.2004.12.026

55. Zwicke GL, Ali Mansoori G, Jeffery CJ. Utilizing the folate receptor for active targeting of cancer nanotherapeutics. *Nano Rev*. (2012) 3:18496. doi: 10.3402/nano.v3i0.18496

56. Nakagawa F, Kawashima H, Morita T, Nakamura H. Water-soluble closo-docecaborate-containing pteroyl derivatives targeting folate receptor-positive tumors for boron neutron capture therapy. *Cells*. (2020) 9:1615. doi: 10.3390/cells9071615

57. Leonelli F, La Bella A, Francescangeli A, Joudioux R, Capodilupo A-L, Quagliariello M, et al. A new and simply available class of hydrosoluble bioconjugates by coupling paclitaxel to hyaluronic acid through a 4-hydroxybutanoic acid derived linker. *Helv Chimica Acta*. (2005) 88:154–9. doi: 10.1002/hlca.200490289

58. Di Meo C, Panza L, Campo F, Capitani D, Mannina L, Banzato A, et al. Novel types of carborane-carrier hyaluronan derivatives via "Click chemistry. *Macromol Biosci*. (2008) 8:670–81. doi: 10.1002/mabi.200700304

59. Yu X, Li Z. Microrna expression and its implications for diagnosis and therapy of tongue squamous cell carcinoma. *J Cell Mol Med*. (2016) 20:10–6. doi: 10.1111/jcmm.12650

60. Zhang T, Du S, Wang Y, Guo Y, Yi Y, Liu B, et al. Novel carborane compounds based on cyclooxygenase-2 inhibitors for effective boron neutron capture therapy of tongue squamous cell carcinoma. *ChemistrySelect*. (2020) 5:14652–60. doi: 10.1002/slct.202004077

61. Xenaki KT, Oliveira S, van Bergen en Henegouwen PMP. Antibody or antibody fragments: implications for molecular imaging and targeted therapy of solid tumors. *Front Immunol*. (2017) 8:1287. doi: 10.3389/fimmu.2017.01287

62. Goldenberg DM, Sharkey RM, Primus FJ, Mizusawa E, Hawthorne MF. Neutron-capture therapy of human cancer: *in vivo* results on tumor localization of boron-10-labeled antibodies to carcinoembryonic antigen in the gw-39 tumor model system. *Proc Natl Acad Sci*. (1984) 81:560–3. doi: 10.1073/pnas.81.2.560

63. Wu G, Yang W, Barth RF, Kawabata S, Swindall M, Bandyopadhyaya AK, et al. Molecular targeting and treatment of an epidermal growth factor receptor–positive glioma using boronated cetuximab. *Clin Cancer Res*. (2007) 13:1260–8. doi: 10.1158/1078-0432.Ccr-06-2399

64. Yang W, Barth RF, Wu G, Kawabata S, Sferra TJ, Bandyopadhyaya AK, et al. Molecular targeting and treatment of egfrviii-positive gliomas using boronated monoclonal antibody L8a4. *Clin Cancer Res*. (2006) 12:3792–802. doi: 10.1158/1078-0432.Ccr-06-0141

65. Yang W, Barth RF, Wu G, Tjarks W, Binns P, Riley K. Boron neutron capture therapy of egfr or egfrviii positive gliomas using either boronated monoclonal antibodies or epidermal growth factor as molecular targeting agents. *Appl Radiat Isotopes*. (2009) 67:S328–S31. doi: 10.1016/j.apradiso.2009.03.030

66. Yang W, Wu G, Barth RF, Swindall MR, Bandyopadhyaya AK, Tjarks W, et al. Molecular targeting and treatment of composite egfr and egfrviii-positive gliomas using boronated monoclonal antibodies. *Clin Cancer Res*. (2008) 14:883–91. doi: 10.1158/1078-0432.Ccr-07-1968

67. Nakase I, Aoki A, Sakai Y, Hirase S, Ishimura M, Takatani-Nakase T, et al. Antibody-based receptor targeting using an fc-binding peptide-dodecaborate conjugate and macropinocytosis induction for boron neutron capture therapy. *ACS Omega*. (2020) 5:22731–8. doi: 10.1021/acsomega.0c01377

68. Sun T, Li Y, Huang Y, Zhang Z, Yang W, Du Z, et al. Targeting glioma stem cells enhances anti-tumor effect of boron neutron capture therapy. *Oncotarget*. (2016) 7:43095. doi: 10.18632/oncotarget.v7i28

69. Yoon T-J, Lee W, Oh Y-S, Lee J-K. Magnetic nanoparticles as a catalyst vehicle for simple and easy recycling. *New J Chem*. (2003) 27:227–9. doi: 10.1039/b209391j

70. Bhatia SN, Chen X, Dobrovolskaia MA, Lammers T. Cancer nanomedicine. *Nat Rev Cancer*. (2022) 22:550–6. doi: 10.1038/s41568-022-00496-9

71. Zhu Y, Hosmane NS. Nanostructured boron compounds for cancer therapy. *Pure Appl Chem*. (2018) 90:653–63. doi: 10.1515/pac-2017-0903

72. Wu J. The enhanced permeability and retention (Epr) effect: the significance of the concept and methods to enhance its application. *J personal Med*. (2021) 11:771. doi: 10.3390/jpm11080771

73. Shukla S, Wu G, Chatterjee M, Yang W, Sekido M, Diop LA, et al. Synthesis and biological evaluation of folate receptor-targeted boronated pamam dendrimers as potential agents for neutron capture therapy. *Bioconjugate Chem*. (2003) 14:158–67. doi: 10.1021/bc025586o

74. Ruan Z, Liu L, Fu L, Xing T, Yan L. An amphiphilic block copolymer conjugated with carborane and a nir fluorescent probe for potential imaging-guided bnct therapy. *Polymer Chem*. (2016) 7:4411–8. doi: 10.1039/C6PY00799F

75. Sumitani S, Oishi M, Yaguchi T, Murotani H, Horiguchi Y, Suzuki M, et al. Pharmacokinetics of core-polymerized, boron-conjugated micelles designed for boron neutron capture therapy for cancer. *Biomaterials*. (2012) 33:3568–77. doi: 10.1016/j.biomaterials.2012.01.039

76. Takeuchi I, Nomura K, Makino K. Hydrophobic boron compound-loaded poly (L-lactide-co-glycolide) nanoparticles for boron neutron capture therapy. *Colloids Surf B: Biointerf*. (2017) 159:360–5. doi: 10.1016/j.colsurfb.2017.08.002

77. Chen J, Yang Q, Liu M, Lin M, Wang T, Zhang Z, et al. Remarkable boron delivery of irgd-modified polymeric nanoparticles for boron neutron capture therapy. *Int J Nanomed*. (2019) 14:8161–77. doi: 10.2147/IJN.S214224

78. Nomoto T, Inoue Y, Yao Y, Suzuki M, Kanamori K, Takemoto H, et al. Poly (Vinyl alcohol) boosting therapeutic potential of P-boronophenylalanine in neutron capture therapy by modulating metabolism. *Sci Adv*. (2020) 6:eaaz1722. doi: 10.1126/sciadv.aaz1722

79. Dai L, Liu J, Zhao X, Li Y, Zhou S, Yuan L, et al. Bpa-containing polydopamine nanoparticles for boron neutron capture therapy in a U87 glioma orthotopic model. *Adv Funct Mater*. (2023) 33:2214145. doi: 10.1002/adfm.202214145

80. Xu H, Liu J, Li R, Lin J, Gui L, Wang Y, et al. Novel promising boron agents for boron neutron capture therapy: current status and outlook on the future. *Coordin Chem Rev*. (2024) 511:215795. doi: 10.1016/j.ccr.2024.215795

81. Luo T, Huang W, Chu F, Zhu T, Feng B, Huang S, et al. The dawn of a new era: tumor-targeting boron agents for neutron capture therapy. *Mol Pharm*. (2023) 20:4942–70. doi: 10.1021/acs.molpharmaceut.3c00701

82. Li L, Li J, Shi Y, Du P, Zhang Z, Liu T, et al. On-demand biodegradable boron nitride nanoparticles for treating triple negative breast cancer with boron neutron capture therapy. *ACS Nano*. (2019) 13:13843–52. doi: 10.1021/acsnano.9b04303

83. Kaur M, Singh P, Singh K, Gaharwar US, Meena R, Kumar M, et al. Boron nitride (10bn) a prospective material for treatment of cancer by boron neutron capture therapy (Bnct). *Mater Lett*. (2020) 259:126832. doi: 10.1016/j.matlet.2019.126832

84. Ciofani G, Raffa V, Menciassi A, Cuschieri A. Boron nitride nanotubes: an innovative tool for nanomedicine. *Nano Today*. (2009) 4:8–10. doi: 10.1016/j.nantod.2008.09.001

85. Nakamura H, Koganei H, Miyoshi T, Sakurai Y, Ono K, Suzuki M. Antitumor effect of boron nitride nanotubes in combination with thermal neutron irradiation on bnct. *Bioorgan med Chem Lett*. (2015) 25:172–4. doi: 10.1016/j.bmcl.2014.12.005

86. Pan J, Li F, Choi JH. Single-walled carbon nanotubes as optical probes for bio-sensing and imaging. *J Mater Chem B*. (2017) 5:6511–22. doi: 10.1039/C7TB00748E

87. Li J, Kong J, Ma S, Li J, Mao M, Chen K, et al. Exosome-coated 10b carbon dots for precise boron neutron capture therapy in a mouse model of glioma *in situ*. *Adv Funct Mater*. (2021) 31:2100969. doi: 10.1002/adfm.202100969

88. Korolkov IV, Ludzik K, Kozlovskiy AL, Fadeev MS, Shumskaya AE, Gorin YG, et al. Carboranes immobilization on fe3o4 nanocomposites for targeted delivery. *Mater Today Commun*. (2020) 24:101247. doi: 10.1016/j.mtcomm.2020.101247

89. Zhu Y, Stubbs LP, Ho F, Liu R, Ship CP, Maguire JA, et al. Magnetic nanocomposites: A new perspective in catalysis. *ChemCatChem*. (2010) 2:365–74. doi: 10.1002/cctc.200900314

90. Wu C-Y, Hsieh H-H, Chang T-Y, Lin J-J, Wu C-C, Hsu M-H, et al. Development of mri-detectable boron-containing gold nanoparticle-encapsulated biodegradable polymeric matrix for boron neutron capture therapy (Bnct). *Int J Mol Sci*. (2021) 22:8050. doi: 10.3390/ijms22158050

91. Hawthorne MF. The role of chemistry in the development of boron neutron capture therapy of cancer. *Angew Chem Int Ed Engl*. (1993) 32:950. doi: 10.1002/anie.199309501

92. Tamanoi F, Chinnathambi S, Laird M, Komatsu A, Birault A, Takata T, et al. Construction of boronophenylalanine-loaded biodegradable periodic mesoporous organosilica nanoparticles for bnct cancer therapy. *Int J Mol Sci*. (2021) 22:2251. doi: 10.3390/ijms22052251

93. Laird M, Matsumoto K, Higashi Y, Komatsu A, Raitano A, Morrison K, et al. Organosilica nanoparticles containing sodium borocaptate (Bsh) provide new prospects for boron neutron capture therapy (Bnct): efficient cellular uptake and enhanced bnct efficacy. *Nanoscale Adv*. (2023) 5:2537–46. doi: 10.1039/D2NA00839D

94. Barth RF, Adams DM, Soloway AH, Mechetner EB, Alam F, Anisuzzaman AKM. Determination of boron in tissues and cells using direct-current plasma atomic emission spectroscopy. *Anal Chem*. (1991) 63:890–3. doi: 10.1021/ac00009a010

95. Mukai K, Nakagawa Y, Matsumoto K. Prompt gamma ray spectrometry for *in vivo* measurement of boron-10 concentration in rabbit brain tissue. *Neurol medico-chirurgica*. (1995) 35:855–60. doi: 10.2176/nmc.35.855

96. Arlinghaus HF, Spaar MT, Switzer RC, Kabalka GW. Imaging of boron in tissue at the cellular level for boron neutron capture therapy. *Anal Chem*. (1997) 69:3169–76. doi: 10.1021/ac970036i

97. Michel J, Sauerwein W, Wittig A, Balossier G, Zierold K. Subcellular localization of boron in cultured melanoma cells by electron energy-loss spectroscopy of freeze-dried cryosections. *J Microsc*. (2003) 210:25–34. doi: 10.1046/j.1365-2818.2003.01172.x

98. Amemiya K, Takahashi H, Kajimoto Y, Nakazawa M, Yanagie H, Hisa T, et al. High-resolution nuclear track mapping in detailed cellular histology using cr-39 with the contact microscopy technique. *Radiat Measure*. (2005) 40:283–8. doi: 10.1016/j.radmeas.2005.01.010

99. Basilico F, Sauerwein W, Pozzi F, Wittig A, Moss R, Mauri PL. Analysis of 10b antitumoral compounds by means of flow-injection into esi-ms/ms. *J Mass Spectrom*. (2005) 40:1546–9. doi: 10.1002/jms.909

100. Masunaga S-i, Sakurai Y, Suzuki M, Nagata K, Maruhashi A, Kinash Y, et al. Combination of the vascular targeting agent zd6126 with boron neutron capture therapy. *Int J Radiat OncologyBiologyPhysics*. (2004) 60:920–7. doi: 10.1016/j.ijrobp.2004.07.672

101. Yokoyama K, Miyatake S-I, Kajimoto Y, Kawabata S, Doi A, Yoshida T, et al. Pharmacokinetic study of bsh and bpa in simultaneous use for bnct. *J Neuro-oncol*. (2006) 78:227–32. doi: 10.1007/s11060-005-9099-4

102. Chandra S, Barth RF, Haider SA, Yang W, Huo T, Shaikh AL, et al. Biodistribution and subcellular localization of an unnatural boron-containing amino acid (Cis-abcpc) by imaging secondary ion mass spectrometry for neutron capture therapy of melanomas and gliomas. *PloS One*. (2013) 8:e75377. doi: 10.1371/journal.pone.0075377

103. Chandra S, Lorey DR II, Smith DR. Quantitative subcellular secondary ion mass spectrometry (Sims) imaging of boron-10 and boron-11 isotopes in the same cell delivered by two combined bnct drugs: *in vitro* studies on human glioblastoma T98g cells. *Radiat Res*. (2002) 157:700–10, 11. doi: 10.1667/0033-7587(2002)157[0700:QSSIMS]2.0.CO;2

104. Wittig A, Arlinghaus HF, Kriegeskotte C, Moss RL, Appelman K, Schmid KW, et al. Laser postionization secondary neutral mass spectrometry in tissue: A powerful tool for elemental and molecular imaging in the development of targeted drugs. *Mol Cancer Ther*. (2008) 7:1763–71. doi: 10.1158/1535-7163.MCT-08-0191

105. Aldossari S, McMahon G, Lockyer NP, Moore KL. Microdistribution and quantification of the boron neutron capture therapy drug bpa in primary cell cultures of human glioblastoma tumour by nanosims. *Analyst*. (2019) 144:6214–24. doi: 10.1039/C9AN01336A

106. Reifschneider O, Schütz CL, Brochhausen C, Hampel G, Ross T, Sperling M, et al. Quantitative bioimaging of P-boronophenylalanine in thin liver tissue sections as a tool for treatment planning in boron neutron capture therapy. *Anal Bioanal Chem*. (2015) 407:2365–71. doi: 10.1007/s00216-014-8012-4

107. Kobayashi T, Sakurai Y, Ishikawa M. A noninvasive dose estimation system for clinical bnct based on pg-spect—Conceptual study and fundamental experiments using hpge and cdte semiconductor detectors. *Med Phys*. (2000) 27:2124–32. doi: 10.1118/1.1288243

108. Morita T, Kurihara H, Hiroi K, Honda N, Igaki H, Hatazawa J, et al. Dynamic changes in 18f-borono-L-phenylalanine uptake in unresectable, advanced, or recurrent squamous cell carcinoma of the head and neck and Malignant melanoma during boron neutron capture therapy patient selection. *Radiat Oncol*. (2018) 13:4. doi: 10.1186/s13014-017-0949-y

109. Nakamura H, Fukuda H, Girald F, Kobayashi T, Hiratsuka J, Akaizawa T, et al. *In vivo* evaluation of carborane gadolinium-dtpa complex as an mr imaging boron carrier. *Chem Pharm Bull*. (2000) 48:1034–8. doi: 10.1248/cpb.48.1034

110. Takahashi K, Nakamura H, Furumoto S, Yamamoto K, Fukuda H, Matsumura A, et al. Synthesis and *in vivo* biodistribution of bpa–gd–dtpa complex as a potential mri contrast carrier for neutron capture therapy. *Bioorgan Medicinal Chem*. (2005) 13:735–43. doi: 10.1016/j.bmc.2004.10.046

111. Slatkin DN. A history of boron neutron capture therapy of brain tumours: postulation of a brain radiation dose tolerance limit. *Brain*. (1991) 114:1609–29. doi: 10.1093/brain/114.4.1609

112. Kawabata S, Miyatake S-I, Kuroiwa T, Yokoyama K, Doi A, Iida K, et al. Boron neutron capture therapy for newly diagnosed glioblastoma. *J Radiat Res*. (2008) 50:51–60. doi: 10.1269/jrr.08043

113. Kageji T, Mizobuchi Y, Nagahiro S, Nakagawa Y, Kumada H. Long-survivors of glioblatoma treated with boron neutron capture therapy (Bnct). *Appl Radiat Isotopes*. (2011) 69:1800–2. doi: 10.1016/j.apradiso.2011.03.021

114. Yamamoto T, Matsumura A, Nakai K, Shibata Y, Endo K, Sakurai F, et al. Current clinical results of the Tsukuba bnct trial. *Appl Radiat Isotopes*. (2004) 61:1089–93. doi: 10.1016/j.apradiso.2004.05.010

115. Miyatake S-I, Kawabata S, Yokoyama K, Kuroiwa T, Michiue H, Sakurai Y, et al. Survival benefit of boron neutron capture therapy for recurrent Malignant gliomas. *J neuro-oncol*. (2009) 91:199–206. doi: 10.1007/s11060-008-9699-x

116. Studying the Safety, Efficacy, and Pharmacokinetic Characteristics of Bnct in Patients with Recurrent High-Grade Gliomas. Available online at: https://clinicaltrials.gov/study/NCT05737212?term=NCT05737212&rank=1 (Accessed September 07, 2024).

117. Kawabata S, Miyatake S-I, Hiramatsu R, Hirota Y, Miyata S, Takekita Y, et al. Phase ii clinical study of boron neutron capture therapy combined with X-ray radiotherapy/temozolomide in patients with newly diagnosed glioblastoma multiforme—Study design and current status report. *Appl Radiat Isotopes*. (2011) 69:1796–9. doi: 10.1016/j.apradiso.2011.03.014

118. Boron Phenylalanine with or without Mannitol in Treating Patients with Glioblastoma Multiforme. Available online at: https://clinicaltrials.gov/study/NCT01233492?term=NCT01233492&rank=1 (Accessed September 07, 2024).

119. Phase I Clinical Bnct Trial to Evaluate the Safty of ibnct001 and spm-011, accelerator-based novel high-power neutron source in patient with newly diagnosed glioblastoma (Ibnct-gbm-01). Available online at: https://jrct.niph.go.jp/latest-detail/jRCT2032230554 (Accessed September 07, 2024).

120. Phase ii clinical trial on clinical efficacy and safety of combination therapy of boron neutron capture therapy and bevacizumab for recurrent glioma with poor prognosis. Available online at: https://jrct.niph.go.jp/en-latest-detail/jRCTs051180218 (Accessed September 07, 2024).

121. Wittig A, Collette L, Appelman K, Bührmann S, Jäckel MC, Jöckel KH, et al. Eortc trial 11001: distribution of two 10b-compounds in patients with squamous cell carcinoma of head and neck, a translational research/phase 1 trial. *J Cell Mol Med*. (2009) 13:1653–65. doi: 10.1111/j.1582-4934.2009.00856.x

122. Wang L-W, Chen Y-W, Ho C-Y, Liu Y-WH, Chou F-I, Liu Y-H, et al. Fractionated boron neutron capture therapy in locally recurrent head and neck cancer: A prospective phase I/ii trial. *Int J Radiat Oncol Biol Phys*. (2016) 95:396–403. doi: 10.1016/j.ijrobp.2016.02.028

123. Bnct and ig-imrt for recurrent head and neck cancer. Available online at: https://clinicaltrials.gov/study/NCT02004795?term=NCT02004795&rank=1 (Accessed September 07, 2024).

124. Kankaanranta L, Seppälä T, Koivunoro H, Saarilahti K, Atula T, Collan J, et al. Boron neutron capture therapy in the treatment of locally recurred head-and-neck cancer: final analysis of a phase I/ii trial. *Int J Radiat Oncol Biol Phys*. (2012) 82:e67–75. doi: 10.1016/j.ijrobp.2010.09.057

125. Dose optimized bnct for head and neck cancer (St-bnct2001). Available online at: https://clinicaltrials.gov/study/NCT05883007?term=NCT05883007&rank=1 (Accessed September 07, 2024).

126. Hirose K, Konno A, Hiratsuka J, Yoshimoto S, Kato T, Ono K, et al. Boron neutron capture therapy using cyclotron-based epithermal neutron source and borofalan (10b) for recurrent or locally advanced head and neck cancer (Jhn002): an open-label phase ii trial. *Radiother Oncol*. (2021) 155:182–7. doi: 10.1016/j.radonc.2020.11.001

127. Establishment of protocol for neutron capture therapy for head and neck cancer (Bnct for hnc). Available online at: https://jrct.niph.go.jp/en-latest-detail/jRCTs051180160 (Accessed September 07, 2024).

128. Clinical study to evaluate the usefulness of 18F-FBPA-PET for patient selection and expanding indication for BNCT. Available online at: https://jrct.niph.go.jp/en-latest-detail/jRCTs031180302 (Accessed September 07, 2024).

129. Boron neutron capture therapy using cyclotron-based epithermal neutron source for squamous cell carcinoma of the head and neck refractory to standard treatments: an open-label phase ii trial. Available online at: https://rctportal.niph.go.jp/s/detail/um?trial_id=UMIN000044118 (Accessed September 07, 2024).

130. A single-center, single-arm clinical trial of the safety and efficacy of boron neutron capture therapy (Bnct) for advanced refractory Malignant tumors. Available online at: https://www.chictr.org.cn/showproj.html?proj=181032 (Accessed September 07, 2024).

131. In-hospital neutron irradiator (Ihni)-based boron neutron capture therapy (Bnct) in the treatment of Malignant melanoma. Available online at: https://clinicaltrials.gov/study/NCT02759536?intr=NCT02759536&rank=1 (Accessed September 07, 2024).

132. Boron neutron capture therapy using boronophenylalanine-fructose complex in treating patients with metastatic melanoma. Available online at: https://clinicaltrials.gov/study/NCT00085059?term=NCT00085059&rank=1 (Accessed September 07, 2024).

133. Boron neutron capture therapy using cics-1 and spm-011 for Malignant melanoma and angiosarcoma. Available online at: https://clinicaltrials.gov/study/NCT04293289?term=NCT04293289&rank=1 (Accessed September 07, 2024).

134. A phase ii study by using cics-1 and spm-011 commissioned by cics and stella pharma. Available online at: https://clinicaltrials.gov/study/NCT05601232?term=NCT05601232&rank=1 (Accessed September 07, 2024).

135. Lee J-C, Chuang K-S, Hsueh Liu Y-W, Lin T-Y, Teng Y-C, Wang L-W. A comparison of dose distributions in gross tumor volume between boron neutron capture therapy alone and combined boron neutron capture therapy plus intensity modulation radiation therapy for head and neck cancer. *PloS One*. (2019) 14:e0210626. doi: 10.1371/journal.pone.0210626

136. Bnct Phase I/Ii Trial for Skin Malignancies. Available online at: https://jrct.niph.go.jp/latest-detail/jRCTs061180066 (Accessed September 07, 2024).

137. Inoue M, Lee CM, Ono K, Suzuki M, Tokunaga T, Sawa Y, et al. Clinical effectiveness of boron neutron capture therapy for a recurrent Malignant peripheral nerve sheath tumor in the mediastinum. *J Thorac Oncol*. (2010) 5:2037–8. doi: 10.1097/JTO.0b013e3181f1cd86

日中笹川医学奨学金制度<学位取得コース>中間評価書
【課程博士：指導教官用】

Supported by 日本財団 THE NIPPON FOUNDATION

第45期　　研究者番号：　G4503

氏名	李 博倫	LI BOLUN	性別	M	生年月日	1992/10/7
所属機関（役職）	自治医科大学（大学院生）					
日本研究先（指導教官）	自治医科大学形成外科学講座（吉村 浩太郎　教授）					
研究テーマ	放射線照射によるマウス・インプラント被膜拘縮モデルに対する脂肪由来幹細胞の治療あるいは予防効果の検討					
専攻種別	論文博士	□	課程博士	☑		

研究者評価（指導教官記入欄）

成績状況	優・良・可・不可から選択してください⇒	優	取得単位数	23
	学業成績係数=	3	取得すべき単位総数	38
学生本人が行った研究の概要	カプセル拘縮の研究、メラノサイト含有培養皮膚の研究を確実に行っている。			
総合評価	【良かった点】 真面目で勤勉である。			
	【改善すべき点】 なし。			
	【今後の展望】 日本語の上達が見込める。			
学位取得見込	2027年の見込み			
評価者（指導教官記名）	吉村　浩太郎	作成日：	2025年　3　月　10　日	

日中笹川医学奨学金制度<学位取得コース>中間報告書
【研究者用】

Supported by 日本財団 THE NIPPON FOUNDATION

第45期　　研究者番号：G4503　　作成日：2025年3月10日

氏名	李 博倫	LI BOLUN	性別	M	生年月日	1992/10/7
中国所属機関(役職)	自治医科大学（大学院生）					
日本研究先（指導教官）	自治医科大学形成外科学講座（吉村 浩太郎　教授）					
研究テーマ(日文)	放射線照射によるマウス・インプラント被膜拘縮モデルに対する脂肪由来幹細胞の治療あるいは予防効果の検討					
Research theme	The Investigation of Therapeutic or Preventive Effects of Adipose Derived Stem Cells on Radiation Induced Capsular Contraction Around Implant in Mouse Model					
専攻種別	論文博士	☐	課程博士	☑		

1．研究概要(1)

1)目的(Goal)

Capsular contracture is one of the most common complications in Implant-based breast reconstruction, and it tends to become more frequent and severe when a patient undergoes radiotherapy. On the other hand, adipose-derived stem cells have attracted attention for their anti-fibrosis effects, such as their therapeutic effect on pulmonary fibrosis. They are theoretically able to suppress or alleviate the formation of capsular contracture around implant. Therefore, we want to use a mouse model to investigate this.

2)戦略(Approach)

We plan to create a capsular contract mouse model by irradiating inserted mini-implant in mouse, after the model is confirmed, we isolated the mouse adipose derived stem cell from other mouse and transplanted them to the capsular contracted mouse. After a period of waiting time, the capsule harvested and analyzed.

3)材料と方法(Materials and methods)

24 black mice were used in this research, mini-Implant were placed under the panniculus carnosus muscle. 1 week after surgery. All mice were randomly assigned into 4 groups, Group A was set up as control group and mice in this group did not receive irradiation and injection. Mice in group B, C and D were irradiated 2 weeks after the surgery at a dose of 2Gy per day for 20 days to induce capsular contracture. 1 week after irradiation, CT scanning was performed on all mice, and the results were used as a baseline for comparison with results 6 months later. After that, mice in group B received peri-implant injection of culture medium, mice in group C received peri-implant injection of ASCs, mice in group D received intraperitoneal injection of ASCs. The adipose derived stem cell we injected was isolated from the inguinal fat of other mice, and passage 3 ASCs were used for in vitro experiment. Each mouse received 1 million ASCs. 6 months after irradiation, CT scanning was performed again, and all mice were sacrificed. The capsule along with the soft tissue and skin were harvested and then fixed. HE staining was performed for histological analysis of peri-implant capsule, immunofluorescence of α-SMA was performed. After that, we isolated ASC from ffLuc marked mouse and transplanted them to capsular contracted mouse model by received peri-implant injection or intraperitoneal injection and use IVIS to track the transplanted ASC.

4)実験結果(Results)

Compared with the control group, the mean thickness in vehicle group is thicker than that in control group, and the mean thickness in ASC treated group is thinner than that in control group and vehicle group, and all differences reach statistical significance. In IVIS tracking experiments, the immigration to the capsular tissue of intraperitoneal injected ASC was revealed by IVIS system.

5)考察(Discussion)

At present, we plan to conduct further research based on the results we have obtained. Through HE staining, we have confirmed that ASC can effectively alleviate the capsule thickening caused by radiation, and we plan to confirm this through immunohistochemical staining. Secondly, in the IVIS experiment, we found that the adipose stem cells injected intraperitoneally were successfully transferred to the periphery of the graft, so we plan to confirm the transplanted stem cells in the tissue through immunohistochemical staining.

1. 研究概要(2)

6)参考文献(References)

1.Lin AJ, Karinja SJ, Bernstein JL, et al. In Search of a Murine Model of Radiation-Induced Periprosthetic Capsular Fibrosis. Ann Plast Surg. Apr 2018;80(4 Suppl 4):S204-s210. doi:10.1097/sap.0000000000001362
2.Kim HB, Han HH, Eom JS. Difference in the occurrence of capsular contracture according to the characteristics of the tissue in an irradiated rat model. Plast Reconstr Surg. Mar 8 2023;doi:10.1097/prs.0000000000010387
3.Diehm YF, Thomé J, Will P, et al. Stem-cell enriched hybrid breast reconstruction reduces risk for capsular contracture in a hybrid breast reconstruction animal model. Plast Reconstr Surg. Feb 2 2023;doi:10.1097/prs.0000000000010260
4.Wright MA, Samadi A, Lin AJ, et al. Periprosthetic Capsule Formation and Contracture in a Rodent Model of Implant-Based Breast Reconstruction With Delayed Radiotherapy. Ann Plast Surg. Apr 2019;82(4S Suppl 3):S264-s270. doi:10.1097/sap.0000000000001892
5.Bui JM, Perry T, Ren CD, Nofrey B, Teitelbaum S, Van Epps DE. Histological characterization of human breast implant capsules. Aesthetic Plast Surg. Jun 2015;39(3):306-15. doi:10.1007/s00266-014-0439-7
6.Kim JB, Jeon HJ, Lee JW, et al. A murine model of radiation-induced capsule-tissue reactions around smooth silicone implants. J Plast Surg Hand Surg. Aug 2018;52(4):217-224. doi:10.1080/2000656x.2018.1444617
7.Katzel EB, Koltz PF, Tierney R, et al. A novel animal model for studying silicone gel-related capsular contracture. Plast Reconstr Surg. Nov 2010;126(5):1483-1491. doi:10.1097/PRS.0b013e3181ef8b8e

2. 執筆論文 Publication of thesis ※記載した論文を添付してください。Attach all of the papers listed below.

論文名 1 Title						
掲載誌名 Published journal						
	年　　月	巻(号)	頁　～　頁	言語 Language		
第1著者名 First author		第2著者名 Second author		第3著者名 Third author		
その他著者名 Other authors						
論文名 2 Title						
掲載誌名 Published journal						
	年　　月	巻(号)	頁　～　頁	言語 Language		
第1著者名 First author		第2著者名 Second author		第3著者名 Third author		
その他著者名 Other authors						
論文名 3 Title						
掲載誌名 Published journal						
	年　　月	巻(号)	頁　～　頁	言語 Language		
第1著者名 First author		第2著者名 Second author		第3著者名 Third author		
その他著者名 Other authors						
論文名 4 Title						
掲載誌名 Published journal						
	年　　月	巻(号)	頁　～　頁	言語 Language		
第1著者名 First author		第2著者名 Second author		第3著者名 Third author		
その他著者名 Other authors						
論文名 5 Title						
掲載誌名 Published journal						
	年　　月	巻(号)	頁　～　頁	言語 Language		
第1著者名 First author		第2著者名 Second author		第3著者名 Third author		
その他著者名 Other authors						

3. 学会発表 Conference presentation ※筆頭演者として総会・国際学会を含む主な学会で発表したものを記載してください。

※Describe your presentation as the principal presenter in major academic meetings including general meetings or international meetings.

学会名 Conference	第33回日本形成外科学会基礎学術集会（IPSRC・ISPRES・TAAT併催）			
演 題 Topic	The Investigation of Therapeutic or Preventive Effect of Adipose Derived Stem Cells on Radiation Induced Capsular Contracture in Mouse Model			
開催日 date	2024 年 10 月 18 日	開催地 venue	東京	
形式 method	☑ 口頭発表 Oral □ ポスター発表 Poster	言語 Language	□ 日本語 ☑ 英語 □ 中国語	
共同演者名 Co-presenter	Sowa Yoshihiro, Yoshimura Kotaro			
学会名 Conference	第24回日本再生医療学会総会（予定）			
演 題 Topic	The Investigation of Therapeutic or Preventive Effect of Adipose Derived Stem Cells on Radiation Induced Capsular Contracture in Mouse Model			
開催日 date	2025 年 3 月 21 日	開催地 venue	横浜	
形式 method	☑ 口頭発表 Oral □ ポスター発表 Poster	言語 Language	☑ 日本語 ☑ 英語 □ 中国語	
共同演者名 Co-presenter	Sowa Yoshihiro, Yoshimura Kotaro, Yoshihiro Toyohara, Shino Higai, Natumi Saito			
学会名 Conference				
演 題 Topic				
開催日 date	年 月 日	開催地 venue		
形式 method	□ 口頭発表 Oral □ ポスター発表 Poster	言語 Language	□ 日本語 □ 英語 □ 中国語	
共同演者名 Co-presenter				
学会名 Conference				
演 題 Topic				
開催日 date	年 月 日	開催地 venue		
形式 method	□ 口頭発表 Oral □ ポスター発表 Poster	言語 Language	□ 日本語 □ 英語 □ 中国語	
共同演者名 Co-presenter				

4. 受賞（研究業績） Award (Research achievement)

名 称 Award name				
	国名 Country name		受賞年 Year of award	年 月
名 称 Award name				
	国名 Country name		受賞年 Year of award	年 月

研究者番号：G4503

5. 本研究テーマに関わる他の研究助成金受給 Other research grants concerned with your resarch theme

受給実績 Receipt record	☐ 有　　☐ 無
助成機関名称 Funding agency	
助成金名称 Grant name	
受給期間 Supported period	年　　月 ～　　年　　月
受給額 Amount received	円
受給実績 Receipt record	☐ 有　　☐ 無
助成機関名称 Funding agency	
助成金名称 Grant name	
受給期間 Supported period	年　　月 ～　　年　　月
受給額 Amount received	円

6. 他の奨学金受給 Another awarded scholarship

受給実績 Receipt record	■ 有　　☐ 無
助成機関名称 Funding agency	マニー松谷医療奨学財団
奨学金名称 Scholarship name	大学院奨学金（医学博士志望）
受給期間 Supported period	2024　年　4　月 ～　2027　年　3　月
受給額 Amount received	50,000 円

7. 研究活動に関する報道発表 Press release concerned with your research activities

※記載した記事を添付してください。Attach a copy of the article described below

報道発表 Press release	☐ 有　　☐ 無	発表年月日 Date of release	
発表機関 Released medium			
発表形式 Release method	・新聞　・雑誌　・Web site　・記者発表　・その他（　　）		
発表タイトル Released title			

8. 本研究テーマに関する特許出願予定 Patent application concerned with your research theme

出願予定 Scheduled	☐ 有　　☐ 無	出願国 Application	
出願内容（概要） Application contents			

9. その他 Others

指導責任者（記名）　Yoshimura Kotaro

日中笹川医学奨学金制度<学位取得コース>中間評価書
【課程博士:指導教官用】

第45期　　研究者番号:　G4504

氏名	張 含煙	ZHANG HANYAN	性別	F	生年月日	1991/5/3
中国所属機関(役職)	西安培華学院人文与国際教育学院外国系(日本語講師)					
日本研究先(指導教官)	杏林大学国際協力研究科外国語学部(宮首 弘子　教授)					
研究テーマ	外国人患者の医療面接モデルから考える医療通訳サービスの向上					
専攻種別	論文博士	□	課程博士	☑		

研究者評価(指導教官記入欄)

成績状況	優・良・可・不可から選択してください⇒	優	取得単位数	10
	学業成績係数=	4	取得すべき単位総数	20

学生本人が行った研究の概要	張さんは、今年度の主な研究を次の5つのテーマを巡って行いました。 ① 医療通訳という研究分野においてこれまでどのような研究が行われているか、日本国内及び海外の先行研究をリサーチして、丹念に文献レビューをしてきました。 ② 医療通訳研究に必要な医療の基礎知識に関する科目を履修・聴講し、日本の医療・保険制度に関する知識の習得に努めると同時に、中国や韓国の医療・保険制度との比較考察を行ってきました。 ③ 日本の医療通訳の現状と問題点を具体的に把握するために、私が所属する厚生労働省の研究班で行っている外国人HIV検査会の中国語翻訳・通訳を勤め、感染症医療通訳研修を受講して、今後中国で医療通訳システムを立ち上げるのに必要な要素を検討してきました。 ④ 厚生労働省が推奨する「医療通訳育成カリキュラム基準」に基づき、医療通訳者に必要なスキルをロールプレイ演習などの実践及びより良い医療通訳とは何かをディスカッションを通して体得しながら、研究の手掛かりを探ってきました。 ⑤ 以上の研究を踏まえて、博士論文の取り上げるテーマの絞り込みをしてきました。
総合評価	【良かった点】 張さんは研究意欲が高く、自ら学習する幅を広げ、研究テーマの絞り込みを試行錯誤しながらも、粘り強く探求する姿勢を有していて、指導教官として高く評価しています。具体的には上記挙げた5つのテーマにおいて、順調に成果を挙げつつあると認められます。また、社会人として働いてきた経験から課題を遂行する責任感と物事を捉える思考の深さが感じられ、博士論文の執筆にも良い影響を与えると考えます。特筆したい点は、自分の研究のみならず、仲間や後輩とのディスカッションに率先して参加し、他者の研究にも熱心に関わる意欲です。
	【改善すべき点】 日本語を用いて学会などで発表する能力についてまだ伸ばす余地があると思います。中国語で理路整然に発表し質疑応答できていることから、日本語でも同レベルのロジカルコミュニケーションができる能力があるものと推測され、より効果的な発表ができると期待しています。
	【今後の展望】 博士論文では野心的なテーマを取り上げていますが、まだ絞り込みで悩んでいるところもあります。ただ、日本の経験を中国で活せるような研究をしたいという意欲が旺盛で、その意欲と視点から必ず研究の良い切り口を見出せると思います。2年目は研究対象を明確にし、研究方法を確立して、研究の一次資料をまとめる予定です。今年の秋には台湾国立政治大学の国際シンポジウムなどで発表、それに備えた小論文を一つ仕上げる予定です。3年目は引きつづき学会等での発表を模索しながら、博士論文の執筆に集中し、学位論文の完成を目指します。
学位取得見込	現在の計画と実践ペースで研究を続けていけば、予定通りに研究が完遂し学位取得できると期待しています。

評価者(指導教官記名)	宮首　弘子	作成日:	2025年　3　月　3　日

日中笹川医学奨学金制度<学位取得コース>中間報告書
【研究者用】

第45期　　研究者番号：G4504　　作成日：2025年3月10日

氏名	張 含煙	ZHANG HANYAN	性別	F	生年月日	1991/5/3
中国所属機関(役職)	西安培華学院人文与国際教育学院外国語学部(日本語講師)					
日本研究先(指導教官)	杏林大学国際協力研究科外国語学部(宮首 弘子　教授)					
研究テーマ(日文)	外国人患者の医療面接モデルから考える医療通訳サービスの向上					
Research theme	Enhancing Medical Interpreting Services Through Analysis of Medical Interview Models for Foreign Patients					
専攻種別	論文博士	□	課程博士	☑		

１．研究概要（1）

1）目的（Goal）
本研究では、日本の医療システムにおける「医療面接（Medical Interview）」モデルを分析し、異文化医療の場面での医療コミュニケーションの最適化および医療通訳の専門化発展に向けた理論的・実践的な指針の提案を試みる。
研究の主要な研究項目は以下の通りである。

1.1 日中の医療コミュニケーションモデルの主要な相違点を明確にする。特に、問診の構造、情報伝達、意思決定の仕組み、精神面のサポートなどの側面に焦点を当てる。
1.2 日本で診療を受ける中国人患者の適応状況および直面するコミュニケーションの課題を分析する。言語理解、文化的衝突、医師の表現スタイルへの適応などの問題を考察する。
1.3 医療面接における医療通訳者の役割と通訳方略の最適化を探る。忠実な翻訳を維持しつつ、文化適応、感情的サポート、患者の意思決定支援をどのように強化できるかを検討し、異文化医療における医療コミュニケーションの質を向上させる。
1.4 医療通訳を最適化する戦略を提案する。日本における中国人患者の医療体験を向上させ、異文化医療コミュニケーションの効果を改善するとともに、中国における将来的な医療通訳の発展および専門化の方向性に寄与する。

2）研究方針（Approach）
本研究では質的研究＋量的研究を採用し、文献分析、半構造化インタビュー、アンケート調査を通じ、日中の医療コミュニケーションモデルおよび医療通訳サービスについて総合的に検討する。主要な研究アプローチは以下の通りである。

2.1文献分析
・日本の医療面接モデルおよび中国の問診モデルの理論的枠組みを収集・分析する。異文化医療、医療通訳、医療コミュニケーションに関する研究を統合し、研究の理論的基盤を構築する。

2.2半構造化インタビュー
・日本在住（或いは在日経験のある）の中国人医師、日本人医師、医療通訳者にインタビューを行い、実際の医療コミュニケーションの状況を探る。異なる医療システムにおけるコミュニケーションの特徴、異文化間の障壁、および通訳実践における課題を分析する。

2.3アンケート調査
・日本在住の中国人患者を対象にアンケートを実施し、日本での診療における実際の体験を収集する。医師のコミュニケーションスタイルの理解度、適応状況、および医療通訳の役割を評価する。

3）研究対象と方法（Materials and methods）
本研究の対象者、データ収集、およびサンプル規模は以下の通りである。

研究対象	研究目標	データ収集方法	サンプル数
在日中国人医師	中国の医療面接のやり方・特徴、日中医療面接モデルの差異と医師の対応	半構造化インタビュー	5〜10人
日本人医師	日本の医療面接のやり方・特徴、日中医療面接モデルの差異と医師の対応	半構造化インタビュー	3〜5人
医療通訳者	医療面接での通訳の役割・課題、ラポール構築、方略	半構造化インタビュー	5〜10人
在日中国人患者	日本の医師のコミュニケーションスタイルへの適応状況や課題・期待	アンケート調査	30〜50人

具体的には、定量的統計分析を用いてアンケートデータを処理し、質的分析を併用してインタビュー結果を整理する。医療コミュニケーションに影響を与える主要な要因を特定し、そこから最適な通訳方略の導出を試みる。

1．研究概要(2)

4) 予期される成果 (Results)
4.1 理論的貢献
・「異文化医療面接コミュニケーション枠組み」を確立し、研究の空白を補完する。
・医療通訳方略の最適化を提案し、異文化医療コミュニケーションの質の向上に貢献する。

4.2 実践的貢献
・在日中国人患者の医療体験を向上させ、医師の表現方法の理解度を高め、コミュニケーション障壁を軽減する。
・日本の医師の異文化コミュニケーション技法の向上を支援する。
・医療通訳者の専門能力向上に貢献し、通訳業務の標準化・職業化を促進し、そして中国における将来的な医療通訳の発展および専門化の方向性を示唆する。

5) 考察すべき課題 (Discussion)
5.1 日中の医療面接モデルの違いと、それが医療コミュニケーションに与える影響
・構造化の程度、情報伝達、意思決定の仕組み、感情的サポートの違い
・医師の表現方法が患者の信頼形成や情報理解にどのように影響するか

5.2 中国人患者の適応状況と、診療時に生じる文化的衝突の影響
・主要なコミュニケーション障壁とその影響
・医師の表現スタイルの違いが患者のアドヒアランスや診療体験に及ぼす影響

5.3 医療通訳の役割と通訳方略の最適化
・現在の医療現場における通訳実践の課題
・通訳の忠実性を確保しつつ、文化適応をどのように実現するか
・医療通訳の専門化と将来的な発展に向けた教育・研修プログラムの構築

6) 参考文献 (References)
・厚生労働省. (2021). 医療の国際展開.
https://www.mhlw.go.jp/stf/seisakunitsuite/bunya/kenkou_iryou/iryou/kokusai/index.html
・日本医師会. (2022). 医師臨床研修指導ガイドライン2023年度版.
https://www.mhlw.go.jp/content/10803000/001173603.pdf
・向原圭. (2006). 医療面接: 根拠に基づいたアプローチ. 文光堂.
・千田彰一・岡田宏基. (2008). 対話に学ぶ医療面接プラクティス. 日経メディカル開発.
・日本医学教育協会. (2021). 医療面接トレーニングガイドライン.
・Hale, S. (2020). Medical Interpreting in Cross-Cultural Contexts: Challenges and Strategies. Journal of Intercultural Communication, 12(3), 45-63.
・Kim, H. Y. (2018). Cultural Competence in Medical Interpreting: A Comparative Analysis. Intercultural Communication Studies, 27(2), 89-107.
・Mayring, P. (2000). Qualitative Content Analysis. Forum: Qualitative Social Research, 1(2).
・Betancourt, J. R., Green, A. R., & Carrillo, J. E. (2003). Cultural competence in health care: Emerging frameworks and practical approaches. The Commonwealth Fund, p.5(文化的差異が医療サービスの提供に与える影響), p.7（患者中心のケアの重要性）.
・Gudykunst, W. B., & Kim, Y. Y. (2003). Communicating with strangers: An approach to intercultural communication. McGraw-Hill, p.15（異文化コミュニケーションの定義と課題）.
・Ting-Toomey, S. (1999). Communicating across cultures. Guilford Press, p.12（異文化コミュニケーションの重要性）, p.45（非言語的コミュニケーションの文化的差異）.
・Pöchhacker, F. (2018). Introducing Interpreting Studies. Routledge, p.123（医療通訳の文化的適応戦略）.
・Stewart, M., Brown, J. B., Donner, A., McWhinney, I. R., Oates, J., Weston, W. W., & Jordan, J. (2000). The impact of patient-centered care on outcomes. Journal of Family Practice, 49(9), 796-804.
・万学红, 卢雪峰. (2024). 诊断学 (第10版). 北京: 人民卫生出版社.
・黄榕翀, 徐鸣悦, 郭宏洲. (2020). 中国医患共同决策现状与挑战. 中华医学杂志, 100(30), 2346-2350. DOI: 10.3760/cma.j.cn112137-20200606-01789.
・邓黎黎, 廖晓阳, 伍佳, 等. (2021). 国外医患沟通模式对我国全科医生沟通技能培训的启示. 中国全科医学, 24(13), 1684-1689.
・庞建欣, 王永晨. (2020). 基于全科医生胜任力的医患沟通能力培训现状及对策研究. 中国全科医学, 23(16).

2. 執筆論文 Publication of thesis ※記載した論文を添付してください。Attach all of the papers listed below.

論文名 1 Title						
掲載誌名 Published journal						
	年　　月	巻(号)	頁　～　　頁	言語 Language		
第1著者名 First author		第2著者名 Second author		第3著者名 Third author		
その他著者名 Other authors						
論文名 2 Title						
掲載誌名 Published journal						
	年　　月	巻(号)	頁　～　　頁	言語 Language		
第1著者名 First author		第2著者名 Second author		第3著者名 Third author		
その他著者名 Other authors						
論文名 3 Title						
掲載誌名 Published journal						
	年　　月	巻(号)	頁　～　　頁	言語 Language		
第1著者名 First author		第2著者名 Second author		第3著者名 Third author		
その他著者名 Other authors						
論文名 4 Title						
掲載誌名 Published journal						
	年　　月	巻(号)	頁　～　　頁	言語 Language		
第1著者名 First author		第2著者名 Second author		第3著者名 Third author		
その他著者名 Other authors						
論文名 5 Title						
掲載誌名 Published journal						
	年　　月	巻(号)	頁　～　　頁	言語 Language		
第1著者名 First author		第2著者名 Second author		第3著者名 Third author		
その他著者名 Other authors						

3. 学会発表 Conference presentation ※筆頭演者として総会・国際学会を含む主な学会で発表したものを記載してください。

※Describe your presentation as the principal presenter in major academic meetings including general meetings or international meetings.

学会名 Conference	日中翻訳文化教育協会		
演 題 Topic	中医学の国際化における医療通訳の課題 —術語翻訳とその改善策の研究		
開催日 date	2024 年 12 月 7 日	開催地 venue	城西国際大学・東京紀尾井町キャンパス
形式 method	☑ 口頭発表 Oral ☐ ポスター発表 Poster	言語 Language	☑ 日本語 ☐ 英語 ☐ 中国語
共同演者名 Co-presenter			
学会名 Conference			
演 題 Topic			
開催日 date	年 月 日	開催地 venue	
形式 method	☐ 口頭発表 Oral ☐ ポスター発表 Poster	言語 Language	☐ 日本語 ☐ 英語 ☐ 中国語
共同演者名 Co-presenter			
学会名 Conference			
演 題 Topic			
開催日 date	年 月 日	開催地 venue	
形式 method	☐ 口頭発表 Oral ☐ ポスター発表 Poster	言語 Language	☐ 日本語 ☐ 英語 ☐ 中国語
共同演者名 Co-presenter			
学会名 Conference			
演 題 Topic			
開催日 date	年 月 日	開催地 venue	
形式 method	☐ 口頭発表 Oral ☐ ポスター発表 Poster	言語 Language	☐ 日本語 ☐ 英語 ☐ 中国語
共同演者名 Co-presenter			

4. 受賞(研究業績) Award (Research achievement)

名 称 Award name				
	国名 Country		受賞年 Year of award	年 月
名 称 Award name				
	国名 Country		受賞年 Year of award	年 月

5. 本研究テーマに関わる他の研究助成金受給 Other research grants concerned with your resarch theme

受給実績 Receipt record	☐ 有　☐ 無
助成機関名称 Funding agency	
助成金名称 Grant name	
受給期間 Supported period	年　月 ～　年　月
受給額 Amount received	円
受給実績 Receipt record	☐ 有　☐ 無
助成機関名称 Funding agency	
助成金名称 Grant name	
受給期間 Supported period	年　月 ～　年　月
受給額 Amount received	円

6. 他の奨学金受給 Another awarded scholarship

受給実績 Receipt record	☐ 有　☐ 無
助成機関名称 Funding agency	
奨学金名称 Scholarship name	
受給期間 Supported period	年　月 ～　年　月
受給額 Amount received	円

7. 研究活動に関する報道発表 Press release concerned with your research activities

※記載した記事を添付してください。Attach a copy of the article described below

報道発表 Press release	■ 有　☐ 無	発表年月日 Date of release	2024年12月7日
発表機関 Released medium	日中翻訳文化教育協会		
発表形式 Release method	・新聞　・雑誌　・Web site　・記者発表　・その他（　　）		
発表タイトル Released title	日中翻译文化教育协会成立10周年纪念国际学术会议成功举办		

8. 本研究テーマに関する特許出願予定 Patent application concerned with your research theme

出願予定 Scheduled	☐ 有　☐ 無	出願国 Application	
出願内容（概要） Application contents			

9. その他 Others

・杏林大学HPにて、「日中笹川医学奨学金を得て、日中医療通訳を研究」の記事が掲載され、医療通訳に関する学習・研究活動が紹介された

指導責任者（記名）　宮首 弘子

日中笹川医学奨学金制度<学位取得コース>中間評価書
【課程博士:指導教官用】

第45期　　研究者番号:　G4505

氏名	孔 令帥	KONG　LINGSHUAI	性別	M	生年月日	1989/8/18
中国所属機関(役職)	山西省儿童医院耳鼻喉科(主治医師)					
日本研究先(指導教官)	北里大学大学院医療系研究科耳鼻咽喉科学(山下　拓　教授)					
研究テーマ	薬剤性蝸牛神経障害モデルの作成と蝸牛損傷に対する遺伝子治療の治療効果					
専攻種別	論文博士	□	課程博士	☑		

研究者評価(指導教官記入欄)

成績状況	優・良・可・不可から選択してください⇒	良	取得単位数	8
	学業成績係数=		取得すべき単位総数	32
学生本人が行った研究の概要	アミノグリコシド系抗菌薬カナマイシンは、蝸牛内に蓄積して有毛細胞を障害し難聴を引き起こすことが知られている。本研究では、蝸牛血管条に発現するイオントランスポーターの一つであるTRPV4が、カナマイシンの内耳移行に関与し、内耳障害を引き起こすかどうかを検討した。カナマイシン投与による薬剤性難聴マウスを作成し、TRPV4アゴニストおよびアンタゴニストの投与が聴覚機能や内耳障害に与える影響を評価した。 まず異なる濃度のカナマイシンをマウスに投与して難聴モデルを作成し、TRPV4の発現を蛍光免疫染色で確認した。また、聴性脳幹反応(ABR)を用いて聴力の変化を測定した。高濃度のカナマイシン投与群では死亡率が高かったため、カナマイシン200mg/kg + フロセミド400mg/kgの投与量が最適と判断された。TRPV4は蝸牛血管条、コルチ器、および蝸牛シナプスに発現しており、内耳の生理機能に関与している可能性が示唆された。さらに、TRPV4アンタゴニストを正常マウスに投与した結果、動物の生存に影響はなく、安全性が確認された。投与後のABR測定では、聴力閾値や波形の変化は認められなかった。TRPV4アゴニストの影響については現在解析中である。 本研究により、TRPV4がカナマイシンの内耳移行や障害に関与する可能性が示唆され、将来的に薬剤性難聴の予防や治療への応用が期待される。			
総合評価	【良かった点】 医療系研究科の必須単位取得と、学位論文作成のための上記研究を行った。まだ論文作成できる状況ではないが、研究には熱心に取り組んでおり、本年6月には日本耳鼻咽喉科学会で研究成果の一部を発表予定である。 【改善すべき点】 本学において医学部校舎の移転があったため、数か月間、事実上実験室が使えない期間があったこと、単位取得のための講義聴講や実習参加のためやや実験に集中できないこともあった。日本語によるコミュニケーションについても勉強中である。改善は見られるが、まだ細部の説明や理解には困難があるように見受けられる。 【今後の展望】 実験をさらに進め、早期に学会発表や論文作成を進めていく予定である。合わせてさらなる日本語でのコミュニケーション能力の向上についても促す予定である。			
学位取得見込	このペースで研究を進めれば、既定の期間内に学位取得は十分可能であると見込まれる。			
評価者(指導教官記名)	山下　拓	作成日:	2025年　3　月　10　日	

日中笹川医学奨学金制度<学位取得コース>中間報告書
【研究者用】

Supported by 日本財団 THE NIPPON FOUNDATION

第45期　　研究者番号：G4505　　作成日：2025年3月10日

氏名	孔 令帥	KONG LINGSHUAI	性別	M	生年月日	1989/8/18
中国所属機関(役職)	山西省儿童医院耳鼻喉科（主治医師）					
日本研究先（指導教官）	北里大学大学院医療系研究科耳鼻咽喉科学（山下　拓　教授）					
研究テーマ(日文)	薬剤性蝸牛神経障害モデルの作成と蝸牛損傷に対する遺伝子治療の治療効果					
Research theme	Creation of a drug-induced cochlear neuropathy model and the therapeutic effect of gene therapy on cochlear damage					
専攻種別	論文博士	☐	課程博士	☑		

1．研究概要（1）

1）目的（Goal）

感染症治療で用いられるアミノグリコシド系抗菌薬は、蝸牛内に蓄積され難聴を引き起こすことが知られている。カナマイシンが蝸牛へ侵入する経路として、蝸牛血管条に存在するイオントランスポーターやチャネルを介して内リンパ液中に取り込まれ、有毛細胞障害を引き起こすのではないかと考えられている*(①)*。Transient Receptor Potential Vanilloid 4 (TRPV4)は蝸牛血管条のイオン輸送や薬物輸送に関与していることが知られており、アミノグリコシド系抗菌薬の蝸牛内への輸送にも関与することで内耳障害を引き起こしていることが推測される。本研究では、アミノグリコシド系抗菌薬を全身投与して薬剤性難聴マウスを作成し、TRPV4アゴニストもしくはアンタゴニストを投与することによる聴覚機能と内耳障害の変化について検討し、薬剤性内耳障害におけるTRPV4の役割について解明する。

2）戦略（Approach）

① 異なる濃度のアミノグリコシド（カナマイシン）をマウスに皮下投与し、難聴モデルを作成する。
② 正常内耳におけるTRPV4の発現部位について、組織の蛍光免疫染色により観察する
③ 正常マウスにTRPV4アゴニストもしくはアンタゴニストを全身投与し、聴覚に及ぼす影響について検討する。
④ カナマイシン投与後の内耳TRPV4の発現変化について検討する。
⑤ カナマイシンによる難聴マウスに対して、TRPV4アゴニストもしくはアンタゴニストを投与し、聴覚に及ぼす影響について比較検討する。
⑥ カナマイシンによる内耳障害機序の検討として、アポトーシスのマーカーであるcleaved caspase-3もしくはTUNEL染色による評価を行う。
⑦ 内耳組織中に滞留するカナマイシンの定量を行い、TRPV4を介した内耳組織移行について検討する。

3）材料と方法（Materials and methods）

① 動物

本研究では、８～１０週齢のCBA/J6雄マウスを用いる。

② 薬剤性難聴マウス

カナマイシン硫酸塩（200～800 mg/Kg; Meiji, Tokyo, Japan）を皮下投与し、30分後にフロセミド（400mg/Kg; Nichiiko, Toyama, Japan）を腹腔内に投与することで内耳障害モデルを作成する。

③ 聴性脳幹反応（ Auditory Brainstem Response：ABR）

ABRはマウスの聴力閾値を測定するための検査である。ABRはNeropack Sigma system(Nihon Koden, Tokyo, Japan)を用いて合計256回の平均で計測する。トーンバースト刺激で4,8,16,32 kHz周波数において、5d B毎に波形を評価する。ABRはカナマイシン投与7日後に計測した。

④ 蛍光免疫染色

正常マウスの蝸牛およびカナマイシン投与7日後に摘出された蝸牛を用いて有毛細胞生存率の評価を行う。４%PFAで灌流後に蝸牛を摘出した。5% EDTA溶液で1日間脱灰した後、蝸牛外側壁と蓋膜を除去し、コルチ器を摘出した。免疫染色は一次抗体としてMyosin7A（ab3481, 1:100, Abcam, Cambridge, UK）、CtBP2, TRPV4を用いて4℃で一晩反応させた。2次抗体はAlexa Fluor (Invitrogen, MA, USA) を用いて室温で1時間反応させ、スライドグラスに封入した。その後、切片を共焦点レーザー顕微鏡（LSM710; Zeiss, Jena, Germany）で観察した。

⑤ 薬物投与(TRPV4アゴニスト、アンタゴニスト)

カナマイシン投与直後に、TRPV4アゴニストとしてGSK-1016790（10mg/Kg、腹腔内）、TRPV4アンタゴニストとしてHC-067047(10μg/Kg、腹腔内)を3日連続で投与する。

⑥ 統計解析

統計解析はGraphpad Prism 10 (Graphpad Software Inc., La Jolla, CA, USA)を用いて行う。正規性の検定はShapiro-Wilk testを用いる。正規分布のデータはtwo-way analysis of variance(ANOVA)と事後検定としてTurkey's post hoc test を行った。非正規性分布のデータは Kruskal-Wallis testと事後検定としてDunn's post hoc test を行った。全てのデータは平均±標準誤差で示した。$P < 0.05$を統計学的に有意とした。

4）実験結果（Results）

① 難聴モデルの確立

CBA/Jマウスにカナマイシン(200～800mg/Kg)とフロセミド(400mg/Kg)を投与し検討を行った。高濃度のカナマイシン投与群では高い死亡率を示した。これまで報告でも、高用量を投与することで効率的に難聴モデルを作成することができる一方で、腎毒性などの全身副作用による死亡率が問題として挙げられている*(②)*。そこで、最も死亡率の低かったKM(200mg/Kg)とフロセミド(400mg/Kg)のモデルについて、投与7日後にABR聴力閾値を測定したところ、有意な閾値上昇を認めため、本投与モデルを本研究では採用した。その他、明らかな前庭障害を示唆する所見は認めなかった。

1．研究概要（2）

② 正常蝸牛におけるTRPV4発現部位の検討
正常マウスの蝸牛を摘出し、TRPV4の発現確認およびMyo7a、CtBP2による有毛細胞と蝸牛シナプスの評価を行った。蝸牛内の血管条、コルチ器、蝸牛シナプスにおいてTRPV4の発現が確認され、蝸牛において何らかの生理的役割を担っていると考えられる。Myo7aの有毛細胞観察では、3列の外有毛細胞と1列の内有毛細胞が観察され、障害は観察されなかった。またCtBP2による蝸牛シナプスの評価も行ったところ正常な蝸牛シナプス障害が多数観察された。

③ 正常マウスへのTRPV4アゴニストもしくはアンタゴニスト投与が聴力に及ぼす影響について
正常マウスにTRPV4アンタゴニストを連日５日間投与を行い、動物死は認めず、薬剤の安全性を確認した。アンタゴニスト投与後に聴力検査を施行したところ、ABRの閾値や振幅、潜時の変化は認めなかった。アゴニストは現在確認中。

④ カナマイシン投与後の内耳TRPV4の発現変化
⑤ カナマイシン難聴マウスに対するTRPV4アゴニストもしくはアンタゴニストの影響
⑥ カナマイシンによる内耳障害機序の検討
⑦ 内耳組織中に滞留するカナマイシンの定量評価

研 究 中

5）考察（Discussion）
耳毒性薬剤にはアミノグリコシド系抗菌薬や白金製剤など約100種類以上が存在する。特にアミノグリコシド系抗菌薬は感染症やcystic fibrosisの特効薬として世界中で使用されている一方で、そのおよそ40%に難聴を引き起こしているとも報告されている*（③）*。このような薬剤性難聴では一般的に、一度難聴が生じると薬剤を中止しても回復は難しいため、早期発見、予防が重要とされている。これまでの基礎研究成果によると、マウスにアミノグリコシド系抗菌薬であるカナマイシンを投与すると蝸牛において有毛細胞やらせん神経節細胞の脱落が観察されることが知られており（*④*）、薬剤性内耳障害研究の動物モデルとしてこれまで頻用されてきた。アミノグリコシド系抗菌薬を投与すると有毛細胞の脱落、らせん神経節細胞に直接障害を起こすことにより、難聴が生じることが報告されている（*⑤*）。カナマイシンは全身投与されると数分以内に血管条を介して内リンパ液に移行し、コルチ器に到達する。有毛細胞内にカナマイシンが取り込まれると活性酸素種やフリーラジカルが生成され、有毛細胞のアポトーシスを引き起こすとされる。カナマイシンの投与により内耳障害モデルが容易に作成できることから本モデルは内耳基礎研究に非常に汎用性が高く、これまでに多くの報告がある一方で、投与量を増やすと容易に動物死をきたすことから、慎重な飼育と経過観察が必要である。今回の我々の検討でも高濃度のカナマイシン投与では高い動物の死亡率に至ったことから、動物死を来たさずに効率よく難聴モデルを作成できるプロトコールの確率が重要であると考えられた。
TRPV4は蝸牛内広範囲に発現しており、イオンや薬物輸送に関係していることから、アミノグリコシドの内耳への取り込みに関与していると予想される。特に全身の血流から内耳へ取り込まれるルートとして、血管条が重要であるが、同部位でTRPV4の発現が確認されたことは、TRPV4の重要性を示唆している。そこで、難聴モデルに対してTRPV4アゴニストもしくはアンタゴニストを投与することによりアミノグリコシドによる内耳障害を軽減できる可能性があると考えられる。今後さらに本研究を進めていくことで、内耳性難聴に対する新しい治療アプローチの確立が期待できる。

6）参考文献（References）

① *Steyger, Peter S. Mechanisms of aminoglycoside-and cisplatin-induced ototoxicity. American journal of audiology 30.3S (2021): 887-900.*
② *Nitta, Yoshihiro, et al. Suppression of the TGF-β signaling exacerbates degeneration of auditory neurons in kanamycin-induced ototoxicity in mice. Scientific Reports 14.1 (2024): 10910.*
③ *Fu, X., et al., Mechanism and Prevention of Ototoxicity Induced by Aminoglycosides. Front Cell Neurosci, 2021. 15: p. 692762.*
④ *Gao, K., et al., Kanamycin Damages Early Postnatal, but Not Adult Spiral Ganglion Neurons. Neurotox Res, 2017. 32(4): p. 603-613.*
⑤ *Ruan, Q., et al., Topographic and quantitative evaluation of gentamicin-induced damage to peripheral innervation of mouse cochleae. Neurotoxicology, 2014. 40: p. 86-96.*

2. 執筆論文 Publication of thesis ※記載した論文を添付してください。Attach all of the papers listed below.

論文名 1 Title						
掲載誌名 Published journal						
	年 月	巻(号)	頁 ～ 頁	言語 Language		
第1著者名 First author		第2著者名 Second author		第3著者名 Third author		
その他著者名 Other authors						
論文名 2 Title						
掲載誌名 Published journal						
	年 月	巻(号)	頁 ～ 頁	言語 Language		
第1著者名 First author		第2著者名 Second author		第3著者名 Third author		
その他著者名 Other authors						
論文名 3 Title						
掲載誌名 Published journal						
	年 月	巻(号)	頁 ～ 頁	言語 Language		
第1著者名 First author		第2著者名 Second author		第3著者名 Third author		
その他著者名 Other authors						
論文名 4 Title						
掲載誌名 Published journal						
	年 月	巻(号)	頁 ～ 頁	言語 Language		
第1著者名 First author		第2著者名 Second author		第3著者名 Third author		
その他著者名 Other authors						
論文名 5 Title						
掲載誌名 Published journal						
	年 月	巻(号)	頁 ～ 頁	言語 Language		
第1著者名 First author		第2著者名 Second author		第3著者名 Third author		
その他著者名 Other authors						

3. 学会発表 Conference presentation ※筆頭演者として総会・国際学会を含む主な学会で発表したものを記載してください。

※Describe your presentation as the principal presenter in major academic meetings including general meetings or international meetings.

学会名 Conference							
演 題 Topic							
開催日 date	年	月	日	開催地 venue			
形式 method	□ 口頭発表 Oral	□ ポスター発表 Poster	言語 Language	□ 日本語	□ 英語	□ 中国語	
共同演者名 Co-presenter							
学会名 Conference							
演 題 Topic							
開催日 date	年	月	日	開催地 venue			
形式 method	□ 口頭発表 Oral	□ ポスター発表 Poster	言語 Language	□ 日本語	□ 英語	□ 中国語	
共同演者名 Co-presenter							
学会名 Conference							
演 題 Topic							
開催日 date	年	月	日	開催地 venue			
形式 method	□ 口頭発表 Oral	□ ポスター発表 Poster	言語 Language	□ 日本語	□ 英語	□ 中国語	
共同演者名 Co-presenter							
学会名 Conference							
演 題 Topic							
開催日 date	年	月	日	開催地 venue			
形式 method	□ 口頭発表 Oral	□ ポスター発表 Poster	言語 Language	□ 日本語	□ 英語	□ 中国語	
共同演者名 Co-presenter							

4. 受賞(研究業績) Award (Research achievement)

名 称 Award name					
	国名 Country		受賞年 Year of award	年	月
名 称 Award name					
	国名 Country		受賞年 Year of award	年	月

5. 本研究テーマに関わる他の研究助成金受給 Other research grants concerned with your resarch theme

受給実績 Receipt record	☐ 有　　■ 無
助成機関名称 Funding agency	
助成金名称 Grant name	
受給期間 Supported period	年　　月 ～　　年　　月
受給額 Amount received	円
受給実績 Receipt record	☐ 有　　☐ 無
助成機関名称 Funding agency	
助成金名称 Grant name	
受給期間 Supported period	年　　月 ～　　年　　月
受給額 Amount received	円

6. 他の奨学金受給 Another awarded scholarship

受給実績 Receipt record	☐ 有　　■ 無
助成機関名称 Funding agency	
奨学金名称 Scholarship name	
受給期間 Supported period	年　　月 ～　　年　　月
受給額 Amount received	円

7. 研究活動に関する報道発表 Press release concerned with your research activities

※記載した記事を添付してください。Attach a copy of the article described below

報道発表 Press release	☐ 有　　■ 無	発表年月日 Date of release	
発表機関 Released medium			
発表形式 Release method	・新聞　・雑誌　・Web site　・記者発表　・その他(　　)		
発表タイトル Released title			

8. 本研究テーマに関する特許出願予定 Patent application concerned with your research theme

出願予定 Scheduled application	☐ 有　　■ 無	出願国 Application	
出願内容(概要) Application contents			

9. その他 Others

指導責任者(記名)　　山下　拓

日中笹川医学奨学金制度〈学位取得コース〉中間評価書
【課程博士：指導教官用】

Supported by 日本財団 THE NIPPON FOUNDATION

第45期　　研究者番号：　G4506

氏名	王 櫟憲	WANG LIXIAN	性別	M	生年月日	1996/6/6
所属機関（役職）	京都大学大学院医学研究科（大学院生）					
日本研究先（指導教官）	京都大学大学院医学研究科附属脳機能総合研究センター（花川　隆　センター長、教授）					
研究テーマ	生体標本MRIコントラスト機序の解明					
専攻種別	論文博士	□	課程博士	☑		

研究者評価（指導教官記入欄）

成績状況	優・良・可・不可から選択してください⇒	良	取得単位数	15
	学業成績係数=	−	取得すべき単位総数	24

学生本人が行った研究の概要	死後脳MRIは生体脳MRIと比較して、生理的要因（心臓や呼吸の動きなど）や体動によるアーチファクトの除去、比吸収率や撮像時間に関する制約などの観点から多くの利点がある。そのため、死後脳MRIは組織学的変化を同定し、放射線学と組織・病理学の関連を確立する上で重要な役割を果たしている。しかし、定量的な死後脳MRI計測は組織固定の影響のみならず死後間隔（PMI）の影響を受けるなど、包括的に理解するための根拠はまだ不十分な状況にある。我々の目標は、死後脳MRIにおける未固定状態と固定状態の関係を系統的に調べ、死後脳MRIを通じて定量的な生体脳MRI定量値の組織・病理学的根拠を高めることである。 ヒト脳と大きさや構造の複雑さが似ている新鮮なブタ脳を使用し、未固定状態および固定状態における定量的MRI計測を実施した。脳標本MRI撮像において問題となる空気の混入を排除するために迅速な脱気システムも開発した。MRI収集には、7T超高磁場MRIスキャナを用いてT1, T2, T2*定量マップを取得するとともに拡散テンソル関連パラメータも算出した。データ解析では、定量解析手法を確立するとともにFSLやANTsツールボックスを用いたブタ脳解析手法の開発を行った。
総合評価	【良かった点】 王氏は一般的に臨床現場で使用されている1.5Tや3T-MRI装置と比べると格段に取り扱いが困難な7T超高磁場MRI装置の操作に習熟しており、本研究のみならず他の研究プロジェクトにおいても撮像プロトコルの決定を行うなど、すでにMRIの専門的知見に基づいた研究を推進できている。ブタ脳という本研究室では取り扱いのない事例においても脳の取り出しや脱気システムの確立、撮像法・固定法の確立など未知の領域に意欲的に挑戦している点は評価に値する。 【改善すべき点】 我々の最終的な目標はあくまでもヒト脳MRIにおける解釈性向上であるため、現在のブタ脳に限らず非ヒト霊長類やヒト死後脳研究との融合研究などさらに意欲的に研究を発展させていくことを期待する。 【今後の展望】 現在のブタ脳撮像数を増やし、統計学的に解釈可能な数まで撮像を行い結果をまとめる。学術論文として取りまとめ、次年度中に国際英文誌への受理ならびに学位取得を目指していく。
学位取得見込	次年度末までの国際英文誌への受理ならびに学位取得を見込んでいる。

評価者（指導教官記名）	花川　隆	作成日：	2025年　3　月　3　日

日中笹川医学奨学金制度<学位取得コース>中間報告書
【研究者用】

Supported by 日本財団 THE NIPPON FOUNDATION

第45期　　研究者番号：G4506　　作成日：2025年3月10日

氏名	王 櫟憲	WANG LIXIAN	性別	M	生年月日	1996/6/6
所属機関(役職)	京都大学大学院医学研究科（大学院生）					
日本研究先（指導教官）	京都大学大学院医学研究科附属脳機能総合研究センター（花川　隆　センター長、教授）					
研究テーマ(日文)	生体標本MRIコントラスト機序の解明					
Research theme	Contrast Mechanism of Ex Vivo MRI					
専攻種別	論文博士	☐	課程博士	☑		

1．研究概要（1）

1）目的（Goal）

Ex vivo MRI offers several advantages over in vivo MRI, including the elimination of physiological factors (such as cardiac and respiratory motion), motion artifacts, and limitations related to the specific absorption rate (SAR) and scan duration1. These benefits enable ultrahigh-resolution imaging with a high signal-to-noise ratio (SNR)2. As a result, postmortem MRI plays a crucial role in identifying pathological changes and establishing radiology-pathology correlations.
However, quantitative MRI measurements are affected by tissue fixation3. Based on our observations, even structural images exhibit contrast variations due to fixation-induced changes in tissue properties. Fixation conditions have been studied from multiple perspectives, but a comprehensive understanding of the entire process is still lacking.
Our goal is to systematically investigate the relationship between unfixed and fixed states, providing more evidence for quantitative in vivo MRI methods through ex vivo brain imaging. Additionally, we aim to develop techniques to reverse fixation-induced alterations, enabling a more accurate interpretation of ex vivo MRI data in the context of in vivo imaging. Ultimately, this research seeks to establish a robust connection between radiology and pathology, contributing to improved radiological diagnosis.

2）戦略（Approach）

The extended scan duration in ex vivo MRI allows for more precise quantitative imaging4. Compared to conventional qualitative MRI, which relies on specific acquisition parameters and tissue properties, quantitative mapping methods (e.g., T1, T2, and T2* maps) offer higher reproducibility. This makes them particularly suitable for correlating MRI findings with histological staining and proteomic data.
Another crucial factor is the impact of postmortem interval (PMI). Very few studies have specifically investigated PMI effects, and those that have primarily used small tissue samples rather than whole brains5,6. Existing studies suggest that PMI alters water relaxation and diffusion properties in rat nervous tissue. However, most research only reports PMI values without thoroughly analyzing their effects. The only human brain study on this topic contradicts prior findings, highlighting the need for further investigation.
Therefore, it is essential to systematically study the influence of PMI on both unfixed and fixed samples to gain a deeper understanding of its effects.

3）材料と方法（Materials and methods）

To address these challenges, we used pig brains, which share similar cerebral size and structural complexity with human brains7. Fresh pig brain samples were purchased, and the brains were extracted for experimentation. To collect both unfixed and fixed states, we developed a rapid degassing system for fresh sample preparation. We mainly utilized vacuum chamber and ultrasound device alternately to build this system, which enabled us to acquire high-quality data across different PMIs.
For MRI acquisition, we conducted experiments using a 7T ultrahigh-field MRI scanner. We employed variable flip angle multi-echo GRE and variable TE T2-TSE sequences to acquire paired T1, T2, and T2* maps for both unfixed and fixed brains. These conventional quantitative methods provide a reliable foundation for validating advanced quantitative techniques in future studies. Additionally, we acquired diffusion-weighted EPI sequences with 128 directions to calculate various diffusion-related parameters.

For data analysis, we utilized the FSL (FMRIB Software Library, Oxford University, UK) and ANTs (Advanced Normalization Tools) toolboxes for preprocessing, including diffusion parameter estimation and image registration. MATLAB was used for further quantitative analyses and calculations.

4）実験結果（Results）

Preliminary results demonstrate that our rapid degassing system effectively minimizes air bubbles in the sample. With this system, only one hour is enough for degassing and no more materials like agarose are required8. B0 susceptibility inhomogeneity led by air bubbles has been well improved, finally we can acquire high-quality imaging data.
After one month of fixation, all T1, T2, and T2* relaxation times were significantly shortened which is same as previous study3. Furthermore, we built a post-processing
pipeline with FSL and ANTs toolbox. With the FSL brain extraction function and ANTs registration function, we have conducted registration between our data and pig brain atlas9. After applying simple linear registration, the images exhibited good spatial alignment between the unfixed and fixed states.

5）考察（Discussion）

Over the past year, I have successfully developed a system for collecting MRI data from both unfixed and fixed specimens. Additionally, I have gained extensive experience in data analysis and MRI acquisition techniques. Preliminary tests have been completed, and I have now begun constructing a comprehensive dataset.
Moving forward, we will collect additional samples with varying PMIs to analyze their effects on both unfixed and fixed specimens. These paired datasets will serve as a foundation for deep learning applications, including efforts to computationally reverse fixation-induced changes.
By elucidating the patterns and correlations between unfixed and fixed states, our research aims to bridge the gap between ex vivo and in vivo MRI. Ultimately, this work aspires to enhance radiology-pathology correlations, contributing to both diagnostic advancements and broader research methodologies.

6）参考文献（References）

1. Shatil, A. S., Matsuda, K. M. & Figley, C. R. A Method for Whole Brain Ex Vivo Magnetic Resonance Imaging with Minimal Susceptibility Artifacts. Front. Neurol. 7, (2016).

2. Edlow, B. L. et al. 7 Tesla MRI of the ex vivo human brain at 100 micron resolution. Sci. Data 6, 244 (2019).

3. Shatil, A. S., Uddin, M. N., Matsuda, K. M. & Figley, C. R. Quantitative Ex Vivo MRI Changes due to Progressive Formalin Fixation in Whole Human Brain Specimens:

Longitudinal Characterization of Diffusion, Relaxometry, and Myelin Water Fraction Measurements at 3T. Front. Med. 5, (2018).

4. Langkammer, C. et al. Quantitative MR Imaging of Brain Iron: A Postmortem Validation Study. Radiology 257, 455–462 (2010).

5. Shepherd, T. M. et al. Postmortem interval alters the water relaxation and diffusion properties of rat nervous tissue — Implications for MRI studies of human autopsy samples. NeuroImage 44, 820–826 (2009).

6. Lenz, C., Berger, C., Bauer, M., Scheurer, E. & Birkl, C. Sensitivity of fiber orientation dependent to temperature and post mortem interval. Magn. Reson. Med. 86, 2703–2715 (2021).

7. Li, C., Li, J., Lai, L., Li, S. & Yan, S. Genetically engineered pig models of neurological diseases. Ageing Neurodegener. Dis. 2 (2022).

8. Birkl, C. et al. Temperature-induced changes of magnetic resonance relaxation times in the human brain: A postmortem study. Magn. Reson. Med. 71, 1575–1580 (2014).

9. Fil, J. E., Joung, S., Zimmerman, B. J., Sutton, B. P. & Dilger, R. N. High-resolution magnetic resonance imaging-based atlases for the young and adolescent domesticated pig (Sus scrofa). J. Neurosci. Methods 354, 109107 (2021).

2. 執筆論文 Publication of thesis ※記載した論文を添付してください。Attach all of the papers listed below.

論文名 1 Title						
掲載誌名 Published journal						
	年　　月	巻(号)	頁　～　　頁	言語 Language		
第1著者名 First author		第2著者名 Second author		第3著者名 Third author		
その他著者名 Other authors						
論文名 2 Title						
掲載誌名 Published journal						
	年　　月	巻(号)	頁　～　　頁	言語 Language		
第1著者名 First author		第2著者名 Second author		第3著者名 Third author		
その他著者名 Other authors						
論文名 3 Title						
掲載誌名 Published journal						
	年　　月	巻(号)	頁　～　　頁	言語 Language		
第1著者名 First author		第2著者名 Second author		第3著者名 Third author		
その他著者名 Other authors						
論文名 4 Title						
掲載誌名 Published journal						
	年　　月	巻(号)	頁　～　　頁	言語 Language		
第1著者名 First author		第2著者名 Second author		第3著者名 Third author		
その他著者名 Other authors						
論文名 5 Title						
掲載誌名 Published journal						
	年　　月	巻(号)	頁　～　　頁	言語 Language		
第1著者名 First author		第2著者名 Second author		第3著者名 Third author		
その他著者名 Other authors						

3. 学会発表 Conference presentation ※筆頭演者として総会・国際学会を含む主な学会で発表したものを記載してください。

※Describe your presentation as the principal presenter in major academic meetings including general meetings or international meetings.

学会名 Conference								
演 題 Topic								
開催日 date	年	月	日	開催地 venue				
形式 method	□ 口頭発表 Oral	□ ポスター発表 Poster		言語 Language	□ 日本語	□ 英語	□ 中国語	
共同演者名 Co-presenter								
学会名 Conference								
演 題 Topic								
開催日 date	年	月	日	開催地 venue				
形式 method	□ 口頭発表 Oral	□ ポスター発表 Poster		言語 Language	□ 日本語	□ 英語	□ 中国語	
共同演者名 Co-presenter								
学会名 Conference								
演 題 Topic								
開催日 date	年	月	日	開催地 venue				
形式 method	□ 口頭発表 Oral	□ ポスター発表 Poster		言語 Language	□ 日本語	□ 英語	□ 中国語	
共同演者名 Co-presenter								
学会名 Conference								
演 題 Topic								
開催日 date	年	月	日	開催地 venue				
形式 method	□ 口頭発表 Oral	□ ポスター発表 Poster		言語 Language	□ 日本語	□ 英語	□ 中国語	
共同演者名 Co-presenter								

4. 受賞（研究業績） Award (Research achievement)

名 称 Award name					
	国名 Country		受賞年 Year of award	年	月
名 称 Award name					
	国名 Country		受賞年 Year of award	年	月

5. 本研究テーマに関わる他の研究助成金受給 Other research grants concerned with your resarch theme

受給実績 Receipt record	■ 有　□ 無
助成機関名称 Funding agency	京都大学
助成金名称 Grant name	リサーチ・フェロー
受給期間 Supported period	2024 年 5 月 ～ 2025 年 3 月
受給額 Amount received	550,000 円
受給実績 Receipt record	□ 有　□ 無
助成機関名称 Funding agency	
助成金名称 Grant name	
受給期間 Supported period	年 月 ～ 年 月
受給額 Amount received	円

6. 他の奨学金受給 Another awarded scholarship

受給実績 Receipt record	□ 有　□ 無
助成機関名称 Funding agency	
奨学金名称 Scholarship name	
受給期間 Supported period	年 月 ～ 年 月
受給額 Amount received	円

7. 研究活動に関する報道発表 Press release concerned with your research activities

※記載した記事を添付してください。Attach a copy of the article described below

報道発表 Press release	□ 有　□ 無	発表年月日 Date of release	
発表機関 Released medium			
発表形式 Release method	・新聞　・雑誌　・Web site　・記者発表　・その他（　　）		
発表タイトル Released title			

8. 本研究テーマに関する特許出願予定 Patent application concerned with your research theme

出願予定 Scheduled application	□ 有　□ 無	出願国 Application	
出願内容（概要） Application contents			

9. その他 Others

指導責任者（記名）　花川　隆

日中笹川医学奨学金制度<学位取得コース>中間評価書
【課程博士:指導教官用】

Supported by 日本財団 THE NIPPON FOUNDATION

第45期　　研究者番号:　G4507

氏名	馮 照祖	FENG ZHAOZU	性別	M	生年月日	1999/5/2
中国所属機関(役職)	西安交通大学医学部(大学院生)					
日本研究先(指導教官)	大阪大学大学院医学系研究科病態病理学(森井 英一　教授)					
研究テーマ	病理検体を用いた腫瘍の多様性に関する解析					
専攻種別	論文博士	□	課程博士	☑		

研究者評価(指導教官記入欄)

成績状況	優・良・可・不可から選択してください⇒	優	取得単位数	10
	学業成績係数=		取得すべき単位総数	30

学生本人が行った研究の概要	病理組織において、慢性間質性肺炎では肺胞上皮が気管支上皮に化生を起こすことが知られている。この化生によりガス交換に重要な役割を担う肺胞の数が減少し、その結果、慢性間質性肺炎では呼吸不全が起こる。本奨学生は、この化生という現象に着目し、患者検体より肺胞上皮オルガノイド、気管支上皮オルガノイドを作成し、種々の培養条件を検討し、肺胞上皮の形質をもつオルガノイドが気管支上皮の形質をもつようになる化生現象をin vitrodで再現する系を立ち上げつつある。この系を立ち上げることにより、慢性炎症により呼吸不全が惹起される機構を解析することが期待され、慢性間質性肺炎に対する新たな治療法の開発につながる可能性がある。今年度は、この系の立ち上げを行うと同時に、肺胞上皮オルガノイド、気管支上皮オルガノイドを比較することで、気管支上皮に高発現を示すlncRNAを単離するプロジェクトにも関与した。単離されたlncRNAが慢性間質性肺炎を増悪させる機構についての解析にも携わり、論文化にも貢献した。
総合評価	【良かった点】 熱心な学生で実験をよく行っている。系の立ち上げはかなりの労働量が必要であるが、日夜実験に勤しんでいる。指導を受ける姿勢も真摯で、大学院生どうしの討議にも積極的に参加している。 【改善すべき点】 自ら出したデータに対して厳しく慎重な解釈をする傾向がややあり、いいデータが出て再現性が確認された後も、より厳しい判断をして何度も実験を繰り返すことがある。慎重なデータ解釈は必要であるが、より経験を積むことにより、データ解釈の見極めができるようになると考え、今後に期待している。 【今後の展望】 熱心で勤勉な学生で、さらなる実験の経験と、データの解釈の経験を積むことで、素晴らしい研究者になることが期待される。
学位取得見込	博士課程修了時に学位を取得できる見込みである。

評価者(指導教官記名)	森井　英一	作成日:	2025年　2　月　14　日

日中笹川医学奨学金制度<学位取得コース>中間報告書
【研究者用】

第45期　　研究者番号：G4507　　作成日：2025年3月10日

氏名	馮 照祖	FENG ZHAOZU	性別	M	生年月日	1999/5/2
中国所属機関(役職)	西安交通大学医学部(大学院生)					
日本研究先(指導教官)	大阪大学大学院医学系研究科病態病理学(森井 英一　教授)					
研究テーマ(日文)	病理検体を用いた腫瘍の多様性に関する解析					
Research theme	Analysis of tumor heterogeneity in pathological specimen					
専攻種別	論文博士	☐	課程博士	☑		

1．研究概要(1)

1)目的(Goal)

組織は多様な細胞で構成されている。この多様性は細胞の分化の多様性、および種々のストレスに対する反応の多様性に起因する。腫瘍細胞も形態的、機能的な多様性をもつことが知られているが、この腫瘍の多様性の原因を知るためには、正常な組織でどのように多様性が生み出されているかを調べることが必要である。慢性間質性肺炎は炎症に伴い本来肺胞上皮であった細胞が気管支上皮に化生をおこす疾患で、呼吸機能が障害されることで致死的となる。また慢性間質性肺炎を背景に発生する腫瘍は多様な形態をとることが知られており、腫瘍の多様性を検討する上でも重要な疾患である。本研究のまず第一の目的は、慢性炎症下で組織を構成する細胞の分化転換の結果おこる化生現象の詳細を解明することで、腫瘍の多様性につながる機構を調べることである。

化生がおこるためには、分化した細胞が一旦未熟な状態に移行し、その後、再度分化していく過程が必要である。この過程はpaligenosisと呼ばれる。Paligenosisにおいて、再度分化していく過程で元と同じ細胞に分化すれば再生という現象になり、元と違う細胞に分化すれば化生現象がおこる。本研究の第二の目的は、再生と化生の分岐点を明らかにすることである。この分岐点を明らかにし、再生を誘導し化生を抑制する因子を見出すことができれば、慢性間質性肺炎の本質的な治療につながると考える。

2)戦略(Approach)

近年、細胞を3次元培養し器官類似の形態にするオルガノイド構築技術が進んでいる。研究材料として汎用されている細胞株は分化誘導刺激にほぼ反応しないため、一旦分化した細胞に慢性炎症刺激を加えるpaligenosisの解析に用いることはできない。Paligenosisの過程を検討する場合、できるだけ正常に近い細胞を用いることが必須である。応募者は、ヒト肺より肺胞上皮への分化を示した細胞群で構成される肺胞オルガノイドと、気管支上皮への分化を示した細胞群で構成される気道オルガノイドを構築することに成功している。肺胞オルガノイドに慢性炎症を惹起する因子をカクテルとして加えることで、肺胞上皮マーカーの発現が低下し、気管支上皮マーカーの発現が誘導された。炎症惹起カクテルを添加した肺胞オルガノイドでは38遺伝子が有意な発現上昇を示し、このうち15遺伝子は気道オルガノイドで高発現を示す気管支上皮マーカーであった。このことは、in vitroで炎症刺激による気管支上皮化生を再現するシステムを構築することができたことを示す。このシステムを利用すれば、単一細胞レベルで遺伝子発現状況を解析するsingle cell RNA-seqで慢性炎症に伴うpaligenosisの詳細な過程を追及でき、どの段階が再生と化生の分岐点となっているか、再生へと向かう本来の分化過程を化生の方向に捻じ曲げる因子は何かという疑問点に答えることができる。さらにpaligenosisの過程や再生と化生の分岐点などに特徴的なマーカーを用いて、実際の慢性間質性肺炎病理組織におけるpaligenosisの過程や分化破綻がどの細胞で起こっているのか可視化することもできる。

3)材料と方法(Materials and methods)

材料：

①細胞培養相関：オルガノイド培養液(Gibco™ Human EGF Recombinant Protein；Qkine recombinant human IGF-1 protein; Gibco™ Human FGF-basic (FGF-2/bFGF) Recombinant Protein; Recombinant Human FGF-10; Recombinant Human KGF (FGF-7); Afamin/Wnt3a CM; Afamin/Wnt3a CM High-Concentration; Recombinant Human R-Spondin-1; Recombinant Human Noggin; Recombinant Human Heregulinβ-1; Tocris Bioscience A83-01; CultureSure® Y-27632; Gibco™ B-27™ Supplement (50X), serum free)；DMEM/ハムF-12培地(L-グルタミン, ピルビン酸, HEPES含有);

②RT-qPCR相関：QTaqMan™ Gene Expression Assay (FAM)_ActB,sftpc,krt17,tp63,abca3,sox2,ager,lamp3,ak1, fads1,pla2g1b,slc34a2; Invitrogen SuperScript™ III Reverse Transcriptase Kit;TaKaRa Genとるくん エタ沈キャリア; TaKaRa RNAiso Plus;

③免疫染色相関：Anti-SFTPC/KRT17/TP63/TTF1/Ki-67/PLA2G1B/pERM/pMLC/p53/pSmad2 Antibody; AKOYA BIOSCIENCES Opal 7-Color Manual IHC Kit; VECTOR LABORATORIES VectaPlex Antibody Removal Kit;

④遺伝子組換え相関：レンチウイルス shRNA_NV/FADS1/PLA2G1B; invitrogen Lipofectamine™ RNAiMAX; TaKaRa Lentiviral High Titer Packaging Mix Transfection Reagent; Clontech Lenti-X™ レンチウイルス濃縮試薬;

⑤その他。

方法：オルガノイド樹立と培養；RT-qPCR；免疫染色；フローサイトメトリー；遺伝子組換え(Knock-Down)；Bulk-RNAシーケンス；ATACシーケンス；画像解析(HALO)；Public Database解析；データ解析など。

1．研究概要（2）

4）実験結果（Results）

①特発性肺線維症（IPF）に関与する遺伝子の解析：
肺胞上皮を構成するalveolar type 2 (AT2) 細胞に着目して、特発性肺線維症（IPF）に特徴的な遺伝子を探索した。その結果、IPFで発現が減弱する遺伝子としてphospholipase A2G1B (PLA2G1B)遺伝子に着目している。
AT2細胞のオルガノイドを作成の上、PLA2G1B遺伝子をKnock-Dwonして、オルガノイドの形成と遺伝子変動を調べた。AT2オルガノイドはPLA2G1B遺伝子のノックダウンにより大きさが減少した。今後、さらにオルガノイドにおける解析を進めることでAT2細胞におけるPLA2G1Bの重要性を調べる予定である。
ヒトIPF検体で、PLA2G1Bの免疫染色を行ない、正常（NC=3）領域と線維化（IP=7）領域における発現状況を比較したところ、PLA2G1Bの発現はNC領域での陽性細胞の比率は高かった。Public scRNA Databasesによると、正常対照のPLA2G1B陽性AT2細胞の比率は約30%は、実際に染めた検体と一致していた。

②ヒト由来肺オルガノイドを用いたpaligenosisの解析：
AT2細胞で構成される肺胞上皮オルガノイドに炎症性サイトカインを加えて、その前後における遺伝子発現変化を検討した。炎症性サイトカインにより、肺胞上皮オルガノイドは数が減少し、AT2細胞マーカーであるsurfactant protein C (SFTPC)の発現が減弱していた。このことは炎症刺激によりAT2細胞の形質が失われることを示している。ただし、化生の指標である気管支上皮マーカーであるTP63, cytokeratin 17の発現上昇はみられなかった。そこで、現在炎症刺激後の培養条件を検討することで、化生の指標である気管支上皮マーカーが増加しないかどうかを検討しているところである。

5）考察（Discussion）

本研究では、慢性間質性肺炎の中でも予後不良の病型であるIPFに着目し、まずIPFで発現が変動する遺伝子としてPLA2G1Bに着目した。ヒト検体における免疫組織化学的解析により、たしかにPLA2G1BがIPFで発現減弱を示すことを確認した。肺胞上皮由来オルガノイドでPLA2G1B遺伝子をノックダウンすると、肺胞上皮に特徴的な遺伝子の発現が減少することも確認できた。次のステップとして、なぜPLA2G1Bが肺胞上皮の維持に重要であるのか、なぜIPFで発現が減弱するのかを検討したい。PLA2G1Bは脂質代謝に重要な酵素である。今後、RNA-seqなどを通して、脂質代謝と肺胞上皮の機能維持との関係も解析していく予定である。
さらに、化生をオルガノイドで再現するために、培養条件を検討する。具体的にはオルガノイド維持のために添加している種々の因子の機能を検討し、化生を阻害している因子を調べ、その因子の除去により化生が進むかどうか検討する。現在、いくつかのpathwayが肺胞上皮の表現型維持に必須であること、その表現型を変化させるためにはどのような条件が必要であるかを絞り込みつつあるところである。化生にいたる系を開発できれば、化生と再生の分岐点を解析するプロジェクトを開始する予定である。

6）参考文献（References）
[1] Umeda, D., Harada, A., Motooka, D. et al. Hypoxia drives the formation of lung micropapillary adenocarcinoma-like structure through hypoxia-inducible factor-1α. Sci Rep 14, 31642 (2024).
[2] Yu, W. et al. Involvement of RhoA, ROCK I and myosin II in inverted orientation of epithelial polarity. EMBO Rep. 9, 923-929 (2008).
[3] Kadur Lakshminarasimha Murthy P, Sontake V, Tata A, et al. Human distal lung maps and lineage hierarchies reveal a bipotent progenitor. Nature. 2022;604(7904):111-119.
...

2. 執筆論文 Publication of thesis ※記載した論文を添付してください。Attach all of the papers listed below.

論文名 1 Title	Involvement of lncRNA MIR205HG in idiopathic pulmonary fibrosis and regulation of IL33 via Alu elements					
掲載誌名 Published journal	JCI insight					
	2025 年 3 月	巻(号)	頁 ～ 頁	言語 Language	英語	
第1著者名 First author	Tsuyoshi Takashima	第2著者名 Second author	Chao Zeng	第3著者名 Third author	Eitaro Murakami	
その他著者名 Other authors	Naoko Fujiwara, Masaharu Kohara, Hideki Nagata, Zhaozu Feng, Ayako Sugai, Yasue Harada, Rika Ichijo, Daisuke Okuzaki, Satoshi Nojima, Takahiro Matsui, Yasushi Shintani, Gota Kawai, Michiaki Hamada, Tetsuro Hirose,					
論文名 2 Title						
掲載誌名 Published journal						
	年 月	巻(号)	頁 ～ 頁	言語 Language		
第1著者名 First author		第2著者名 Second author		第3著者名 Third author		
その他著者名 Other authors						
論文名 3 Title						
掲載誌名 Published journal						
	年 月	巻(号)	頁 ～ 頁	言語 Language		
第1著者名 First author		第2著者名 Second author		第3著者名 Third author		
その他著者名 Other authors						
論文名 4 Title						
掲載誌名 Published journal						
	年 月	巻(号)	頁 ～ 頁	言語 Language		
第1著者名 First author		第2著者名 Second author		第3著者名 Third author		
その他著者名 Other authors						
論文名 5 Title						
掲載誌名 Published journal						
	年 月	巻(号)	頁 ～ 頁	言語 Language		
第1著者名 First author		第2著者名 Second author		第3著者名 Third author		
その他著者名 Other authors						

3. 学会発表 Conference presentation ※筆頭演者として総会・国際学会を含む主な学会で発表したものを記載してください。

※Describe your presentation as the principal presenter in major academic meetings including general meetings or international meetings.

学会名 Conference						
演　題 Topic						
開催日 date	年　月　日		開催地 venue			
形式　method	□ 口頭発表　Oral	□ ポスター発表　Poster	言語　Language	□ 日本語	□ 英語	□ 中国語
共同演者名 Co-presenter						
学会名 Conference						
演　題 Topic						
開催日 date	年　月　日		開催地 venue			
形式　method	□ 口頭発表　Oral	□ ポスター発表　Poster	言語　Language	□ 日本語	□ 英語	□ 中国語
共同演者名 Co-presenter						
学会名 Conference						
演　題 Topic						
開催日 date	年　月　日		開催地 venue			
形式　method	□ 口頭発表　Oral	□ ポスター発表　Poster	言語　Language	□ 日本語	□ 英語	□ 中国語
共同演者名 Co-presenter						
学会名 Conference						
演　題 Topic						
開催日 date	年　月　日		開催地 venue			
形式　method	□ 口頭発表　Oral	□ ポスター発表　Poster	言語　Language	□ 日本語	□ 英語	□ 中国語
共同演者名 Co-presenter						

4. 受賞（研究業績） Award (Research achievement)

名　称 Award name				
	国名 Country		受賞年 Year of	年　月
名　称 Award name				
	国名 Country		受賞年 Year of	年　月

5. 本研究テーマに関わる他の研究助成金受給 Other research grants concerned with your resarch theme

受給実績 Receipt record	□ 有　■ 無
助成機関名称 Funding agency	
助成金名称 Grant name	
受給期間 Supported period	年　月 ～　年　月
受給額 Amount received	円
受給実績 Receipt record	□ 有　■ 無
助成機関名称 Funding agency	
助成金名称 Grant name	
受給期間 Supported period	年　月 ～　年　月
受給額 Amount received	円

6. 他の奨学金受給 Another awarded scholarship

受給実績 Receipt record	□ 有　■ 無
助成機関名称 Funding agency	
奨学金名称 Scholarship name	
受給期間 Supported period	年　月 ～　年　月
受給額 Amount received	円

7. 研究活動に関する報道発表 Press release concerned with your research activities

※記載した記事を添付してください。Attach a copy of the article described below

報道発表 Press release	□ 有　■ 無	発表年月日 Date of release	
発表機関 Released medium			
発表形式 Release method	・新聞　・雑誌　・Web site　・記者発表　・その他（　　）		
発表タイトル Released title			

8. 本研究テーマに関する特許出願予定 Patent application concerned with your research theme

出願予定 Scheduled	□ 有　■ 無	出願国 Application	
出願内容（概要） Application contents			

9. その他 Others

指導責任者（記名）　森井英一

JCI insight

Involvement of lncRNA *MIR205HG* in idiopathic pulmonary fibrosis and IL-33 regulation via *Alu* elements

Tsuyoshi Takashima, … , Kazuhiko Nakatani, Eiichi Morii

JCI Insight. 2025;10(5):e187172. https://doi.org/10.1172/jci.insight.187172.

Research Article | Inflammation | Pulmonology

Graphical abstract

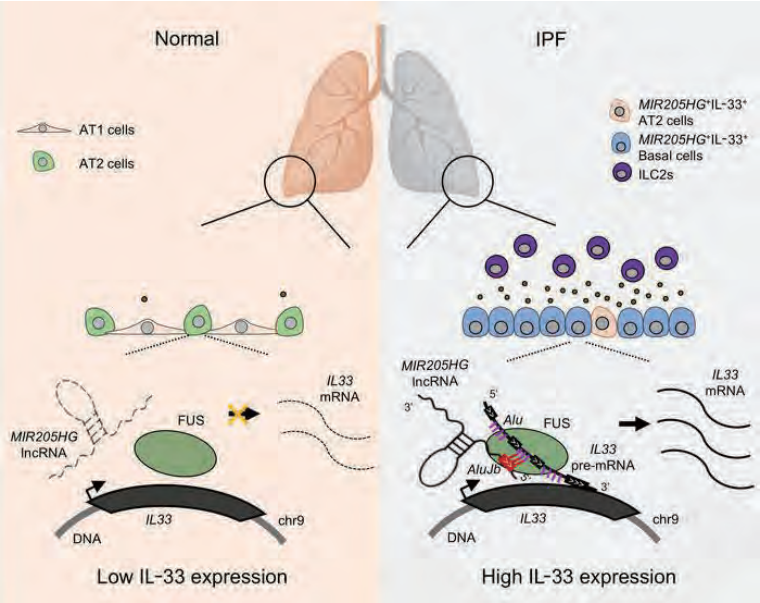

Find the latest version:

https://jci.me/187172/pdf

JCI insight

RESEARCH ARTICLE

Involvement of lncRNA *MIR205HG* in idiopathic pulmonary fibrosis and IL-33 regulation via *Alu* elements

Tsuyoshi Takashima,[1] Chao Zeng,[2] Eitaro Murakami,[3] Naoko Fujiwara,[4] Masaharu Kohara,[1] Hideki Nagata,[5] Zhaozu Feng,[1] Ayako Sugai,[3] Yasue Harada,[3] Rika Ichijo,[6] Daisuke Okuzaki,[7,8] Satoshi Nojima,[1] Takahiro Matsui,[1] Yasushi Shintani,[5] Gota Kawai,[6] Michiaki Hamada,[2,9] Tetsuro Hirose,[4,8] Kazuhiko Nakatani,[3,8] and Eiichi Morii[1,8]

[1]Department of Pathology, Osaka University Graduate School of Medicine, Osaka, Japan. [2]Faculty of Science and Engineering, Waseda University, Tokyo, Japan. [3]Department of Regulatory Bioorganic Chemistry, SANKEN (the Institute of Scientific and Industrial Research), Osaka, Japan. [4]Graduate School of Frontier Biosciences, Osaka University, Osaka, Japan. [5]Department of General Thoracic Surgery, Osaka University Graduate School of Medicine, Osaka, Japan. [6]Department of Life Science, Graduate School of Advanced Engineering, Chiba Institute of Technology, Chiba, Japan. [7]Laboratory of Human Immunology (Single Cell Genomics), WPI Immunology Frontier Research Center, and [8]Institute for Open and Transdisciplinary Research Initiatives, Osaka University, Osaka, Japan. [9]AIST-Waseda University Computational Bio Big-Data Open Innovation Laboratory (CBBD-OIL), National Institute of Advanced Industrial Science and Technology, Tokyo, Japan.

Idiopathic pulmonary fibrosis (IPF) causes remodeling of the distal lung. Pulmonary remodeling is histologically characterized by fibrosis, as well as appearance of basal cells; however, the involvement of basal cells in IPF remains unclear. Here, we focus on the long noncoding RNA *MIR205HG*, which is highly expressed in basal cells, using RNA sequencing. Through RNA sequencing of genetic manipulations using primary cells and organoids, we discovered that *MIR205HG* regulates IL-33 expression. Mechanistically, the *AluJb* element of *MIR205HG* plays a key role in IL-33 expression. Additionally, we identified a small molecule that targets the *AluJb* element, leading to decreased IL-33 expression. IL-33 is known to induce type 2 innate lymphoid cells (ILC2s), and we observed that *MIR205HG* expression was positively correlated with the number of ILC2s in patients with IPF. Collectively, these findings provide insights into the mechanisms by which basal cells contribute to IPF and suggest potential therapeutic targets.

Introduction

Idiopathic pulmonary fibrosis (IPF) is a progressive lung disease that causes remodeling and fibrosis of the distal lung, ultimately leading to respiratory failure and death (1, 2). The pathogenesis of IPF has not been fully elucidated, but repeated inflammation is thought to cause epithelial cell damage and dysfunction, which lead to fibroblast activation, deposition of extracellular matrix, and subsequent tissue fibrosis (3). Nintedanib and pirfenidone, currently the only US Food and Drug Administration–approved drugs, do not completely halt disease progression (4, 5). Therefore, it is crucial to understand the pathogenesis of IPF and uncover molecular mechanisms to improve the prognosis of IPF.

The distal region of normal lungs is histologically composed of 2 types of epithelial cells: alveolar type I (AT1) cells, which are responsible for gas exchange, and alveolar type II (AT2) cells, which produce surfactant and act as tissue stem cells. However, the distal region of the IPF exhibits histologically characteristic findings termed "honeycombed" cysts, where AT1 and AT2 cells are reduced and replaced by aberrant AT2-like cells and airway epithelial cells, such as basal cells, goblet cells, and ciliated cells (2, 6). This pulmonary remodeling has also been robustly demonstrated in comprehensive single-cell RNA-sequencing (scRNA-Seq) analyses (7–9). Additionally, transcriptomic analysis of bronchoalveolar lavage fluid from patients with IPF has shown that a basal cell signature is associated with enhanced disease progression and mortality (10). However, until recently, it remained uncertain whether this pulmonary remodeling directly contributed to the pathogenesis of IPF or was simply a bystander phenomenon or end-stage finding. Recent studies have revealed that IPF-derived basal cells induced fibroblast proliferation and extracellular matrix

Conflict of interest: The authors have declared that no conflict of interest exists.

Submitted: September 20, 2024
Accepted: January 22, 2025
Published: March 10, 2025

Reference information: *JCI Insight*. 2025;10(5):e187172. https://doi.org/10.1172/jci.insight.187172.

deposition both in vitro and in vivo (11, 12). These reports suggest that basal cells directly contribute to the fibrosis of IPF, but insight into the contributions of basal cells to the pathogenesis of IPF remains limited.

lncRNAs, defined as noncoding RNA transcripts longer than 200 nucleotides, are involved in various regulatory steps of gene expression, such as chromatin remodeling, transcription, RNA stability, and translation (13–15). These transcripts are shown to be involved in the biological processes of diseases, including pulmonary fibrosis (15, 16). For example, the lncRNA *DNM3OS* has been identified as a critical downstream effector of TGF-β–induced myofibroblast activation, regulating the lung fibrotic process by producing pro-fibrotic mature miRNAs (17). Furthermore, the lncRNA *FENDRR* can reduce lung fibroblast activation by decreasing cellular iron concentration via interactions with IRP1 and acting as a pro-fibrotic *miR-214* (18). However, most of these findings have focused on fibroblasts and myofibroblasts; little is known regarding the function of lncRNA expressed in basal cells involved in the pathogenesis of IPF. Therefore, we focused on lncRNA to gain insights concerning the involvement of basal cells in the pathogenesis of IPF.

In this work, we first analyzed public scRNA-Seq data from patients with IPF and identified lncRNA *MIR205HG*, which is highly expressed in basal cells. *MIR205HG* was revealed as a prognostic factor in patients with IPF. Through comprehensive analysis of genetic manipulations using primary cells, alveolar epithelial organoids, and airway organoids from IPF patient samples (IPF patient–derived airway organoids), we found that *MIR205HG* is involved in the regulation of IL-33 expression, which is thought to contribute to the pathogenesis of IPF. Intriguingly, the interaction between the *AluJb* element of *MIR205HG* and the *Alu* element of *IL33* was important for these regulatory mechanisms. Additionally, we identified DQzG, a small molecule that reduced IL-33 expression, likely by inhibiting the interaction between *Alu* elements. Furthermore, *MIR205HG* expression was positively correlated with IL-33 expression and the number of type 2 innate lymphoid cells (ILC2s) in tissue samples from patients with IPF. These data highlight the involvement of lncRNA *MIR205HG* in the pathogenesis of IPF and provide important insights into a therapeutic target.

Results

lncRNA MIR205HG is highly expressed in basal cells and an independent poor prognostic factor in IPF. We examined the differences in histological features in alveolar regions between healthy lungs and IPF patient samples. In healthy lungs, alveoli beneath the pleura were lined with AT1 and AT2 cells, whereas in patients with IPF, these alveoli were lined with basophilic bronchial cells due to metaplasia (Figure 1A). The lining cells of normal lungs were positive for SFTPC, whereas those of patients with IPF were positive for KRT5 (Figure 1A). We analyzed public scRNA-Seq data from National Center for Biotechnology Information (NCBI) Gene Expression Omnibus (GEO) (GSE136831) (7), which included samples from healthy lungs (n = 28) and patients with IPF (n = 32) (Figure 1B and Supplemental Figure 1A; supplemental material available online with this article; https://doi.org/10.1172/jci.insight.187172DS1), and found that the number of alveolar epithelial cells (including AT2 cells) decreased whereas the number of airway epithelial cells (including basal cells) increased in IPF (Figure 1C). These findings, including the histological features, were consistent with the previous report (7).

Next, we searched for lncRNAs preferentially expressed in basal cells by comparing AT2 cells and basal cells in public scRNA-Seq data, identifying *MIR205HG* as the most significant differentially expressed gene (DEG) in basal cells (Figure 1D). Among the lncRNAs expressed in basal cells, *MIR205HG* was localized to the epithelial cluster and was particularly highly expressed in basal cells (Figure 1E and Supplemental Figure 1B). We sorted AT2 cells and basal cells from metaplastic lesions of 2 IPF cases and performed RNA-Seq, which verified that *MIR205HG* was among the DEGs preferentially expressed in basal cells (Supplemental Figure 2, A–G). Bulk RNA-Seq data also showed significantly higher expression of *MIR205HG* in patients with IPF than in healthy controls (GSE92592, ref. 19, and GSE124685, ref. 20) (Figure 1F). These findings indicate that *MIR205HG* is highly expressed in basal cells within metaplastic lesions.

To assess the clinical implications of *MIR205HG* in IPF, we conducted in situ hybridization (ISH) on 29 samples from patients with IPF (Figure 2A). The expression level of *MIR205HG* was scored using HALO software (Figure 2B), and patients were divided into a high-*MIR205HG* group (n = 15) and a low-*MIR205HG* group (n = 14) based on the median value (Figure 2C). Kaplan-Meier analysis revealed that the high-*MIR205HG* group had a significantly lower overall survival (OS) rate than the low-*MIR205HG* group (HR, 5.23; 95% CI, 1.80–15.17; P = 0.0042) (Figure 2D). Univariate and multivariate Cox regression analyses further demonstrated that *MIR205HG* was an independent risk factor affecting the OS of patients with

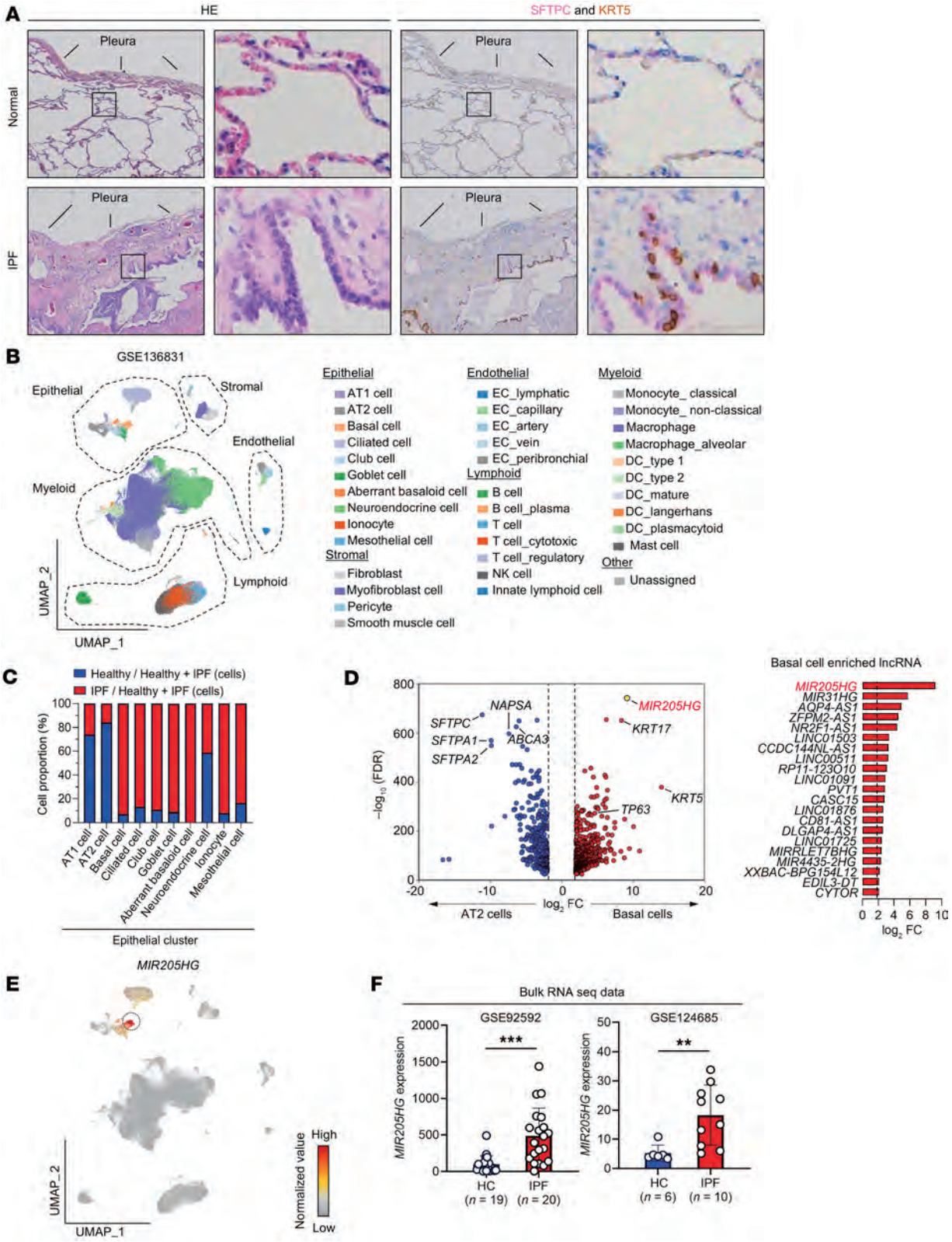

Figure 1. lncRNA *MIR205HG* is upregulated in basal cells. (**A**) Representative images of HE, SFTPC IHC, and KRT5 IHC staining in alveoli beneath the pleura of healthy and IPF lungs. Scale bar: 100 μm. HE, hematoxylin and eosin; SFTPC, surfactant protein C; KRT5, keratin 5. (**B**) Uniform manifold approximation and projection (UMAP) visualization of cell types in healthy and IPF lungs. (**C**) Proportion of epithelial cell type distribution in healthy and IPF lungs. (**D**) Volcano plot and bar graph (basal cell enriched lncRNA) of DEGs in AT2 cells and basal cells. The cutoff values were $\log_2$FC > 1, FDR < 0.05. (**E**) UMAP visualization of *MIR205HG* expression. (**F**) Expression of *MIR205HG* in healthy control and IPF patients. Public bulk RNA-Seq datasets (GSE92592, ref. 19, and GSE124685, ref. 20) were used. Data represent mean ± SD. $^{**}P < 0.01$, $^{***}P < 0.001$; *P* values were determined by 2-tailed Mann-Whitney *U* test. (**B**–**E**) Public scRNA-Seq data (GSE136831) (7) were used for analysis.

IPF (Figure 2E). To reconfirm the significance of *MIR205HG* in the prognosis of IPF, we compared the expression of *MIR205HG* between 2 groups of IPF patients: the favorable-prognosis group (n = 16) (survival ≥ 3 years) and the unfavorable-prognosis group (n = 19) (survival < 3 years, n = 13, and lung transplant recipients, n = 6). The expression level of *MIR205HG* was significantly higher in the unfavorable- than favorable-prognosis group (Figure 2F).

The MIR205HG$^+$IL33$^+$ cell subset in the alveolar region increases in IPF. To clarify the detailed spatial expression of *MIR205HG* in IPF, we conducted *MIR205HG* ISH combined with IHC for SFTPC (an AT2 cell marker) and KRT5 (a basal cell marker). The *MIR205HG* ISH signal exhibited a nuclear staining pattern and was predominantly detected in KRT5$^+$ cells within fibrotic areas but not in SFTPC$^+$ cells of nonfibrotic areas (Figure 3A). The number of *MIR205HG* ISH signal-positive cells was higher in fibrotic areas than in nonfibrotic areas (Figure 3B).

Notably, we found that *MIR205HG*$^+$ cells were detected in the alveolar region and that these cells were also positive for SFTPC, indicating that abnormal AT2 cells expressing *MIR205HG* were present in the alveolar region of patients with IPF (Figure 3C). These *MIR205HG*$^+$ abnormal AT2 cells were negative for KRT5, and such cells were not detected in the nonfibrotic areas of patients or in alveolar normal lungs (Figure 3, A and C, and Supplemental Figure 3A). Consistent with this finding, public scRNA-Seq data (GSE136831) revealed that the proportion of *MIR205HG*$^+$ abnormal AT2 cells was higher in IPF than in healthy lungs (Figure 3D).

Gene ontology (GO) analysis indicated that signatures involved in the inflammatory response were mainly enriched in *MIR205HG*$^+$ AT2 cells relative to *MIR205HG*$^-$ AT2 cells in IPF (Figure 4A). We then constructed a putative cell–cell communication network by mapping known receptor–ligand pairs across cell types. *MIR205HG*$^+$ AT2 cells were revealed to interact with a variety of immune cells, including B cells, monocytes, and innate lymphoid cells (Figure 4B and Supplemental Figure 3B). Among the cytokines and chemokines inducing these immune cells, the *IL33* gene was identified as the most DEG, being highly expressed in *MIR205HG*$^+$ AT2 cells (Figure 4C). Another scRNA-Seq dataset (GSE159354) (21) also revealed that *MIR205HG*$^+$ AT2 cells found in IPF expressed high levels of *IL33* mRNA (Supplemental Figure 3, C and D). Indeed, *MIR205HG*$^+$HTII-280$^+$ (another AT2 marker) cells expressed IL-33 protein in IPF, whereas such *MIR205HG*$^+$HTII-280$^+$IL-33$^+$ cells were not detected in healthy lungs (Figure 4, D and E). IL-33 is known to induce ILC2s (22–24), and scRNA-Seq data (GSE136831) showed that *CD127$^+$GATA3$^+$* ILC2s were significantly increased in IPF (Figure 4F). Furthermore, we found *CD127$^+$GATA3$^+$* ILC2s in proximity to *MIR205HG*$^+$ cells (Figure 4G), suggesting that *MIR205HG*$^+$ abnormal AT2 cells in IPF may be involved in the regulation of ILC2s via IL-33.

Overexpression of lncRNA MIR205HG increases IL33 mRNA expression in alveolar organoids. To more precisely examine the role of *MIR205HG* in IL-33 expression, we established alveolar organoids from the healthy lungs of 3 independent cases (Supplemental Figure 4A). The established alveolar organoids expressed AT2 cell markers (SFTPC and HTII-280) but not basal cell markers, including *MIR205HG*, as verified by IHC and ISH (Supplemental Figure 4, B and C). We then overexpressed *MIR205HG* in the established alveolar organoids, creating *MIR205HG*-overexpressing (*MIR205HG*-OE) alveolar organoids (Figure 5, A–C). When *MIR205HG* was overexpressed, the number of organoids increased compared with the control (Figure 5D). Next, we performed RNA-Seq (GSE275717) in *MIR205HG*-OE alveolar organoids generated from 3 independent cases. As observed in basal cells (NGFR$^+$) cells (Supplemental Figure 2G), we confirmed that *MIR205HG*-OE alveolar organoids have transcripts of *MIR205HG* (Supplemental Figure 5A). GO analysis revealed that processes related to the inflammatory response were enriched in the upregulated genes of the *MIR205HG*-OE alveolar organoids (Supplemental Figure 5B). Among the inflammatory response genes, *IL33* was consistently enriched in *MIR205HG*-OE alveolar organoids (Figure 5E and Supplemental Figure 5C). Indeed, quantitative reverse transcription polymerase chain reaction (qRT-PCR) revealed a significant increase in *IL33* mRNA expression in *MIR205HG*-OE alveolar organoids (Figure 5F). In addition to genetic manipulation such as overexpression, the correlation of *MIR205HG* and *IL33* expression was evaluated by treatment with reagents. We searched for reagents and found that bleomycin treatment increased *MIR205HG* expression. When treated with bleomycin, *IL33* was highly expressed as well as *MIR205HG* (Supplemental Figure 4D). These findings were consistent with the earlier results showing that the *IL33* gene was highly expressed in *MIR205HG*$^+$ AT2 cells but not in *MIR205HG*$^-$ AT2 cells.

Because transcripts of *MIR205HG* contained the region coding *microRNA-205* (*miR-205*) (25), it is possible that *miR-205* but not *MIR205HG* affects *IL33* expression. To exclude this possibility, we investigated public data from miRDB (26) and TargetMiner (27); we did not find *IL33* among the target genes of *miR-205-3p*

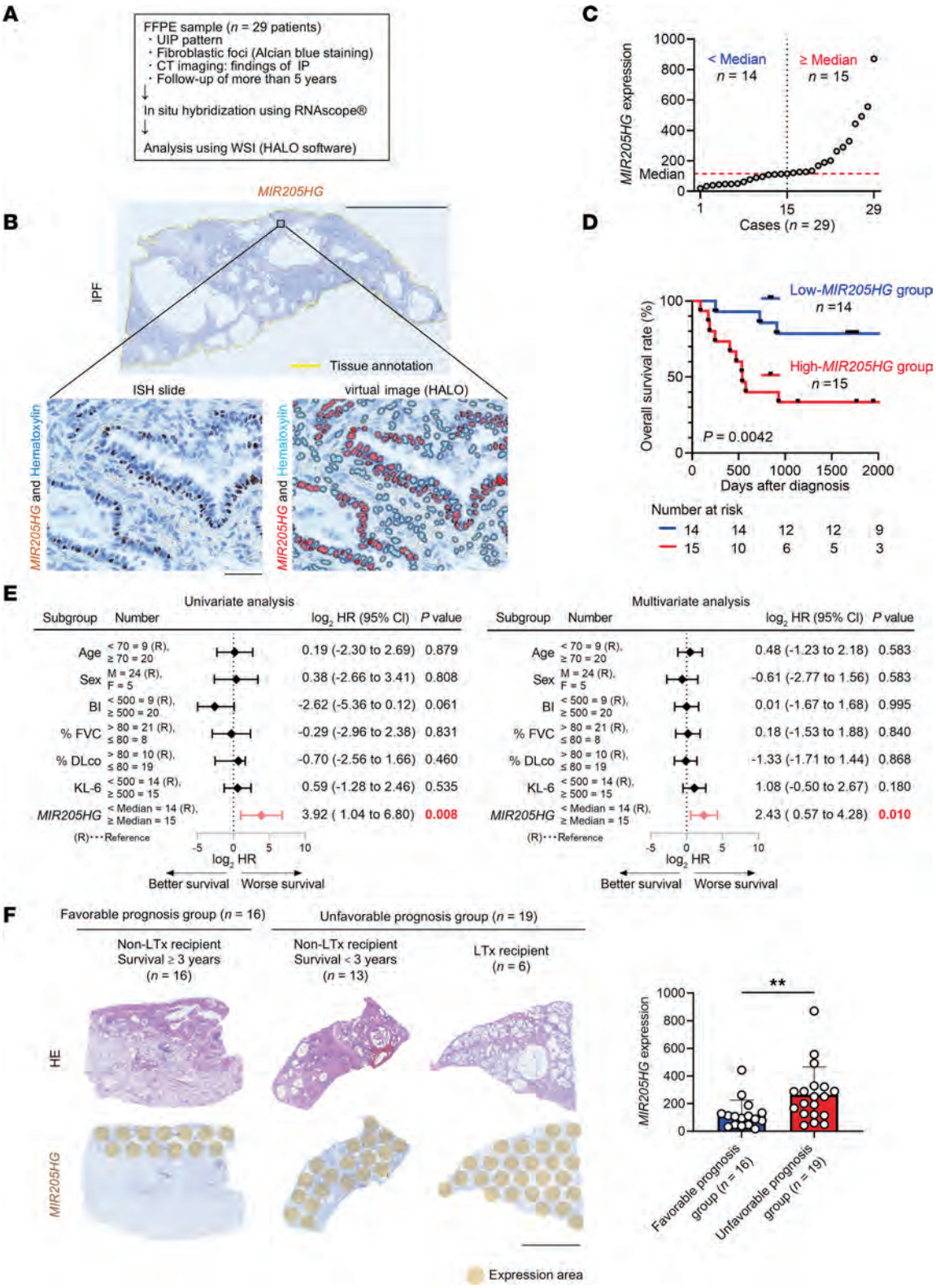

Figure 2. lncRNA *MIR205HG* is an independent poor prognostic factor in patients with IPF. (**A**) Overview of clinical implication assessment based on *MIR205HG* expression in patients with IPF (n = 29). UIP, usual interstitial pneumonia. (**B**) Representative images of *MIR205HG* ISH staining in patients with IPF. Scale bar: 10 mm. Zoomed image and virtual composite image after HALO software analysis are shown. Scale bar: 50 μm. (**C**) Plots of *MIR205HG* expression in patients with IPF (n = 29). The median was used as a cutoff value. (**D**) Kaplan-Meier curves for OS rate (%) in patients with IPF (n = 29) divided into high-*MIR205HG* group (n = 15) and low-*MIR205HG* group (n = 14). HR, 5.23; 95% CI, 1.80–15.17; P = 0.0042. P values were determined by log-rank test. (**E**) Forest plots of univariate and multivariate Cox regression analysis in the correlation between *MIR205HG* expression and other clinical factors. P values were determined by Cox proportional hazards method. (**F**) Representative of whole image of HE and *MIR205HG* ISH staining. Bar graph of

MIR205HG expression in patients with IPF of the favorable-prognosis group (survival ≥ 3 years, *n* = 16) and the unfavorable-prognosis group (survival < 3 years, *n* = 13, and lung transplant recipients [LTx recipients], *n* = 6). Scale bar: 10 mm. Data represent mean ± SD. $^{**}P < 0.01$; *P* values were determined by 2-tailed Mann-Whitney *U* test.

and *miR-205-5p* (Figure 6A and Supplemental Figure 6). For experimental validation, we overexpressed pre–*miR-205* in alveolar organoids (*miR-205*–OE alveolar organoids) (Figure 6B). Even when *miR-205-3p* and *miR-205-5p* were overexpressed (Figure 6C), the expression levels of *MIR205HG* (Figure 6D) and *IL33* (Figure 6E) were not affected. These results indicated that the lncRNA *MIR205HG* is involved in the increased expression of *IL33* and that *miR-205* is not involved in this process.

Knockdown of MIR205HG reduces IL33 mRNA and IL33 protein expression levels in basal cells. To clarify the relationship between *MIR205HG* and *IL33* expression, we knocked down *MIR205HG* in human bronchial epithelial (NHBE) primary cells exhibiting the basal cell phenotype using the CRISPR interference/dCas9-KRAB (CRISPR/dCas9) system (Figure 7A and Supplemental Figure 7, A and B). The knockdown of *MIR205HG* (*MIR205HG*-KD) was verified in NHBE cells by qRT-PCR and ISH (Figure 7B and Supplemental Figure 7C). *MIR205HG*-KD significantly reduced cell proliferation in NHBE cells (Figure 7C).

We performed RNA-Seq (GSE275709) on *MIR205HG*-KD NHBE cells. Among 1,465 genes highly expressed in basal cells identified by scRNA-Seq (Figure 1D, GSE136831), 11 genes were downregulated after *MIR205HG*-KD: *CCDC138*, *GLMN*, *IL33*, *MICOS10-NBL1*, *PTPRZ1*, *RGCC*, *TNXB*, *TSHZ2*, *ASTN2*, *WDR49*, and *PLEKHS1* (Figure 7, D and E). Among them, 4 genes (*IL33*, *PLEKHS1*, *PTPRZ1*, and *RGCC*) were upregulated in the *MIR205HG*-OE alveolar organoids. These findings indicate that the expression level of *IL33* was correlated with that of *MIR205HG*. Indeed, the downregulation of *IL33* mRNA and IL-33 protein in *MIR205HG*-KD cells was verified by qRT-PCR, Western blot, and IHC (Figure 7, F and G, and Supplemental Figure 7D).

To validate these results, we established IPF patient–derived airway organoids that expressed basal cell markers (Supplemental Figure 8, A–C), and *MIR205HG*-KD was performed in these organoids using the CRISPR/dCas9 system (Figure 7H). The qRT-PCR results revealed that *IL33* mRNA was downregulated in *MIR205HG*-KD IPF patient–derived airway organoids (Figure 7, I and J). Consistent with this finding, public scRNA-Seq data (GSE136831) showed enrichment of *IL33* expression in *MIR205HG*$^{+}$ basal cells (Figure 7K). Histologically, we found that basal cells and aberrant basaloid cells with high *MIR205HG* expression coexpressed IL-33 protein in patients with IPF (Figure 7L and Supplemental Figure 8D). These results indicate that *MIR205HG* is responsible for regulating IL-33 expression in basal cells as well as alveolar cells affected by IPF.

Fused in sarcoma RNA-binding protein stabilizes MIR205HG and IL33 mRNA in NHBE cells and IPF patient–derived airway organoids. We next investigated the molecular mechanisms by which *MIR205HG* regulates IL-33 expression. Because several known lncRNAs cooperate with RNA-binding proteins (RBPs) (28–31), we searched for RBPs commonly bound by *MIR205HG* and *IL33* RNA using starBase v2.0 (32) (Figure 8A). In the public HITS-CLIP dataset (GSE43308) (33), fused in sarcoma (FUS) was identified as an RBP that binds to both *MIR205HG* and *IL33* mRNA (Figure 8B). The FUS-binding sequence on *MIR205HG* did not contain the *miR-205* locus (Figure 8B).

We then performed RNA-immunoprecipitation (RIP) in NHBE cells and IPF patient–derived airway organoids (Figure 8C). FUS protein–enriched samples contained significantly higher amounts of *MIR205HG* and *IL33* mRNA relative to control IgG samples in both NHBE cells and IPF patient–derived airway organoids (Figure 8, D and E, and Supplemental Figure 9, A and B). In IPF patient–derived airway organoids, *MIR205HG* and *IL33* double ISH staining revealed that *MIR205HG* was localized in proximity to *IL33* mRNA (Figure 8F). This observation was also found in patients with IPF (Figure 8G).

Because FUS protein contributes to RNA stabilization (34–36), we hypothesized that FUS-KD could affect the amounts of *MIR205HG* and *IL33* mRNA. As expected, FUS-KD significantly decreased *MIR205HG* and *IL33* mRNA amounts in NHBE cells and IPF patient–derived airway organoids, indicating the role of FUS in stabilizing *MIR205HG* and *IL33* mRNA (Figure 9A and Supplemental Figure 9C). We then hypothesized that *MIR205HG* regulates *IL33* mRNA expression by affecting FUS expression. To examine this hypothesis, we investigated the relationship between FUS expression and the amounts of *MIR205HG* and *IL33* mRNA. However, *FUS* mRNA and FUS protein expression were not affected in *MIR205HG*-KD NHBE cells (Supplemental Figure 9, D and E). Moreover, there was no difference in *FUS* mRNA and FUS protein expression in IPF patient–derived airway organoids with high *MIR205HG*

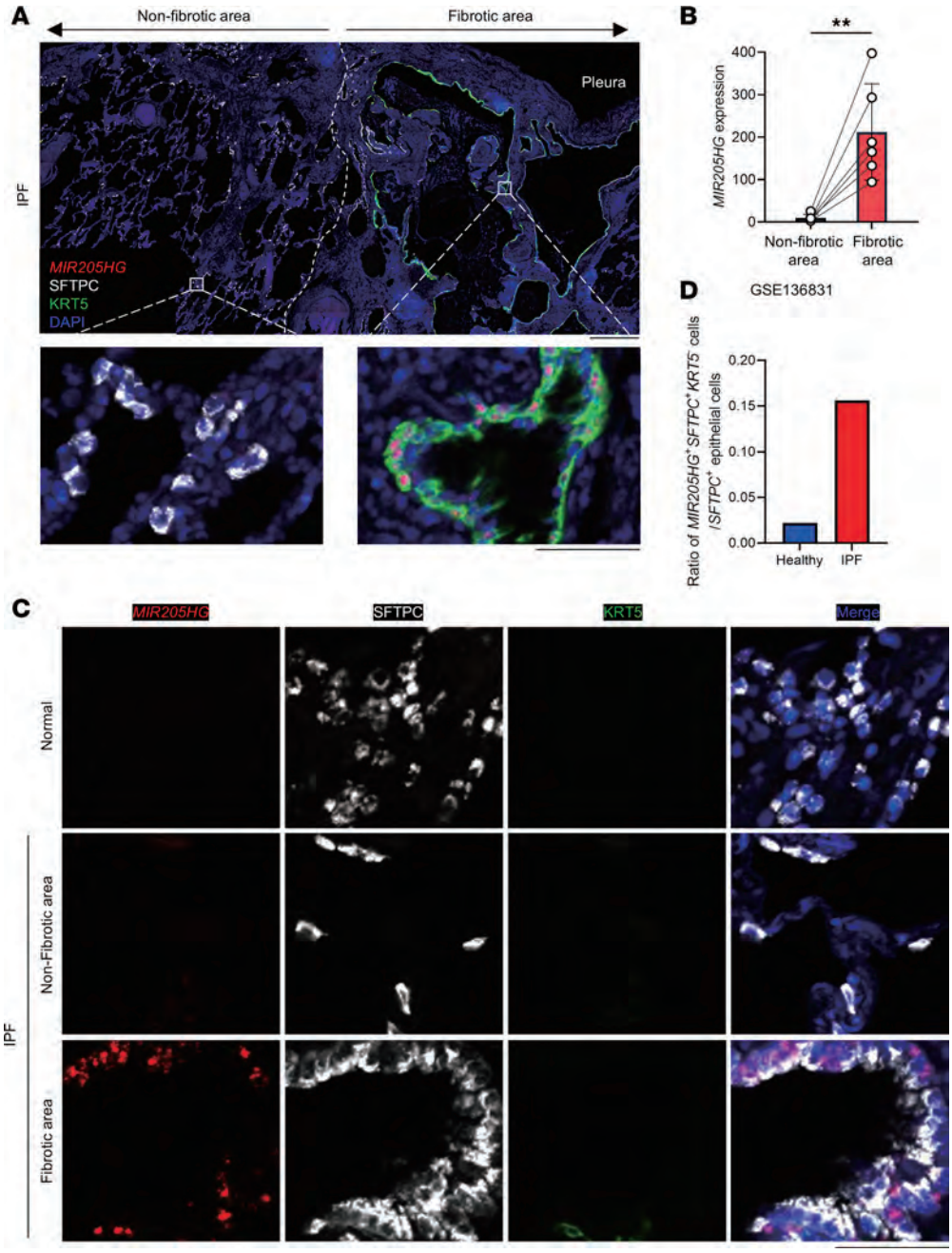

Figure 3. A subset of *MIR205HG*⁺ abnormal AT2 cells is increased in patients with IPF. (**A**) Representative confocal images of *MIR205HG* ISH, SFTPC IHC, and KRT5 IHC staining in nonfibrotic and fibrotic areas of patients with IPF (n = 6). Scale bars: 500 μm (upper) and 50 μm (lower). (**B**) Quantification of *MIR205HG* expression in nonfibrotic and fibrotic areas. Data represent mean ± SD. $^{**}P < 0.01$; P values were determined by 2-tailed paired t test. (**C**) Representative confocal images of *MIR205HG* ISH, SFTPC IHC, and KRT5 IHC staining in healthy (n = 6) and nonfibrotic or fibrotic area of patients with IPF (n = 6). Scale bar: 50 μm. (**D**) Ratio of *MIR205HG*⁺*SFTPC*⁺*KRT5*⁻ cells in *SFTPC*⁺ epithelial cell population in healthy and IPF lungs. Public scRNA-Seq data (GSE136831) were used for analysis.

and IL-33 expression relative to alveolar organoids with low *MIR205HG* and IL-33 expression (Figure 9B and Supplemental Figure 9, F and G). Additionally, IHC showed that FUS protein was expressed in almost all cells, including the alveolar and airway epithelium, with no obvious difference in FUS expression between healthy lungs and patients with IPF (Figure 9C). Therefore, it is unlikely that *MIR205HG* affects *IL33* mRNA expression by modulating FUS expression. Instead, FUS protein itself stabilized *MIR205HG* and *IL33* mRNA, pointing to another mechanism such as a direct interaction between *MIR205HG* and *IL33* mRNA (Figure 9D).

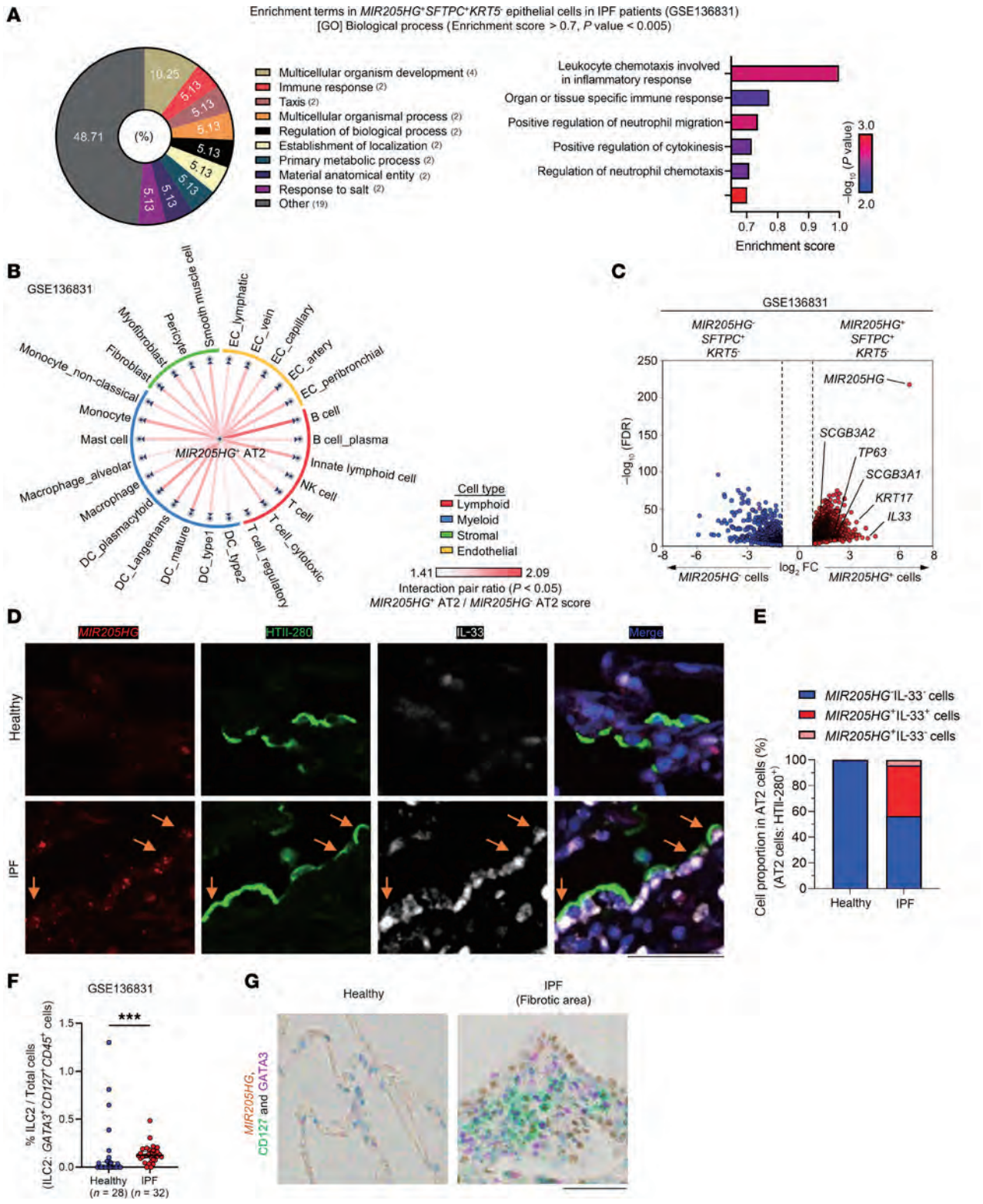

Figure 4. A subset of *MIR205HG*⁺ abnormal AT2 cells express IL-33 and exist in close proximity to ILC2s in patients with IPF. (**A**) GO analysis of biological processes upregulated in *MIR205HG*⁺*SFTPC*⁺*KRT5*⁻ epithelial cells compared with *MIR205HG*⁻*SFTPC*⁺*KRT5*⁻ epithelial cells. Pie chart showing 39 processes with significant differences. The parentheses indicate the number of enrichment terms that belong to the process. Significant differences were determined using an enrichment score > 0.7, $P < 0.005$. Bar graph showing 6 inflammation-related processes among 39 processes. (**B**) Cell–cell communication network showing the ratio of receptor–ligand pairs between the *MIR205HG*⁺*SFTPC*⁺*KRT5*⁻ cells (*MIR205HG*⁺ AT2 cells) and other meta cell types, classified as lymphoid, myeloid, stromal, and endothelial cell clusters (Figure 1B) compared with *MIR205HG*⁻*SFTPC*⁺*KRT5*⁻ cells (*MIR205HG*⁻ AT2 cells). *P* values were determined by the permutation test. (**C**) Volcano plot of DEGs in *MIR205HG*⁻*SFTPC*⁺*KRT5*⁻ cells and *MIR205HG*⁺*SFTPC*⁺*KRT5*⁻ cells. The cutoff values were $\log_2$FC > 1, FDR < 0.05. (**D**) Representative confocal images of *MIR205HG* ISH, HTII-280 IHC, and IL-33 IHC staining in control ($n = 3$) and IPF patients ($n = 3$). Orange arrows

indicate *MIR205HG*$^+$HTII-280$^+$IL-33$^+$ AT2 cells. Scale bar: 50 μm. (**E**) Quantification of AT2 cells expressing *MIR205HG* and IL-33 in healthy and IPF patients in **D**. (**F**) Number of *CD127*$^+$*GATA3*$^+$*CD45*$^+$ cells in healthy (n = 28) and IPF (n = 32) lungs. Bars represent the median and 95% CI. $^{**}P < 0.01$; P values were determined by 2-tailed Mann-Whitney U test. (**G**) Representative images of *MIR205HG* ISH, CD127 IHC, and GATA3 IHC staining in control (n = 4) and IPF patients (n = 4). Scale bar: 50 μm. (**A**, **B**, **E**, and **F**) Public scRNA-Seq data (GSE136831) were used for analysis.

The AluJb element of MIR205HG is essential for regulation of IL33 expression. To investigate the direct interaction between *MIR205HG* and *IL33* mRNA, we performed chromatin isolation via RNA precipitation (ChIRP) experiments (Figure 10A). In these ChIRP experiments, the *MIR205HG* probe coprecipitated more *IL33* mRNA compared with the control *LacZ* probe in NHBE cells and IPF patient–derived airway organoids (Figure 10B). We next examined sequence similarity between *MIR205HG* and *IL33* in genes enriched in basal cells (1,465 genes). The sequence similarity between these 2 is among the top 20% of the 1,465 genes (Supplemental Figure 10, A and B). When searching for motifs of sequence similarity, the *AluJb* element of *MIR205HG* was found to possess similarity to 9 (6 sense and 3 antisense) sites of *Alu* elements located in the intron region of the *IL33* gene (Figure 10C and Supplemental Figure 11A). These *Alu* elements were not found in the exon regions of the *IL33* gene, indicating that *IL33* pre-mRNA but not *IL33* mRNA possessed these elements. Because *Alu* elements have been reported to interact with each other (37–39), it is possible that the *AluJb* element of *MIR205HG* may be responsible for the interaction between *MIR205HG* and *IL33* pre-mRNA.

We then investigated whether the *AluJb* element of *MIR205HG* affected *IL33* mRNA amount (Figure 10, D and E). When the full-length *MIR205HG* vector was transfected into *MIR205HG*-KD NHBE cells, it restored *IL33* mRNA and pre-mRNA amounts (Figure 10F). In contrast, the Δ*AluJb* element vector, in which the *AluJb* element of *MIR205HG* was deleted, did not upregulate *IL33* mRNA and pre-mRNA amounts compared to full-length vector (Figure 10F), indicating that the *AluJb* element of *MIR205HG* was responsible for regulating IL-33 mRNA amount. Hi-C public data showed that *MIR205HG* (located on chromosome 1) and *IL33* gene (located on chromosome 9) were in close genomic proximity in cells expressing *MIR205HG* and *IL33* mRNA (Supplemental Figure 11B). These results suggest that *MIR205HG* might stabilize *IL33* pre-mRNA through its *AluJb* element immediately after the transcription of the *IL33* gene, thereby upregulating *IL33* mRNA amounts (Figure 10G).

Small molecule DQzG targets the AluJb element of MIR205HG and reduces IL-33 expression. Furthermore, to complement the relevance of the *AluJb* element of *MIR205HG*, we explored small molecules that could target the *AluJb* element to inhibit IL-33 expression (Figure 11A). To identify binding molecules using SPR, we selected 7 internal and hairpin loop motifs from the secondary structure predicted by CentroidFold (40) and designed SPR-measurable RNA sequences (Figure 11, B and C, and Supplemental Figure 12A). SPR-based screening with a library of 1,273 small molecules identified ANP77 (41), DQzG (42), and TO239 as promising candidates that showed strong binding to the *AluJb* element (Supplemental Figure 12, A and B). These molecules were then screened for their suppressive effect on *IL33* expression in NHBE cells; DQzG exhibited the greatest inhibitory effect on *IL33* mRNA expression (Figure 11D and Supplemental Figure 12C). Nuclear magnetic resonance (NMR) and SPR analysis at multiple concentrations further supported the ability of DQzG to bind to the *AluJb* element (Supplemental Figure 12, B and D).

We comprehensively examined DEGs in NHBE cells and IPF patient–derived airway organoids treated with DQzG using RNA-Seq analysis. DQzG treatment identified several DEGs and identified *IL33* as one of the genes common to both NHBE cells and IPF patient–derived airway organoids (Supplemental Figure 13A). We verified time- and concentration-dependent suppression of *IL33* mRNA, *IL33* pre-mRNA, and IL-33 protein in NHBE cells and IPF patient–derived airway organoids (Figure 12, A–D). Interestingly, *MIR205HG* expression was also slightly reduced in NHBE cells and IPF patient–derived airway organoids following DQzG treatment (Figure 12, A and B). We verified that cell numbers were not affected under these conditions (Supplemental Figure 13B). As a control experiment, we treated NHBE cells and IPF patient–derived airway organoids with DNpG, a small molecule without binding that does not bind to the sequence in the *AluJb* element recognized by DQzG. Treatment with DNpG had no effect on *IL33* mRNA, *IL33* pre-mRNA, or *MIR205HG* expression (Supplemental Figure 14, A–C). Taken together, these results highlight the important role of the *AluJb* element of *MIR205HG* in the regulation of *IL33* expression (Figure 12E).

The high-MIR205HG group shows high IL-33 expression and increased number of ILC2s compared with the low-MIR205HG group in IPF. We investigated the clinical significance of elevated IL-33 expression in IPF. IL-33 IHC was performed on the same healthy lungs (n = 15) and patients with IPF (n = 29) as used in Figure 2A

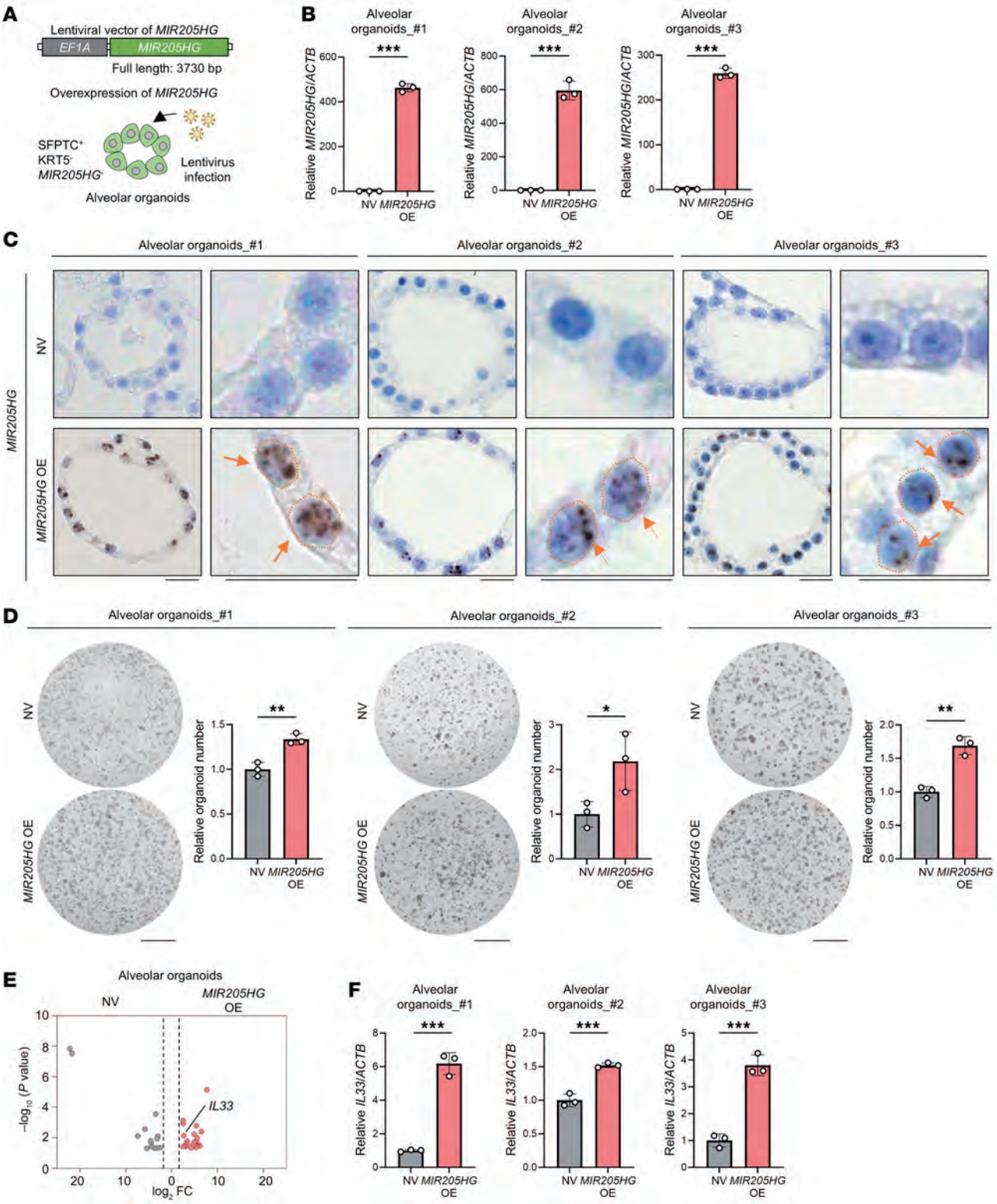

Figure 5. Overexpression of lncRNA *MIR205HG* upregulates *IL33* mRNA in alveolar organoids. (**A**) Schematic of experimental design for identification of *MIR205HG*-regulated genes in *MIR205HG*-OE alveolar organoids. (**B**) qRT-PCR showing *MIR205HG* expression in negative vector (NV) and *MIR205HG*-OE alveolar organoids. (**C**) Representative images of *MIR205HG* ISH staining in NV and *MIR205HG*-OE alveolar organoids. Orange arrows indicate *MIR205HG* signals, which are detected in nuclei (circled by orange dotted line). Scale bar: 20 μm. (**D**) Quantification of organoid number in NV and *MIR205HG*-OE alveolar organoids. Scale bar: 1 mm. (**E**) Volcano plot of DEGs in NV and *MIR205HG*-OE alveolar organoids. Top 40 DEGs are shown. The *IL33* gene is indicated among upregulated genes in *MIR205HG*-OE alveolar organoids. The cutoff values were $\log_2$FC > 2, $P < 0.05$. (**F**) qRT-PCR showing *IL33* expression in NV and *MIR205HG*-OE alveolar organoids. (**B**, **D**, and **F**) Data represent mean ± SD. *$P < 0.05$, **$P < 0.01$, ***$P < 0.001$; P values were determined by 2-tailed t test.

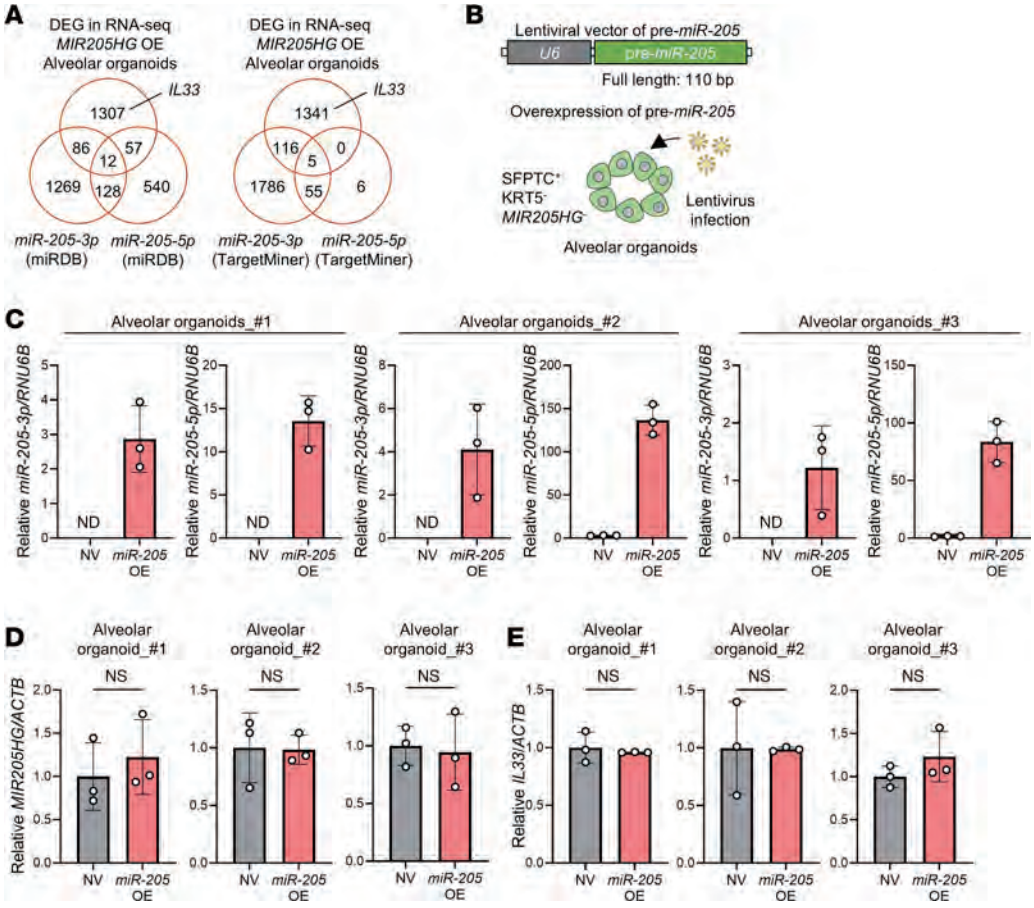

Figure 6. Overexpression of pre–*miR-205* does not upregulate *IL33* mRNA in alveolar organoids. (**A**) Venn diagram showing DEGs of *MIR205HG*-OE alveolar organoids (upper) and target genes of *miR-205* with miRDB (26) (lower left) and TargetMiner (27) (lower right) datasets. (**B**) Schematic of experimental design for identification of pre–*mir-205* regulated genes in *miR-205*–OE alveolar organoids. (**C**) qRT-PCR showing *miR-205-3p* and *miR-205-5p* expression in NV and *miR-205*–OE alveolar organoids. Data represent mean ± SD. N.D., not detected. (**D**) qRT-PCR showing *MIR205HG* expression in NV and *miR-205*–OE alveolar organoids. (**E**) qRT-PCR showing *IL33* expression in NV and *miR-205*–OE alveolar organoids. (**D** and **E**) Data represent mean ± SD. *P* values were determined by 2-tailed *t* test.

(Supplemental Figure 15A). The results revealed that IL-33 protein expression was significantly higher in IPF than in normal lungs (Supplemental Figure 15B). However, IL-33 protein expression was comparable between the low-*MIR205HG* and high-*MIR205HG* groups used in Figure 2C (Supplemental Figure 15C). Additionally, Kaplan-Meier analysis showed that IL-33 expression was not associated with the OS rate when the low–IL-33 group was compared with the high–IL-33 group (Supplemental Figure 15, D and E).

UMAP analysis of scRNA-Seq data (GSE136831) showed that *IL33* mRNA expression was detected in various cells, such as epithelial cells, fibroblasts, and endothelial cells (Supplemental Figure 15, F–H). Previous studies have reported that increased IL-33 expression in the epithelium contributes to long-term innate immune activity and pathogenesis in diseases such as chronic obstructive pulmonary disease and emphysema (43–46). When healthy lungs were compared with IPF patient scRNA-Seq data (GSE136831), the difference in the *IL33* expression level was most pronounced in epithelial clusters (Figure 13A and Supplemental Figure 15I). Consequently, we focused on epithelial IL-33 expression. In the same samples as in Supplemental Figure 15A, double IHC staining with EpCAM (an epithelial marker) and IL-33 was performed (Figure 13B). The number of $EpCAM^+$ and $IL\text{-}33^+$ cells was significantly higher in IPF than in normal lungs (Figure 13C). Furthermore, the number of $EpCAM^+$ and $IL\text{-}33^+$ cells was higher in the high-*MIR205HG* group than in the low-*MIR205HG* group (Figure 13D). We divided the cases into 2 groups: those with high $EpCAM^+$ and $IL\text{-}33^+$ epithelial cells, and those with low $EpCAM^+$ and $IL\text{-}33^+$ epithelial cells (Figure 13E). Kaplan-Meier analysis showed that the former group had significantly lower OS rates than the latter group (HR, 4.49; 95% CI, 1.57–12.86; $P = 0.011$) (Figure 13F).

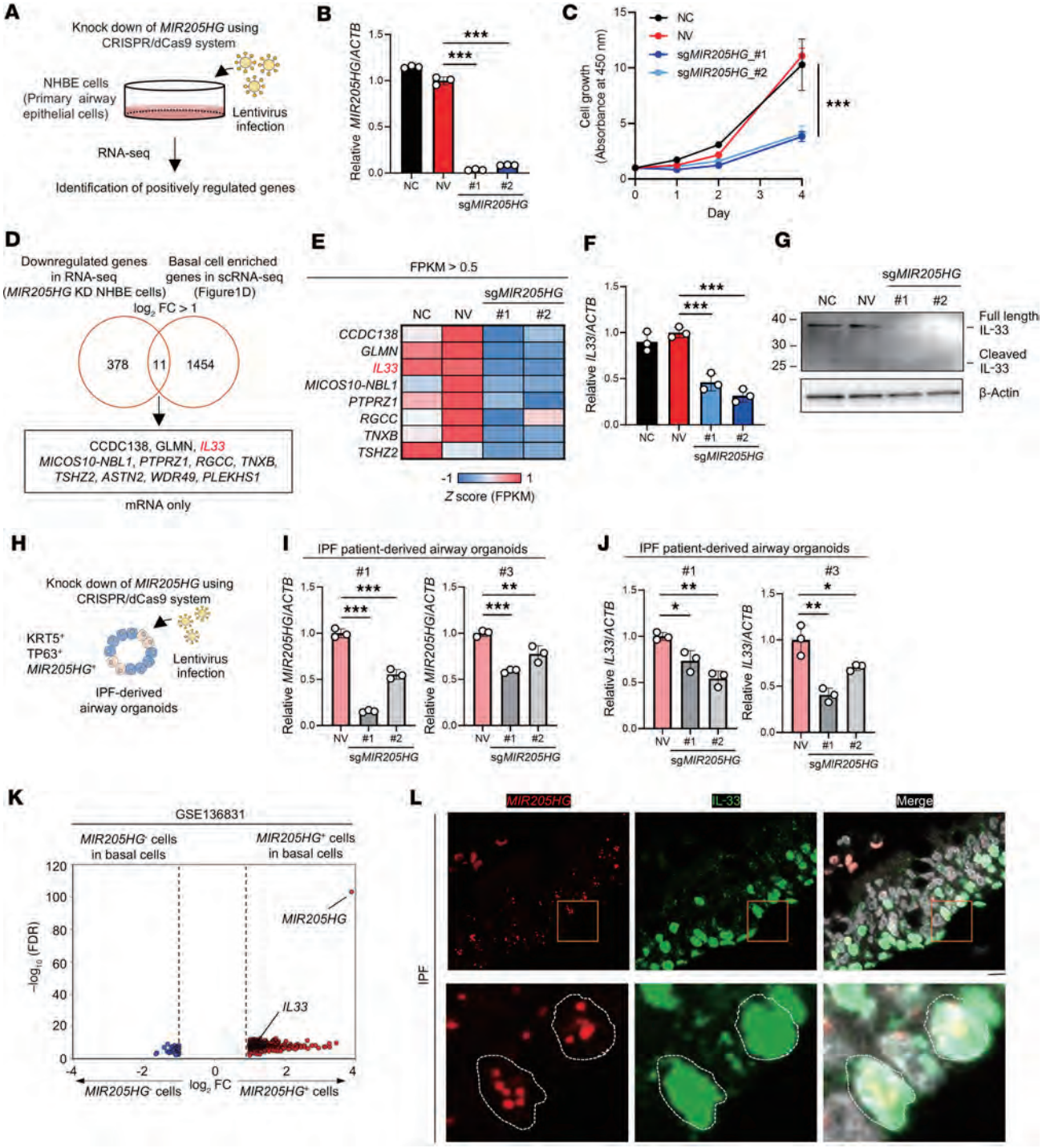

Figure 7. Downregulation of *MIR205HG* decreases *IL33* mRNA and IL-33 protein expression in basal cells. (**A**) Experimental procedure for the identification of genes positively regulated by *MIR205HG* in NHBE cells using the CRISPR interference/dCas9-KRAB (CRISPR/dCas9) system. (**B**) qRT-PCR showing *MIR205HG* expression in NV and *MIR205HG*-KD NHBE cells. NC, negative control. (**C**) Cell growth assay in NV and *MIR205HG*-KD NHBE cells. (**D**) Venn diagram showing downregulated genes in *MIR205HG*-KD NHBE cells (bulk RNA-Seq, left) and basal cell enriched genes in Figure 1D (scRNA-Seq, right). The cutoff values were $\log_2$FC > 1 (bulk RNA-Seq and scRNA-Seq). Two common mRNAs are listed below. (**E**) Heatmap showing common mRNAs that are downregulated genes in *MIR205HG*-KD NHBE cells and basal cell enriched genes shown in **D**. Fragments per kilobase of exon per million mapped fragment (FPKM) > 0.5 mRNAs were visualized. (**F**) qRT-PCR showing *IL33* mRNA expression in NV and *MIR205HG*-KD NHBE cells. (**G**) Western blot showing IL-33 protein expression in NV and *MIR205HG*-KD NHBE cells. (**H**) Schematic of experimental design for identification of *MIR205HG*-regulated genes in IPF patient–derived airway organoids using the CRISPR/dCas9 system. (**I**) qRT-PCR showing *MIR205HG* expression in NV and *MIR205HG*-KD IPF patient–derived airway organoids. (**J**) qRT-PCR showing *IL33* mRNA expression in NV and *MIR205HG*-KD of IPF patient–derived airway organoids. (**K**) Volcano plot of DEGs in *MIR205HG*$^-$ basal cell and *MIR205HG*$^+$ basal cell in public scRNA-Seq data (GSE136831). The cutoff values were $\log_2$FC > 1, FDR < 0.05. (**L**) Representative images of *MIR205HG* ISH and IL-33 IHC staining in patients with IPF. Scale bar: 10 μm. (**B**, **C**, **F**, **I**, and **J**) Data represent mean ± SD. **P* < 0.05, ***P* < 0.01, ****P* < 0.001; *P* values were determined by 1-way ANOVA with Holm-Šídák post hoc test.

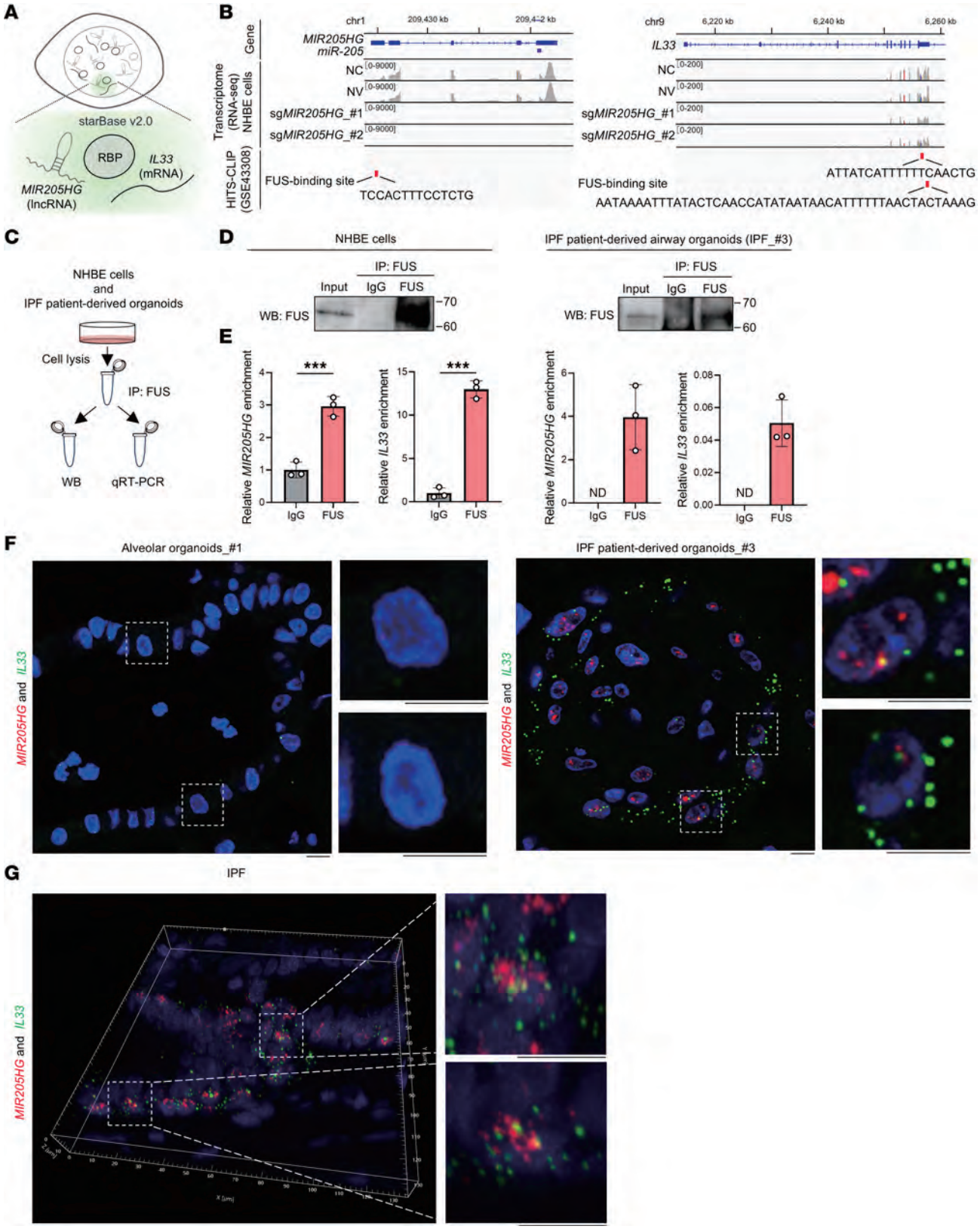

Figure 8. *MIR205HG* and *IL33* mRNA binds to fused in sarcoma RBP in NHBE cells and IPF patient–derived airway organoids. (**A**) Schematic illustration for the identification of RBPs common to *MIR205HG* and *IL33* using starBase v2.0 (32). (**B**) Integrative Genomics Viewer (IGV) showing *MIR205HG* and *IL33* loci in NV and *MIR205HG*-KD NHBE cells. The motif sequences of the respective *MIR205HG* and *IL33* recognized by the FUS protein are shown. Motif sequences were obtained from public HITS-CLIP dataset (GSE43308) (33). (**C**) RIP workflow to examine the binding of the respective *MIR205HG* and *IL33* to the FUS protein. Immunoprecipitation (IP) was performed using an FUS antibody and an IgG antibody as control. RNA enrichment in the FUS antibody was calculated using the IgG antibody as control. (**D**) Western blot showing FUS protein expression in FUS IP using NHBE cells and IPF patient–derived airway organoids.

(**E**) qRT-PCR showing *MIR205HG* and *IL33* in FUS RIP using NHBE cells and IPF patient–derived airway organoids. N.D., not detected. Data represent mean ± SD. ***$P < 0.001$; P values were determined by 2-tailed t test. (**F**) Representative images of *MIR205HG* and *IL33* double ISH staining in alveolar organoids and IPF patient–derived airway organoids. Scale bar: 10 μm. (**G**) Representative images of *MIR205HG* and *IL33* double ISH staining in IPF tissue samples. Scale bar: 10 μm.

Finally, we examined the relationship between *MIR205HG*-expressing cells and ILC2s. The number of CD127$^+$GATA3$^+$ ILC2s was immunohistochemically examined in the low-*MIR205HG* group and the high-MIR205HG group (Figure 13G). The results revealed that the number of CD127$^+$GATA3$^+$ ILC2s was significantly higher in the high-*MIR205HG* group than in the low-*MIR205HG* group (Figure 13H). Additionally, the expression of *MIR205HG* and *IL33* in epithelial cells was plotted for patients with IPF (n = 32), demonstrating a positive correlation between *MIR205HG* and *IL33* expression in epithelial cells using public scRNA-Seq data (GSE136931) (Figure 13I). When these 32 patients with IPF were divided into low-*MIR205HG* (n = 16) and high-*MIR205HG* (n = 16) groups, the high-*MIR205HG* group showed significantly increased expression of *IL33* in epithelial cells and increased numbers of ILC2s (Figure 13, J–L). In summary, we revealed that *MIR205HG* plays a crucial role in regulating epithelial IL-33 expression and is involved in the pathogenesis of IPF.

Discussion

IPF is histologically characterized by the appearance of basal cells in alveolar regions, but evidence on their involvement in the pathogenesis of IPF is limited. This paper demonstrates that *MIR205HG*, a lncRNA highly expressed in basal cells, contributes to the pathogenesis of IPF. *MIR205HG* was upregulated in IPF compared with healthy lungs and was identified as an independent poor prognostic factor in IPF. Through overexpression and knockdown of *MIR205HG* using primary cells and organoids, we demonstrated that *MIR205HG* regulates IL-33 expression. As for the regulatory mechanism, we clarified that the *AluJb* element of *MIR205HG* impacts *IL33* expression through direct interaction. Moreover, we showed that DQzG, a small molecule targeting the *AluJb* element of *MIR205HG*, suppressed IL-33 expression. IL-33 is known to strongly induce ILC2s, which are important cells in the pathogenesis of IPF (47). Indeed, a positive correlation between *MIR205HG*-regulated IL-33 expression and the number of ILC2s was observed in patients with IPF. This work provides insight that *MIR205HG* contributes to IPF progression through IL-33 expression. However, this study did not evaluate in vivo whether *MIR205HG* expression enhances fibrosis by affecting IL-33 expression and the number of ILC2s. We investigated whether *Mir205hg* is upregulated in bleomycin treatment, a commonly used model of pulmonary fibrosis. However, we did not detect *Mir205hg* expression by ISH in control and bleomycin-treated mice. Moreover, public RNA-Seq data analysis showed that *Mir205hg* expression was not induced under different conditions of bleomycin treatment compared to controls (Supplemental Figure 16, A and B). Additionally, an *AluJb* element was identified in human *MIR205HG* but not in mouse *Mir205hg* because the insertion of the *AluJb* element into the *MIR205HG* gene occurred in a common ancestor of the Haplorhini (Supplemental Figure 16C). It has been reported that mouse models of bleomycin-induced fibrosis do not resemble human pathogenesis, which may explain why our findings cannot be validated in the mouse (48, 49). In the future, we should explore animal models of pulmonary fibrosis that reflect human pathogenesis and validate our proposed mechanism.

The pathology of IPF is characterized by spatially and temporally heterogeneous pulmonary remodeling (2). From our detailed histological analysis of IPF samples, we found cells with high *MIR205HG* expression levels in fibrotic regions of IPF. Most *MIR205HG*$^+$ cells were positive for the basal cell marker KRT5, whereas a limited number of *MIR205HG*$^+$ cells were positive for the AT2 markers SFTPC and HTII-280. *MIR205HG*$^+$ AT2 cells were in close proximity to *MIR205HG*$^-$ AT2 cells in fibrotic regions, which may represent an early stage of IPF pathogenesis. Previous reports have demonstrated that abnormally differentiated AT2 cells promote lung fibrosis (50) and are involved in the pathogenesis of IPF (7, 51–54). According to public scRNA-Seq data, *MIR205HG*$^+$ AT2 cells highly expressed *KRT17*, *TP63*, *SCGB3A1*, and *SCGB3A2* compared with *MIR205HG*$^-$ AT2 cells (Figure 4C). These findings suggest that *MIR205HG*$^+$ AT2 cells may represent abnormally differentiated AT2 cells during transformation to basal cells, referred to as alveolar-basal intermediates (53), aberrant basaloid cells (7), AT0 (54), and terminal and respiratory bronchiole secretory cells (54). Unfortunately, *MIR205HG* overexpression did not increase the expression of basal cell markers, such as *KRT17* and *TP63*, in established alveolar organoids, indicating that the transformation to basal cells is a more complex molecular process. Although the proportion of *MIR205HG*$^+$ AT2 cells was low in the IPF sample, these cells expressed IL-33, and ILC2s were found

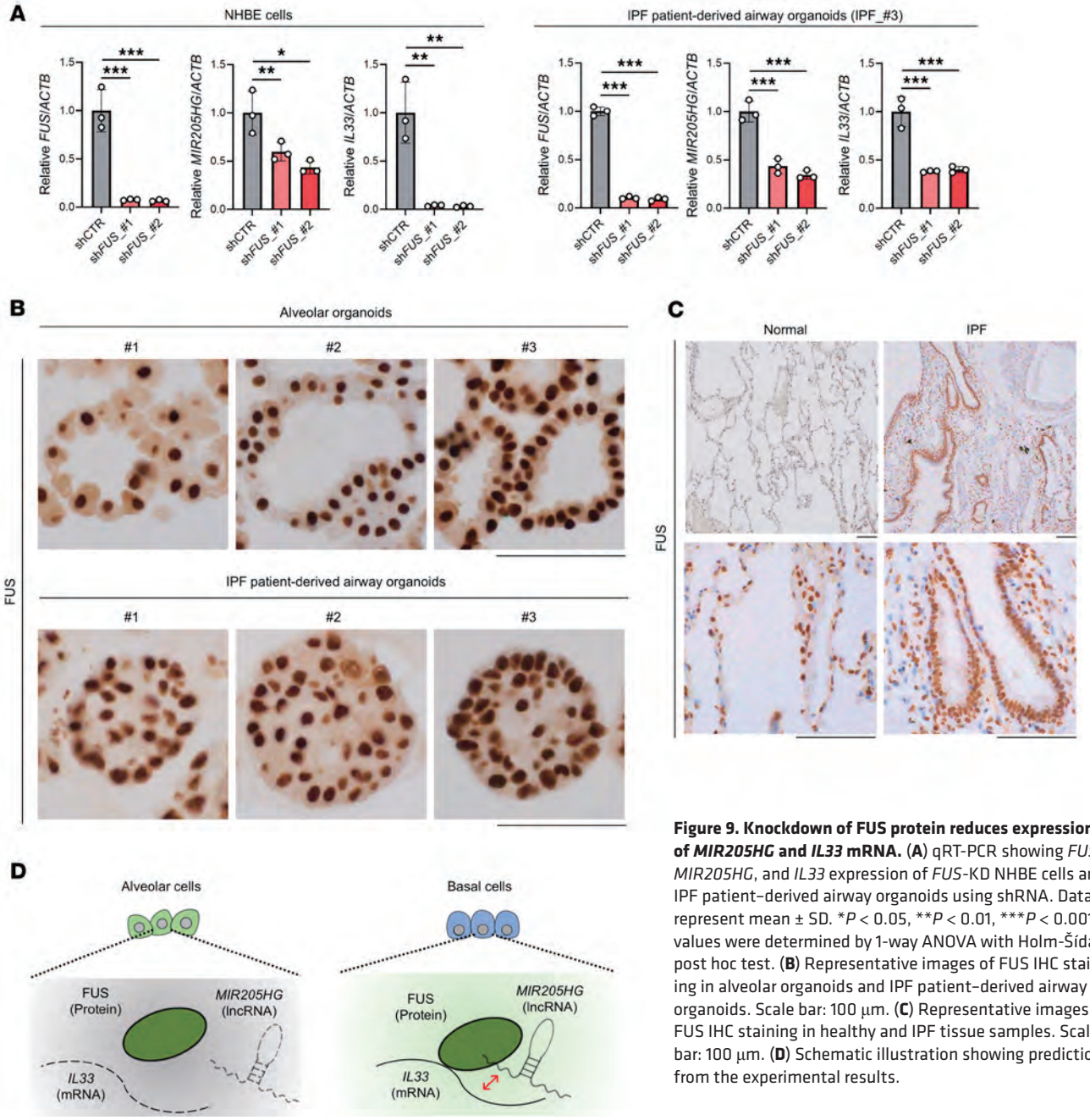

Figure 9. Knockdown of FUS protein reduces expression of *MIR205HG* and *IL33* mRNA. (**A**) qRT-PCR showing *FUS*, *MIR205HG*, and *IL33* expression of *FUS*-KD NHBE cells and IPF patient–derived airway organoids using shRNA. Data represent mean ± SD. $^{*}P < 0.05$, $^{**}P < 0.01$, $^{***}P < 0.001$; *P* values were determined by 1-way ANOVA with Holm-Šídák post hoc test. (**B**) Representative images of FUS IHC staining in alveolar organoids and IPF patient–derived airway organoids. Scale bar: 100 μm. (**C**) Representative images of FUS IHC staining in healthy and IPF tissue samples. Scale bar: 100 μm. (**D**) Schematic illustration showing predictions from the experimental results.

around them. In support of reports that abnormal AT2 cells contribute to pathogenesis, we may have uncovered a role for *MIR205HG*$^{+}$ abnormal AT2 cells that induce various inflammatory responses and contribute to the progression of IPF.

IL-33 is expressed in various cell types other than the epithelium, such as fibroblasts and vascular endothelial cells (55). Consistent with this pattern, our IHC analysis demonstrated that IL-33 was expressed in various cell types, including epithelial cells. We divided IPF cases into high– and low–IL-33 groups but detected no difference in prognosis between these 2 groups. Public scRNA-Seq data revealed that the difference in *IL33* expression levels between healthy lungs and patients with IPF was most pronounced in the epithelial cell cluster. We then counted IL-33–positive epithelial cells (EpCAM^{+} cells) and divided patients with IPF into cases with highly IL-33–expressing epithelial cells and lowly IL-33–expressing epithelial cells. Cases with high–IL-33–expressing epithelial cells showed a worse prognosis relative to cases with low–IL-33–expressing epithelial cells. The relationship between IL-33 and lung fibrosis has been reported in mice, in which fibroblast-derived IL-33 is important in fibrosis (47). The controversy over the cell types responsible for fibrosis as the IL-33 source might

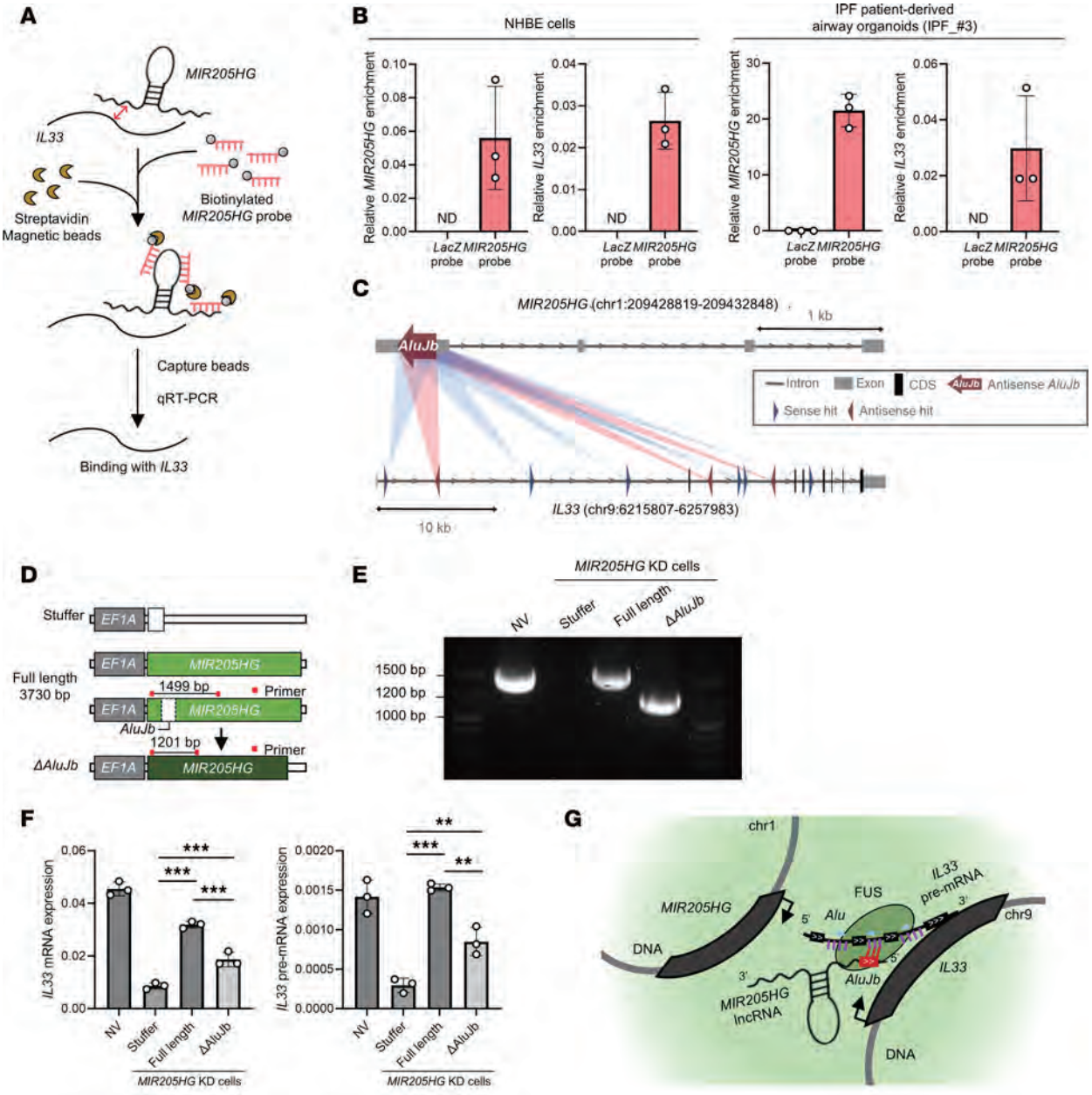

Figure 10. *AluJb* element of *MIR205HG* regulates *IL33* expression. (**A**) Workflow of ChIRP for binding of *IL33* using the *MIR205HG* probe. (**B**) qRT-PCR of *MIR205HG* and *IL33* in ChIRP for *MIR205HG* enrichment in NHBE cells and IPF patient–derived airway organoids. ChIRP was performed using *MIR205HG* probe and *LacZ* probe as control. Data represent mean ± SD. N.D., not detected. (**C**) Predicted binding sites of the *AluJb* element of *MIR205HG* and the *Alu* elements (intron) of *IL33*. A total of 9 sites with similarity to *AluJb* or *Alu* elements were found in the *Alu* element of *IL33*. Blue and red indicate sequence similarity between the *AluJb* element of *MIR205HG* and the sense/antisense strand of the *Alu* elements of *IL33*, respectively. (**D**) Vector design for functional analysis of the *AluJb* element of *MIR205HG*. (**E**) RT-PCR products obtained by transfection of NHBE cells with primers shown in **D**. Deletion of the *AluJb* element (Δ*AluJb*) of *MIR205HG* was confirmed. (**F**) qRT-PCR showing *IL33* mRNA and *IL33* pre-mRNA expression under **E** conditions. Data represent mean ± SD. $^{**}P < 0.01$, $^{***}P < 0.001$; *P* values were determined by 1-way ANOVA with Holm-Šídák post hoc test. (**G**) Schematic illustration of the experimental results.

be due to species differences. Indeed, the expression pattern of IL-33 differs between humans and mice; for example, IL-33 is detected in mouse alveolar epithelium (56, 57) but not in human alveolar epithelium.

Overexpression of *MIR205HG* increased *IL33* expression, and its knockdown reduced *IL33* expression. The transfection of full-length *MIR205HG* vector increased *IL33* expression in *MIR205HG*-KD NHBE cells. When *MIR205HG* deleting the *AluJb* element (Δ*AluJb* element) vector was transfected, the increase in *IL33* expression was attenuated. These findings indicate that the *AluJb* element of *MIR205HG* was responsible for *IL33* expression. Although the function of *Alu* elements is not fully understood, recent analyses have revealed that *Alu* elements are involved in various transcriptional regulations (38). The *AluJb* element of

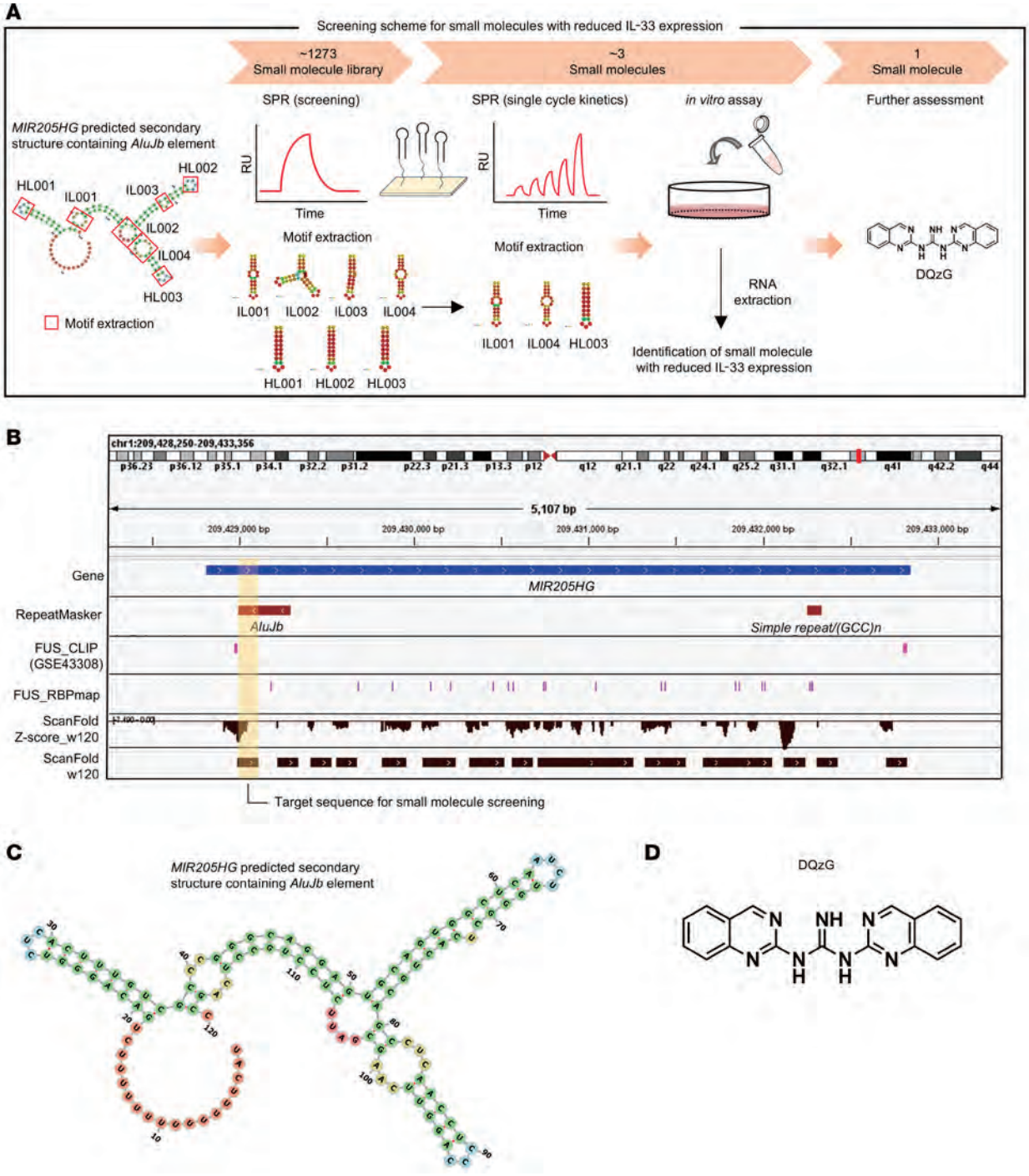

Figure 11. Screening of small molecules that reduce IL-33 expression by targeting the *AluJb* element. (**A**) Overview of the screening scheme for the identification of small molecules that reduce *IL33* expression. surface plasmon resonance (SPR) experiments were carried out on 7 motifs from the *MIR205HG* predicted secondary structure containing the *AluJb* element. The SPR experiments identified 3 small molecules (ANP77, DQzG, and TO239) from a library of 1,273 small molecules. These 3 small molecules were assessed for *IL33* expression in NHBE cells. (**B**) IGV plot showing the target sequence region for small molecule screening. The target sequence was selected as the yellow background region containing the *AluJb* element. (**C**) Predicted secondary structure containing *AluJb* element of *MIR205HG*. RNA secondary structure was predicted with RNAfold and visualized with forna. (**D**) The structure of the small molecule DQzG.

MIR205HG is essential for transcriptional regulation of genes specific for luminal cells of the prostate (37). *MIR205HG* binds to the *Alu* element in the promoter region of luminal genes via its *AluJb* element and interferes with the binding of interferon-regulatory factor (IRF) that transactivates luminal specific genes. Deletion of the *AluJb* element of *MIR205HG* abolishes the occupation of *MIR205HG*, allowing IRF to bind to the promoter region of luminal genes (37). These reports suggest the importance of direct interaction

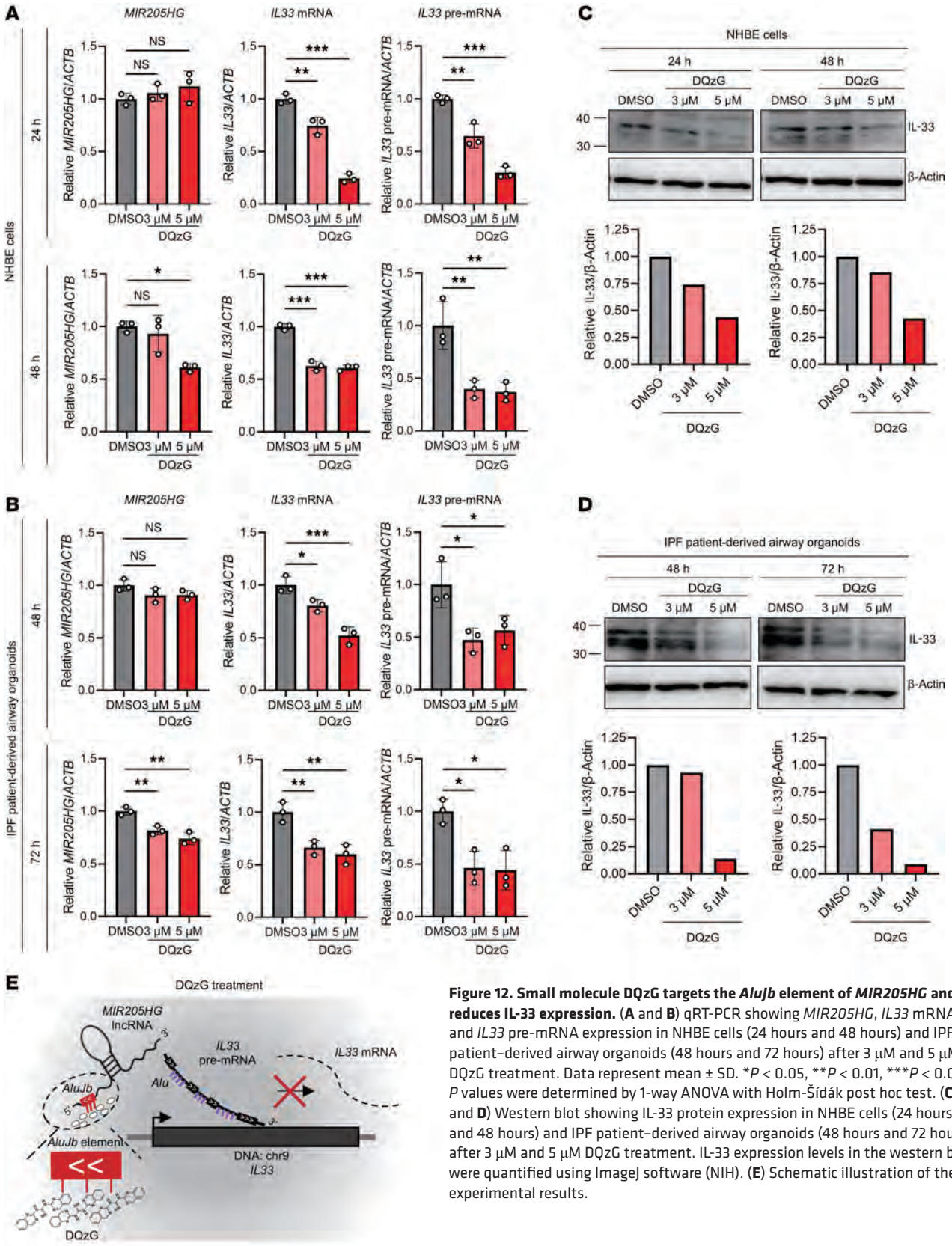

Figure 12. Small molecule DQzG targets the *AluJb* element of *MIR205HG* and reduces IL-33 expression. (**A** and **B**) qRT-PCR showing *MIR205HG*, *IL33* mRNA, and *IL33* pre-mRNA expression in NHBE cells (24 hours and 48 hours) and IPF patient–derived airway organoids (48 hours and 72 hours) after 3 μM and 5 μM DQzG treatment. Data represent mean ± SD. *$P < 0.05$, **$P < 0.01$, ***$P < 0.001$; P values were determined by 1-way ANOVA with Holm-Šídák post hoc test. (**C** and **D**) Western blot showing IL-33 protein expression in NHBE cells (24 hours and 48 hours) and IPF patient–derived airway organoids (48 hours and 72 hours) after 3 μM and 5 μM DQzG treatment. IL-33 expression levels in the western blot were quantified using ImageJ software (NIH). (**E**) Schematic illustration of the experimental results.

between *Alu* elements in transcriptional regulation. With respect to the *IL33* gene, there are 9 *Alu* elements possessing sequence similarity to the *AluJb* element of *MIR205HG*. In this context, our results suggest that the *AluJb* element of *MIR205HG* plays a functional role through direct interaction with the *Alu* element of *IL33* in the regulation of IL-33 expression.

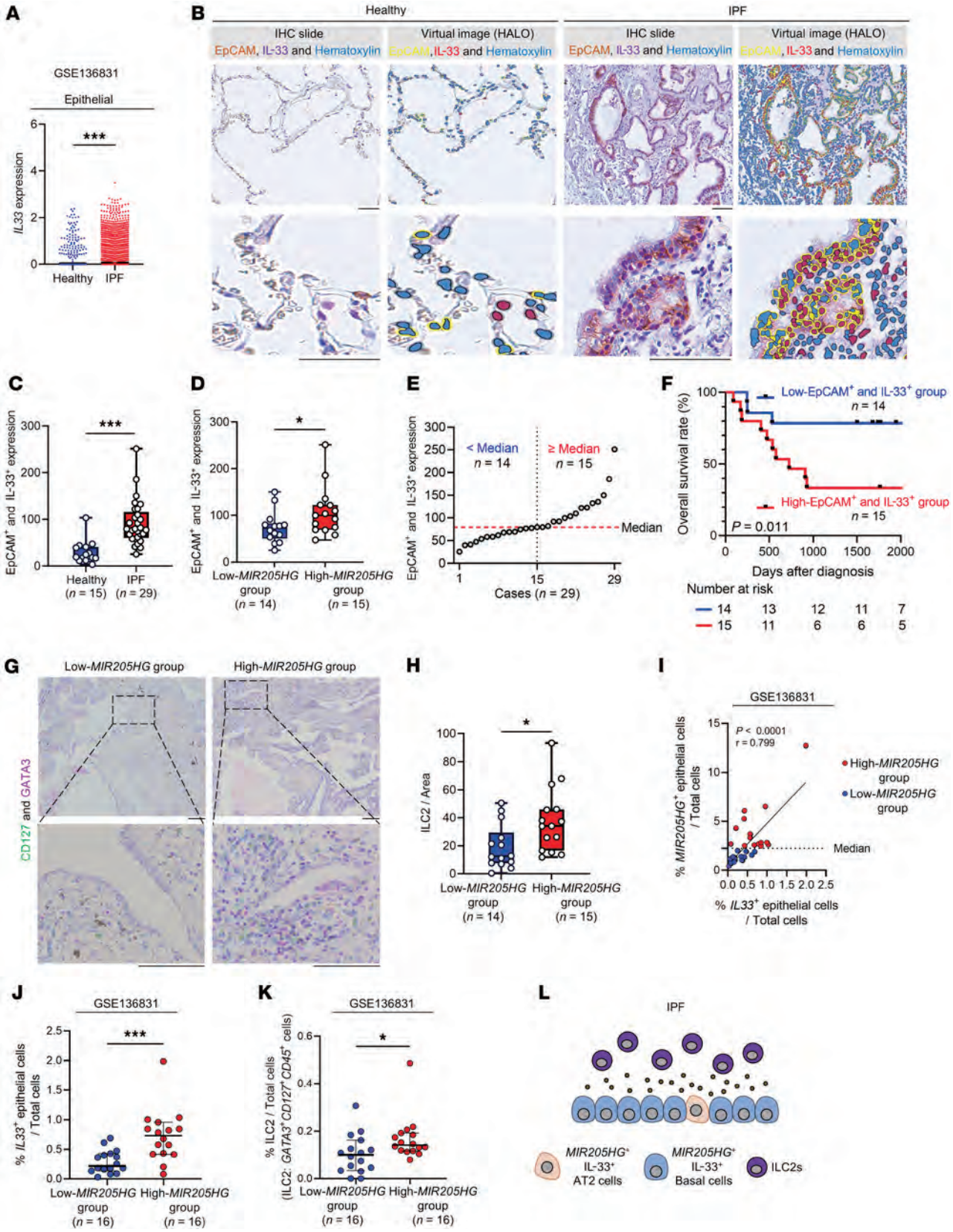

Figure 13. The high-*MIR205HG* group exhibits high IL-33 expression and increased number of ILC2s compared with the low-*MIR205HG* group in patients with IPF. (**A**) Plot of *IL33* expression for healthy lungs (n = 28) and patients with IPF (n = 32) in epithelial cell cluster. (**B**) Representative images of EpCAM IHC and IL-33 IHC staining in healthy lungs (n = 15) and patients with IPF (n = 29) in the cohort from Supplemental Figure 15A. Scale bar: 100 μm. (**C**) Plot of EpCAM$^+$ and IL-33$^+$ expression in **B**. (**D**) Plot of EpCAM$^+$ and IL-33$^+$ expression in high-*MIR205HG* group (n = 15) and low-*MIR205HG* group (n = 14). The 2 groups based on expression of *MIR205HG* in Figure 1I were used. (**E**) Plots of EpCAM$^+$ and IL-33$^+$ expression in patients with IPF (n = 29). The median was

used as the cutoff value of EpCAM$^+$ and IL-33$^+$ expression. (**F**) Kaplan-Meier curves for OS rate (%) in patients with IPF (n = 29) divided into high-EpCAM$^+$ and IL-33$^+$ group (n = 15) and low-EpCAM$^+$ and IL-33$^+$ group (n = 14). HR, 4.49; 95% CI, 1.57–12.86; P = 0.0011; P values determined by log-rank test. (**G**) Representative images of CD127 IHC and GATA3 IHC staining in high-*MIR205HG* group (n = 15) and low-*MIR205HG* group (n = 14). Scale bar: 100 μm. (**H**) Plot of number of ILC2s (CD127$^+$ and GATA3$^+$) in **G**. *P < 0.05; P values determined by 2-tailed Student's t test. (**I**) Correlation analysis of *MIR205HG*$^+$ and *IL33*$^+$ epithelial cells using patients with IPF (n = 32). Pearson's r = 0.799 and P < 0.0001; P values are 2 sided. (**J**) Plot of *IL33*$^+$ epithelial cells in high-*MIR205HG* group (n = 16) and low-*MIR205HG* group (n = 16). (**K**) Number of ILC2s (*CD127*$^+$*GATA3*$^+$*CD45*$^+$ cells) in high-*MIR205HG* group (n = 16) and low-*MIR205HG* group (n = 16). (**L**) Schematic illustration of the experimental results. (**A**, **C**, **D**, **J**, and **K**) *P < 0.05, ***P < 0.001; P values were determined by 2-tailed Mann-Whitney U test. (**J** and **K**) Bars represent the median and 95% CI. (**A** and **I**–**K**) Public scRNA-Seq data (GSE136831) were used for analysis.

The *AluJb* element of *MIR205HG* is present in both genomic DNA and the lncRNA itself. When *MIR205HG*-KD was carried out, we utilized the CRISPR/dCas9 system but not the CRISPR/Cas9 system. In this method, *MIR205HG*-coding genomic DNA remains, but transcription from the locus is abolished. Because the downregulation of *IL33* mRNA amount was detected in this knockdown, the *AluJb* element of *MIR205HG* lncRNA, but not of genomic DNA, was essential for *IL33* transcriptional regulation.

Analysis of the public HITS-CLIP data identified FUS as an RBP that binds to both *MIR205HG* and *IL33*. Knockdown of FUS downregulated the amounts of *MIR205HG* and *IL33* mRNA. However, FUS is also present in cells without *MIR205HG* and *IL33* mRNA, indicating that FUS itself does not transactivate *MIR205HG* and *IL33* mRNA. RBPs, including FUS, contribute to RNA stabilization (34–36). These findings suggest that FUS stabilizes *MIR205HG* and *IL33* mRNA. The *Alu* elements were located in the intron of the *IL33* gene but not in the exon. Therefore, *IL33* pre-mRNA possessed *Alu* elements, whereas *IL33* mRNA did not. The Hi-C analysis showed a close genomic distance between the *MIR205HG* and *IL33* loci. *IL33* pre-mRNA, immediately after transcription from the *IL33* locus, may interact with *MIR205HG* via *Alu* elements. As an RBP binding to both *MIR205HG* and *IL33*, FUS may provide a niche enabling interactions with both RNAs.

Finally, we attempted to find a small molecule that could reduce IL-33 expression by disrupting the interaction between *Alu* elements. ANP77, DQzG, and TO239 were selected as small molecules binding to the *AluJb* element through SPR experiments. Among the 3, DQzG exhibited the most inhibitory effect on IL-33 expression. In contrast, DNpG, a small molecule that does not bind to the *AluJb* element recognized by DQzG, did not inhibit *IL33* expression, suggesting that DQzG reduced *IL33* expression by inhibiting the interaction between *Alu* elements.

Methods

Sex as a biological variable. Sex was not considered as a biological variable.

Patient tissue samples. IPF tissues were obtained from 29 patients who underwent surgery or video-assisted thoracoscopic surgery at Osaka University Hospital between 2012 and 2017. Lung transplant tissues for IPF were obtained from 6 patients at Osaka University Hospital between 2012 and 2020. Pathologically, all IPF samples showed a usual interstitial pneumonia pattern with fibroblastic foci positive for Alcian blue staining (catalog 4085-2, Muto Pure Chemicals). Patients who were followed up for at least 5 years were included. The OS time of enrolled patients ranged from 3 to 103 months (median, 56 months). Normal lung tissues were obtained from 14 patients with normal background lungs undergoing tumor resection.

Antibodies. Details of the information concerning antibodies (clone, catalog, dilution, source) are summarized in Supplemental Table 1.

IHC staining. FFPE tissues and organoids were cut at a thickness of 4 μm, deparaffinized in xylene, dehydrated in 100% ethanol, and then rinsed in water. IHC staining was conducted using the Dako Autostainer Link 48 (Agilent Technologies), in accordance with the manufacturer's instructions. The slides were incubated with the indicated primary antibody for 1 hour, followed by the indicated secondary antibody for 1 hour. Details of the antibodies are described in Supplemental Table 1. Signals were detected by staining with DAB (catalog SK005, Agilent Technologies), Stayright Purple (catalog 45906, AAT Bioquest), Ventana DISCOVERY Purple Kit (catalog 760-229, Roche), or Ventana DISCOVERY Green Kit (catalog 760-271, Roche), followed by counterstaining with hematoxylin.

RNA ISH staining. FFPE tissue and organoid sections were cut at a thickness of 4 μm, then subjected to ISH staining using the RNAscope 2.5 HD Detection Reagents-BROWN Kit (catalog 322300, Advanced Cell Diagnostics), in accordance with the manufacturer's instructions. Detailed methods are described in the Supplemental Methods.

Scoring of IHC and ISH staining. Stained slides were scanned and imaged with the NanoZoomer 2.0-HT (Hamamatsu Photonics) at ×20 or ×40 original magnification. Whole-slide images were analyzed using

HALO v3.5 software (Indica Labs). The expression scores for *MIR205HG* ISH staining, IL-33 single IHC staining, EpCAM and IL-33 double IHC staining, and CD127 and GATA3 (ILC2s) double IHC staining were calculated by dividing the number of positive cells by the tissue area (mm^2).

Public data analysis of scRNA-Seq and bulk RNA-Seq. Public scRNA-Seq data were downloaded from GSE136831 (7) and GSE159354 (21) in the NCBI GEO public database. The datasets were reanalyzed and visualized using BioTuring Single Cell Browser (BBrowser) software. For cell–cell interaction analysis, we used the raw gene count data from GSE136831 and applied the statistical analysis method of CellPhoneDB v2.0 (58) with the CellPhoneDB-data v5.0 database to predict enriched receptor–ligand interactions. Bulk RNA-Seq datasets were downloaded from the GEO datasets GSE92592 (19) and GSE124685 (20); *MIR205HG* expression levels were compared between healthy controls and IPF patient samples.

Establishment of human lung organoids. Human lung organoids (alveolar organoids and IPF patient–derived airway organoids) were obtained from patients who underwent surgery at the Department of Thoracic Surgery at Osaka University Hospital. All organoids were established and maintained at 37°C in a 5% CO_2 atmosphere as previously described, with modifications (59). Clinical data for all organoids are summarized in Supplemental Table 3. Detailed methods are described in the Supplemental Methods. To isolate AT2 and basal cells, the cells were sorted using a FACSAria III (BD Biosciences). Isolated AT2 cells and basal cells were embedded in Matrigel (catalog 356231, Corning), seeded at 10,000 cells per well (48-well plate, catalog 677180, Greiner Bio-One), and cultured in 250 μL of lung organoid medium per well. The organoid media are summarized in Supplemental Table 4.

Generation of MIR205HG or pre–miR-205 overexpression in alveolar organoids. Lentiviral production of the following vectors was carried out according to the lentiviral production method, using the plasmids pLV[ncRNA]-EGFP-EF1A>{hMIR205HG[NC_000001.11]}_whole sequencing (catalog VB220908-1312ftg, Vector Builder), pLV-EGFP-EF1A>ORF_stuffer (referred to as "NV") (catalog VB900124-3812qdj, Vector Builder), and pre–*miR-205* (catalog VB230626-1545krg, Vector Builder). Single-cell pellets of alveolar organoid were prepared; the cells were suspended with 10 μL of lentiviral suspension and incubated for 10 minutes. Matrigel was then added to the tubes at a volume of 20 μL/well and spread onto a 48-well plate.

Generation of MIR205HG-KD NHBE cells and IPF patient–derived airway organoids using the CRISPR/dCas9 system. sgRNAs targeting human *MIR205HG* were designed using the CRISPR design website CRISPick (https://portals.broadinstitute.org/gppx/crispick/public). The following *MIR205HG*-targeting sequences were used in this study: sg*MIR205HG*_#1: 5′-GGACTCAGCCCATTTCAAGG-3′ and sg*MIR205HG*_#2: 5′-GCAAGTCAAGGGTGAGCAAGA-3′. sgRNAs were inserted into the BsmBI/Esp3I (catalog FD0454, Thermo Fisher Scientific) sites of the pLV hU6-sgRNA hUbC-dCas9-KRAB-T2a-Puro vector (catalog 71236, Addgene). Each vector plasmid was transformed into STBL3 (catalog C737303, Thermo Fisher Scientific) and spread on Luria-Bertani agar plates. After 20 hours of incubation, a single colony was selected and propagated in Luria-Bertani medium (catalog 20068-75, Nacalai Tesque) for 24 hours. The plasmid DNA was then purified using the NucleoBond Xtra Maxi EF kit (catalog 2403002M, Takara), in accordance with the manufacturer's recommendations. Knockdown of *MIR205HG* was verified by qRT-PCR.

Generation of FUS-KD NHBE cells and IPF patient–derived airway organoids using the shRNA system. The following 2 shRNA plasmids targeting the human *FUS* gene were provided by the Center for Medical Research and Education, Graduate School of Medicine, Osaka University: MISSION shRNA #1 (catalog TRCN0000001134, target sequence: CCGGGCCTGGGTGAGAATGTTACAACTCGAGTTGTAACATTCTCACCCAGGCTTTTT, Clone ID: NM_008599.4-276s21c1, referred to as "sh*FUS*_#1") and MISSION shRNA #2 (catalog TRCN0000001133, target sequence: CCGGCGTGGTGGCTTCAATAAATTTCTCGAGAAATTTATTGAAGCCACCACGTTTTT, Clone ID: NM_008599.4-276s21c1, referred to as "sh*FUS*_#2") (Merck). The nontarget shRNA control plasmid (referred to as "shCTR"), MISSION pLKO.1-puro (catalog SHC002, Merck), was used. Knockdown of *FUS* was verified by qRT-PCR.

Generation of plasmid cells with MIR205HG full-length or AluJb element deletion (ΔAluJb) in MIR205HG-KD NHBE cells. Lentiviral production of the following vectors was carried out according to the lentiviral production method described above, using the plasmids pLV[ncRNA]-EGFP-EF1A>{h-*MIR205HG*[NC_000001.11]}_whole sequencing (referred to as "Full length") (Vector Builder), pLV-EGFP-EF1A>ORF_stuffer (referred to as "Stuffer") (Vector Builder), and pLV[ncRNA]-EGFP-EF1A>{h*MIR205HG*[NC_000001.11]}*_AluJb* element deletion (−298 bp) (referred to as "*ΔAluJb*")

(catalog VB231012-1778ges, Vector Builder). *MIR205HG*-KD NHBE cells were infected with the above lentiviral vectors. Target sequences were confirmed by RT-PCR or qRT-PCR.

Analysis of RBP–RNA interaction. We queried the starBase v2.0 (32) database (RBP–Target, type = lncRNA, database = hg19) and found that the HITS-CLIP data for FUS (GSE43308) (33) support interactions between FUS and *MIR205HG*, as well as between FUS and *IL33*. The data were retrieved on June 12, 2023.

RIP. RIP assays were performed with 0.6 μg/μL anti-FUS and 0.6 μg/μL rabbit IgG whole molecule antibody (catalog 011-000-003, Jackson ImmunoResearch). Briefly, 2.0×10^7 cells were collected and lysed in ice-cold lysis buffer (1% NP-40, 20 mM Tris-HCl, 150 mM NaCl, and 1 mM EDTA) containing cOmplete Protease Inhibitor Cocktail (Roche) and PhosSTOP (Roche). The lysate was sonicated for 10 seconds and incubated for 30 minutes. The cell lysate was harvested by centrifugation at 10,000*g*, followed by incubation in reaction buffer (50 mM Tris-HCl pH 7.5, 5 M NaCl, and TBS-Tween) with the indicated antibodies and Dynabeads Protein G (catalog DB10003, Veritas) at 4°C overnight. The next day, the FUS–RNA complexes were washed 3 times with PBS. Proteins were denatured for Western blot. RNA was extracted and quantified by qRT-PCR. *ACTB* was used as an internal control.

ChIRP. ChIRP was performed as previously described (60). Approximately 2.0×10^7 cells were immediately cross-linked in 1% paraformaldehyde/PBS (catalog 09154-85, Nacalai Tesque) for 15 minutes at room temperature, and the cross-linking reaction was stopped by adding 1.5 M glycine (catalog 17109-35, Nacalai Tesque). The cross-linked cells were then washed twice with ice-cold PBS. After PBS removal, the cells were resuspended in 350 μL of lysis buffer (50 mM Tris-HCl pH 7.0, 10 mM EDTA, 1% SDS, 1 mM PMSF [catalog 10837091001, Roche], cOmplete Protease Inhibitor Cocktail from Roche, and RNAse inhibitor [catalog 10777019, Thermo Fisher Scientific]) and disrupted using a Bioruptor II Type 12 (Sonicbio) (30 seconds ON, 30 seconds OFF, 120 cycles). Subsequently, the insoluble fraction was removed by centrifugation at 10,000*g* for 10 minutes at 15°C, and the supernatant was used for ChIRP. Two volumes of hybridization buffer (750 mM NaCl, 1% SDS, 50 mM Tris-HCl pH 7.0, 1 mM EDTA, 15% v/v formamide, 1 mM PMSF, cOmplete Protease Inhibitor Cocktail, and RNAse inhibitor) and the 500 nM *MIR205HG* ChIRP probe (Supplemental Table 5) (LGC Biosearch Technologies) or 500 nM *LacZ* control probe (catalog 03-307, Merck) were added. The mixture was incubated at 37°C for 4 hours and then at 4°C overnight, mixed with Dynabeads MyOne Streptavidin C1 (catalog 65801D, Thermo Fisher Scientific), and incubated for 60 minutes. The beads were then washed 5 times for 5 minutes at 37°C with 0.8 mL of wash buffer (2× saline sodium citrate and 0.5% SDS). The bound proteins were eluted and reverse–cross-linked by boiling in SDS sample buffer (95°C for 30 minutes). The bound RNAs were eluted by protease K treatment (50°C for 45 minutes) followed by heating (95°C for 10 minutes). RNA was then extracted and analyzed by qRT-PCR. *ACTB* was used as an internal control.

Small molecule treatments for NHBE cells and IPF patient–derived airway organoids. NHBE cells and IPF patient–derived airway organoids were seeded with the indicated number of cells 2 days prior to small molecule treatment. ANP77, DQzG, TO239, and DNpG (in-house small molecules) were administered at concentrations of 3 μM and 5 μM. The control was a 0.05% DMSO solution. After small molecule treatment, cells were collected at the indicated time points, and samples were prepared for RNA and protein extraction.

RNA-Seq. Reverse transcription to cDNA was performed using the GenNext RamDA-Seq Single Cell Kit (catalog RMD-101, TOYOBO), and the library was prepared using the Nextera XT DNA Library Preparation Kit (catalog FC-131-1096, Illumina). Sequencing was performed on the NovaSeq 6000 platform in a 101+101 base paired-end mode (Illumina). Generated reads were mapped to the human (hg38) reference genome using HISAT2 ver.2.1.0 (https://github.com/DaehwanKimLab/hisat2; commit ID 7e01700). FPKMs were calculated using Cuffdiff 2.2.1 (http://cole-trapnell-lab.github.io/cufflinks/cuffdiff/).

Sequence similarity analysis between MIR205HG and IL33. Local sequence alignment was performed to evaluate sequence similarity. *MIR205HG* (hg38, chr1:209428819-209432848) and *IL33* (hg38, chr9:6215807-6257983) were used as the query and subject sequences, respectively, for sequence alignment using the discontinuous MegaBLAST program of the BLAST web (61) with default parameters.

Statistics. Statistical differences were evaluated using GraphPad Prism 9 and JMP Pro software version 16.0 (SAS Institute). OS rates were analyzed using a Kaplan-Meier curve, log-rank test, and multivariate analysis based on the Cox proportional hazards method using GraphPad Prism 9. Results are expressed as the mean ± SD of triplicate replicates. $P < 0.05$ were considered statistically significant.

Study approval. All experiments were approved by the Ethical Review Board of the Graduate School of Medicine, Osaka University (approval no. 15234), and were conducted in accordance with relevant

institutional guidelines and regulations. All animal experimental protocols were approved by the Animal Research Committee of Osaka University (approval no. 05-039-004). This study was performed in accordance with the ethical guidelines of the Declaration of Helsinki.

Data availability. Our original RNA-Seq data in this study are available at NCBI GEO under the accession numbers GSE275700 (alveolar organoids and IPF-derived airway organoids), GSE275709 (*MIR205HG*-KD NHBE cells), GSE275717 (*MIR205HG*-OE alveolar organoids), GSE275720 (HTII-280$^+$ cells and NGFR$^+$ cells) and GSE283175 (DQzG-treated NHBE cells and airway organoids from patients with IPF). Source data are provided with this paper. Previously published sequencing data that were reanalyzed are available under the accession numbers GSE136831 (7), GSE159354 (21), GSE92592 (19), GSE124685 (20), and GSE43308 (33). Raw data are also provided in the Supporting Data Values file for this study.

Author contributions

TT and E Morii designed the study. TT, CZ, DO, MH, and E Morii analyzed the public data. TT performed most of the in vitro experiments and IHC and ISH staining with assistance from CZ, E Murakami, NF, MK, and ZF. TT, HN, YS, and E Morii collected and analyzed the patient clinical data. HN collected the samples from healthy lungs and patients with IPF, and TT established organoids. TT, DO, and E Morii performed and analyzed the RNA-Seq. E Murakami, AS, YH, and KN performed and analyzed the SPR experiments. RI and GK performed and analyzed the NMR experiments. CZ, E Murakami, NF, MK, SN, TM, GK, MH, TH, and KN provided advice regarding experimental techniques and data interpretation. E Morii supervised the project. TT, CZ, E Murakami, NF, and E Morii wrote the initial draft and edited the paper. All the authors read and approved the final paper.

Acknowledgments

The authors appreciate Tomohiro Yamazaki for the CRISPR/dCas9 experiment and Kensuke Ninomiya and Tsuyoshi Ueno for the ChIRP experiment, experimental protocols, and technical support. We thank Kosuke Maeda for providing the scanFold prediction results. We acknowledge the next-generation sequencing core facility at the Research Institute for Microbial Diseases of Osaka University for the sequencing and data analysis. We thank Naoharu Shimada, Takako Sawamura, Megumi Nihei, and Etsuko Fujinami for assistance with prepared specimens and staining. We thank Hiroshi Yamazaki and Yuri Terao (Center for Medical Research and Education, Graduate School of Medicine, Osaka University) for the support of flow cytometric analysis and technical assistance. We thank Takayuki Funato and Toyofumi Kameoka (Nikon Imaging Center at Osaka University) and Yasuhiko Sato (Microscopy Expert, Product and Application Sales Specialist RMS, Carl Zeiss Co., Ltd) for technical support. We used the bioresearch sources of MISSION shRNA library in Center for Medical Research and Education, Graduate School of Medicine, Osaka University. This work was supported by Japan Agency for Medial Research and Development under Grant Number JP21ae0121049 and by Japan Society for the Promotion of Science KAKENHI Grant Numbers T23K273910 (to EM), T22KJ22010 (to TT), and 22K15093 (to CZ).

Address correspondence to: Eiichi Morii, Department of Pathology, Osaka University Graduate School of Medicine. 2-2 Yamada-Oka, Suita, Osaka 565-0871, Japan. Phone: 81.6.6879.3871; Email: morii@molpath.med.osaka-u.ac.jp.

1. Lederer DJ, Martinez FJ. Idiopathic pulmonary fibrosis. *N Engl J Med*. 2018;378(19):1811–1823.
2. Richeldi L, et al. Idiopathic pulmonary fibrosis. *Lancet*. 2017;389(10082):1941–1952.
3. Katzen J, Beers MF. Contributions of alveolar epithelial cell quality control to pulmonary fibrosis. *J Clin Invest*. 2020;130(10):5088–5099.
4. Richeldi L, et al. Efficacy and safety of nintedanib in idiopathic pulmonary fibrosis. *N Engl J Med*. 2014;370(22):2071–2082.
5. King TE, et al. A phase 3 trial of pirfenidone in patients with idiopathic pulmonary fibrosis. *N Engl J Med*. 2014;370(22):2083–2092.
6. Seibold MA, et al. The idiopathic pulmonary fibrosis honeycomb cyst contains a mucocilary pseudostratified epithelium. *PLoS One*. 2013;8(3):e58658.
7. Adams TS, et al. Single-cell RNA-seq reveals ectopic and aberrant lung-resident cell populations in idiopathic pulmonary fibrosis. *Sci Adv*. 2020;6(28):eaba1983.
8. Xu Y, et al. Single-cell RNA sequencing identifies diverse roles of epithelial cells in idiopathic pulmonary fibrosis. *JCI Insight*. 2016;1(20):e90558.

9. Habermann AC, et al. Single-cell RNA sequencing reveals profibrotic roles of distinct epithelial and mesenchymal lineages in pulmonary fibrosis. *Sci Adv*. 2020;6(28):eaba1972.
10. Prasse A, et al. BAL cell gene expression is indicative of outcome and airway basal cell involvement in idiopathic pulmonary fibrosis. *Am J Respir Crit Care Med*. 2019;199(5):622–630.
11. Jaeger B, et al. Airway basal cells show a dedifferentiated KRT17^{high}Phenotype and promote fibrosis in idiopathic pulmonary fibrosis. *Nat Commun*. 2022;13(1):5637.
12. Wang S, et al. Cloning a profibrotic stem cell variant in idiopathic pulmonary fibrosis. *Sci Transl Med*. 2023;15(693):eabp9528.
13. Fatica A, Bozzoni I. Long non-coding RNAs: new players in cell differentiation and development. *Nat Rev Genet*. 2014;15(1):7–21.
14. Vance KW, Ponting CP. Transcriptional regulatory functions of nuclear long noncoding RNAs. *Trends Genet*. 2014;30(8):348–355.
15. Pachera E, et al. Long noncoding RNA H19X is a key mediator of TGF-β-driven fibrosis. *J Clin Invest*. 2020;130(9):4888–4905.
16. Sakamoto K, et al. Decreased expression of FENDRR, a lung mesenchymal long non-coding RNA, regulates fibroblast phenotypes in IPF through NOX4. *Eur Respir J*. 2017;50(suppl 61):OA2909.
17. Savary G, et al. The long noncoding RNA DNM3OS is a reservoir of fibromiRs with major functions in lung fibroblast response to TGF-β and pulmonary fibrosis. *Am J Respir Crit Care Med*. 2019;200(2):184–198.
18. Huang C, et al. Long noncoding RNA FENDRR exhibits antifibrotic activity in pulmonary fibrosis. *Am J Respir Cell Mol Biol*. 2020;62(4):440–453.
19. Schafer MJ, et al. Cellular senescence mediates fibrotic pulmonary disease. *Nat Commun*. 2017;8:14532.
20. McDonough JE, et al. Transcriptional regulatory model of fibrosis progression in the human lung. *JCI Insight*. 2019;4(22):e131597.
21. DePianto DJ, et al. Molecular mapping of interstitial lung disease reveals a phenotypically distinct senescent basal epithelial cell population. *JCI Insight*. 2021;6(8):e143626.
22. Moro K, et al. Innate production of T(H)2 cytokines by adipose tissue-associated c-Kit(+)Sca-1(+) lymphoid cells. *Nature*. 2010;463(7280):540–544.
23. Neill DR, et al. Nuocytes represent a new innate effector leukocyte that mediates type-2 immunity. *Nature*. 2010;464(7293):1367–1370.
24. Stier MT, et al. IL-33 promotes the egress of group 2 innate lymphoid cells from the bone marrow. *J Exp Med*. 2018;215(1):263–281.
25. Ferrari E, Gandellini P. Unveiling the ups and downs of miR-205 in physiology and cancer: transcriptional and post-transcriptional mechanisms. *Cell Death Dis*. 2020;11(11):980.
26. Chen Y, Wang X. miRDB: an online database for prediction of functional microRNA targets. *Nucleic Acids Res*. 2020;48(d1):D127–D131.
27. Bandyopadhyay S, Mitra R. TargetMiner: microRNA target prediction with systematic identification of tissue-specific negative examples. *Bioinformatics*. 2009;25(20):2625–2631.
28. Lee S, et al. Noncoding RNA NORAD regulates genomic stability by sequestering PUMILIO proteins. *Cell*. 2016;164(1–2):69–80.
29. Hentze MW, et al. A brave new world of RNA-binding proteins. *Nat Rev Mol Cell Biol*. 2018;19(5):327–341.
30. Statello L, et al. Gene regulation by long non-coding RNAs and its biological functions. *Nat Rev Mol Cell Biol*. 2021;22(2):96–118.
31. Li Z, et al. The long noncoding RNA THRIL regulates TNFα expression through its interaction with hnRNPL. *Proc Natl Acad Sci U S A*. 2014;111(3):1002–1007.
32. Li JH, et al. starBase v2.0: decoding miRNA-ceRNA, miRNA-ncRNA and protein-RNA interaction networks from large-scale CLIP-Seq data. *Nucleic Acids Res*. 2014;42(database issue):D92–D97.
33. Nakaya T, et al. FUS regulates genes coding for RNA-binding proteins in neurons by binding to their highly conserved introns. *RNA*. 2013;19(4):498–509.
34. Kapeli K, et al. Distinct and shared functions of ALS-associated proteins TDP-43, FUS and TAF15 revealed by multisystem analyses. *Nat Commun*. 2016;7:12143.
35. Udagawa T, et al. FUS regulates AMPA receptor function and FTLD/ALS-associated behaviour via GluA1 mRNA stabilization. *Nat Commun*. 2015;6:7098.
36. Loughlin FE, et al. The solution structure of FUS bound to RNA reveals a bipartite mode of RNA recognition with both sequence and shape specificity. *Mol Cell*. 2019;73(3):490–504.
37. Profumo V, et al. LEADeR role of miR-205 host gene as long noncoding RNA in prostate basal cell differentiation. *Nat Commun*. 2019;10(1):307.
38. Liang L, et al. Complementary Alu sequences mediate enhancer-promoter selectivity. *Nature*. 2023;619(7971):868–875.
39. Holdt LM, et al. Alu elements in ANRIL non-coding RNA at chromosome 9p21 modulate atherogenic cell functions through trans-regulation of gene networks. *PLoS Genet*. 2013;9(7):e1003588.
40. Hamada M, et al. Prediction of RNA secondary structure using generalized centroid estimators. *Bioinformatics*. 2009;25(4):465–473.
41. Das B, et al. A small-molecule fluorescence probe ANP77 for sensing RNA internal loop of C, U and A/CC motifs and their binding molecules. *Nucleic Acids Res*. 2021;49(15):8462–8470.
42. Murakami E, et al. Kinetics of photon upconversion by triplet-triplet annihilation: a comprehensive tutorial. *Phys Chem Chem Phys*. 2024;23(34):18268–18282.
43. Byers DE, et al. Long-term IL-33-producing epithelial progenitor cells in chronic obstructive lung disease. *J Clin Invest*. 2013;123(9):3967–3982.
44. Katz-Kiriakos E, et al. Epithelial IL-33 appropriates exosome trafficking for secretion in chronic airway disease. *JCI Insight*. 2021;6(4):e136166136166.
45. John AE, et al. Loss of epithelial Gq and G11 signaling inhibits TGFβ production but promotes IL-33-mediated macrophage polarization and emphysema. *Sci Signal*. 2013;9(451):ra104.
46. Strickson S, et al. Oxidised IL-33 drives COPD epithelial pathogenesis via ST2-independent RAGE/EGFR signalling complex. *Eur Respir J*. 2023;62(3):2202210.
47. Otaki N, et al. Activation of ILC2s through constitutive IFNγ signaling reduction leads to spontaneous pulmonary fibrosis. *Nat Commun*. 2023;14(1):8120.

48. Borzone G, et al. Bleomycin-induced chronic lung damage does not resemble human idiopathic pulmonary fibrosis. *Am J Respir Crit Care Med*. 2001;163(7):1648–1653.
49. Redente EF, et al. Tumor necrosis factor-α accelerates the resolution of established pulmonary fibrosis in mice by targeting pro-fibrotic lung macrophages. *Am J Respir Cell Mol Biol*. 2014;50(4):825–837.
50. Enomoto Y, et al. Autocrine TGF-β-positive feedback in profibrotic AT2-lineage cells plays a crucial role in non-inflammatory lung fibrogenesis. *Nat Commun*. 2023;14(1):4956.
51. Kobayashi Y, et al. Persistence of a regeneration-associated, transitional alveolar epithelial cell state in pulmonary fibrosis. *Nat Cell Biol*. 2020;22(8):934–946.
52. Mayr CH, et al. Integrative analysis of cell state changes in lung fibrosis with peripheral protein biomarkers. *EMBO Mol Med*. 2021;13(4):e12871.
53. Kathiriya JJ, et al. Human alveolar type 2 epithelium transdifferentiates into metaplastic KRT5^{+} basal cells. *Nat Cell Biol*. 2022;24(1):10–23.
54. Kadur Lakshminarasimha Murthy P, et al. Human distal lung maps and lineage hierarchies reveal a bipotent progenitor. *Nature*. 2022;604(7904):111–119.
55. Liew FY, et al. Interleukin-33 in health and disease. *Nat Rev Immunol*. 2016;16(11):676–689.
56. Kearley J, et al. Cigarette smoke silences innate lymphoid cell function and facilitates an exacerbated type I interleukin-33-dependent response to infection. *Immunity*. 2015;42(3):566–579.
57. Hardman CS, et al. IL-33 citrine reporter mice reveal the temporal and spatial expression of IL-33 during allergic lung inflammation. *Eur J Immunol*. 2013;43(2):488–498.
58. Efremova M, et al. CellPhoneDB: inferring cell-cell communication from combined expression of multi-subunit ligand-receptor complexes. *Nat Protoc*. 2020;15(4):1484–1506.
59. Ebisudani T, et al. Direct derivation of human alveolospheres for SARS-CoV-2 infection modeling and drug screening. *Cell Rep*. 2021;35(10):109218.
60. Chu C, et al. Genomic maps of long noncoding RNA occupancy reveal principles of RNA-chromatin interactions. *Mol Cell*. 2011;44(4):667–678.
61. Zhang Z, et al. A greedy algorithm for aligning DNA sequences. *J Comput Biol*. 2000;7(1–2):203–214.

日中笹川医学奨学金制度<学位取得コース>中間評価書
【課程博士:指導教官用】

第45期　　研究者番号:　G4508

氏名	李 英豪	LI YINGHAO	性別	M	生年月日	1996/9/7
中国所属機関(役職)	佛山市中医院骨傷八科(医師)					
日本研究先(指導教官)	奈良県立医科大学整形外科学教室(田中　康仁　教授)					
研究テーマ	足疾患に対する病因究明ならびに外科治療効果判定のための形態学的な研究					
専攻種別	論文博士	□	課程博士	☑		

研究者評価(指導教官記入欄)

成績状況	優・良・可・不可から選択してください⇒	優	取得単位数	33
	学業成績係数=		取得すべき単位総数	34
学生本人が行った研究の概要	外反母趾の手術治療である第1足根中足関節固定術をもちいたLapidus法についての研究をしています。手術前後の足部立位単純X線と患者立脚評価型の臨床スコアから治療成績の予後不良因子を検討する研究内容です。また成績良好例と不良例を分けて、当教室で開発したMapping法を用いてX線像の解析を行うと、両者で明らかに違う特徴を発見いたしました。			
総合評価	【良かった点】 第1足根中足関節の固定肢位が成績に関係するのではないかという研究の仮説に基づき、適切に情報収集が出来ました。			
	【改善すべき点】 収集した情報から得られた内容を今後一流英文雑誌への投稿にむけて、考察していく必要があります。			
	【今後の展望】 研究を進めていく過程において、問題点はなく、計画通りに進んでいます。来年1年間で成果をまとめることが出来る見込みです。			
学位取得見込	日本での生活にも慣れてきて、研究の振興の程度も順調です。学位を取得できる見込みは極めて高いと評価します。			
評価者(指導教官記名)	田中康仁/黒川紘章	作成日:	2025年　3　月　4　日	

日中笹川医学奨学金制度<学位取得コース>中間報告書
【研究者用】

Supported by 日本財団 THE NIPPON FOUNDATION

第45期　　研究者番号：G4508　　作成日：2025年3月10日

氏名	李 英豪	LI YINGHAO	性別	M	生年月日	1996/9/7
中国所属機関(役職)	佛山市中医院骨傷八科（医師）					
日本研究先（指導教官）	奈良県立医科大学整形外科学教室（田中　康仁　教授）					
研究テーマ(日文)	足疾患に対する病因究明ならびに外科治療効果判定のための形態学的な研究					
Research theme	Morphological studies for investigating the etiology of foot diseases and evaluating the effectiveness of surgical treatment					
専攻種別	論文博士	☐	課程博士	☑		

1．研究概要（1）

1）目的（Goal）

Hallux valgus (HV) is a prevalent forefoot deformity with a global incidence of 19%.[1-6] The deformity of hallux valgus is progressive, and involves several stages, but begins with lateral deviation of the great toe (hallux) and medial deviation of the first metatarsal (metatarsus primus varus)[1]. To date, based on severity with respect to radiographic parameters, more than 140 surgical procedures have been described in the literature to correct hallux valgus[1, 2, 6].

The Lapidus procedure corrects hallux valgus and its associated first TMT joint hypermobility by fusing the first metatarso-cuneiform joint [7,8]. It has good long-term outcomes and a low recurrence rate [9]. However, the relationship between medial arch collapse and hallux valgus recurrence remains unclear. In the Lapidus procedure, the sagittal plane angle of the first metatarso-cuneiform joint fusion and its impact on the medial arch are still not well understood [10, 11, 12]. It also remains unclear whether medial arch lowering is associated with postoperative recurrence after Lapidus procedure. Here, We hypothesize that the two-dimensional coordinate system of AP view and Lateral view will indicate the lowering of the medial longitudinal arch of the foot is associated with the recurrence of hallux valgus after Lapidus procedure. The assessment is conducted through radiographic analysis using a two-dimensional coordinate system[13, 14].

2）戦略（Approach）

We divided the patients into two groups based on whether hallux valgus recurred two years after surgery: the recurrence group and the non-recurrence group. To further minimize errors, we defined the recurrence group as patients with an HVA angle of ≥20° at two years postoperatively and the non-recurrence group as those with an HVA angle of <15° at two years postoperatively. Additionally, we measured the datas of weight-bearing anteroposterior and lateral radiographs for both groups.

3）材料と方法（Materials and methods）

From January 1, 2014, to December 31, 2021, a total of 88 patients (95 feet) were included in this study, consisting of 13 males and 75 females. After excluding patients with no 2-year postoperative data and those with a postoperative HVA between 15° and 20° , the final study cohort included 28 patients (35 feet), comprising 3 males and 25 females. The study has been approved by the Ethics Committee of Nara Medical University Hospital (Approval No. 3799).

The angles and 2-dimensional coordinate measurements were conducted in accordance with the method conducted by Professor Tanaka.

4）実験結果（Results）

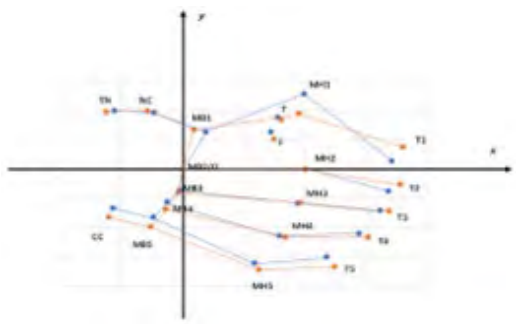

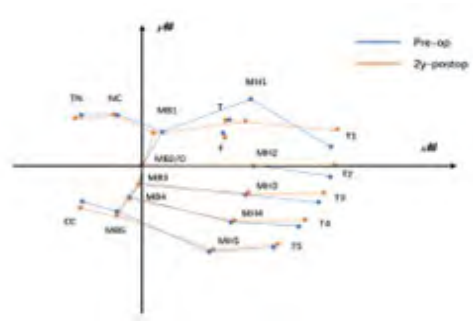

（Recurrence Group, AP 2-dimensional mapping）（Control Group, AP 2-dimensional mapping）

1．研究概要(2)

5)考察(Discussion)

From the AP view X-ray coordinate system shown in the figure, we can observe that the lateral points in the recurrence group, including CC, MB5, MH5, and T5, are all shifted laterally. This suggests a lowering of the medial arch, which in turn may lead to an elevation of the lateral part of the foot.

However, this is only our preliminary hypothesis, and further lateral view data and angular measurements will be required to verify this hypothesis in subsequent analyses.

6)参考文献(References)

[1] HECHT P J, LIN T J. Hallux valgus[J]. Med Clin North Am, 2014,98(2): 227-232.
[2] MANN R A, COUGHLIN M J. Hallux valgus--etiology, anatomy, treatment and surgical considerations[J]. Clin Orthop Relat Res, 1981(157): 31-41.
[3] TABLANTE A, KUROKAWA H, UENO Y, et al. Second metatarsophalangeal joint dislocation in hallux valgus: a radiographic study using a two-dimensional coordinate system[J]. BMC Musculoskelet Disord, 2025,26(1): 204.
[4] NIX S, SMITH M, VICENZINO B. Prevalence of hallux valgus in the general population: a systematic review and meta-analysis[J]. J Foot Ankle Res, 2010,3: 21.
[5] CAI Y, SONG Y, HE M, et al. Global prevalence and incidence of hallux valgus: a systematic review and meta-analysis[J]. J Foot Ankle Res, 2023,16(1): 63.
[6] RAIKIN S M, MILLER A G, DANIEL J. Recurrence of hallux valgus: a review[J]. Foot Ankle Clin, 2014,19(2): 259-274.
[7] DUJELA M D, LANGAN T, COTTOM J M, et al. Lapidus Arthrodesis[J]. Clin Podiatr Med Surg, 2022,39(2): 187-206.
[8] 秋山唯, 仁木久照. 外側趾症状,外側趾MTP関節脱臼を伴う重度外反母趾に対する前足部再建手術：中足骨近位短縮骨切り組み合わせ手術[CMOS:Lapidus変法+第2-4中足骨近位短縮骨切り術(+Coughlin変法)][J]. 整形外科surgical technique：手術が見える・わかる専門誌, 2017,7(6): 659-667.
[9] KOPP F J, PATEL M M, LEVINE D S, et al. The modified Lapidus procedure for hallux valgus: a clinical and radiographic analysis[J]. Foot Ankle Int, 2005,26(11): 913-917.
[10] CONTI M S, CAOLO K C, ELLIS S J, et al. Radiographic and Clinical Outcomes of Hallux Valgus and Metatarsus Adductus Treated With a Modified Lapidus Procedure[J]. Foot Ankle Int, 2021,42(1): 38-45.
[11] CONTI M S, PATEL T J, ZHU J, et al. Association of First Metatarsal Pronation Correction With Patient-Reported Outcomes and Recurrence Rates in Hallux Valgus[J]. Foot Ankle Int, 2022,43(3): 309-320.
[12] KIM J, EL M S, SRIKUMAR S, et al. Association Between Postoperative Medial-Middle Intercuneiform Joint Widening and Recurrence Rates in Hallux Valgus Treated With Modified Lapidus Procedure[J]. Foot Ankle Int, 2024,45(12): 1349-1358.
[13] KOMEDA T, TANAKA Y, TAKAKURA Y, et al. Evaluation of the longitudinal arch of the foot with hallux valgus using a newly developed two-dimensional coordinate system[J]. J Orthop Sci, 2001,6(2): 110-118.
[14] TANAKA Y, TAKAKURA Y, KUMAI T, et al. Radiographic analysis of hallux valgus. A two-dimensional coordinate system[J]. J Bone Joint Surg Am, 1995,77(2): 205-213.

2. 執筆論文 Publication of thesis ※記載した論文を添付してください。Attach all of the papers listed below.

論文名 1 Title	Talonavicular-cuneiform arthrodesis for the treatment of Müller-Weiss: mid-term results of 15 cases after 5 years				
掲載誌名 Published journal	BMC Musculoskeletal disorders				
	2023 年 3 月	24 巻(号)	頁 ～ 頁	言語 Language	English
第1著者名 First author	Wenbo Bai	第2著者名 Second author	Yinghao Li	第3著者名 Third author	Guodong Shen
その他著者名 Other authors	Hongning Zhang, Xue Li, Yongzhan Zhu				
論文名 2 Title	Glucose microenvironment sensitive degradation of arginine modified calcium sulfate reinforced poly(lactide- co-glycolide) composite scaffolds				
掲載誌名 Published journal	Journal of Materials Chemistry B				
	2023 年 12 月	12(2) 巻(号)	508 頁 ～ 524 頁	言語 Language	English
第1著者名 First author	Yongzhan Zhu	第2著者名 Second author	Yinghao Li	第3著者名 Third author	Xiaosong Zhou
その他著者名 Other authors	Haoxuan Li, Min Guo, Peibiao Zhang				
論文名 3 Title	Medial opening low tibial osteotomy shifts the load laterally not only at the ankle joint but also at the knee joint				
掲載誌名 Published journal	Journal of Experimental Orthopaedics				
	2024 年 12 月	11(4) 巻(号)	頁 ～ 頁	言語 Language	English
第1著者名 First author	Yoshihiro Wanezaki	第2著者名 Second author	Hiroaki Kurokawa	第3著者名 Third author	Yuki Ueno
その他著者名 Other authors	Adrian Tablante, Nan Mei, Li Yinghao, Akira Taniguchi, Akemi Suzuki, Yuya Takakubo, Michiaki Takagi, Yasuhito Tanaka				
論文名 4 Title	Second metatarsophalangeal joint dislocation in hallux valgus: a radiographic study using a two-dimensional coordinate system.				
掲載誌名 Published journal	BMC Musculoskeletal disorders				
	2025 年 2 月	1 巻(号)	204 頁 ～ 頁	言語 Language	English
第1著者名 First author	drian Joseph Castor Tablan	第2著者名 Second author	Hiroaki Kurokawa	第3著者名 Third author	Yuki Ueno
その他著者名 Other authors	Yoshihiro Wanezaki, Nan Mei, Yinghao Li, Akira Taniguchi, Emiliano Baula Tablante, Yasuhito Tanaka				
論文名 5 Title					
掲載誌名 Published journal					
	年 月	巻(号)	頁 ～ 頁	言語 Language	
第1著者名 First author		第2著者名 Second author		第3著者名 Third author	
その他著者名 Other authors					

3. 学会発表　Conference presentation　※筆頭演者として総会・国際学会を含む主な学会で発表したものを記載してください。

※Describe your presentation as the principal presenter in major academic meetings including general meetings or international meetings.

学会名 Conference	–					
演　題 Topic	–					
開催日 date	年　　月　　日		開催地 venue			
形式　method	□　口頭発表　Oral	□　ポスター発表　Poster	言語　Language	□　日本語	□　英語	□　中国語
共同演者名 Co-presenter						
学会名 Conference	–					
演　題 Topic	–					
開催日 date	年　　月　　日		開催地 venue			
形式　method	□　口頭発表　Oral	□　ポスター発表　Poster	言語　Language	□　日本語	□　英語	□　中国語
共同演者名 Co-presenter						
学会名 Conference	–					
演　題 Topic	–					
開催日 date	年　　月　　日		開催地 venue			
形式　method	□　口頭発表　Oral	□　ポスター発表　Poster	言語　Language	□　日本語	□　英語	□　中国語
共同演者名 Co-presenter						
学会名 Conference	–					
演　題 Topic	–					
開催日 date	年　　月　　日		開催地 venue			
形式　method	□　口頭発表　Oral	□　ポスター発表　Poster	言語　Language	□　日本語	□　英語	□　中国語
共同演者名 Co-presenter						

4. 受賞（研究業績）　Award (Research achievement)

名　称 Award name				
	国名 Country		受賞年 Year of award	年　　月
名　称 Award name				
	国名 Country		受賞年 Year of award	年　　月

5. 本研究テーマに関わる他の研究助成金受給 Other research grants concerned with your resarch theme

受給実績 Receipt record	☐ 有　　☐ 無
助成機関名称 Funding agency	
助成金名称 Grant name	
受給期間 Supported period	年　　月 ～　　年　　月
受給額 Amount received	円
受給実績 Receipt record	☐ 有　　☐ 無
助成機関名称 Funding agency	
助成金名称 Grant name	
受給期間 Supported period	年　　月 ～　　年　　月
受給額 Amount received	円

6. 他の奨学金受給 Another awarded scholarship

受給実績 Receipt record	☐ 有　　☐ 無
助成機関名称 Funding agency	
奨学金名称 Scholarship name	
受給期間 Supported period	年　　月 ～　　年　　月
受給額 Amount received	円

7. 研究活動に関する報道発表 Press release concerned with your research activities

※記載した記事を添付してください。Attach a copy of the article described below

報道発表 Press release	☐ 有　　☐ 無	発表年月日 Date of release	
発表機関 Released medium			
発表形式 Release method	・新聞　・雑誌　・Web site　・記者発表　・その他（　　）		
発表タイトル Released title			

8. 本研究テーマに関する特許出願予定 Patent application concerned with your research theme

出願予定 Scheduled application	☐ 有　　☐ 無	出願国 Application	
出願内容（概要） Application contents			

9. その他 Others

指導責任者（記名） 田中康仁

Received: 19 March 2024 | Accepted: 25 July 2024

DOI: 10.1002/jeo2.70029

ORIGINAL PAPER

Journal of Experimental Orthopaedics WILEY

Medial opening low tibial osteotomy shifts the load laterally not only at the ankle joint but also at the knee joint

Yoshihiro Wanezaki[1,2] | Hiroaki Kurokawa[1] | Yuki Ueno[1] | Adrian Tablante[1] | Nan Mei[1] | Li Yinghao[1] | Akira Taniguchi[1] | Akemi Suzuki[2] | Yuya Takakubo[2] | Michiaki Takagi[2] | Yasuhito Tanaka[1]

[1]Department of Orthopedic Surgery, Nara Medical University, Kashihara city, Nara, Japan

[2]Department of Orthopedic Surgery, Faculty of Medicine, Yamagata University, Yamagata, Japan

Correspondence

Yoshihiro Wanezaki, Department of Orthopedic Surgery, Nara Medicine University, 840, Shijyo-cho, Kashihara-city, Nara 634-8521, Japan.
Email: wane3775@yahoo.co.jp

Funding information

This study did not receive any specific grants from funding agencies in the public, commercial, or non-profit sectors

Abstract

Purpose: The purpose of this study was to determine the effects of medial opening low tibial osteotomy (LTO) on lower limb alignment, including the knee joint, 1 year after low tibial osteotomy.

Methods: This study included 20 legs of 20 patients (mean age, 66.8 ± 5.4 years) who underwent LTO for medial ankle osteoarthritis and evaluated the changes in the hip–knee–ankle angle (HKA), percentage hip-to-ankle line (%HA), percentage hip-to-calcaneal line (%HC), medial proximal tibial angle (MPTA), knee joint line convergence angle (K-JLCA), tibio-calcaneal angle (TCA), tibial anterior surface angle (TAS), tibio-plafond inclination (TPI), talar inclination (TI), ankle joint line convergence angle (A-JLCA), mechanical ankle joint axis point (MAJAP) on radiographs and the Japanese Society for Surgery of the Foot (JSSF) ankle/hindfoot scale before and 1 year after low tibial osteotomy.

Results: The mean preoperative/postoperative measured values showed the following: HKA (degrees) of 1.0 ± 3.7/−0.8 ± 3.7; %HC of 38.8 ± 10.0/53.8 ± 16.1; MPTA (degrees) of 85.6 ± 2.4/87.6 ± 2.1; and A-JLCA (degrees) of 4.2 ± 2.9/1.1 ± 2.3 respectively. Including other measurements, a significant increase in the %HA, %HC, MPTA, TCA, TAS, MAJAP and JSSF ankle/hindfoot scale was observed postoperatively, whereas a significant decrease in the HKA, TPA, TI and A-JLCA was observed postoperatively ($p < 0.05$). With the numbers available, no significant differences were observed between the preoperative and postoperative values of K-JLCA (n.s.).

Conclusion: After LTO, the entire lower limb alignment became valgus, and the loading points of the knee and ankle joints shifted laterally. These

Abbreviations: A-JLCA, ankle joint line convergence angle; HKA, hip–knee–ankle angle; HTO, high tibial osteotomy; ICC, intraclass correlation coefficients; JSSF, Japanese Society for Surgery of the Foot; K-JLCA, knee joint line convergence angle; LTO, low tibial osteotomy; MAJAP, mechanical ankle joint axis point; MPTA, medial proximal tibial angle; OA, osteoarthritis; TAS, tibial anterior surface angle; TCA, tibio-calcaneal angle; TI, talar inclination; TKA, total knee arthroplasty; TPI, tibio-plafond inclination; TT, talar tilt; %HA, percentage hip-to-ankle line; %HC, percentage hip-to-calcaneal line.

Hiroaki Kurokawa, Yuki Ueno, Adrian Tablante, Nan Mei, Li Yinghao, Akira Taniguchi, Akemi Suzuki, Yuya Takakubo, Michiaki Takagi and Yasuhito Tanaka are co-authors of this study.

changes must be considered when performing LTO, especially in patients with lateral knee OA.

Level of Evidence: IV

KEYWORDS
ankle osteoarthritis, knee alignment, low tibial osteotomy, lower limb alignment

INTRODUCTION

Approximately 6% of the population is affected by ankle osteoarthritis (OA) [6]. Ankle OA caused by trauma is more prevalent in Western countries. In contrast, primary ankle OA with no identifiable cause is more prevalent in Japan, which may be attributed to the tibial anterior surface angle (TAS) of patients in Japan being more varus than that in the patients in Western countries [25]. Evidence supporting the efficacy of conservative treatment for ankle OA, as well as the treatment options, remain limited [7, 29]. Surgical treatment strategies for ankle OA include osteotomy, ankle arthroplasty, and ankle arthrodesis. Osteotomy and ankle arthroplasty facilitate the preservation of joint motion; however, patient activity limits the indications for arthroplasty [20]. Medial opening low tibial osteotomy (LTO) is one of the osteotomies best indicated for malalignment corresponding to Takakura–Tanaka classification stage 3a with significant cartilage wear on the medial side only. As the number of active older adults increases in recent years with the ageing of society, the importance of osteotomy, similar to LTO, may increase owing to its ability to preserve joint motion [21, 24].

Knee OA, one of the most prevalent joint diseases in Japan, affects 35.2%, 48.2% and 51.6% of patients in their 60s, 70s and 80s in Japan, respectively [15, 30]. Previous studies have reported an association between knee OA and ankle OA [14, 18]. Total knee arthroplasty (TKA) and high tibial osteotomy (HTO) result in changes in ankle and hindfoot alignment in patients with knee OA postoperatively, impacting ankle and hindfoot symptoms [10, 24]. Therefore, a different preoperative plan, which considers the postoperative changes in the ankle and hindfoot alignment, must be formulated for patients undergoing HTO or TKA complicated ankle joint symptoms [1, 3].

It is important to understand the effects of LTO on the knee joints. However, no study has comprehensively examined the effect of LTO on lower limb alignment, including the knee joint. Therefore, this study aimed to determine the effect of LTO on lower limb alignment, including the knee joint. Our hypothesis is that LTO not only causes changes in the ankle joint alignment and loading point but also in the knee joint alignment and loading point.

MATERIAL AND METHODS

Patients who had undergone primary LTO for ankle OA at our hospital between 2008 and 2022 were included in this retrospective study. After excluding patients with neurological diseases, rheumatoid arthritis, congenital diseases, history of undergoing lower limb surgery, missing radiographs and other cases deemed unsuitable by the physician in charge, 20 legs of 20 patients (mean age at the time of surgery, 66.8 ± 5.4 years; mean body mass index, 24.4 ± 3.6 kg/m^2) (Figure 1) were included. The study cohort comprised four male and 16 female participants. The Takakura–Tanaka classification [24] stages were 3a and 3b in 18 and two legs, respectively.

Surgical technique

Weightbearing ankle radiographs were used for preoperative planning. Tibial osteotomy was performed 4–5 cm proximal to the inferior end of the medial malleolus. The target TAS was set as 96–98 degrees after correction via open wedge osteotomy. The surgery was performed with the patient in the supine position. The level of the tibial osteotomy was determined using the radiographs. The osteotomy level of the fibula was slightly proximal to that of the tibia. The fibula was osteotomized obliquely from the proximal posterior region to the distal anterior region. A Kirschner wire was inserted from the tip of the fibula and fixed similar to an intramedullary nail. Tibial osteotomy was performed vertically to the tibial axis, and the tibia was

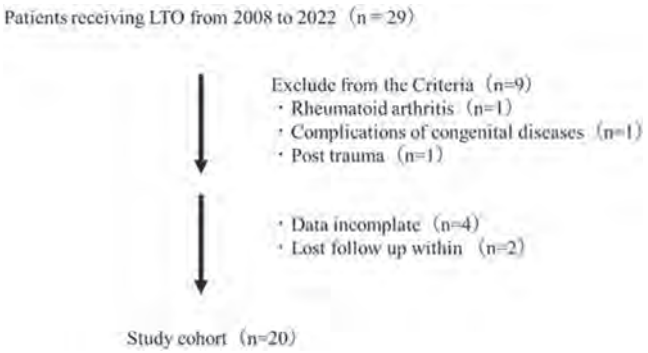

FIGURE 1 Flowchart of patients excluded from the analysis.

opened in accordance with the preoperative plan. A wedge-shaped artificial bone was implanted into the osteotomy site and fixed with a locking plate. A below-knee cast was used for 4–6 weeks postoperatively, followed by an ankle joint supporter for 8–12 weeks. Weightbearing was commenced gradually from the fourth postoperative week depending upon the pain, with the goal of achieving a full weightbearing gait at 6 weeks postoperatively. The Kirschner wire inserted into the fibula was removed 3–4 weeks postoperatively [21, 24].

Radiographic technique and measurement parameters

Radiographic examinations were performed before and 1 year after LTO surgery. Whole-leg and weightbearing subtalar radiographs were acquired for all patients. Weightbearing subtalar radiographs were acquired as described in previous reports [2, 5].

The following parameters were measured: (1) Hip–knee–ankle angle (HKA), defined as the angle between the mechanical axes of the femur (centre of the femoral head to femoral intercondylar point) and tibia (tibial interspinous point to tibial mid-plafond point) [14] (positive for varus). (2) Percentage hip-to-ankle line (%HA), defined as the ratio of the distance between the point where the hip-to-ankle line passes and the medial edge of the tibia to the width of the tibial plateau [23]. (3) Percentage hip-to-calcaneal line (%HC), defined as the ratio of the distance between the point where the hip-to-calcaneal line passes and the medial edge of the tibia to the width of the tibial plateau [8]. (4) Medial proximal tibial angle (MPTA), defined as the angle between the mechanical axis and the proximal articular surface of the tibia [19]. (5) Knee joint line convergence angle (K-JLCA), defined as the angle between the distal femoral and proximal tibial joint surfaces (positive for lateral opening). (6) Tibio-calcaneal angle (TCA), defined as the angle between the tibial and calcaneal axes. The tibial axis was defined as the line between the midpoints of the tibial shaft 8 and 13 cm above the tip of the medial malleolus. The calcaneal axis was defined by two points. The first point was 7 mm proximal to the most distal part of the calcaneus on the horizontal line, which divided the bone at a 40:60 ratio, with the 40% segment beginning on the lateral side. The second point was at the middle of the horizontal line, 30 mm proximal to the most distal part of the calcaneus [27] (positive for valgus). (7) TAS, defined as the angle between the lines drawn on the axis of the distal one-third of the tibia and the plafond [25]. (8) Tibio-plafond inclination (TPI), defined as the angle between the tibial plafond and the ground (positive for lateral inclination). (9) Talar inclination (TI), defined as the angle between the talar joint surface and the ground (positive for lateral inclination). (10) Ankle joint line convergence angle (A-JLCA), defined as the angle between the tibial plafond and the talar joint surface [3, 22]. (11) Mechanical ankle joint axis point (MAJAP), defined as the percentage of the intersection of the tibial plafond with the line connecting the centre of the femoral head to the lowest point of the calcaneus to the entire tibial plafond [4] (Figure 2).

All image analyses were performed using SYNAPSE version 5 (FUJIFILM Medical System, Inc.). The Japanese Society for Surgery of the Foot (JSSF) ankle-hindfoot scale was used for subjective evaluation preoperatively and 1 year postoperatively. This scale comprises three categories: pain (40 points), function (50 points) and alignment (10 points): total, 100 points [16, 17].

Statistical analysis

All statistical analyses were performed using IBM SPSS Statistics for Windows version 25 (IBM). The normality of the data was evaluated using the Shapiro–Wilk test. Paired *t* test and Wilcoxon signed-rank test were used to evaluate statistically significant differences. Statistical significance was set at $p < 0.05$. All radiographic assessments were performed twice by two researchers. The intra- and interobserver reliability were determined based on the intraclass correlation coefficients (ICC) of the radiographic assessments [21, 22]. ICCs were evaluated using ICC (1, 2) and ICC (2, 2) for intra- and interobserver reliabilities, respectively. The ICCs were classified as almost perfect (0.81–1.00), excellent (0.61–0.80), good (0.41–0.60) and slight (0.00–0.20), as described by Landis et al. [12]. The ICCs for intra- and interobserver reliabilities were greater than 0.76 (range, 0.76–0.99) for all measurements. The measurements obtained by one researcher were used in the analysis based on these results [12, 26–28]. The sample size was calculated using G*Power version 3.1.9. The significance level and power were set as 0.05 and 0.80, respectively, to analyze the difference between the two paired groups. Sixteen legs were included per group.

RESULTS

Radiographic measurement parameters are shown in Table 1. The mean change in each parameter is as follows: HKA was 1.8° of valgus, the knee loading point was 8.1% or 15% more lateralized, MPTA was 2.0° of varus, K-JLCA was unchanged, TCA was 5.4° of valgus, TAS was 12.1° of valgus, TPI was 13.3° of valgus, TI was 16.4° of valgus, A-JLCA decreased by 3.1° and MPJAP was 38.3° lateralized. The JSSF ankle/hindfoot scale pain, function, alignment and total scores were

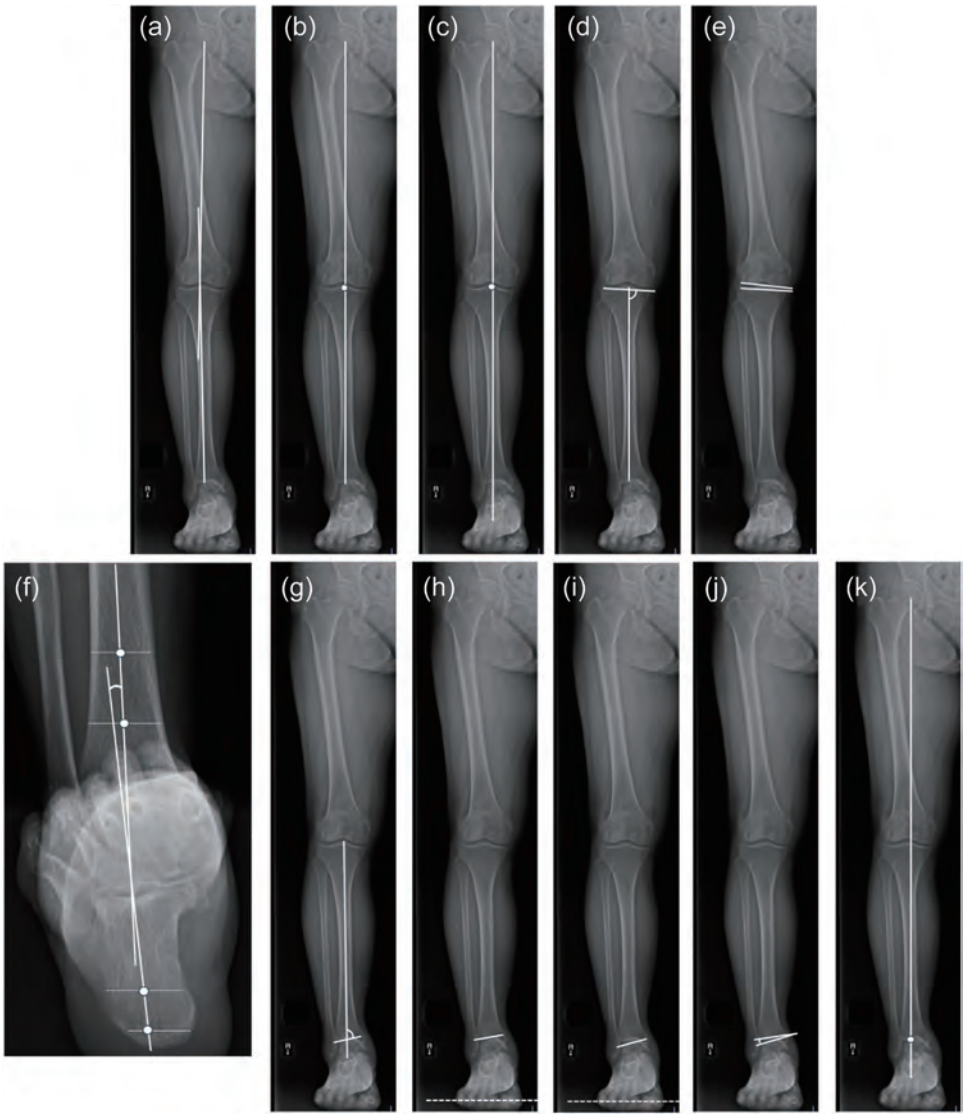

FIGURE 2 Measurement parameters. (a) Hip-knee-ankle angle (HKA); defined as the angle between the mechanical axes of the femur (centre of the femoral head to femoral intercondylar point) and tibia (tibial interspinous point to tibial mid-plafond point), (b) % hip-to-ankle line (%HA); defined as the ratio of the distance between the point where the hip-to-ankle line passes and the medial edge of the tibia to the width of the tibial plateau, (c) % hip-to-calcaneus line (%HC); defined as the ratio of the distance between the point where the hip-to-calcaneal line passes and the medial edge of the tibia to the width of the tibial plateau, (d) medial proximal tibial angle (MPTA); defined as the angle between the mechanical axis and the proximal articular surface of the tibia, (e) knee joint line convergence angle (K-JLCA); defined as the angle between the distal femoral and proximal tibial joint surfaces (positive for lateral opening), (f) tibiocalcaneal angle (TCA); defined as the angle between the tibial and calcaneal axes. The tibial axis was defined as the line between the midpoints of the tibial shaft 8 and 13 cm above the tip of the medial malleolus. The calcaneal axis was defined by two points. The first point was 7 mm proximal to the most distal part of the calcaneus on the horizontal line, which divided the bone at a 40:60 ratio, with the 40% segment beginning on the lateral side. The second point was at the middle of the horizontal line, 30 mm proximal to the most distal part of the calcaneus, (g) tibial anterior surface angle (TAS); defined as the angle between the lines drawn on the axis of the distal one-third of the tibia and the plafond, (h) tibial plafond inclination (TPI); defined as the angle between the tibial plafond and the ground (positive for lateral inclination), (i) talar Inclination (TI); defined as the angle between the talar joint surface and the ground (positive for lateral inclination), (j) ankle joint line convergence angle (A-JLCA); defined as the angle between the tibial plafond and the talar joint surface, (k) mechanical ankle joint axis point (MAJAP); defined as the percentage of the intersection of the tibial plafond with the line connecting the centre of the femoral head to the lowest point of the calcaneus to the entire tibial plafond.

15.3 ± 8.5/34.1 ± 6.0, 33.9 ± 7.0/46.8 ± 5.1, 5.9 ± 1.9/9.7 ± 1.2 and 55.1 ± 13.6/91.2 ± 8.1, respectively. In the statistical differences, %HA, %HC, MPTA, TCA, TAS, MAJAP and all the subscale and total JSSF ankle/hindfoot scale increased significantly postoperatively ($p < 0.05$). With the numbers available, no significant differences were observed between the preoperative and postoperative values of K-JLCA. The results showed that the lower limb alignment as a whole, including the hindfoot, became valgus and the loading points of the knee and ankle joints became more lateralized. The tilt of the ankle joint with relation to the

TABLE 1 Pre- and postoperative parameters.

	Preoperative	Postoperative	*p* Value
HKA (°)	1.0 ± 3.7	−0.8 ± 3.7	0.002
%HA	38.2 ± 8.3	47.5 ± 13.0	<0.001
%HC	38.8 ± 10.0	53.8 ± 16.1	<0.001
MPTA (°)	85.6 ± 2.4	87.6 ± 2.1	<0.001
K-JLCA (°)	1.4 ± 1.1	1.4 ± 1.2	n.s.
TCA (°)	−2.5 ± 6.3	2.9 ± 4.0	<0.001
TAS (°)	85.5 ± 3.4	97.6 ± 2.5	<0.001
TPI (°)	6.3 ± 3.0	−7.0 ± 4.0	<0.001
TI (°)	10.5 ± 3.4	−5.9 ± 5.2	<0.001
A-JLCA (°)	4.2 ± 2.9	1.1 ± 2.3	<0.001
MAJAP (%)	38.5 ± 15.9	76.8 ± 14.5	<0.001
JSSF ankle/hindfoot scale pain	15.3 ± 8.5	34.1 ± 6.0	<0.001
JSSF ankle/hindfoot scale function	33.9 ± 7.0	46.8 ± 5.1	<0.001
JSSF ankle/hindfoot scale alignment	5.9 ± 1.9	9.7 ± 1.2	<0.001
JSSF ankle/hindfoot scale total	55.1 ± 13.6	91.2 ± 8.1	<0.001

Note: Values are represented as mean ± SD.

Abbreviations: A-JLCA, ankle joint line convergence angle; HKA, hip knee ankle angle; JSSF, Japanese Society for Surgery of the Foot; K-JLCA, knee joint line convergence angle; MAJAP, mechanical ankle joint axis point; MPTA, medial proximal tibial angle; TAS, tibial anterior surface angle; TCA, tibiocalcaneal angle; TI, talar inclination; TPI, tibial plateau inclination; %HA, % hip-to-ankle line; %HC, % hip-to-calcaneus line.

ground was reduced. No obvious influence on the alignment of the knee joint surface was observed (Figure 3).

DISCUSSION

The most important findings of the present study were the identification of the effect of LTO on lower limb alignment, including the knee. After LTO surgery, the lower limb alignment as a whole becomes valgus and hindfoot alignment is closer to normal. The knee and ankle joint loading points are accordingly lateralized; however, this does not affect the knee surface alignment at the 1-year follow-up period. Several studies have investigated the effects of knee surgery on the foot. The ankle plane becomes parallel to the ground, and the hindfoot alignment improves to near-normal values when TKA or HTO is performed to improve the varus knee alignment [3, 10, 13]. However, excessive correction of varus knee alignment can lead to overcorrection of ankle and hindfoot alignment and increased loading on the foot and hindfoot [3, 10, 13]. Thus, the symptoms associated with the foot must be considered preoperatively for knee surgery [3, 9, 10, 13]. However, the effect of LTO on lower limb alignment, including the knee joint, remains unclear.

The ideal TAS after LTO ranges from 96 to 98° [21, 24]. The mean postoperative TAS was 97.6° in the present study, indicating that good correction alignment was achieved. The JSSF ankle/hindfoot scale scores exhibited a significant improvement postoperatively. The MAJAP results revealed a shift in the load axis located on the medial side of the ankle joint to the lateral side. Moreover, TPI and TT exhibited a significant decrease postoperatively, whereas A-JLCA exhibited a significant decrease postoperatively, indicating an improvement in ankle joint conformity.

LTO can be sufficiently corrective to the distal tibial articular surface, as the mean TAS became 12.1° valgus after LTO, but the effect on the tibial axis was approximately 2° of valgus, because mean HKA was 1.8° valgus and the mean MPTA was 2.0° valgus after LTO. In addition, %HA and %HC exhibited a significant increase, indicating that the knee joint load axis was lateralized postoperatively. With the numbers available, no significant differences were observed between %HA and %HC preoperatively in the present study; however, %HC was significantly greater than %HA postoperatively. %HC may be a more reliable load axis than %HA [8]. The differences between the postoperative %HA and %HC values observed in the present study may be attributed to the change of TCA to valgus after LTO. Changes in the hindfoot alignment reportedly cause differences in the %HC and %HA. Kim and colleagues reported that the hip to calcaneus line and hip to tatus line vary in patients with knee OA, which they considered to be attributed to the differences in the hindfoot alignment [11]. Choi and colleagues reported similar changes in the alignment of the hindfoot after LTO [19]. The change in TCA to valgus after LTO may have caused lateralization of the lowest point of the calcaneus. Thus, %HC was significantly higher than %HC postoperatively. The mean age before LTO surgery was 66.8 ± 5.4 years in the present study, and the prevalence of knee OA in this age group was over 35%; thus, the effect of LTO on the knee joint is very important [30]. The results of this study showed that both %HA and %HC were approximately 50%. Otsuka and colleagues recommended that the weightbearing axis be made neutral for highly active patients after HTO [18]. The change in the weightbearing axis in this study may have resulted in a change to a more natural loading axis for the knee joint as well. TKA for knee OA improved the symptoms of ankle OA owing to lateralization of the MAJAP in a previous study [26]. A similar effect can be achieved via LTO in patients with medial knee OA complications by lateralizing the load axis of the knee joint. The importance of changes in the load axis in the knee is evident from the concept of HTO.

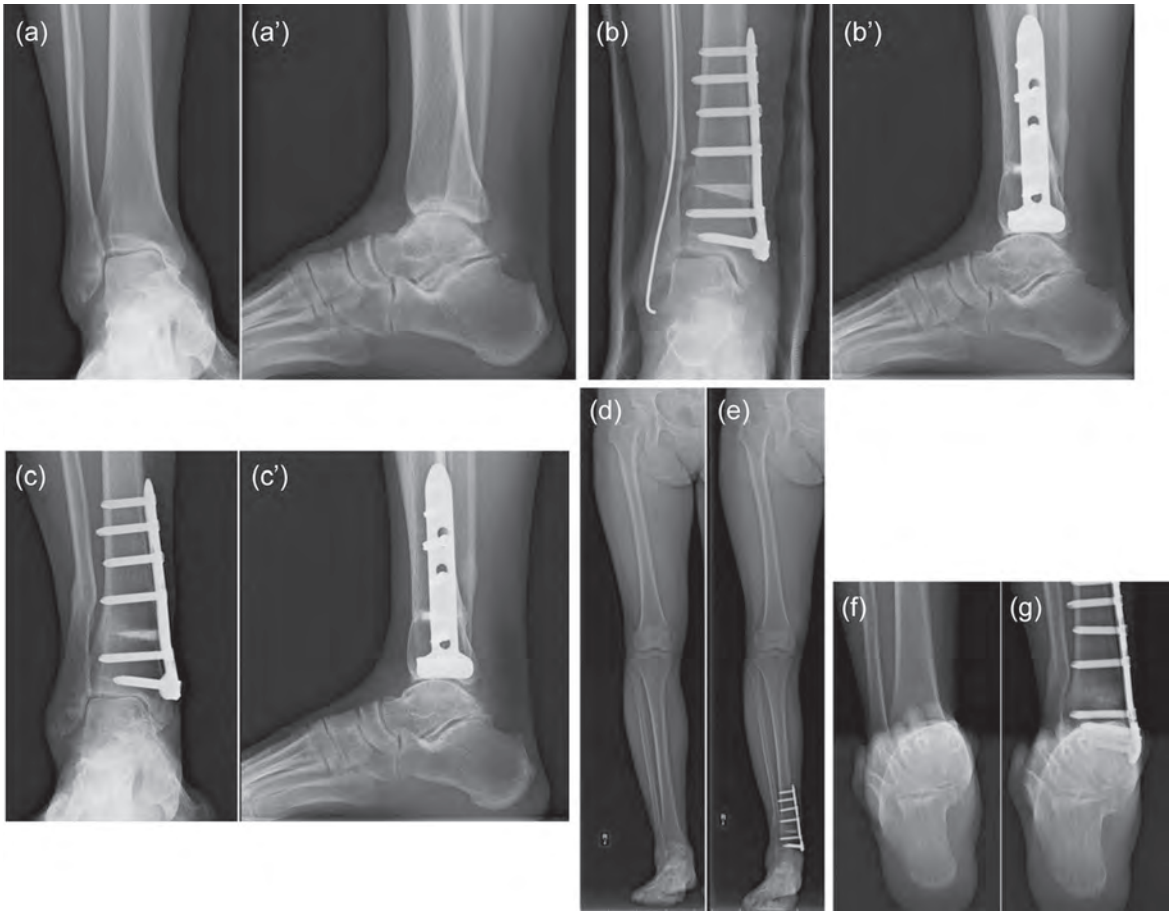

FIGURE 3 Case: 58-year-old female. (a and a') Preoperative radiograph of the frontal and lateral ankle joints. (b and b') Postoperative radiograph of the frontal and lateral ankle joints acquired immediately after the surgery. (c and c') Radiograph of the frontal and lateral ankle joints acquired 1 year postoperatively. (d) Radiograph of the whole leg standing radiography of preoperatively. (e) Radiograph of the whole leg standing radiography of 1 year postoperatively. (f) Weightbearing Subtalar radiograph acquired preoperatively. (g) Weightbearing Subtalar radiograph acquired 1 year postoperatively.

HTO, a surgery for medial-type knee OA, has resulted in good outcomes due to its effect on reducing the load on the medial knee joint by lateralizing the axis of loading of the knee joint [22]. Furthermore, with the numbers available, no significant differences were observed in the K-JLCA scales before and after LTO, indicating no progression of medial or lateral knee OA for at least 1 year postoperatively. Nevertheless, patients with lateral knee OA should be monitored as they are susceptible to experiencing worsening lateral knee joint pain after LTO. Furthermore, patients with progressive collapsing foot deformities whose TCA is highly valgus should be informed regarding the possibility of the TCA becoming more valgus after LTO.

The present study had certain limitations. First, the sample size of the present study was small. Second, the knee joint symptoms could not be evaluated, and detailed examinations other than radiography, such as the K-JLCA, could not be performed. Thus, the assessment of the cartilaginous surface may not be accurate. Third, a two-dimensional alignment evaluation was performed using radiographs in the present study; a three-dimensional evaluation was not performed. Furthermore, the present study focused on evaluation of the whole lower limb in the coronal plane; evaluation in the sagittal plane was not considered. Fourth, the follow-up period was only 1 year. However, this study is important in that it provides insights into the effects of LTO on the knee joints, which is crucial as society ages. Understanding that the knee joint loading point becomes more lateralized after LTO may help us confidently recommend surgery to patients planned for LTO, even if they have concomitant medial knee OA. Conversely, it is important to understand the possibility of increased pain on the lateral side of the knee joint when LTO is performed in patients with concomitant lateral knee OA.

CONCLUSION

The present study demonstrated that after LTO, when the TAS was corrected to an average of 12.1° valgus, lower limb alignment became 1.8° valgus following

HKA, the loading points of the knee and ankle joints were lateralized and the hindfoot alignment changed in the valgus direction. These changes must be considered when performing LTO in patients with lateral knee OA.

AUTHOR CONTRIBUTIONS

All authors have (1) made substantial contributions to the study concept or the data analysis or interpretation; (2) drafted the manuscript or revised it critically; (3) approved the final version of the manuscript to be published; and (4) agreed to be accountable for all aspects of the work.

ACKNOWLEDGEMENTS

We sincerely thank the staff of our institution. This study did not receive any specific grants from funding agencies in the public, commercial or nonprofit sectors.

CONFLICT OF INTEREST STATEMENT

The authors declare no conflict of interest.

DATA AVAILABILITY STATEMENT

N/A.

ETHICS STATEMENT

Ethical approval for this study was obtained from the Institutional Ethics Committee (approval number: IRB3724). All patients were informed that data from the case would be submitted for publication, and they provided their consent.

REFERENCES

1. Choi, J.Y., Song, S.J., Kim, S.J., Kim, S.H., Park, J.S. & Suh, J.S. (2018) Changes in hindfoot alignment after high or low tibial osteotomy. *Foot & Ankle International*, 39, 1097–1105. Available from: https://doi.org/10.1177/1071100718773767
2. Fujimaki, T., Kurokawa, H., Ueno, Y., Sasaki, T., Pradana, A.S., Zainudin, T. et al. (2023) Assessment of changes in hindfoot alignment of total ankle arthroplasty for ankle osteoarthritis on weightbearing subtalar X-ray view. *Foot & Ankle Orthopaedics*, 8, 24730114231205299. Available from: https://doi.org/10.1177/24730114231205299
3. Gursu, S., Sofu, H., Verdonk, P. & Sahin, V. (2016) Effects of total knee arthroplasty on ankle alignment in patients with varus gonarthrosis: do we sacrifice ankle to the knee? *Knee Surgery, Sports Traumatology, Arthroscopy: Official Journal of the ESSKA*, 24, 2470–2475. Available from: https://doi.org/10.1007/s00167-015-3883-2
4. Haraguchi, N., Ota, K., Tsunoda, N., Seike, K., Kanetake, Y. & Tsutaya, A. (2015) Weight-bearing-line analysis in supramalleolar osteotomy for varus-type osteoarthritis of the ankle. *The Journal of Bone and Joint Surgery. American Volume*, 97, 333–339. Available from: https://doi.org/10.2106/JBJS.M.01327
5. Hayashi, K., Tanaka, Y., Kumai, T., Sugimoto, K. & Takakura, Y. (2008) Correlation of compensatory alignment of the subtalar joint to the progression of primary osteoarthritis of the ankle. *Foot & Ankle International*, 29, 400–406. Available from: https://doi.org/10.3113/FAI.2008.0400
6. Hermans, J.J., Beumer, A., de Jong, T.A. & Kleinrensink, G.J. (2010) Anatomy of the distal tibiofibular syndesmosis in adults: a pictorial essay with a multimodality approach. *Journal of Anatomy*, 217, 633–645. Available from: https://doi.org/10.1111/j.1469-7580.2010.01302.x
7. Horisberger, M., Valderrabano, V. & Hintermann, B. (2009) Posttraumatic ankle osteoarthritis after ankle-related fractures. *Journal of Orthopaedic Trauma*, 23, 60–67. Available from: https://doi.org/10.1097/BOT.0b013e31818915d9
8. Kikuchi, N., Kanamori, A., Kadone, H., Okuno, K., Hyodo, K. & Yamazaki, M. (2022) Radiographic analysis using the hip-to-calcaneus line and its association with lower limb joint kinetics in varus knee osteoarthritis. *The Knee*, 35, 142–148. Available from: https://doi.org/10.1016/j.knee.2022.03.005
9. Kim, C.W., Gwak, H.C., Kim, J.H., Lee, C.R., Kim, J.G., Oh, M. et al. (2018) Radiologic factors affecting ankle pain before and after total knee arthroplasty for the Varus osteoarthritic knee. *The Journal of Foot and Ankle Surgery: Official Publication of the American College of Foot and Ankle Surgeons*, 57, 865–869. Available from: https://doi.org/10.1053/j.jfas.2018.02.002
10. Kim, J.G., Suh, D.H., Choi, G.W., Koo, B.M. & Kim, S.G. (2021) Change in the weight-bearing line ratio of the ankle joint and ankle joint line orientation after knee arthroplasty and high tibial osteotomy in patients with genu varum deformity. *International Orthopaedics*, 45, 117–124. Available from: https://doi.org/10.1007/s00264-020-04799-0
11. Kim, S.G., Choi, G.W., Kim, H.K. & Kim, J.G. (2021) Hip-to-calcaneus alignment differs from hip-to-talus alignment in patients with genu varum deformity. *Knee Surgery, Sports Traumatology, Arthroscopy: Official Journal of the ESSKA*, 29, 975–981. Available from: https://doi.org/10.1007/s00167-020-06060-y
12. Landis, J.R. & Koch, G.G. (1977) The measurement of observer agreement for categorical data. *Biometrics*, 33, 159–174. Available from: https://doi.org/10.2307/2529310
13. Lee, J.H. & Jeong, B.O. (2012) Radiologic changes of ankle joint after total knee arthroplasty. *Foot & Ankle International*, 33, 1087–1092. Available from: https://doi.org/10.3113/FAI.2012.1087
14. Lindstrand, A., Boegård, T., Egund, N. & Thorngren, K.G. (1982) Use of a guide instrument for compartmental knee arthroplasty. *Acta Orthopaedica Scandinavica*, 53, 633–639. Available from: https://doi.org/10.3109/17453678208992270
15. Muehleman, C., Bareither, D., Huch, K., Cole, A.A. & Kuettner, K.E. (1997) Prevalence of degenerative morphological changes in the joints of the lower extremity. *Osteoarthritis and Cartilage*, 5, 23–37. Available from: https://doi.org/10.1016/s1063-4584(97)80029-5
16. Niki, H., Aoki, H., Inokuchi, S., Ozeki, S., Kinoshita, M., Kura, H. et al. (2005) Development and reliability of a standard rating system for outcome measurement of foot and ankle disorders, I: development of standard rating system. *Journal of Orthopaedic Science: Official Journal of the Japanese Orthopaedic Association*, 10, 457–465. Available from: https://doi.org/10.1007/s00776-005-0936-2
17. Niki, H., Aoki, H., Inokuchi, S., Ozeki, S., Kinoshita, M., Kura, H. et al. (2005) Development and reliability of a standard rating system for outcome measurement of foot and ankle disorders, II: interclinician and intraclinician reliability and validity of the newly established standard rating scales and Japanese Orthopaedic Association rating scale. *Journal of Orthopaedic Science: Official Journal of the Japanese Orthopaedic Association*, 10, 466–474. Available from: https://doi.org/10.1007/s00776-005-0937-1
18. Otsuki, S., Wakama, H., Ikeda, K., Okuno, N., Okamoto, Y., Okayoshi, T. et al. (2021) Progression of pelvic retroversion is a critical factor for clinical outcome after Opening-wedge high tibial osteotomy among elderly patients. *Journal of Experimental Orthopaedics*, 8, 65. Available from: https://doi.org/10.1186/s40634-021-00376-5

19. Paley, D. (2003) *Principles of deformity correction*. Heidelberg, Germany: Springer-Verlag.
20. Takakura, Y., Tanaka, Y., Kumai, T., Sugimoto, K. & Ohgushi, H. (2004) Ankle arthroplasty using three generations of metal and ceramic prostheses. *Clinical Orthopaedics and Related Research*, 424, 130–136. https://doi.org/10.1097/01.blo.0000131246.79993.ec
21. Takakura, Y., Tanaka, Y., Kumai, T. & Tamai, S. (1995) Low tibial osteotomy for osteoarthritis of the ankle. Results of a new operation in 18 patients. *The Journal of Bone and Joint Surgery British Volume*, 77, 50–54. Available from: https://doi.org/10.1302/0301-620X.77B1.7822395
22. Takeuchi, R., Ishikawa, H., Aratake, M., Bito, H., Saito, I., Kumagai, K. et al. (2009) Medial opening wedge high tibial osteotomy with early full weight bearing. *Arthroscopy: The Journal of Arthroscopic & Related Surgery: Official Publication of the Arthroscopy Association of North America and the International Arthroscopy Association*, 25, 46–53. Available from: https://doi.org/10.1016/j.arthro.2008.08.015
23. Tallroth, K., Harilainen, A., Kerttula, L. & Sayed, R. (2008) Ankle osteoarthritis is associated with knee osteoarthritis. Conclusions based on mechanical axis radiographs. *Archives of Orthopaedic and Trauma Surgery*, 128, 555–560. Available from: https://doi.org/10.1007/s00402-007-0502-9
24. Tanaka, Y., Takakura, Y., Hayashi, K., Taniguchi, A., Kumai, T. & Sugimoto, K. (2006) Low tibial osteotomy for varus-type osteoarthritis of the ankle. *The Journal of Bone and Joint Surgery. British Volume*, 88, 909–913. Available from: https://doi.org/10.1302/0301-620X.88B7.17325
25. Tochigi, Y., Gakihana, M., Kaneko, T., Ogawa, M. & Ozeki, S. (2015) Factors in the incidence of ankle osteoarthritis in Japan. *The Japanese Society for Surgery of the Foot [in Japanese]*, 36, 173–175.
26. Wanezaki, Y., Hariu, M., Ishigaki, D., Takakubo, Y., Suzuki, A., Takagi, M. et al. (2020) Two cases of improvement of symptoms of ankle osteoarthritis after total knee arthroplasty. *The Japanese Society for Surgery of the Foot [in Japanese]*, 41, 205–208.
27. Wanezaki, Y., Suzuki, A., Takakubo, Y., Nakajima, T., Toyono, S., Toyoshima, S. et al. (2022) Evaluation of hindfoot and knee alignment by the hip-to-calcaneus view in patients with knee osteoarthritis and healthy individuals. *The Knee*, 38, 184–192. Available from: https://doi.org/10.1016/j.knee.2022.08.014
28. Wanezaki, Y., Suzuki, A., Takakubo, Y., Nakajima, T., Toyono, S., Toyoshima, S. et al. (2023) Lower limb alignment in healthy Japanese adults. *Journal of Orthopaedic Science: Official Journal of the Japanese Orthopaedic Association*, 28, 200–203. Available from: https://doi.org/10.1016/j.jos.2021.10.016
29. Witteveen, A.G., Hofstad, C.J. & Kerkhoffs, G.M. (2015) Hyaluronic acid and other conservative treatment options for osteoarthritis of the ankle. *The Cochrane Database of Systematic Reviews*, 2015, 010643. Available from: https://doi.org/10.1002/14651858.CD010643.pub2
30. Yoshimura, N., Muraki, S., Oka, H., Mabuchi, A., En-Yo, Y., Yoshida, M. et al. (2009) Prevalence of knee osteoarthritis, lumbar spondylosis, and osteoporosis in Japanese men and women: the research on osteoarthritis/osteoporosis against disability study. *Journal of Bone and Mineral Metabolism*, 27, 620–628. Available from: https://doi.org/10.1007/s00774-009-0080-8

How to cite this article: Wanezaki, Y., Kurokawa, H., Ueno, Y., Tablante, A., Mei, N., Yinghao, L. et al. (2024) Medial opening low tibial osteotomy shifts the load laterally not only at the ankle joint but also at the knee joint. *Journal of Experimental Orthopaedics*, 11, e70029. https://doi.org/10.1002/jeo2.70029

Tablante *et al. BMC Musculoskeletal Disorders* (2025) 26:204
https://doi.org/10.1186/s12891-025-08431-3

BMC Musculoskeletal Disorders

RESEARCH Open Access

Second metatarsophalangeal joint dislocation in hallux valgus: a radiographic study using a two-dimensional coordinate system

Adrian Joseph Castor Tablante[1,2*], Hiroaki Kurokawa[2], Yuki Ueno[2], Yoshihiro Wanezaki[2,3], Nan Mei[2], Yinghao Li[2], Akira Taniguchi[2], Emiliano Baula Tablante[1] and Yasuhito Tanaka[2]

Abstract

Background Hallux valgus (HV) poses additional challenges when accompanied by second metatarsophalangeal (MTP) joint dislocation, often requiring complex surgical intervention. This study aimed to analyze HV feet with second MTP joint dislocation using a 2-dimensional coordinate system to better understand the anatomical structure of this condition.

Methods Weightbearing foot radiographs of 49 HV feet with second MTP joint dislocation (group D), 68 HV feet without second MTP joint dislocation (group W), and 54 control feet (group N) were analyzed. A 2-dimensional coordinate system was used to map standardized points on radiographs into X and Y coordinates, which were compared across groups. Radiographic parameters measured included hallux valgus angle (HVA), intermetatarsal angle (IMA), second toe MTP angle (2MTPA), metatarsus adductus angle (MAA), great toe length, first metatarsal (MT1) length, second toe length, and second metatarsal (MT2) length. The 2MTPA was further analyzed based on the deviation direction (medial, neutral, or lateral).

Results The proximal phalanx head of the third toe in groups D and W was lateral compared to group N ($P<.05$ and $P<.001$, respectively), while the distal point in group D was medial to group W ($P<.001$). The base of MT1 in group D was significantly medial compared to other groups ($P<.001$). Additionally, the distal point of the great toe in group D was significantly lateral compared to other groups ($P<.01$ and $P<.001$, respectively).

Conclusions Patients with second MTP joint dislocation exhibited a proximally translated second toe, an adducted third toe, a medialized MT1 base, and a lateralized great toe tip. The M1/2 angle influenced dislocation direction: higher angles led to medial or neutral deviation, while lower angles caused lateral deviation. Radiographic coordinate mapping provided novel insights into foot anatomy in HV with second MTP joint dislocation, laying the groundwork for future research on anatomical risk factors and optimizing surgical approaches to improve patient outcomes.

Keywords Hallux valgus, Second metatarsophalangeal dislocation, Forefoot deformities, Mapping system, Radiographic analysis

*Correspondence:
Adrian Joseph Castor Tablante
ajctablante@gmail.com
[1]Department of Orthopaedic Surgery, Jose R. Reyes Memorial Medical Center, San Lazaro Compound, Rizal Avenue, Sta. Cruz, Manila, Metro Manila 1012, Manila, Philippines
[2]Department of Orthopaedic Surgery, Nara Medical University, Kashihara, Nara, Japan
[3]Department of Orthopaedic Surgery, Yamagata University Faculty of Medicine, Yamagata City, Yamagata, Japan

Background

Hallux valgus (HV) is a prevalent forefoot deformity with a global incidence of 19%.[5,19,29] Lesser toe deformities, including crossover toes, flexion deformities, and lateral deviation have been associated with HV deformities [7, 10, 24, 36]. In some cases of HV, dislocation of the second metatarsophalangeal (MTP) joint occurs and necessitates a supplementary procedure alongside HV correction [27]. Second MTP joint dislocation is seen as an end-stage deformity of various conditions in previous studies [7, 10, 17, 47]. Anatomical studies show second MTP joint dislocation restraints include the volar plate, collateral ligaments, and deep transverse metatarsal ligament [1, 6, 16, 38, 39, 44]. Previous reports suggested a potential link between second metatarsal (MT2) length and crossover toe, ultimately leading to MTP dislocation if untreated [7, 10, 46]. However, conflicting reports found no clear relationship between MT2 length and second toe deformity [24].

Plantar plate injury, frequently affecting the second MTP joint, has been identified as a cause of dislocation [14, 22]. However, limited evidence exists regarding how HV predisposes individuals to second MTP joint dislocation, despite reports suggesting the HV severity as a risk factor [34]. Additionally, factors such as medial deviation (e.g., crossover toe) [7, 14, 47], or lateral deviation [36] may contribute to second MTP joint dislocation. It remains unclear how osseous architecture of the HV forefoot influences the plantar soft-tissue and plantar plate, eventually leading to a second MTP joint dislocation [24, 26, 27].

Only a few studies have evaluated the relationship between HV and second MTP joint dislocation, and more specifically, the risk factors that may influence the progression of one over the other. To learn about the anatomic structure of this deformity, this study aimed to use a 2-dimensional coordinate system to evaluate radiographic alignments and osseous features [41], shedding light on the relationship between HV and second MTP joint dislocation. The advantage of a 2-dimensional coordinate system lies in its ability to visually map the entire foot and highlight key differences of normal and abnormal feet using standard radiographs. We hoped to determine any potential anatomic factors in HV that may affect second MTP joint dislocation. The findings could enhance diagnostic accuracy, guide surgical planning, and improve treatment outcomes for patients with these deformities, ultimately optimizing patient care in clinical practice.

Table 1 Patient demographics for each group

	Hallux valgus foot with second toe dislocation (Group D)	Hallux valgus without second toe dislocation (Group W)	Normal foot (Group *N*)
Number of patients	47	49	49
Number of feet	49	68	54
Left feet	22	38	24
Right feet	27	30	29
Mean age (range)	69.49 years (56–80)	67.62 years (40–87)	54.85 years (18–80)
Mean HVA (range)	48.61 degrees (40–59)	48.00 degrees (40–59)	13.09 degrees (0–20)

HVA: hallux valgus angle

Methods

This is a retrospective study comparing radiographic parameters among three groups of females aged at least 18 years: those with hallux valgus (HV) and second MTP joint dislocation (Group D), those with HV without second MTP joint dislocation (Group W), and individuals with control feet (Group N). Standardized points on weightbearing anteroposterior (AP) radiographs were mapped using a 2-dimensional coordinate system. Dislocation was defined as less than 50% articulation of the proximal phalanx articular surface with the metatarsal head [4, 11]. Patients with a hallux valgus angle (HVA) ranging from 40 to 59 degrees were included to match groups and minimize variables associated with severity, while controls had an HVA of 20 degrees or less and no abnormal radiographic findings or history of ipsilateral ankle arthritis or flatfoot. Patients with peripheral nerve disease, rheumatoid arthritis, cerebral palsy, or other conditions predisposing to HV were excluded.

Data were gathered from hospital records spanning January 2013 to August 2023. Of the 368 patients with HV (430 feet) who underwent surgery, 288 feet were excluded for not meeting the inclusion criteria, leaving 142 feet. Further exclusions for rheumatoid arthritis (25 feet) resulted in 117 feet being categorized into Group D (47 patients, 49 feet) and Group W (49 patients, 68 feet). Group N included 49 control subjects (54 feet). Table 1 presents the mean age, laterality, and HVA. The study was approved by the Institutional Review Board.

Radiographic technique

Weightbearing AP and lateral radiographs of feet were performed at a distance of 100 cm. The tube was tilted approximately 15 degrees from the vertical plane for the AP view, with the center aligned to the midfoot. For the lateral view, the navicular was positioned at the center.

Mapping system

Marked points on digital radiographs were converted into X and Y coordinates in the 2-dimensional framework [41]. The metatarsal axis, defined as a line connecting the midpoints of the proximal and distal metaphyses,

served as the reference line. The X-axis was aligned along the second metatarsal (MT2), with its origin (0,0) positioned at the intersection of the X-axis and MT2 base. The Y-axis, perpendicular to the X-axis and passing through the origin, was established accordingly (Fig. 1).

In this coordinate framework:

- Positive X values indicate locations distal to the origin, while negative X values indicate proximal locations.
- Positive Y values indicate medial deviations, while negative Y values indicate lateral deviations.

To standardize measurements across varying foot sizes, all coordinate values were expressed as a percentage of MT2 length, allowing for consistent comparisons. The base of MT2 (MB2) was consistently defined as (0,0), while the MT2 head (MH2) was always mapped to (100,0).

A set of key anatomical landmarks were selected for mapping to assess foot morphology and alignment, including:

- Distal ends of distal phalanges (DPH1-DPH5), distal ends of proximal phalanges (PPH1-PPH5), and midpoints of proximal phalangeal joint surfaces (PPB1-PPB5) to analyze toe positioning.
- Intersections of metatarsal axes with distal (MH1-MH5) and proximal (MB1-MB5) metatarsal ends to assess metatarsal positioning.
- Joint space midpoints of the first metatarsocuneiform (1MC), talonavicular (TN), fifth metatarsocuboid (5MC), and calcaneocuboid (CC) joints to evaluate midfoot alignment.

By overlaying coordinate maps of different groups (e.g., HV with vs. without second MTP joint dislocation), the spatial relationships between key foot structures were visualized, providing insights beyond conventional angular measurements. This technique offers a novel approach to quantifying foot morphology and identifying structural patterns in hallux valgus with second MTP joint dislocation.

To validate the accuracy and reproducibility of this method, twenty randomly selected radiographs were analyzed twice by two independent observers on separate occasions. The standard deviation for all angular measurements remained within 1 degree, while the standard deviation of X and Y coordinates was within 1% for all measured points. The absolute value of the coefficient of variation was within 5%, confirming the system's reliability. The reliability of the mapping system has been previously validated [41, 42].

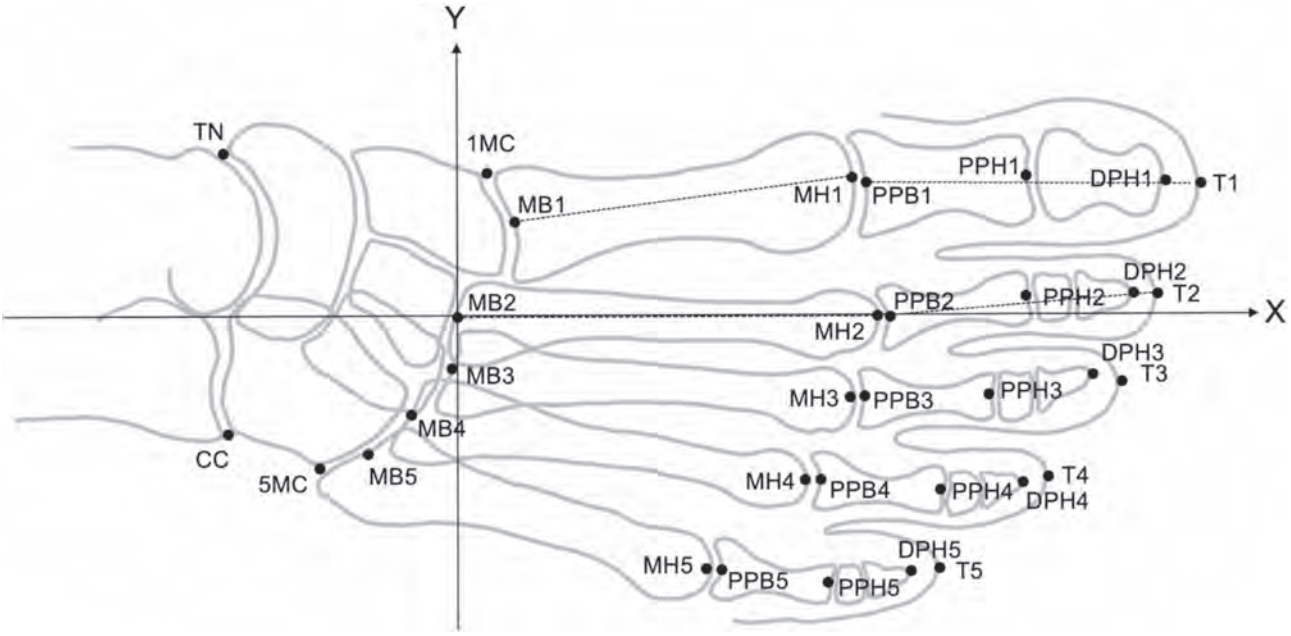

Fig. 1 Points marked on the radiograph for the mapping system (points) and length measured (dotted line). T1 to T5: most distal point of soft tissue; DPH1 to DPH5: distal phalanx tips; PPH1 to PPH5: midpoint of distal joint surface of proximal phalanx; PPB1 to PPB5: midpoint of proximal joint surface of proximal phalanx; MH1 to MH5: point of intersection of metatarsal axes with distal metatarsal ends; MB1 to MB5: point of intersection of metatarsal axes with proximal metatarsal ends; 1MC: most medial edge of first metatarsocuneiform joint; TN: most medial edge of talonavicular joint; 5MC: most lateral edge of fifth metatarsocuboid joint; CC: most lateral edge of the calcaneocuboid joint; big toe length: distance of the point T1 to PPB1; second toe length: distance of the point T2 to PPB2; first metatarsal length: distance of point MH1 to MB1; second metatarsal length: distance of point MH2 to MB2

Radiographic examination

Measured parameters included the HVA, intermetatarsal angles (IMA), second toe metatarsophalangeal angle (2MTPA), metatarsus adductus angle (MAA), and toe and metatarsal length. This selection was based on findings establishing associations between HV and radiographic features including toe length [41], increased first-second intermetatarsal angle (M1/2),[8,12,29] metatarsus adductus (MA) [8, 9, 19], and splay foot [2, 18]. The 2MTPA was associated with second MTP joint dislocation [27]. The central axis of each metatarsal was determined by connecting the midpoints of the proximal and distal ends of its diaphysis [35]. This method was used to determine the IMA and HVA. The proximal phalanx axis was formed by connecting the most concave points on its proximal and distal articular surfaces, and any pronation of the proximal phalanx had minimal impact on these points [41]. The HVA was defined as the line formed by the axes of the first metatarsal (MT1) and first proximal phalanx. The IMA was defined as the angle formed by the axes of adjacent metatarsals. The angle between the axes of the second and fourth metatarsals formed the 2–4 intermetatarsal angle (M2/4), while the 2–5 intermetatarsal angle (M2/5) was determined by the axes of the second and fifth metatarsals. The 2MTPA represented the angle formed by the axes of MT2 and the second proximal phalanx, with medial deviation considered negative and lateral deviation considered positive. Group D (dislocation group) was subdivided into 3 subgroups according to the 2MTPA: group D1 (2MTPA less than – 5 degrees: medial-deviation type), group D2 (2MTPA not less than – 5 degrees and less than 20 degrees: neutral type), and group D3 (2MTPA 20 degrees or more: lateral-deviation type). The absolute (mm) and relative (%) lengths of toes and metatarsals were also measured (Fig. 1). Great toe length was defined as the distance between T1 and PPB1. Second toe length was the distance between T2 and PPB2. The lengths of MT1 and MT2 were measured as distances from MH1 to MB1 and MH2 to BM2, respectively. The great toe, second toe, and MT1 were measured in percentages relative to MT2. Coughlin's method [29] for measuring MA was used (Fig. 2). Figures of all groups were rotated on its origin (MB2) according to its MAA to visualize each result. The new X-axis was defined as the midfoot axis extending beyond MB2, with the new Y-axis perpendicular and passing through MB2.

Statistical analysis

Using SPSS software version 26 (SPSS, Inc, an IBM Company, Chicago, IL), a Multivariate Analysis of Variance (MANOVA) and post hoc comparison (Games-Howell) were used to differentiate the same point in each group. One-factor analysis of variance and post hoc pairwise comparison (Scheffe) were used to estimate the

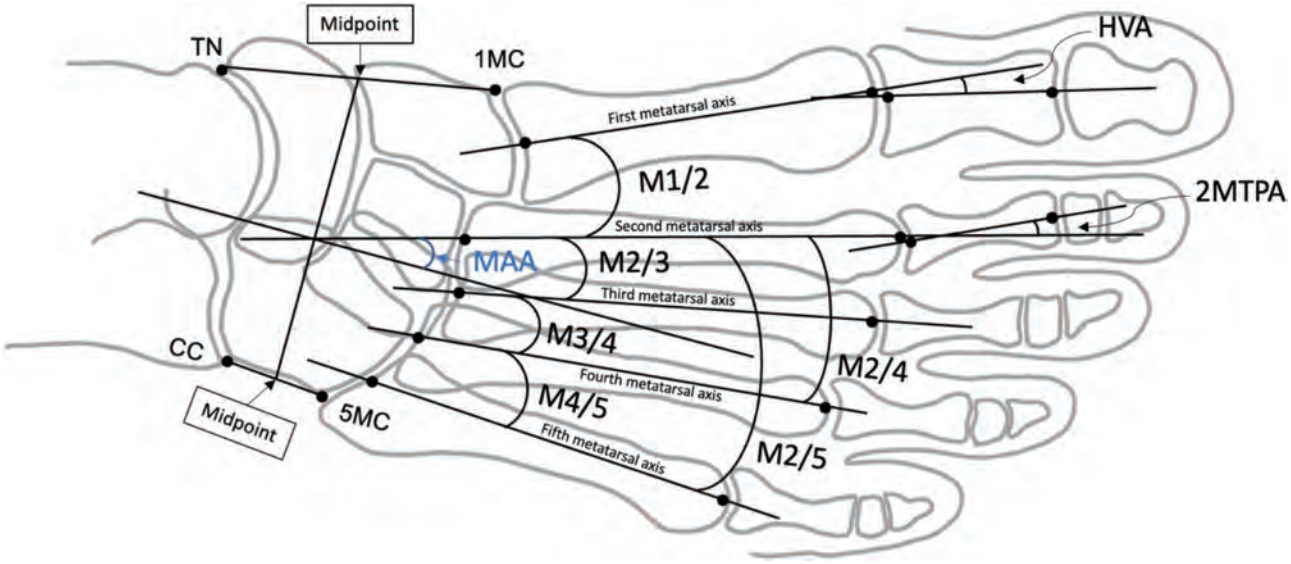

Fig. 2 Angles measured on the radiographs. HVA: Hallux valgus angle; M1/2 angle: angle between first and second metatarsals axes; M2/3 angle: angle between second and third metatarsal axes; M3/4 angle: angle between third and fourth metatarsal axes; M4/5 angle: angle between fourth and fifth metatarsal axes; M2/4 angle: angle between second and fourth metatarsal axes; M2/5 angle: angle between second and fifth metatarsal axes; 2MTPA: angle between second metatarsal and the second proximal phalangeal axes; MAA: metatarsus adductus angle - A line was drawn along the medial border of the midfoot connecting 2 points: the most medial edge of the first metatarsocuneiform joint (1MC) and the most medial edge of the talonavicular joint (TN). Afterwards, a line was drawn along the lateral border of the midfoot connecting 2 points: the most lateral edge of the calcaneocuboid joint (CC) and the most lateral edge of the fifth metatarsocuboid joint (5MC). A line was then drawn connecting the 2 midpoints that bisected the midfoot. The line perpendicular to the line bisecting the midfoot is the midfoot axis. The angle formed by the axis of the second metatarsal and the midfoot axis is the metatarsus adductus angle

difference between the angles and lengths measured. The level of significance was 0.05.

Results

Measured angles are outlined in Table 2. Coordinates for each point are detailed in Table 3. Mapping results are seen in Fig. 3.

Intermetatarsal angles

There was no significant difference in M1/2 angle between group D and group W; however, both HV groups were significantly larger than group N ($P<.001$).

The 2–3 intermetatarsal angle (M2/3) and 2–4 intermetatarsal angle (M2/4) of group D were larger than group N ($P<.01$). The 3–4 intermetatarsal (M3/4), 4–5 intermetatarsal (M4/5), and 2–5 intermetatarsal (M2/5) angles were not significant among all groups (Table 2).

Position of the lesser metatarsals

The Y-coordinates of lesser metatarsal heads (MH3, MH4, MH5) in groups D and W were significantly lateral to group N demonstrating widening of HV feet (Fig. 3). The MH4 of both HV groups was significantly proximal to group N (Table 3).

Position of the second toe

All second toe points of group D were proximal to other groups ($P<.001$), with the second toe base located proximal to the MT2 head denoting MTP joint dislocation (Fig. 3). The distal phalanx head, proximal phalanx head, and proximal phalanx base of the second toe of groups D and N had no difference in the Y-axis but were significantly lateral in group W (Table 3).

Second toe deviation after dislocation

In group D, the 2MTPA ranged from −41 to 36. Neutral type (subgroup D2) was the most common (25 feet) followed by lateral-deviation type or subgroup D3 (14 feet) then medial-deviation type or subgroup D1 (10 feet). Mean M1/2 angles of D1, D2, and D3 were: 21.0 ± 2.4, 19.0 ± 4.0, 16.4 ± 3.5 degrees, respectively. The 2MTPA of D1 was significantly medially deviated compared to D3, but not D2. The MA angles were 14.1 ± 3.9, 14.8 ± 4.5, and 17.6 ± 3.5 for subgroups D1, D2, D3, respectively. No differences in other IMA among subgroups were found.

Position of the lesser toes

The third metatarsal base of group D was proximal to group N ($P<.05$). The third metatarsal heads of both HV groups were lateral to group N ($P<.001$). The third proximal phalanx bases of both HV groups were lateral to group N ($P<.001$). The third proximal phalanx head of group D is proximal to groups W and N ($P<.01$ and $P<.001$, respectively). The proximal phalanx heads of both HV groups were similar to each other and lateral to group N ($P<.05$ and $P<.001$, respectively). The third distal phalanx head of group D is proximal to both groups W and N ($P<.01$), while group W deviated laterally among the groups ($P<.001$).

The fourth metatarsal bases of both HV groups was significantly proximal and lateral than control (Table 3). The fourth proximal phalanx heads of both group D and group W were lateral to group N ($P<.01$). The fourth distal phalanx head of group W was lateral to group N ($P<.001$).

The fifth metatarsal bases of both HV groups was proximal to control feet ($P<.05$) with group D deviating laterally to group N ($P<.01$). There were no significant differences in proximal phalanx head location and distal point of the fifth toe among all groups.

These results show an adducted position with a lateralized base and a medialized third toe distal tip in group D (Fig. 3).

Table 2 Results of the angles and P values

				P			
Mean Value ± 1 Standard Deviation (Degrees)	**Group D**	**Group W**	**Group N**	**Between groups**	**Group D vs. Group W**	**Group D vs. Group N**	**Group W vs. Group N**
HVA	48.61 ± 5.8	48.00 ± 5.7	13.1 ± 4.3	< 0.001	ns	< 0.001	< 0.001
2MTPA	7.94 ± 18.0	14.75 ± 8.4	3.37 ± 4.3	< 0.001	< 0.01	ns	< 0.001
M1/2	18.65 ± 3.9	19.32 ± 3.1	10.02 ± 2.3	< 0.001	ns	< 0.001	< 0.001
M2/3	4.61 ± 2.1	3.79 ± 1.8	3.20 ± 1.4	< 0.01	ns	< 0.01	ns
M3/4	6.67 ± 2.2	6.50 ± 2.4	6.02 ± 1.7	ns	ns	ns	ns
M4/5	8.86 ± 2.4	9.90 ± 2.8	9.17 ± 2.1	ns	ns	ns	ns
M2/4	11.24 ± 3.6	10.21 ± 3.5	9.07 ± 2.3	< 0.01	ns	<0.01	ns
M2/5	20.00 ± 3.7	20.00 ± 5.1	18.33 ± 3.2	ns	ns	ns	ns
Metatarsus adductus angle	15.47 ± 4.2	17.01 ± 5.4	15.48 ± 5.1	0.147	0.345	0.972	0.246

HVA: hallux valgus angle; 2MTPA: second toe metatarsophalangeal angle

Table 3 Coordinates and P values for each point in the 3 groups

				P (X, Y)		
Point	**Group D**	**Group W**	**Group N**	**Group D vs. Group W**	**Group D vs. Group N**	**Group W vs. Group N**
T1	(164.1 ± 7.5, -4.2 ± 11.6)	(166.5 ± 7.4, 1.8 ± 9.6)	(176.8 ± 5.6, 22.1 ± 6.9)	(ns, *)	(***, ***)	(***, ***)
T2	(153.0 ± 7.7, -6.8 ± 21.2)	(171.1 ± 6.8, -18.0 ± 10.5)	(173.6 ± 5.8, -4.8 ± 7.0)	(***, **)	(***, ns)	(ns, ***)
T3	(155.7 ± 6.8, -24.5 ± 13.5)	(160.3 ± 6.8, -35.6 ± 9.7)	(161.6 ± 6.4, -24.4 ± 6.6)	(**, ***)	(***, ns)	(ns, ***)
T4	(139.7 ± 6.3, -42.0 ± 11.5)	(141.6 ± 6.9, -46.2 ± 9.3)	(143.4 ± 7.3, -40.8 ± 6.1)	(ns, ns)	(*, ns)	(ns, **)
T5	(116.8 ± 6.1, -57.2 ± 9.6)	(117.5 ± 6.9, -60.7 ± 7.3)	(118.4 ± 8.0, -57.9 ± 5.3)	(ns, ns)	(ns, ns)	(ns, *)
DPH1	(158.0 ± 7.3, -0.8 ± 10.7)	(159.7 ± 7.2, 6.2 ± 9.1)	(169.7 ± 5.5, 24.1 ± 6.1)	(ns, **)	(***, ***)	(***, ***)
DPH2	(147.5 ± 7.7, -6.1 ± 19.9)	(165.8 ± 7.0, -16.6 ± 9.8)	(168.1 ± 5.6, -4.3 ± 6.1)	(***, **)	(***, ns)	(ns, ***)
DPH3	(150.4 ± 6.7, -25.2 ± 12.5)	(154.8 ± 6.8, -34.3 ± 8.8)	(155.3 ± 6.4, -24.9 ± 6.2)	(**, ***)	(**, ns)	(ns, ***)
DPH4	(134.3 ± 6.2, -43.9 ± 10.4)	(135.8 ± 6.9, -47.5 ± 7.8)	(137.0 ± 7.3, -42.8 ± 5.2)	(ns, ns)	(ns, ns)	(ns, ***)
DPH5	(111.0 ± 5.8, -60.5 ± 8.7)	(111.0 ± 6.8, -62.8 ± 6.6)	(111.5 ± 8.0, -60.3 ± 5.2)	(ns, ns)	(ns, ns)	(ns, ns)
PPH1	(130.3 ± 5.8, 16.5 ± 8.0)	(131.8 ± 5.4, 18.8 ± 6.2)	(138.2 ± 4.6, 33.6 ± 4.1)	(ns, ns)	(***, ***)	(***, ***)
PPH2	(119.9 ± 6.6, -3.5 ± 12.4)	(136.8 ± 4.0, -9.2 ± 6.5)	(139.2 ± 2.3, -0.8 ± 3.6)	(***, *)	(***, ns)	(***, ***)
PPH3	(125.7 ± 5.4, -27.2 ± 7.9)	(128.5 ± 4.5, -28.6 ± 5.9)	(130.1 ± 3.8, -23.7 ± 3.5)	(**, ns)	(***, *)	(ns, ***)
PPH4	(112.9 ± 4.8, -48.8 ± 6.0)	(113.0 ± 5.8, -48.6 ± 5.0)	(115.3 ± 5.3, -45.5 ± 4.3)	(ns, ns)	(ns, **)	(ns, **)
PPH5	(92.6 ± 5.4, -67.4 ± 6.5)	(92.1 ± 7.3, -66.3 ± 4.8)	(93.9 ± 7.5, -61.6 ± 18.4)	(ns, ns)	(ns, ns)	(ns, ns)
PPB1	(96.7 ± 4.4, 36.1 ± 4.9)	(97.3 ± 4.1, 36.2 ± 3.8)	(100.9 ± 3.0, 35.7 ± 2.8)	(ns, ns)	(***, ns)	(***, ns)
PPB2	(89.6 ± 5.1, -0.2 ± 4.7)	(102.9 ± 1.1, -1.4 ± 2.1)	(103.5 ± 0.8, 0.4 ± 1.3)	(***, ns)	(***, ns)	(**, ***)
PPB3	(95.0 ± 3.7, -22.3 ± 3.4)	(95.6 ± 3.1, -22.3 + 2.4)	(96.9 ± 2.9, -19.9 ± 2.0)	(ns, ns)	(*, ***)	(*, ***)
PPB4	(81.7 ± 4.1, -43.2 ± 3.8)	(82.4 ± 4.6, -42.2 ± 3.0)	(85.3 ± 4.8, -39.9 ± 3.0)	(ns, ns)	(***, ***)	(**, ***)
PPB5	(63.0 ± 4.9, -65.1 ± 5.1)	(63.2 ± 6.5, -63.3 ± 4.2)	(66.1 ± 6.8, -61.6 ± 4.4)	(ns, ns)	(*, **)	(*, ns)
MH1	(96.7 ± 4.5, 52.7 ± 5.6)	(96.0 ± 4.1, 50.8 ± 4.4)	(97.0 ± 3.1, 38.9 ± 3.4)	(ns, ns)	(ns, ***)	(ns, ***)
MH2	(100.0 ± 0.0, 100.0 ± 0.0)	(100.0 ± 0.0, 100.0 ± 0.0)	(100.0 ± 0.0, 100.0 ± 0.0)	—	—	—
MH3	(93.1 ± 2.3, -22.8 ± 2.8)	(93.0 ± 2.9, -21.7 ± 1.9)	(93.9 ± 2.7, -19.9 ± 2.1)	(ns, ns)	(ns, ***)	(ns, ***)
MH4	(79.5 ± 3.6, -43.7 ± 4.4)	(79.7 ± 4.6, -42.1 ± 3.2)	(82.3 ± 4.8, -39.9 ± 3.1)	(ns, ns)	(**, ***)	(**, **)
MH5	(60.1 ± 4.9, -67.8 ± 5.7)	(60.1 ± 6.6, -65.9 ± 5.1)	(62.9 ± 7.0, -63.2 ± 5.1)	(ns, ns)	(ns, ***)	(ns, **)
MB1	(16.2 ± 2.3, 26.5 ± 2.0)	(17.1 ± 2.8, 24.6 ± 2.0)	(15.7 ± 2.2, 23.1 ± 2.4)	(ns, ***)	(ns, ***)	(**, **)
MB2	(0.0 ± 0.0, 0.0 ± 0.0)	(0.0 ± 0.0, 0.0 ± 0.0)	(0.0 ± 0.0, 0.0 ± 0.0)	—	—	—
MB3	(-2.8 ± 1.5, -14.8 ± 2.0)	(-2.7 ± 2.1, -14.7 ± 2.4)	(-1.8 ± 2.2, -14.7 ± 2.4)	(ns, ns)	(*, ns)	(ns, ns)
MB4	(-12.4 ± 3.2, -24.9 ± 3.8)	(-11.2 ± 3.7, -24.8 ± 4.7)	(-10.2 ± 3.9, -24.5 ± 4.3)	(ns, ns)	(**, ns)	(ns, ns)
MB5	(-22.8 ± 3.9, -37.1 ± 5.5)	(-21.6 ± 4.3, -35.7 ± 7.2)	(-20.8 ± 4.9, -34.6 ± 6.0)	(ns, ns)	(ns, ns)	(ns, ns)
1MC	(9.3 ± 2.9, 36.5 ± 2.6)	(11.0 ± 3.2, 34.3 ± 2.7)	(9.8 ± 2.5, 33.3 ± 3.6)	(**, ***)	(ns, ***)	(ns, ns)
TN	(-60.4 ± 5.4, 37.3 ± 4.9)	(-53.9 ± 5.9, 36.5 ± 6.5)	(-57.5 ± 5.7, 34.5 ± 5.9)	(***, ns)	(*, *)	(**, ns)
5MC	(-31.4 ± 4.7, -41.2 ± 5.9)	-29.7 ± 5.3, -40.1 ± 7.2)	(-28.3 ± 5.5, -39.5 ± 5.9)	(ns, ns)	(**, ns)	(ns, ns)
CC	(-55.8 ± 4.7, -29.4 ± 6.3)	(-52.3 ± 5.5, -28.7 ± 8.0)	(-53.2 ± 5.5, -29.2 ± 7.4)	(**, ns)	(*, ns)	(ns, ns)

Coordinates are expressed as (X ± 1 SD, Y ± 1 SD); unit: percentages

*** = $p < .001$; **, $p < .01$; *, $p < .05$; —, not available; ns, not significant

Toe length and metatarsal length

There were no differences in great toe length among the groups (Table 4). The second toe length (%) and true length (mm) of group D were significantly shorter than other groups. However, the second toe length was likely affected by sagittal plane deformities. The MT1 length (%) of group D was longer than group N ($P < .05$). Lastly, MT2 length (mm) of group D was shorter than group N ($P < .001$).

Midfoot to hindfoot

The MB1 and 1MC points of group D were significantly medial among groups, while the TN and CC points were proximal among groups (Table 3). The TN point of group D was medial to group N ($P < .05$). The 5MC point of group D was proximal to group N. These findings show a wider midfoot associated with second toe dislocation (Fig. 3).

Metatarsus adductus

There were no significant differences in MAA among groups. Figure 4 shows lesser metatarsals and lesser toe proximal phalanges of group D diverge laterally from other groups according to the midfoot axis. Additionally, third toe distal tip of group D is medial to group W,

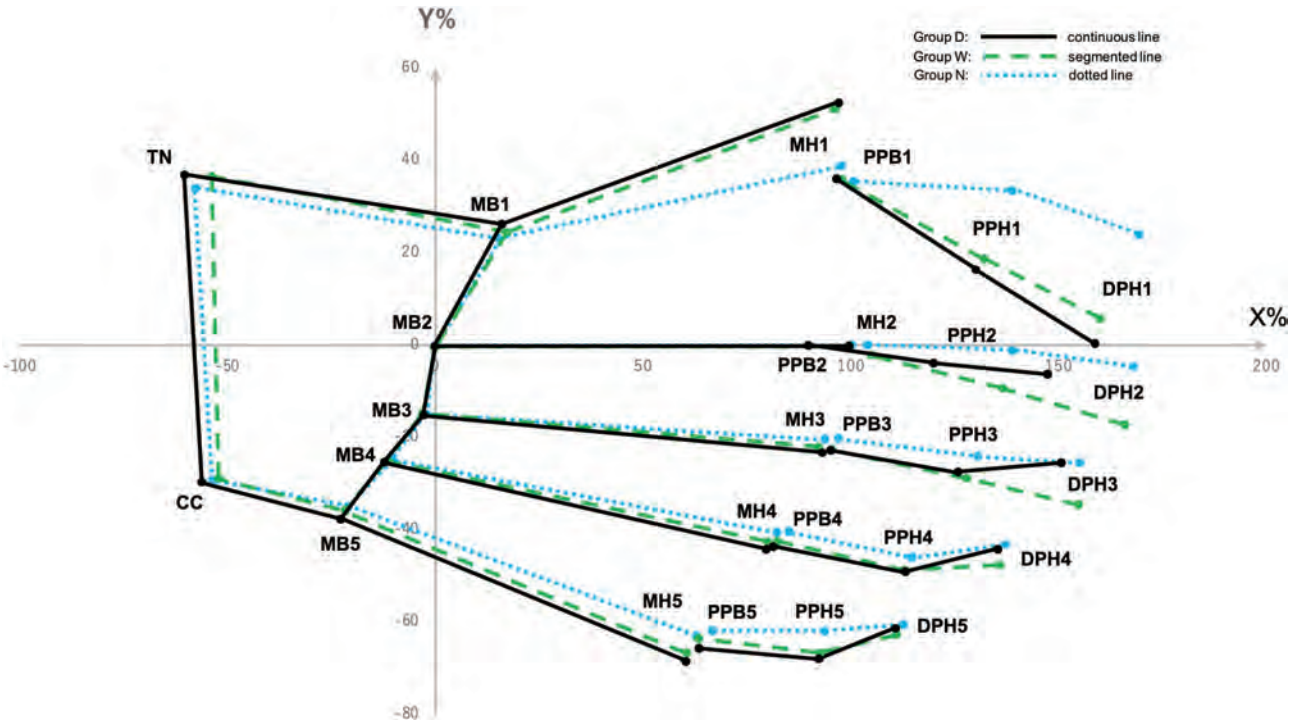

Fig. 3 Mapping representation of the 3 groups. D = hallux valgus with second metatarsophalangeal joint dislocation (continuous line); W = hallux valgus foot with normal lesser toes (segmented line); N = normal foot (dotted line); DPH1 to DPH5 = distal phalangeal head of first to fifth toe; PPH1 to PPH5 = proximal phalangeal head of first to fifth toe; PPB1 to PPB5 = proximal phalangeal base of first to fifth toe; MH1 to MH5 = metatarsal head of first to fifth metatarsal; MB1 to MB5 = metatarsal base of first to fifth metatarsal; TN = talonavicular junction; CC = calcaneocuboid junction

Table 4 Length (unit: percentages) and true length (unit: mm) of toes and metatarsals

				P			
	Group D	**Group W**	**Group N**	**Between groups**	**Group D vs. Group W**	**Group D vs. Group N**	**Group W vs. Group N**
Big toe length (T1-PPB1, %)	78.9 ± 4.5	77.6 ± 4.6	77.2 ± 3.8	ns	ns	ns	ns
Second toe length (T2-PPB2, %)	67.3 ± 6.3	70.6 ± 5.4	70.9 ± 5.0	< 0.01	< 0.01	< 0.01	ns
First metatarsal length (MH1-MB1, %)	84.1 ± 3.3	82.9 ± 2.7	82.2 ± 3.4	< 0.01	ns	< 0.01	ns
True big toe length (T1-PPB1, mm)	55.5 ± 3.5	55.8 ± 3.9	56.7 ± 3.9	ns	ns	ns	ns
True second toe length (T2-PPB2, mm)	47.3 ± 4.8	50.8 ± 4.2	52.1 ± 4.3	< 0.001	< 0.001	< 0.001	ns
True first metatarsal length (MH1-MB1, mm)	59.1 ± 3.0	59.7 ± 3.3	60.4 ± 4.1	ns	ns	ns	ns
Second metatarsal length (MH2-MB2, mm)	70.3 ± 3.4	72.0 ± 4.2	73.5 ± 4.6	ns	ns	< 0.01	ns

ns, not significant

showing toe adduction even when rotated according to MAA.

All feet were rotated counterclockwise according to its metatarsus adductus angle, making the midfoot axis the same direction as the new X-axis, the angle formed by the line connecting MH2 and MB2 and the x-axis was the metatarsus adductus angle.

Discussion

Second MTP joint dislocation is the most common chronic foot dislocation [26]. The mechanism is reportedly due to chronic overload during push-off with a transverse axis delivering power and oblique axis balancing the foot [17, 43]. Limited studies have evaluated second MTP joint dislocation associated with HV [27, 34]. In our institution, we observed an 11% incidence of dorsal second MTP joint dislocation over 10 years. This prompted us to assess second MTP joint dislocation in HV by analyzing matched HV groups, focusing on similar HVA and radiographic analysis of osseous structural features.

Severity of HV is a risk factor for second MTP joint dislocation [27, 34]. As HVA increases, plantar pressure distribution shifts from medial to lateral in the forefoot [28],

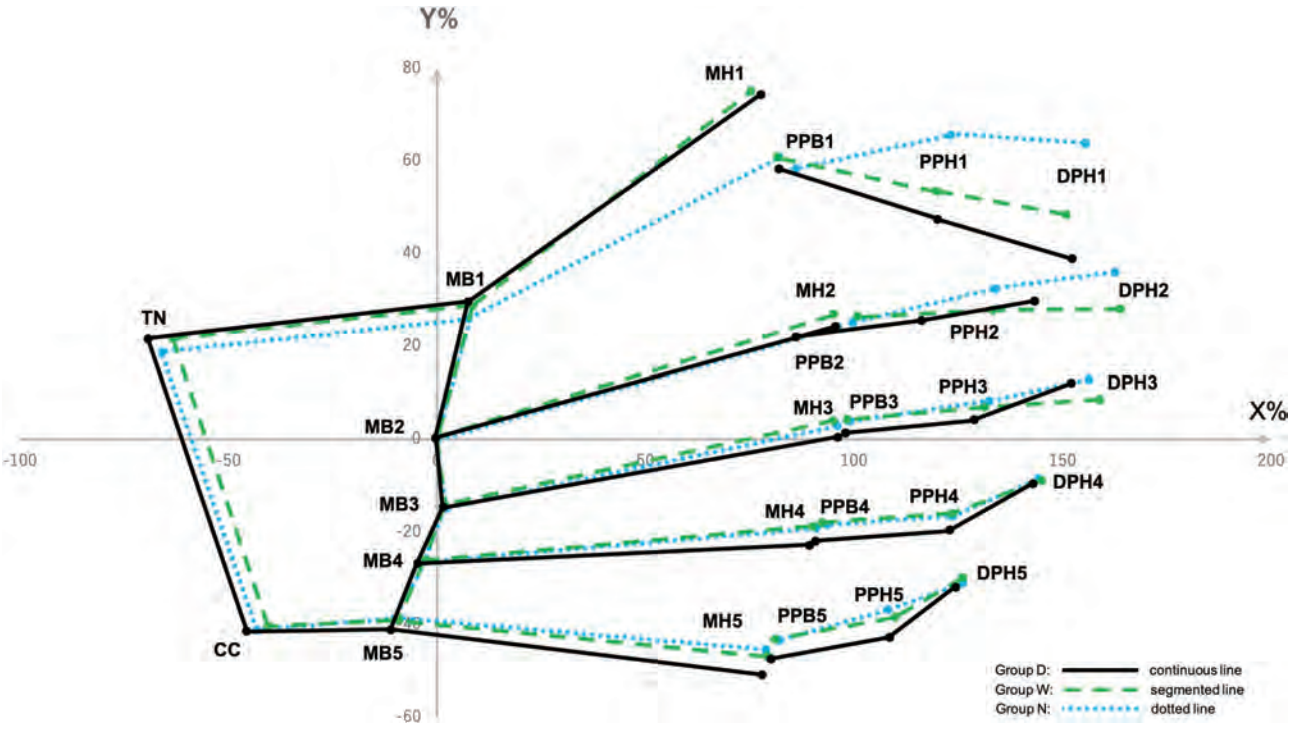

Fig. 4 Mapping representation of the 3 groups according to metatarsus adductus angle

resulting in great toe dysfunction during gait and heightened mechanical load on second and third metatarsal heads in moderate-to-severe HV [21]. Despite similar HVA between groups D and W, the great toe proximal phalanx head and distal phalanx head were significantly lateralized in the dislocation group and distal phalanx head overlapped the X-axis line near the second toe of control group.

The second toe buttresses the great toe [40], and both toes influence each other's position [25]. However, it is unclear how second MTP joint dislocation affects the rest of the forefoot structure. Those with dislocation exhibited proximal translation and deviation of the second toe. Additionally, the proximal phalanx of the adjacent lesser toe displayed lateral deviation, while the distal phalanx showed medial deviation and apparent adduction. The sequence of these positional changes, whether preceding or following dislocation, remain uncertain. A study on lesser toe deviation in HV highlighted the importance of the second MTP joint integrity and the role of the second toe as a supportive structure to the great toe [36]. Second toe dislocation creates a void between the great and third toe, allowing convergence of the great and lesser toes toward the second toe space. Alternatively, preexisting adducted alignment of lateral lesser toes could potentially push on the second toe laterally, with great toe pressing medially, eventually leading to dislocation. Causal relationship between adduction of lateral lesser toes and second toe dislocation, or vice versa, was undetermined. Consistent lateral shifting of the proximal phalanx with medialization of the distal third toe was observed exclusively in group D. Additionally, the fourth and fifth toes showed parallel adduction with the third toe (Fig. 3); although statistical significance was not observed in these coordinates compared to other groups.

This is the first study to demonstrate that lesser toes tend to lean towards adduction in cases of second MTP joint dislocation, suggesting progressive instability in the lateral forefoot. The adducted position of the third toe distal tip potentially indicates a pattern of forefoot collapse. Failure to correct distal deviations may lead to residual deformity, abnormal weight distribution, or recurrence of symptoms [30]. Surgical treatment must address both medial and lateral column corrections to relieve pressure on the lateral rays and restore proper forefoot alignment, reducing postoperative complications [28]. Further studies are needed to clarify the causal relationship underlying these findings.

A study found decreased M1/2 angle increases second MTP joint dislocation risk wherein severe HV leads to sustained pressure on the second toe, contributing to dislocation [27]. Conversely, less severe HV and M1/2 angle widening might theoretically alleviate pressure on the second toe. Our results show no direct association between the M1/2 angle and second MTP joint dislocation. Despite this, upon analyzing the dislocated second toe deviation, we found a significant association of M1/2 angle with deviation direction. Specifically, the M1/2

angle of the medial-deviation group was significantly higher than the lateral-deviation group. This supports findings that while M1/2 angle doesn't directly affect second MTP joint dislocation, it influences the direction of deviation. A higher M1/2 angle and lower MA likely lead to medial or neutral second toe dislocation due to intermetatarsal splaying, which creates space for the second toe. Conversely, a lower M1/2 angle reduces the distance between the hallux and second toe, causing mechanical crowding and lateral deviation [27]. These findings highlight the need for further research to explore whether the direction of toe dislocation may affect treatment outcomes or has clinical implications, such as whether medial deviation may benefit from proximal procedures like proximal metatarsal osteotomies or Lapidus fusion to address intermetatarsal splaying.

The role of plantar plate and collateral ligaments in second MTP stability has been established [1, 6, 10, 17, 47]; however, the influence of MT2 length remains uncertain [7, 10, 24, 27, 46]. A study found longer MT2 exhibited higher loads beneath the second MTP joint and concluded longer MT2 was related to plantar plate injuries [15]. Moreover, longer MT2 also lead to second MTP joint dislocation [7, 10, 46]. However, others still doubt that MT2 length is a factor [23, 24]. We found relative MT1 length in group D was significantly longer than group N while absolute length was similar. Additionally, the absolute MT2 length of group D was significantly shorter than control. The reason for the apparent lengthening of MT1 in group D is possibly due to absolute shortening of MT2 in group D which increases the relative value of MT1 and affects the percent measurement. In complete dislocation, plantar plate disappearance, MT2 head flattening, and cartilage degeneration could cause absolute shortening of MT2 [27]. Dorsal dislocation of the proximal phalanx further depresses the MT2 head [3, 37], which could lead to subtle sagittal deviation of MT2 and distorted longitudinal positioning on AP radiographs due to the presence of the second toe proximal phalanx on the dorsal aspect of MT2. However, it is possible MT2 shortening was present before dislocation and potentially associated with second MTP joint dislocation. With these findings, we cannot conclude MT2 length contributes to second MTP joint dislocation.

Medial positioning of the MT1 base and TN in the dislocation group was seen, indicating medial midfoot widening. A potential correlation is an associated progressive collapsing foot deformity (PCFD) [32]. Medial arch collapse and valgus deformity in PCFD may produce medialization of midfoot points in our 2-dimensional coordinate system. However, the association of PCFD and HV is still inconclusive [13, 20]. Furthermore, we did not assess lateral radiographs making it difficult to confirm the role of PCFD in second toe dislocation.

Management for second MTP joint dislocation with HV is usually performed subsequently with HV surgery which complicates treatment and affects outcome. Various surgical techniques have been developed for second toe dislocation [6, 31, 33, 43, 45]. The present study shows the osseous configuration of the HV foot with an associated second MTP joint dislocation. An understanding of associated anatomy is crucial for surgical planning to improve future treatment methods and outcomes.

This study has limitations, including the retrospective design and the lack of detailed clinical information for the included patients. While this is a radiographic study that describes deformities without determining their causes, it provides a deeper analysis of HV with second MTP joint dislocation by offering a visual map not typically appreciated on standard radiographs. Additionally, we only analyzed AP radiographs. Incorporating lateral views might have offered additional insights, given that these are sagittal deformities; however, we aimed to minimize variability in imaging parameters and enhance the reliability of their measurements and analyses by focusing on only one radiographic view. Including weightbearing CT scans would have provided more insight into the anatomy of this condition; however, since this is a relatively recent diagnostic imaging modality, only a small number of patients underwent this modality. Finally, an unequal number of patients across groups may have impacted results; a larger sample size could enhance the significance of results.

In conclusion, patients with second MTP joint dislocation exhibited a proximally translated second toe, an adducted third toe, a medialized MT1 base, and a lateralized great toe tip. Despite these differences, they shared similarities with HV feet without dislocations, including HVA, IMA, MAA, MT1 length, MT2 length, and first toe length. Notably, the M1/2 angle influenced the direction of second MTP joint dislocation: high M1/2 angles allowed the second toe to remain neutral or deviate medially, while low M1/2 angles caused lateral deviation of the second toe. The value of this study lies in its ability to visually map the entire HV foot with second MTP joint dislocation using coordinates on radiographs, providing a deeper understanding of foot anatomy that has not been previously demonstrated in earlier studies. These findings provide a foundation for future studies utilizing advanced imaging to explore anatomical risk factors and relationships. Understanding these structural dynamics could help surgeons predict associated risks, refine surgical techniques, and optimize patient outcomes.

Acknowledgements
NA.

Author contributions
AJT: Writing of the original draft, preparation of manuscript; HK: Design of the work, data analysis, manuscript revision; YU, YW, NM, YL: data collection and analysis; AT, ET: manuscript revision; YT: design of the work, final approval of manuscript.

Funding
NA.

Data availability
The data used and/or analyzed during the current study are available from the corresponding author on reasonable request.

Declarations

Ethics approval and consent to participate
Ethical approval for this study was obtained from Nara Medical University (IRB No. 3725). Due to the retrospective nature of this study, the requirement for individual informed consent was waived by the Institutional Review Board in accordance with national regulations. An opt-out statement regarding the use of medical data was published on our institution's website, allowing participants the opportunity to decline participation. This study was conducted in accordance with the principles of the World Medical Association Declaration of Helsinki.

Consent for publication
NA.

Competing interests
The authors declare no competing interests.

Received: 23 May 2024 / Accepted: 13 February 2025
Published online: 27 February 2025

References

1. Bhatia D, Myerson MS, Curtis MJ, et al. Anatomical restraints to dislocation of the second metatarsophalangeal joint and assessment of a repair technique. J Bone Joint Surg Am. 1994;76(9):1371–5.
2. Bishop J, Kahn A 3rd, and, Turba JE. Surgical correction of the splayfoot: the Giannestras procedure. Clin Orthop Relat Res, 1980(146): pp. 234–8.
3. Bolland BJ, Sauve PS, Taylor GR. Rheumatoid forefoot reconstruction: first metatarsophalangeal joint fusion combined with Weil's metatarsal osteotomies of the lesser rays. J Foot Ankle Surg. 2008;47(2):80–8.
4. Branch HE. Pathologic dislocation of the second toe. J Bone Joint Surg. 1937;19:978–84.
5. Cai Y, Song Y, He M, et al. Global prevalence and incidence of hallux valgus: a systematic review and meta-analysis. J Foot Ankle Res. 2023;16(1):63.
6. Chalayon O, Chertman C, Guss AD, et al. Role of plantar plate and surgical reconstruction techniques on static stability of lesser metatarsophalangeal joints: a biomechanical study. Foot Ankle Int. 2013;34(10):1436–42.
7. Coughlin MJ. Crossover second toe deformity. Foot Ankle. 1987;8(1):29–39.
8. Coughlin MJ. Hallux valgus. J Bone Joint Surg Am. 1996;78(6):932–66.
9. Coughlin MJ, Roger A. Mann Award. Juvenile hallux valgus: etiology and treatment. Foot Ankle Int. 1995;16(11):682–97.
10. Coughlin MJ. Second metatarsophalangeal joint instability in the athlete. Foot Ankle. 1993;14(6):309–19.
11. Coughlin MJ, Baumfeld DS, Nery C. Second MTP joint instability: grading of the deformity and description of surgical repair of capsular insufficiency. Phys Sportsmed. 2011;39(3):132–41.
12. Coughlin MJ, Grebing BR, Jones CP. Arthrodesis of the first metatarsophalangeal joint for idiopathic hallux valgus: intermediate results. Foot Ankle Int. 2005;26(10):783–92.
13. Coughlin MJ, Jones CP. Hallux valgus: demographics, etiology, and radiographic assessment. Foot Ankle Int. 2007;28(7):759–77.
14. Deland JT, Sung IH. The medial crosssover toe: a cadaveric dissection. Foot Ankle Int. 2000;21(5):375–8.
15. Fleischer AE, Hshieh S, Crews RT, et al. Association between Second Metatarsal Length and forefoot loading under the second Metatarsophalangeal Joint. Foot Ankle Int. 2018;39(5):560–7.
16. Ford LA, Collins KB, Christensen JC. Stabilization of the subluxed second metatarsophalangeal joint: flexor tendon transfer versus primary repair of the plantar plate. J Foot Ankle Surg. 1998;37(3):217–22.
17. Fortin PT, Myerson MS. Second metatarsophalangeal joint instability. Foot Ankle Int. 1995;16(5):306–13.
18. Hadi M, Walker C, Fahad A, et al. Radiological outcome of patients with Splay Foot following First and Fifth Metatarsal Osteotomies Performed simultaneously on the same foot. J Orthop Trauma Rehabilitation. 2012;16(2):59–61.
19. Haskell AC. Hallux Valgus. Coughlin and Mann's surgery of the Foot and Ankle. St. Louis: Elsevier; 2024. pp. 152–263.
20. Heyes GJ, Vosoughi AR, Weigelt L, et al. Pes Planus Deformity and its Association with Hallux Valgus Recurrence following Scarf Osteotomy. Foot Ankle Int. 2020;41(10):1212–8.
21. Hida T, Okuda R, Yasuda T, et al. Comparison of plantar pressure distribution in patients with hallux valgus and healthy matched controls. J Orthop Sci. 2017;22(6):1054–9.
22. Johnston RB 3rd, Smith J, Daniels T. The plantar plate of the lesser toes: an anatomical study in human cadavers. Foot Ankle Int. 1994;15(5):276–82.
23. Kaipel M, Krapf D, Wyss C. Metatarsal length does not correlate with maximal peak pressure and maximal force. Clin Orthop Relat Res. 2011;469(4):1161–6.
24. Kaz AJ, Coughlin MJ. Crossover second toe: demographics, etiology, and radiographic assessment. Foot Ankle Int. 2007;28(12):1223–37.
25. Kilmartin TE, O'Kane C. Correction of valgus second toe by closing wedge osteotomy of the proximal phalanx. Foot Ankle Int. 2007;28(12):1260–4.
26. Klein EE, Weil L Jr., Weil LS. The underlying osseous deformity in plantar plate tears: a radiographic analysis. Foot Ankle Spec. 2013;6(2):108–18.
27. Kokubo T, Hashimoto T, Suda Y, et al. Radiographic shape of Foot with Second Metatarsophalangeal Joint Dislocation Associated with Hallux Valgus. Foot Ankle Int. 2017;38(12):1374–9.
28. Koller U, Willegger M, Windhager R, et al. Plantar pressure characteristics in hallux valgus feet. J Orthop Res. 2014;32(12):1688–93.
29. Mann RA, Coughlin MJ. Hallux valgus–etiology, anatomy, treatment and surgical considerations. Clin Orthop Relat Res, 1981(157): pp. 31–41.
30. Monteagudo M, Martinez-de-Albornoz P. Management of complications after Hallux Valgus Reconstruction. Foot Ankle Clin. 2020;25(1):151–67.
31. Myerson MS, Jung HG. The role of toe flexor-to-extensor transfer in correcting metatarsophalangeal joint instability of the second toe. Foot Ankle Int. 2005;26(9):675–9.
32. Myerson MS, Thordarson DB, Johnson JE, et al. Classification and nomenclature: progressive collapsing foot deformity. Foot Ankle Int. 2020;41(10):1271–6.
33. Nery C, Coughlin MJ, Baumfeld D, et al. Lesser metatarsophalangeal joint instability: prospective evaluation and repair of plantar plate and capsular insufficiency. Foot Ankle Int. 2012;33(4):301–11.
34. Okuda R, Yoshimura Y, Shima H. Prevalence and radiological characteristics of the dislocation of the second metatarsophalangeal joint in patients undergoing hallux valgus surgery; a matched control study. J Orthop Sci. 2023;28(4):853–9.
35. Piggott H. The natural history of Hallux Valgus in Adolescence and early adult life. J Bone Joint Surg Br Volume. 1960;42–B(4):749–60.
36. Roan LY, Tanaka Y, Taniguchi A, et al. Why do lesser toes deviate laterally in hallux valgus? A radiographic study. Foot Ankle Int. 2015;36(6):664–72.
37. Saltzman CL, Johnson KA, Donnelly RE. Surgical treatment for mild deformities of the rheumatoid forefoot by partial phalangectomy and syndactylization. Foot Ankle. 1993;14(6):325–9.
38. Sarrafian SK. K.S., Anatomy of the Foot and Ankle. Philadelphia, PA: J. B. Lippincott; 1992.
39. Stainsby GD. Pathological anatomy and dynamic effect of the displaced plantar plate and the importance of the integrity of the plantar plate-deep transverse metatarsal ligament tie-bar. Ann R Coll Surg Engl. 1997;79(1):58–68.
40. Sundaram RO, Walsh HPJ. Amputation of a crossover 2nd toe in the presence of hallux valgus. Foot. 2003;13:196–8.
41. Tanaka Y, Takakura Y, Kumai T, et al. Radiographic analysis of hallux valgus. A two-dimensional coordinate system. J Bone Joint Surg Am. 1995;77(2):205–13.
42. Tanaka Y, Takakura Y, Sugimoto K, et al. Precise anatomic configuration changes in the first ray of the hallux valgus foot. Foot Ankle Int. 2000;21(8):651–6.
43. Thompson FM, Deland JT. Flexor tendon transfer for metatarsophalangeal instability of the second toe. Foot Ankle. 1993;14(7):385–8.

44. Wang B, Guss A, Chalayon O, et al. Deep transverse metatarsal ligament and static stability of lesser metatarsophalangeal joints: a cadaveric study. Foot Ankle Int. 2015;36(5):573–8.
45. Watson TS, Reid DY, Frerichs TL. Dorsal Approach for Plantar plate repair with Weil Osteotomy: operative technique. Foot Ankle Int. 2014;35(7):730–9.
46. Weber JR, Aubin PM, Ledoux WR, et al. Second metatarsal length is positively correlated with increased pressure and medial deviation of the second toe in a robotic cadaveric simulation of gait. Foot Ankle Int. 2012;33(4):312–9.
47. Yu GV, Judge MS, Hudson JR, et al. Predislocation syndrome. Progressive subluxation/dislocation of the lesser metatarsophalangeal joint. J Am Podiatr Med Assoc. 2002;92(4):182–99.

Publisher's note

日中笹川医学奨学金制度<学位取得コース>中間評価書
【課程博士：指導教官用】

Supported by 日本財団 THE NIPPON FOUNDATION

第45期　　研究者番号：　G4509

氏名	李 琬晴	LI WANQING	性別	F	生年月日	1997/1/2
中国所属機関（役職）	北京中医薬大学東方医院品質管理室（研究実習生）					
日本研究先（指導教官）	九州大学生体防御医学研究所（佐田亜衣子　教授）					
研究テーマ	皮膚再生プロセスにおける幹細胞制御機構の解明					
専攻種別	論文博士	□	課程博士	☑		

研究者評価（指導教官記入欄）

成績状況	優・良・可・不可から選択してください⇒	良	取得単位数	
	学業成績係数=		取得すべき単位総数	

学生本人が行った研究の概要

皮膚は、損傷時に組織を修復する高い再生能力を持つが、真皮に到達する深い傷を再生することは未だ困難である。指導教官である佐田は、表皮において、分裂頻度の異なる2種類の幹細胞集団が存在することを見出し、その役割や加齢変化について研究を進めてきた。低分裂、高分裂の表皮幹細胞は、組織の中で領域化し、規則的に配置する空間パターンを示す。恒常状態でそれぞれの幹細胞は、自らの領域のターンオーバーに寄与するが、損傷に応答し、一過的に互いの領域へと移動して機能を補完する潜在的な可塑性を有している。マウス毛包幹細胞において、組織損傷に応答した可塑性の発揮は、エピゲノム変化に伴う細胞系譜の書き換えによって制御されることが報告されているが）、佐田らが同定した2種類の表皮幹細胞で、損傷時に可塑性（低分裂から高分裂幹細胞への細胞運命の転換）が誘導される分子機構は不明である。LI氏は、表皮および皮膚全層の創傷治癒モデルを用い、損傷に応答した表皮幹細胞ダイナミクスの変化についての解析を進めた。その結果、皮膚全層の損傷では、高頻度分裂表皮幹細胞集団および毛包構造が喪失し、皮膚の再生が不完全である可能性を見出した。このことは、皮膚再生における真皮画分の重要性を示唆し、現在制御因子の同定を進めている。

総合評価

【良かった点】

プロジェクトは概ね順調に進行している。LI氏は、皮膚再生における表皮幹細胞変化に関する興味深いデータを取得している。

【改善すべき点】

研究に関する基礎的な知識や技量が不足している部分があり、さらなる努力が必要である。また、プロジェクトを質の高い論文として完成させるためには、研究背景に関する理解と考察、さらなるデータの蓄積が必須である。

【今後の展望】

今後、観察された表皮幹細胞変化を引き起こす分子標的の同定と機能解析を進めていく。

学位取得見込

奨学金支援終了後2年以内に学位取得が見込まれる。

評価者（指導教官記名）	佐田亜衣子	作成日：	2025年　3　月　5　日

日中笹川医学奨学金制度<学位取得コース>中間報告書
【研究者用】

第45期　　研究者番号：G4509　　作成日：2025年3月10日

氏名	李 琬晴	LI WANQING	性別	F	生年月日	1997/1/2
中国所属機関(役職)	北京中医薬大学東方医院品質管理室（研究実習生）					
日本研究先（指導教官）	九州大学生体防御医学研究所（佐田亜衣子　教授）					
研究テーマ(日文)	皮膚再生プロセスにおける幹細胞制御機構の解明					
Research theme	Understanding the dynamics of epidermal stem cells in skin regeneration					
専攻種別	論文博士	☐	課程博士	☑		

1．研究概要（1）

1）目的（Goal）

As the body's outermost layer, the skin is constantly exposed to external threats that can compromise its barrier function. To restore this barrier, wound healing follows a highly organized and progressive process consisting of four overlapping stages: homeostasis, inflammatory, proliferative, and remodeling phases[1]. During the proliferation phase, epidermal stem cells (EpiSCs) play a vital role in re-epithelialization, contributing to tissue regeneration[2-3].

A key aspect of this regenerative process is lineage plasticity, which enables stem cells to adapt their fate in response to injury[4] . Notably, hair follicle (HF) cells adjacent to the wound begin expressing KLF5, a transcription factor (TF) associated with the interfollicular epidermis (IFE). As HF-derived progenies migrate toward the wound's leading edge, KLF5 silences Sox9 (an HF TF), driving a complete fate switch and ensuring the permanent restoration of the epidermal barrier [5-6].

The mouse IFE consists of two distinct EpiSC populations[7]: slow-cycling SCs (marked by Dlx1), primarily residing in the interscale region, and fast-cycling SCs (marked by Slc1a3), located in the scale region. Similar patterns of stem cell heterogeneity and compartmentalization have also been observed in the human epidermis[8]. The plasticity of epidermal cells is not limited to HFSCs, as epidermis scratch wounds also demonstrate a dynamic response in these EpiSC populations: Slow-cycling and fast-cycling stem cell populations can temporarily migrate out of their typical territories to contribute to wound repair [7]. However, these stem cells returned to their typical territories once the wound was healed, indicating that the two stem cell populations were functionally interchangeable, highlighting a certain level of plasticity during epidermis-only wounds. However, it remains unknown how slow- and fast-cycling EpiSCs behave when skin wounds reach the dermis.

My project aims to investigate how the presence or absence of the dermal fraction influences epidermal stem cell behavior during wound healing and to elucidate the role of the dermis in regulating stem cell populations and tissue regeneration.

2）戦略（Approach）

Comparison of Two Wounding Models in Wild-Type Mice:
(1) Full-thickness wounds (epidermis + dermis injury)
(2) Epidermis-only scratch wounds
Lineage Tracing Analysis:
Using Dlx1-CreER (slow-cycling epidermal stem cells) and Slc1a3-CreER (fast-cycling epidermal stem cells) mouse models to track epidermal stem cell behavior.
Molecular and Cellular Analysis:
(1) Investigating the role of Wnt/β-catenin signaling in stem cell heterogeneity.
(2) Applying spatial omics to identify dermis-derived regeneration factors.

3）材料と方法（Materials and methods）

Animal Models:
Two-month-old C57BL/6J mice and genetically modified Dlx1-CreER and Slc1a3-CreER lineage tracing mice
Wounding Models:
2.5 × 10 mm full-thickness wounds or epidermis-only scratch wounds were created on the mouse tail epidermis using a scalpel.
Histological and Molecular Analysis:
Whole-mount staining (K10, K36, K14)
H&E staining for tissue morphology
Immunofluorescence to assess cellular marker expression

4）実験結果（Results）

To investigate the impact of the dermal fraction on EpiSC behavior during wound healing, we compared two wound models: full-thickness wounds and epidermis-only scratch wounds. Skin histology at the wound front indicates that the re-epithelialization process was complete by 6 weeks post-wounding. Whole-mount staining analysis revealed distinct alterations in slow-cycling (K10+) and fast-cycling (K36+) stem cell lineages between the two wound models. K36+ fast-cycling stem cells, which contribute to the scale region, were permanently lost in full-thickness wounds at both 6- and 12- weeks post-wounding. In contrast, previous study has demonstrated that the scale region undergoes complete regeneration in epidermis-only scratch wounds[7]. These findings suggest that the absence of the dermal fraction leads to the irreversible loss of the scale region, highlighting the essential role of dermal-epidermal interactions in regulating EpiSC lineage identity and skin regeneration.

1．研究概要(2)

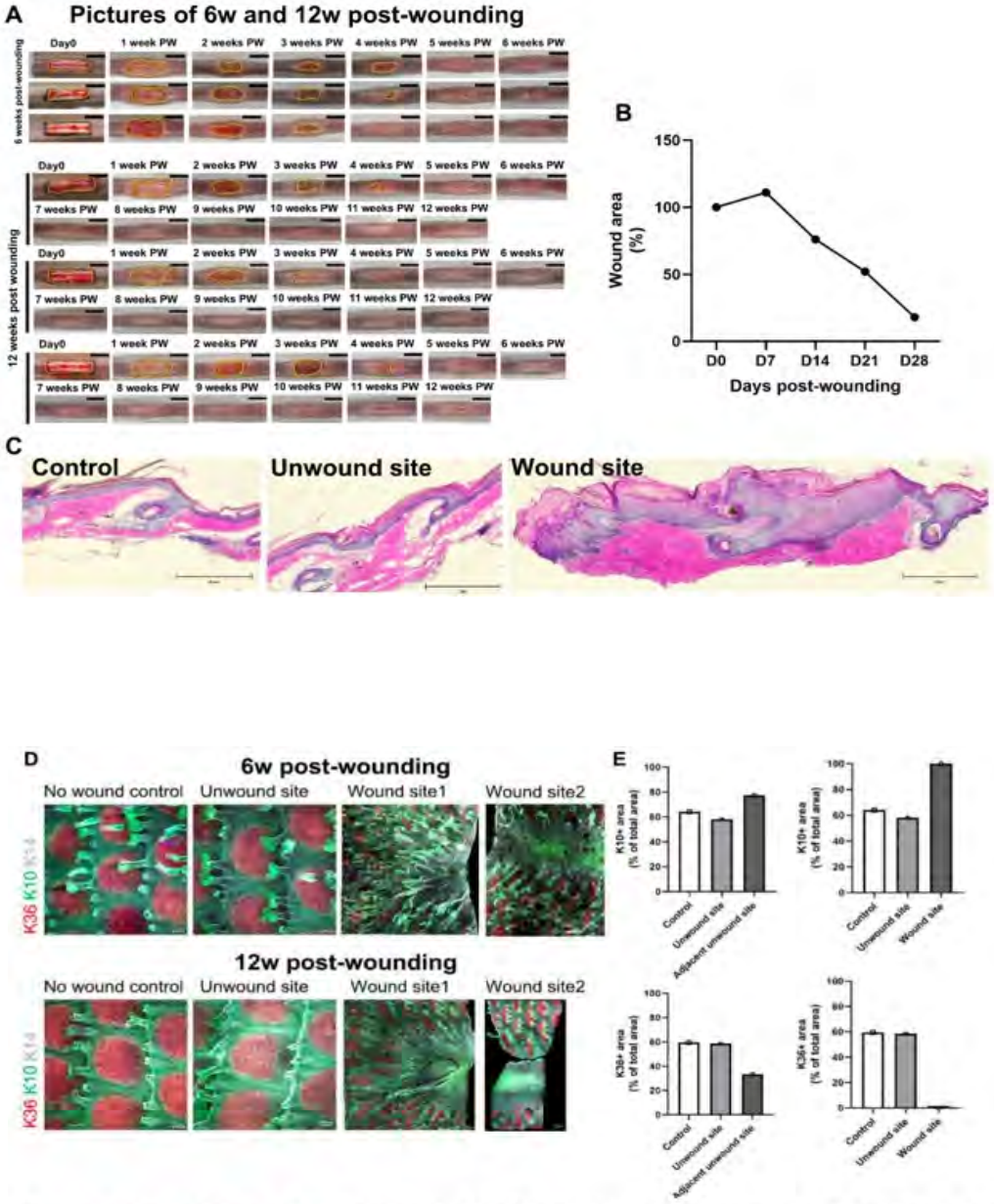

Figure 1. Histological and Molecular Analysis of Full-Thickness Wound Healing in Wild-Type Mice
A: Representative images of full-thickness wounds at 6- and 12-weeks post-wounding in 2-month-old WT mice. Scale bar: 5 mm. WT, wild-type.
B: Quantification of wound area over time.
C: Hematoxylin and eosin staining of tail sections from non-wounded WT mice, unwounded and wound sites of wounded WT mice. Scale bar: 300 μm.
D–E: Whole-mount staining of K10, K36, and K14 in the tail epidermis of non-wounded WT mice and WT mice at 6- and 12- weeks post-wounding, with quantification in (E). Scale bar: 100 μm (non-wounded control, unwounded site); 200 μm (wound site).

1．研究概要(3)

5)考察(Discussion)
Our findings indicate that the scale region is lost at full-thickness wound sites. Since fast-cycling EpiSCs primarily contribute to the scale region and slow-cycling EpiSCs to the interscale region, this suggests that the absence of the dermal fraction influences the behavior of fast-cycling EpiSCs. Two hypotheses arise:
1. Fast-cycling EpiSCs undergo a fate conversion into slow-cycling EpiSCs under full-thickness wound conditions.
2. Fast-cycling EpiSCs are lost during full-thickness wound regeneration.

To address these possibilities, lineage tracing using Dlx1-CreER and Slc1a3-CreER will be performed to elucidate how each EpiSCs population responds to full-thickness wounds. Utilizing these models, we aim to explore the cellular dynamics of EpiSCs and identify potential dermis-derived regulatory factors that may influence their regenerative capacity.

Gaining a deeper understanding of these mechanisms will offer valuable insights into the complex interplay between epidermal and dermal components during wound healing. The findings from this study could have significant clinical implications for treating chronic wounds, burns, and other severe skin injuries, ultimately paving the way for more effective therapeutic strategies to enhance skin regeneration.

6)参考文献(References)
[1] Xu, Z., Han, S., Gu, Z., & Wu, J. (2020). Advances and impact of antioxidant hydrogel in chronic wound healing. Advanced Healthcare Materials, 9(5), 1–18.
[2] Liu, Y., Ho, C., Wen, D., Sun, J., Huang, L., Gao, Y., et al. (2022). Targeting the stem cell niche: Role of collagen XVII in skin aging and wound repair. Theranostics, 12(15), 6446–6454.
[3] Rousselle, P., Braye, F., & Dayan, G. (2019). Re-epithelialization of adult skin wounds: Cellular mechanisms and therapeutic strategies. Advanced Drug Delivery Reviews, 146, 344–365.
[4] Joost, S., Jacob, T., Sun, X., La Manno, G., Sur, I., & Kasper, M. (2018). Single-cell transcriptomics of traced epidermal and hair follicle stem cells reveals rapid adaptations during wound healing. Cell Stem Cell, 25(3), 585–597.
[5] Ge, Y., Gomez, N. C., Adam, R. C., Nikolova, M., Yang, H., Verma, A., Lu, C. P. J., Polak, L., Yuan, S., & Elemento, O. (2017). Stem cell lineage infidelity drives wound repair and cancer. Cell, 169(4), 636–650.
[6] Adam, R. C., Yang, H., Ge, Y., Infarinato, N. R., Gur-Cohen, S., Miao, Y., Wang, P., Zhao, Y., Lu, C. P., & Kim, J. E. (2020). NFI transcription factors provide chromatin access to maintain stem cell identity while preventing unintended lineage fate choices. Nature Cell Biology, 22(6), 640–650.
[7] Sada, A., Jacob, F., Leung, E., Wang, S., White, B. S., Shalloway, D., et al. (2016). Defining the cellular lineage hierarchy in the interfollicular epidermis of adult skin. Nature Cell Biology, 18(6), 619–631.
[8] Ghuwalewala, S., Lee, S. A., Jiang, K., Baidya, J., Chovatiya, G., et al. (2022). Binary organization of epidermal basal domains highlights robustness to environmental exposure. The EMBO Journal, 41(18), e110488.

2. 執筆論文 Publication of thesis ※記載した論文を添付してください。Attach all of the papers listed below.

論文名 1 Title						
掲載誌名 Published journal						
	年 月	巻(号)	頁 ～ 頁	言語 Language		
第1著者名 First author		第2著者名 Second author		第3著者名 Third author		
その他著者名 Other authors						
論文名 2 Title						
掲載誌名 Published journal						
	年 月	巻(号)	頁 ～ 頁	言語 Language		
第1著者名 First author		第2著者名 Second author		第3著者名 Third author		
その他著者名 Other authors						
論文名 3 Title						
掲載誌名 Published journal						
	年 月	巻(号)	頁 ～ 頁	言語 Language		
第1著者名 First author		第2著者名 Second author		第3著者名 Third author		
その他著者名 Other authors						
論文名 4 Title						
掲載誌名 Published journal						
	年 月	巻(号)	頁 ～ 頁	言語 Language		
第1著者名 First author		第2著者名 Second author		第3著者名 Third author		
その他著者名 Other authors						
論文名 5 Title						
掲載誌名 Published journal						
	年 月	巻(号)	頁 ～ 頁	言語 Language		
第1著者名 First author		第2著者名 Second author		第3著者名 Third author		
その他著者名 Other authors						

3. 学会発表 Conference presentation ※筆頭演者として総会・国際学会を含む主な学会で発表したものを記載してください。

※Describe your presentation as the principal presenter in major academic meetings including general meetings or international meetings.

学会名 Conference						
演 題 Topic						
開催日 date	年 月 日		開催地 venue			
形式 method	□ 口頭発表 Oral	□ ポスター発表 Poster	言語 Language	□ 日本語	□ 英語	□ 中国語
共同演者名 Co-presenter						
学会名 Conference						
演 題 Topic						
開催日 date	年 月 日		開催地 venue			
形式 method	□ 口頭発表 Oral	□ ポスター発表 Poster	言語 Language	□ 日本語	□ 英語	□ 中国語
共同演者名 Co-presenter						
学会名 Conference						
演 題 Topic						
開催日 date	年 月 日		開催地 venue			
形式 method	□ 口頭発表 Oral	□ ポスター発表 Poster	言語 Language	□ 日本語	□ 英語	□ 中国語
共同演者名 Co-presenter						
学会名 Conference						
演 題 Topic						
開催日 date	年 月 日		開催地 venue			
形式 method	□ 口頭発表 Oral	□ ポスター発表 Poster	言語 Language	□ 日本語	□ 英語	□ 中国語
共同演者名 Co-presenter						

4. 受賞(研究業績) Award (Research achievement)

名 称 Award name				
	国名 Country		受賞年 Year of award	年 月
名 称 Award name				
	国名 Country		受賞年 Year of award	年 月

5. 本研究テーマに関わる他の研究助成金受給 Other research grants concerned with your resarch theme

受給実績 Receipt record	☐ 有　☐ 無
助成機関名称 Funding agency	
助成金名称 Grant name	
受給期間 Supported period	年　月 ～　年　月
受給額 Amount received	円
受給実績 Receipt record	☐ 有　☐ 無
助成機関名称 Funding agency	
助成金名称 Grant name	
受給期間 Supported period	年　月 ～　年　月
受給額 Amount received	円

6. 他の奨学金受給 Another awarded scholarship

受給実績 Receipt record	☐ 有　☐ 無
助成機関名称 Funding agency	
奨学金名称 Scholarship name	
受給期間 Supported period	年　月 ～　年　月
受給額 Amount received	円

7. 研究活動に関する報道発表 Press release concerned with your research activities

※記載した記事を添付してください。Attach a copy of the article described below

報道発表 Press release	☐ 有　☐ 無	発表年月日 Date of release	
発表機関 Released medium			
発表形式 Release method	・新聞　・雑誌　・Web site　・記者発表　・その他(　　)		
発表タイトル Released title			

8. 本研究テーマに関する特許出願予定 Patent application concerned with your research theme

出願予定 Scheduled	☐ 有　☐ 無	出願国 Application	
出願内容(概要) Application contents			

9. その他 Others

指導責任者(記名)　　佐田亜衣子

日中笹川医学奨学金制度<学位取得コース>中間評価書
【課程博士:指導教官用】

第45期　　研究者番号:　G4510

氏名	劉 夢潔	LIU　MENGJIE	性別	F	生年月日	1994/2/2
所属機関(役職)	長崎大学原爆後障害医療研究所国際保健医療福祉学研究分野(大学院生)					
日本研究先(指導教官)	長崎大学原爆後障害医療研究所国際保健医療福祉学研究分野(高村 昇　教授)					
研究テーマ	福島第一原子力発電所周辺立ち入り禁止区域における外部被曝線量・内部被曝線量推定と視覚的解析					
専攻種別	論文博士	□	課程博士	☑		

研究者評価(指導教官記入欄)

成績状況	優・良・可・不可から選択してください⇒	優	取得単位数	12
	学業成績係数=	3.5	取得すべき単位総数	35
学生本人が行った研究の概要	東京電力福島第一原子力発電所が立地する福島県大熊町、双葉町の中間貯蔵施設内、および除染を進めている特定復興再生拠点における空間線量率の変化を車載搭載型の線量計を用いてを評価した。 その結果、中間貯蔵施設では空間線量率の変化がほとんど見られなかったのに対して、特定復興再生拠点では除染に伴って空間線量率の低下が顕著にみられ、住民が帰還した場合の被ばく線量も年間1ミリシーベルト未満ときわめて限られることが推定された。 以上のことより、継続的な空間線量率の評価は、福島における避難区域の線量の推移を視覚化し、住民に帰還するかどうか決定するための判断材料として非常に重要であると考えられた。			
総合評価	【良かった点】 積極的に研究に取り組んでおり、これまで当該論文を含めて4編の論文が採択されている。			
	【改善すべき点】 特になし。			
	【今後の展望】 今後さらに数編の論文を執筆予定である。			
学位取得見込	順調にいけば2025年9月に博士号を取得予定である。			
評価者(指導教官記名)	高村　昇	作成日:	2025年　2　月　17　日	

日中笹川医学奨学金制度<学位取得コース>中間報告書
【研究者用】

第45期　　研究者番号：　G4510　　作成日：2025年3月10日

氏名	劉 夢潔	LIU　MENGJIE	性別	F	生年月日	1994/2/2
所属機関(役職)	長崎大学原爆後障害医療研究所国際保健医療福祉学研究分野（大学院生）					
日本研究先（指導教官）	長崎大学原爆後障害医療研究所国際保健医療福祉学研究分野（高村 昇　教授）					
研究テーマ(日文)	福島第一原子力発電所周辺立ち入り禁止区域における外部被曝線量・内部被曝線量推定と視覚的解析					
Research theme	External and Internal Exposure Dose Estimation and Visual Analysis at Restricted areas around the Fukushima Daiichi Nuclear Power Plant					
専攻種別	論文博士	☐	課程博士	☑		

1．研究概要（1）

1）目的（Goal）
Although 12 years have passed since the Fukushima Daiichi Nuclear Power Plant (FDNPP) accident, radionuclides with long half-lives such as Cs-134 (half-life: 2.1 years) and Cs-137 (30 years) remain in the environment. The Japanese government has already lifted the evacuation order for most restricted areas, excluding the difficult-to-return zone (DRZ), and set the specific reconstruction and regeneration base areas (SRRB) for future revitalization in Fukushima prefecture. Meanwhile, the interim storage facility areas (ISF), established in Futaba town and Okuma town, were used to store radioactive waste until final disposal. To estimate the current environmental contamination and the external and internal radiation exposure doses, we are going to conduct a one-year radiation monitoring program by the car-borne survey to evaluate the temporal ambient dose rate and the detected radiocesium rate in Futaba town and Okuma town.

2）戦略（Approach）
To help ensure the safety and future prosperity of residents and communities in the affected areas around the FDNPP, such long-term follow-up monitoring of radiation contamination levels during the reconstruction phases are essential.

3）材料と方法（Materials and methods）
Our study conducted in the ISF within DRZ and the SRRB(including the evacuation-order-lifted area) of Futaba and Okuma towns from October 2021 to November 2022.
1. Use Car-borne survey system (Radi-probe) to detect the ambient dose rate and the detection rates of radiocesium (134+137Cs), then calculated the annual external effective doses of decontamination workers and estimated the median doses.
2. Airborne dust sampling using a high-volume air sampler (HV) and radionuclides analyses using gamma spectrometry (HPGe) to estimate the internal radiation exposure by inhalation.

4）実験結果（Results）
The ambient dose rate in the ISF area clustered < 0.38 μSv/h in Futaba town (79%-89%) and 0.38-1.9 μSv/h in Okuma town (73%-83%). By contrast, the ambient dose rate clustered < 0.19 μ Sv/h (79%-90%) in the evacuation order lifted areas in Futaba town and 0.19-0.95 μ Sv/h (66%-94%) in the SRRB in Okuma town.
The detection rates of Cs-134 and Cs-137 ranged from 0%-2.6% and 1.7%-5.9% in Futaba town, 10.4%-24.2% and 13.2%-29.5% in Okuma town, respectively.
The median ambient dose rate in the ISF and evacuation order lifted areas in Futaba town ranged from 0.15-0.21 ❍Sv/h and from 0.053-0.086 ❍Sv/h, the value in the ISF and SRRB in Okuma town ranged from 0.68-0.90 ❍Sv/h and from 0.23-0.38 ❍Sv/h, respectively.
The estimated annual external effective doses for decontamination workers in the ISF were estimated at 0.17 mSv/y in Futaba town and 0.84 mSv/y in Okuma town, for residents were estimated at 0.091 mSv/y in Futaba town and 0.76 mSv/y in Okuma town. Although the environmental radioactivity in the ISF was higher than that in open areas (i.e., the evacuation order lifted areas in Futaba town and the SRRB in Okuma town), only minor temporal changes were seen in the ambient dose and detection rate of radiocesium (the proportion of radiocesium detected points per all measuring points) in those areas, respectively. The estimated annual effective doses for decontamination workers as well as residents in the each area were less than <1 mSv/y.

1．研究概要(2).

5)考察(Discussion)

The ambient dose rate and detection rate of radiocesium were significantly higher in the ISF area than in SRRB, and the values in Okuma town were significantly higher than in Futaba town, which is attributed to decontamination.

Minor temporal changes seen in the ambient dose and detection rate of radiocesium may be the result of physical decay and decontamination. Resuspension caused by human activities and weather could also affect the detection rate of radiocesium.

The annual external effective doses in Futaba town and Okuma town were estimated to be at a limited level （< 1 mSv/y), less than the recommended value by the Japanese government based on the recommendation of the International Commission on Radiological Protection (ICRP).

Environmental radioactivity monitoring and radiation education are necessary to ensure the safety for workers who engage in decontamination work and residents who will return to the SRRB.

In conclusion, our research not only provides valuable insights into the temporal variations of environmental radioactivity but also emphasizes the ongoing commitment required to safeguard the health and safety of those involved in Fukushima's recovery efforts.

6)参考文献(References)

1. Ministry of the Environment of Japan. Environmental Remediation: Decontamination. http://josen.env.go.jp/en/decontamination/
2. Ministry of the Environment of Japan. Environmental remediation: Interim Storage Facility. http://josen.env.go.jp/en/storage/
3. Ministry of the Environment of Japan. Annual Report on the Environment in Japan 2021, Chapter 4: Efforts for Reconstruction and Environmental Restoration from the Great East Japan Earthquake. https://www.env.go.jp/content/900457471.pdf
4. The International Commission on Radiological Protection (ICRP). The 2007 Recommendations of the International Commission on Radiological Protection (2007).
5. The International Commission on Radiological Protection (ICRP). Application of the Commission's Recommendations to the Protection of People Living in Long-term Contaminated Areas after a Nuclear Accident or a Radiation Emergency. (2011).
6. Kobayashi, S. et al. Radioactive contamination mapping of northeastern and eastern Japan by a car-borne survey system, RadiProbe. J. Environ. Radioact. 139, 281-293 (2015).

2. 執筆論文 Publication of thesis ※記載した論文を添付してください。Attach all of the papers listed below.

論文名 1 Title	Temporal variation in environmental radioactivity and radiation exposure doses in the restricted areas around the Fukushima Daiichi Nuclear Power Plant				
掲載誌名 Published journal	Scientific reports				
	2023 年 12 月	13(1) 巻(号)	頁 ～ 頁	言語 Language	English
第1著者名 First author	Mengjie Liu	第2著者名 Second author	Yasuyuki Taira	第3著者名 Third author	Masahiko Matsuo
その他著者名 Other authors	Makiko Orita, Hitomi Matsunaga, Yuya Kashiwazaki, Xu Xiao, Noboru Takamura				
論文名 2 Title	Comparative analysis of public concerns regarding treated water discharged from the Fukushima Daiichi Nuclear Power Station: perspectives before and after the initial release.				
掲載誌名 Published journal	Journal of radiation research				
	2025 年 1 月	66(1) 巻(号)	103 頁 ～ 105 頁	言語 Language	English
第1著者名 First author	Mengjie Liu	第2著者名 Second author	Hitomi Matsunaga	第3著者名 Third author	Makiko Orita
その他著者名 Other authors	Yuya Kashiwazaki, Xu Xiao, Noboru Takamura				
論文名 3 Title	Residents of the towns in which the Fukushima Daiichi nuclear station is located express more worries about reputational damage than about the discharge of treated water itself.				
掲載誌名 Published journal	Journal of radiation research				
	2025 年 2 月	rraf003 巻(号)	頁 ～ 頁	言語 Language	English
第1著者名 First author	Mengjie Liu, Hitomi Matsunaga	第2著者名 Second author	Makiko Orita	第3著者名 Third author	Yuya Kashiwazaki
その他著者名 Other authors	Xu Xiao, Noboru Takamura				
論文名 4 Title					
掲載誌名 Published journal					
	年 月	巻(号)	頁 ～ 頁	言語 Language	
第1著者名 First author		第2著者名 Second author		第3著者名 Third author	
その他著者名 Other authors					
論文名 5 Title					
掲載誌名 Published journal					
	年 月	巻(号)	頁 ～ 頁	言語 Language	
第1著者名 First author		第2著者名 Second author		第3著者名 Third author	
その他著者名 Other authors					

3. 学会発表 Conference presentation ※筆頭演者として総会・国際学会を含む主な学会で発表したものを記載してください。

※Describe your presentation as the principal presenter in major academic meetings including general meetings or international meetings.

学会名 Conference	The 9th International Symposium of the Network-type Joint Usage/Research Center for Radiation Disaster Medical Science Presenter			
演 題 Topic	The Impact of Nuclear Disaster Experiences on Spatial Stigma: A Study of Fukushima Residents at 13 Years after the Nuclear Accident			
開催日 date	2025 年 2 月 19 日	開催地 venue	Fukushima city	
形式 method	☑ 口頭発表 Oral ☑ ポスター発表 Poster	言語 Language	☐ 日本語 ☑ 英語 ☐ 中国語	
共同演者名 Co-presenter	Yuya Kashiwazaki, Hitomi Matsunaga, Xu Xiao, Makiko Orita, and Noboru Takamura			
学会名 Conference	The 95th Annual Meeting of The Japanese Society for Hygiene			
演 題 Topic	Addressing Spatial Stigma and Promoting Community Recovery in Post-FDNPP Fukushima			
開催日 date	2025 年 3 月 21 日	開催地 venue	Saitama	
形式 method	☑ 口頭発表 Oral ☐ ポスター発表 Poster	言語 Language	☐ 日本語 ☑ 英語 ☐ 中国語	
共同演者名 Co-presenter	Yuya Kashiwazaki, Hitomi Matsunaga, Xu Xiao, Makiko Orita, and Noboru Takamura			
学会名 Conference				
演 題 Topic				
開催日 date	年 月 日	開催地 venue		
形式 method	☐ 口頭発表 Oral ☐ ポスター発表 Poster	言語 Language	☐ 日本語 ☐ 英語 ☐ 中国語	
共同演者名 Co-presenter				
学会名 Conference				
演 題 Topic				
開催日 date	年 月 日	開催地 venue		
形式 method	☐ 口頭発表 Oral ☐ ポスター発表 Poster	言語 Language	☐ 日本語 ☐ 英語 ☐ 中国語	
共同演者名 Co-presenter				

4. 受賞（研究業績） Award (Research achievement)

名 称 Award name				
	国名 Country		受賞年 Year of award	年 月
名 称 Award name				
	国名 Country		受賞年 Year of award	年 月

研究者番号：G4510

5. 本研究テーマに関わる他の研究助成金受給 Other research grants concerned with your resarch theme

受給実績 Receipt record	☐ 有　　☐ 無
助成機関名称 Funding agency	
助成金名称 Grant name	
受給期間 Supported period	年　　月 ～　　年　　月
受給額 Amount received	円
受給実績 Receipt record	☐ 有　　☐ 無
助成機関名称 Funding agency	
助成金名称 Grant name	
受給期間 Supported period	年　　月 ～　　年　　月
受給額 Amount received	円

6. 他の奨学金受給 Another awarded scholarship

受給実績 Receipt record	■ 有　　☐ 無
助成機関名称 Funding agency	Nagasaki University
奨学金名称 Scholarship name	Nagasaki University Special Research Student Scholarship
受給期間 Supported period	2024　年　4　月 ～　2025　年　4　月
受給額 Amount received	600,000 円

7. 研究活動に関する報道発表 Press release concerned with your research activities

※記載した記事を添付してください。Attach a copy of the article described below

報道発表 Press release	☐ 有　　☐ 無	発表年月日 Date of release	
発表機関 Released medium			
発表形式 Release method	・新聞　・雑誌　・Web site　・記者発表　・その他（　　）		
発表タイトル Released title			

8. 本研究テーマに関する特許出願予定 Patent application concerned with your research theme

出願予定 Scheduled	☐ 有　　☐ 無	出願国 Application	
出願内容（概要） Application contents			

9. その他 Others

指導責任者（記名）Noboru Takamura

scientific reports

Check for updates

OPEN

Temporal variation in environmental radioactivity and radiation exposure doses in the restricted areas around the Fukushima Daiichi Nuclear Power Plant

Mengjie Liu[1], Yasuyuki Taira[1,2], Masahiko Matsuo[1], Makiko Orita[1,2], Hitomi Matsunaga[1], Yuya Kashiwazaki[1], Xu Xiao[1] & Noboru Takamura[1]✉

Temporal variation and fluctuation in environmental contamination in Futaba town and Okuma town, the location of the Fukushima Daiichi Nuclear Power Plant (FDNPP), were evaluated based on a car-borne survey conducted from October 2021 to November 2022. Although the environmental radioactivity in the interim storage facility area (ISF) was higher than that in open areas (i.e., the evacuation order lifted areas in Futaba town and the Specific Reconstruction and Regeneration Base area [SRRB] in Okuma town), only minor temporal changes were seen in the ambient dose and detection rate of radiocesium (the proportion of radiocesium detected points per all measuring points) in those areas, respectively. These findings suggest that the observed variations may result from physical decay and environmental remediation. Resuspension caused by human activities and weather could also affect the detection rate of radiocesium. The annual external effective doses in Futaba town and Okuma town were estimated to be at a limited level (< 1 mSv/year). Nevertheless, to help ensure the safety and future prosperity of residents and communities in the affected areas around the FDNPP, long-term follow-up monitoring of temporal exposure dose levels during the recovery and reconstruction phases is extremely important.

On March 11, 2011, the Great East Japan Earthquake (magnitude 9.0) occurred off the east coast of Honshu Island and triggered a massive tsunami that severely affected Iwate, Miyagi, and Fukushima Prefectures, causing a nuclear accident at the Fukushima Daiichi Nuclear Power Plant (FDNPP), located approximately 200 km northeast of Tokyo[1–4]. Immediately after the FDNPP accident, the Japanese government implemented emergency protective measures for the public, such as planning for evacuation, sheltering, and relocation, distributing stable iodine to help prevent further radioactive iodine uptake by the thyroid gland, and restricting food and water consumption. Evacuation of the 20-km area around the FDNPP began immediately on March 11, 2011, and was completed 1 day later. In areas within a 20–30 km radius, residents were ordered to remain indoors and then advised to evacuate voluntarily[4]. Subsequently, NRA, TEPCO and other institutes have continuously conducted a comprehensive monitoring program using airborne survey, car-borne survey, aerial-vehicle survey and radionuclide analysis, including measurements of environmental dose rates and radionuclide activity concentrations in soil, crops, food, and animal feed[2,3,5–7]. Therefore, such survey and monitoring programs are extremely important for the precise evaluation of environmental remediation and the revitalization of Fukushima Prefecture.

By March 19, 2018, the residential areas that had been under evacuation orders, including surrounding roads, residential areas, farmland, and forests, but excluding the difficult to return zones (DRZs), were nearly

[1]Department of Global Health, Medicine and Welfare, Atomic Bomb Disease Institute, Nagasaki University Graduate School of Biomedical Sciences, 1-12-4 Sakamoto, Nagasaki City, Nagasaki Prefecture 852-8523, Japan. [2]Fukushima Global Medical Science Center and Radiation Medical Science Center for the Fukushima Health Management Survey Fukushima Medical University, Fukushima City, Fukushima Prefecture, Japan. ✉email: takamura@nagasaki-u.ac.jp

completely decontaminated[5]. At the same time, an Interim Storage Facility (ISF) was built to store and manage the contaminated soil and waste removed during off-site decontamination work, as well as specified waste (radioactive waste exceeding 8000 Bq/kg) in Fukushima Prefecture, safely until final disposal. Construction of the ISF began in November 2016, and storage of the removed soil and waste began in Okuma town in October 2017 and Futaba town in December 2017[8–11]. Moreover, under the provisions of the Act on Special Measures for the Reconstruction and Revitalization of Fukushima, which was revised in May 2017, six municipalities in restricted areas, including the DRZs in Futaba town and Okuma town, developed revitalization plans[8,10,11]. Under these plans, the Ministry of the Environment conducts decontamination and demolition work in these areas. Due to the efficiency of the decontamination work, on March 4, 2020, the evacuation order was lifted in part of Futaba (evacuation order lifted area)[8]. Subsequently, the evacuation orders for the Specific Reconstruction and Regeneration Base area (SRRB) in Okuma and Futaba were lifted on June 30 and August 30, 2022, respectively[12].

The nuclear accident resulted in the release of various artificial radionuclides, including cesium-134 (^{134}Cs), cesium-137 (^{137}Cs), and iodine-131 (^{131}I) into the atmosphere and eventual deposition on land and sea in the areas around the FDNPP[1–3]. Radionuclides with long half-lives such as ^{134}Cs (half-life: 2.1 years) and ^{137}Cs (half-life: 30 years) remain in the environment, although more than 12 years have passed in March 2023 since the FDNPP accident, which was one source of the ambient dose rate[1,4,6]. Although environmental remediation in the SRRB might allow new residential areas to be constructed in Futaba town and Okuma town in the future, residents in Fukushima still have concerns about radiation which affects their intention to return[13,14]. In addition, environmental radioactivity around the restricted areas, including the ISF, should be monitored and controlled because these areas are next to the SRRB. Therefore, in the present study, a car-borne survey was conducted to evaluate temporal variation in ambient dose and detection rate of radiocesium in Futaba town and Okuma town (Fig. 1).

Results

In the present study, 10 surveys were conducted in Futaba town and Okuma town from October 2021 to November 2022. The frequency distributions of the ambient dose rate and detection rate of radiocesium (^{134}Cs and ^{137}Cs) within the ISF, SRRB, and evacuation order lifted areas of Futaba town and Okuma town are shown in Tables 1 and 2 and Figs. 2 and 3. The median ambient dose rate in the ISF and evacuation order lifted areas in Futaba town ranged from 0.15 to 0.21 μSv/h (measurement points are 887–1800) and from 0.053 to 0.086 μSv/h (477–781), respectively, and those in the ISF and SRRB in Okuma town ranged from 0.68 to 0.90 μSv/h (2420–3688) and from 0.23 to 0.38 μSv/h (503–1317), respectively (Tables 1 and 2). Moreover, the ambient dose rate in the ISF areas (> 0.95 μSv/h) were significantly higher than those in the evacuation order lifted areas in Futaba town and the SRRB in Okuma town ($p < 0.01$). The proportions of the ISF area exceeding this value (> 0.95 μSv/h) were approximately 1–5% in Futaba town and 29–46% in Okuma town, and approximately 0% and 1–10% in the evacuation order lifted areas and SRRB, respectively (Figs. 2 and 3). The ambient dose rate in the ISF area clustered < 0.38 μSv/h in Futaba town (79–89%) and 0.38–1.9 μSv/h in Okuma town (73–83%). By contrast, the ambient dose rate clustered < 0.19 μSv/h (79–90%) in the evacuation order lifted areas in Futaba town and 0.19–0.95 μSv/h (66–94%) in the SRRB in Okuma town.

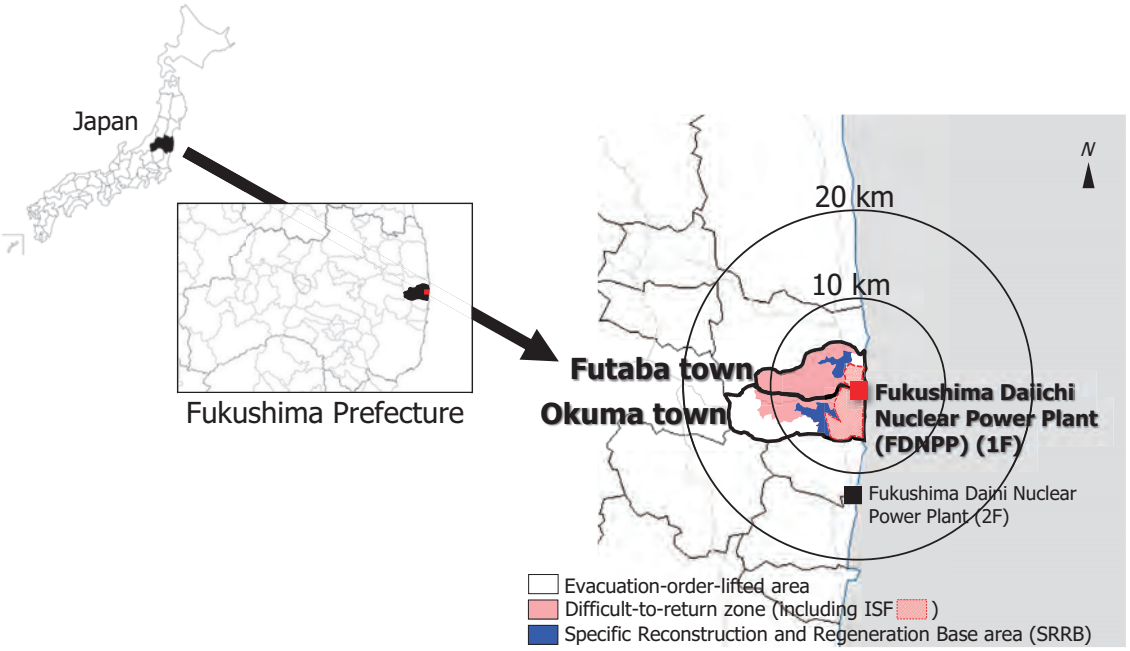

Figure 1. Location of Futaba town and Okuma town, Fukushima Prefecture, Japan. The second author (Y.T.) created the map using GIS software (Green Map III; Tokyo Shoseki, Tokyo, Japan; https://shop.tokyo-shoseki.co.jp/map). Reprinted from Green Map III under a CC BY license, with permission from Tokyo Shoseki; original copyright 2003.

	ISF		Evacuation order lifted area	
Survey date	Measurement points	Median (min–max) (μSv/h)	Measuring points	Median (min–max) (μSv/h)
19/10/2021	887	0.21 (0.050–1.8)	477	0.059 (0.029–0.63)
20/11/2021	1800	0.20 (0.048–1.8)	746	0.062 (0.029–0.60)
18/12/2021	1701	0.21 (0.039–2.0)	781	0.064 (0.029–0.51)
28/5/2022	1450	0.16 (0.042–1.3)	778	0.086 (0.025–1.0)
25/6/2022	1266	0.16 (0.032–1.3)	697	0.060 (0.025–0.71)
23/7/2022	1189	0.15 (0.040–1.3)	727	0.053 (0.020–0.49)
27/8/2022	1178	0.21 (0.034–1.6)	600	0.070 (0.030–0.68)
17/9/2022	1185	0.19 (0.035–1.5)	567	0.067 (0.027–0.82)
15/10/2022	1109	0.19 (0.040–1.5)	579	0.083 (0.024–0.72)
19/11/2022	1147	0.21 (0.049–1.9)	585	0.083 (0.030–0.85)
Annual estimated effective doses of *workers* in mSv/year (average)		0.17	Annual estimated effective doses of *residents* in mSv/year (average)	0.091

Table 1. Ambient dose rate in the interim storage facility (ISF) area and evacuation order lifted area in Futaba town from October 2021 to November 2022.

	ISF		SRRB	
Survey date	Measurement points	Median (min–max) (μSv/h)	Measuring points	Median (min–max) (μSv/h)
18/10/2021	2420	0.83 (0.11–3.4)	535	0.38 (0.13–1.3)
21/11/2021	3211	0.86 (0.11–4.0)	836	0.35 (0.15–1.3)
19/12/2021	2839	0.90 (0.10–3.4)	1317	0.32 (0.081–1.3)
29/5/2022	3688	0.69 (0.10–3.3)	503	0.23 (0.12–2.0)
26/6/2022	3493	0.68 (0.10–4.1)	526	0.25 (0.12–2.1)
24/7/2022	2484	0.69 (0.10–2.9)	942	0.24 (0.11–1.9)
28/8/2022	3464	0.77 (0.11–3.7)	576	0.27 (0.15–2.2)
18/9/2022	2960	0.75 (0.10–4.2)	560	0.26 (0.11–2.2)
16/10/2022	2669	0.73 (0.094–5.1)	627	0.24 (0.12–2.0)
20/11/2022	2658	0.82 (0.094–4.9)	526	0.25 (0.11–2.4)
Annual estimated effective doses of *workers* in mSv/year (average)		0.84	Annual estimated effective doses of *residents* in mSv/year (average)	0.76

Table 2. Ambient dose rate in the interim storage facility (ISF) area and Specific Reconstruction and Regeneration Base (SRRB) area in Okuma town from October 2021 to November 2022.

In other words, the ambient dose rate (> 0.38 μSv/h) in the ISF areas showed a significantly higher distribution ($p < 0.01$) in Okuma town (80–90%) than in Futaba town (10–23%). On the other hand, the ambient dose rate in the SRRB in Okuma town (0.38 μSv/h; 59–87%) was higher than that in the evacuation order lifted areas in Futaba town (< 0.19 μSv/h; 79–90%) (Figs. 2 and 3). The ambient dose rate has stabilized at the relatively low level in Futaba town and Okuma town, although there were some fluctuations during the survey period (Figs. 2 and 3). For example, the median ambient dose rate in the SRRB in Okuma town seems decreased by 34%, from 0.38 μSv/h in October 2021 to 0.25 μSv/h in November 2022, in Futaba town seems increased from 0.059 μSv/h in October 2021 to 0.083 μSv/h in November 2022, and the ISF areas showed relatively lower values in May, June, and July 2022 in both towns (Tables 1 and 2).

Furthermore, the detection rate of radiocesium (^{134}Cs and ^{137}Cs) indicated the proportion of measurement points where ^{134}Cs and ^{137}Cs could be detected compared to all measurement points in Futaba town and Okuma town as shown in Figs. 2 and 3. The detection rate of ^{134}Cs and ^{137}Cs ranged from 0 to 2.6% and from 1.7 to 5.9% in Futaba town, respectively, and from 10.4 to 24.2% and from 13.2 to 29.5% in Okuma town, respectively. The detection rate of radiocesium in Okuma town were significantly higher than those in Futaba town ($p < 0.01$). Additionally, the value in the evacuation order lifted area and SRRB were lower compared to those for the ISF area, with the detection rate of ^{137}Cs ranging from 0 to 1.2% in Futaba town (^{134}Cs no detected points), and the detection rate of ^{134}Cs ranging from 0 to 8.2% and the detection rate of ^{137}Cs ranging from 0.5 to 7.8% in Okuma town (Figs. 2 and 3 and Supplementary Figs. S1, S2 and S3). The detection rate of ^{134}Cs were lower than those of ^{137}Cs because 12 years had passed since the FDNPP accident (approximately six times the physical half-life of ^{134}Cs). The physical decay of radiocesium was estimated to be 4.9% from October 2021 to November 2022, which contributed to the decrease of the detection rate of radiocesium and ambient dose rate in Futaba town and Okuma town, respectively (Supplementary Table S1).

The annual external effective doses for decontamination workers in the ISF were estimated at 0.17 mSv/year in Futaba town and 0.84 mSv/year in Okuma town. By contrast, the annual effective doses (corresponding to

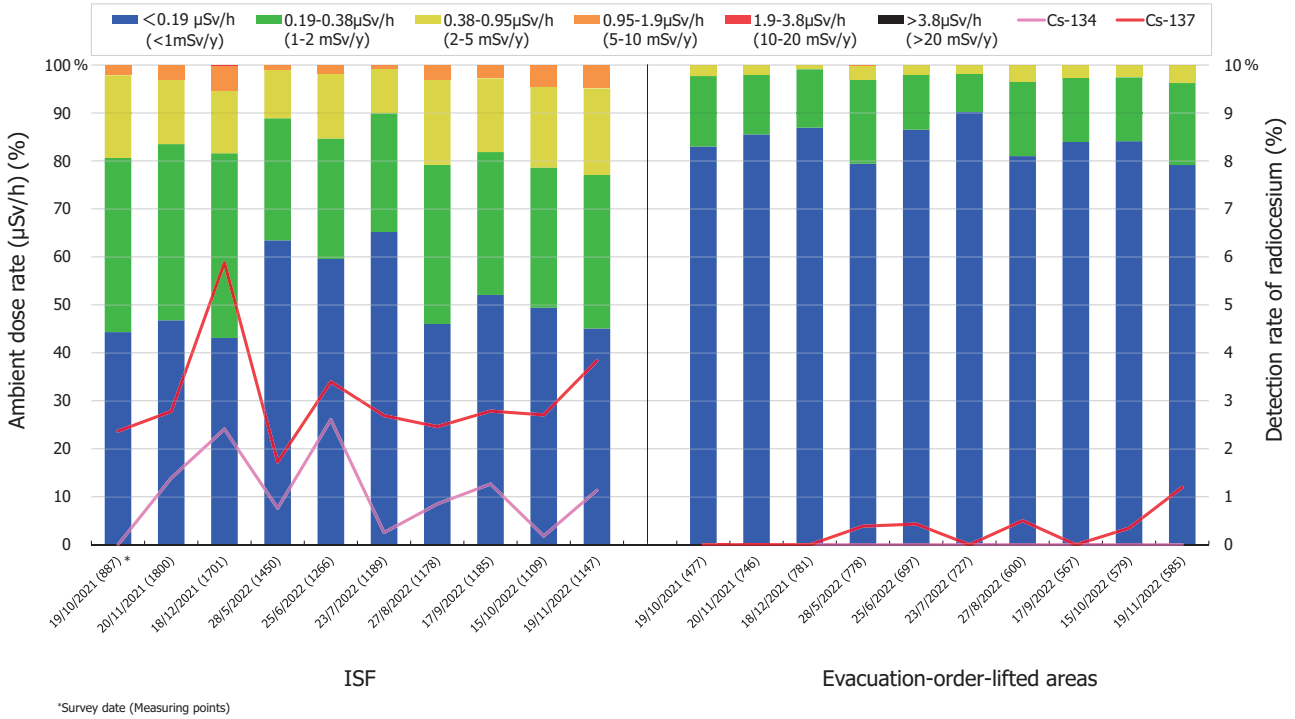

Figure 2. Temporal variation in the ambient dose rate distribution and detection rate of radiocesium in Futaba town.

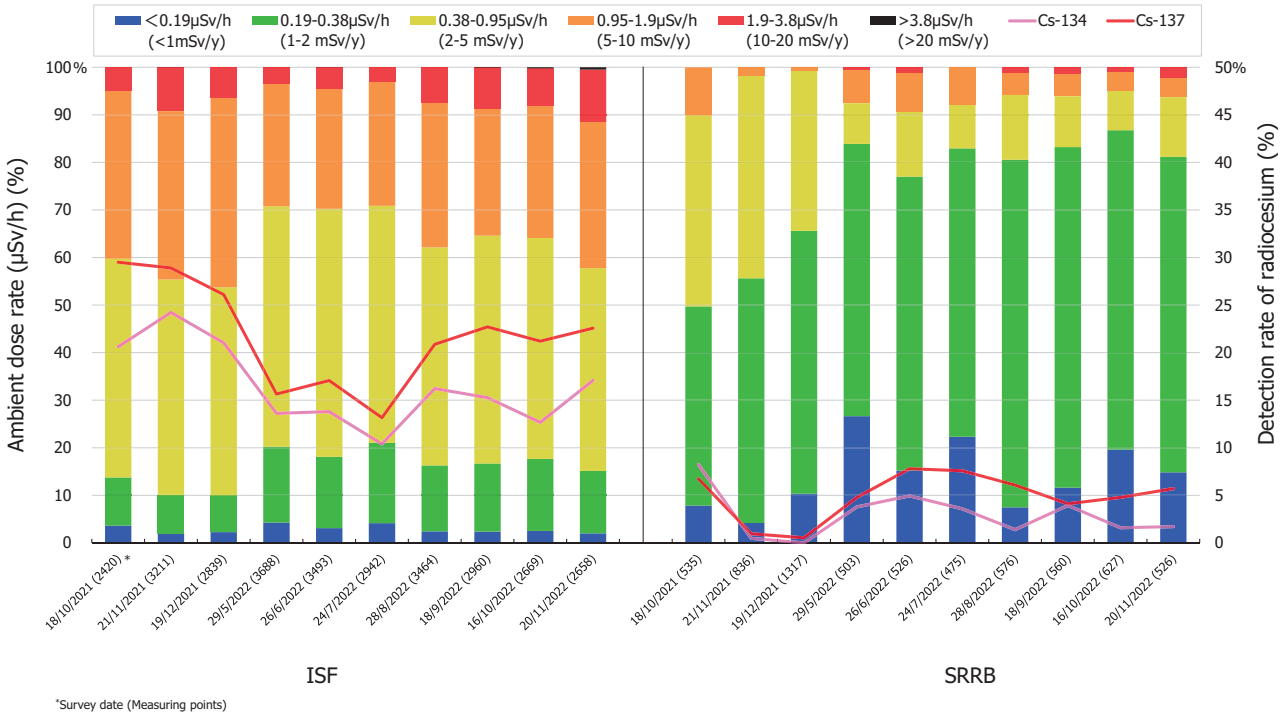

Figure 3. Temporal variation in the ambient dose rate distribution and detection rate of radiocesium in Okuma town.

indoor and outdoor activities of daily living) for residents who might return to the evacuation order lifted areas and SRRB were estimated at 0.091 mSv/year in Futaba town and 0.76 mSv/year in Okuma town (Supplementary Tables S2 and S3, Figs. S2 and S3).

Discussion

Construction of the ISF in Futaba town and Okuma town began in 2017, with storage facility for removed soil set up in three areas in Futaba town and five areas in Okuma town[9–11,15]. The total capacity for contaminated soil was 3.1 million m^3 in Futaba town and 10 million m^3 in Okuma town. As of March 2023, two storage facilities in Futaba town and one in Okuma town have been completed[15]. During the construction of ISF, radioactive waste is covered with soil or concrete as a protective layer to prevent the spread of radioactive materials, while to prevent the dispersion of radioactive materials when bringing them into ISF, the radioactive waste is carried in flexible containers during transportation[9,15,16]. In the present study, the stable ambient dose in ISF suggested that there was no obvious leakage or scattering of radioactive material in the ISF area during the construction process in our survey period. From October 2021 to November 2022, the ambient dose rate and detection rate of radiocesium in Okuma town were significantly higher in Futaba town ($p < 0.001$). Immediately after the FDNPP accident, various radionuclides were released from around the FDNPP into the atmosphere, eventually being deposited on land and at sea in the surrounding areas[5]. Due to the influence of terrain and weather, the amounts of artificial radionuclides released from nuclear reactors and diffusion scales absolutely differed between Futaba town and Okuma town[4,8,17,18]. The databases of NRA's car-borne survey showed that the ambient dose rate in Okuma town was significantly higher than that in Futaba town after the accident[18]. Therefore, the difference in the initial contamination in Futaba town and Okuma town are considered to provide a direct reflection of the ambient dose rate and detection rate of radiocesium, even after the decontamination process, because whole contamination materials such as deposits, soil, and trees were not completely removed in the forest near the town[8,10,11]. Moreover, the ISF remains a restricted area and decontamination work has not yet been carried out, which contributed to the higher environmental radioactivity value in Okuma town. Our results show that the average ambient dose in Okuma town and Futaba town during the survey period were 0.37 μSv/h and 0.11 μSv/h in the SRRB and evacuation order lifting areas. In the ISF the value was 0.91 μSv/h and 0.27 μSv/h in Okuma town and Futaba town, respectively. The ambient dose rate and detection rate of radiocesium were significantly higher in the ISF than in the evacuation order lifted area and SRRB in Futaba town and Okuma town ($p < 0.001$). In general, the efficient and thorough decontamination processes can reduce ambient dose by removing radioactive materials from affected areas (environmental remediation)[19–24]. In our previous study in Tomioka town, Fukushima Prefecture, a significant difference in ambient dose rate since 2017 was observed between the decontaminated and non-decontaminated areas[19–21]. The ambient dose rate in the decontaminated area decreased by 71.9% (from 1.0 to 0.32 μSv/h during 2018–2019)[19]. According to another report, the average ambient dose rate in decontaminated locations was about 20% lower than that in non-decontaminated areas[22]. Reports from the Ministry of the Environment showed decontamination reducing the ambient dose rate by 60% at 1 m above ground level in residential areas and by 42% on roads[8,23]. In Futaba town and Okuma town, the decontamination processes at the SRRB started on September 12, 2017 and March 9, 2018, respectively, mainly targeting public facilities such as station square, nurseries, and gymnasium[8,10–12]. The decontamination process in the evacuation order lifted area in Futaba town started much earlier than that at the SRRB and was completed in March 2016, well before the evacuation order was lifted on March 4, 2020[8]. Additionally, towards the goal of lifting evacuation order at entire SRRB in Spring of 2022–2023, the Ministry of the Environment is conducting demolition and decontamination cooperating with Futaba town and Okuma town during our survey periods[8]. Therefore, the ambient dose rates in SRRB decreased from 0.38 μSv/h in October 2021 to 0.23 μSv/h in May 2022 in Okuma Town, which has been maintained at a relatively low level since then can be considered the benefit of decontamination. Moreover, the environmental radioactivity in the evacuation order lifted areas in Futaba town has been continuously stabilized at extremely low levels as a result of decontamination as well, despite some fluctuations being noticed. Although we noticed a smaller ambient dose rate in May, June, and July 2022 in the ISF areas, it is difficult to clarify the relationship between season and ambient dose rate. We believe that the smaller values observed during this period may be related to the precipitation brought by the seasonal rainfall in this area from May to July[25–27]. Precipitation increases soil moisture, and higher water content in the soil limits gamma-ray emission[26]. The wash-out caused by precipitation can also cause surface radioactive materials to migrate to deeper layers, thereby reducing observed ambient dose rates[27].

On the other hand, although the detection rate of radiocesium (mainly ^{137}Cs) fluctuated in a small range throughout the survey period, it always remained at a relatively low level. In our previous study, accident-derived ^{137}Cs levels in the SRRB in Tomioka were observed in airborne dust samples, which suggested that the ^{137}Cs radioactivity in the airborne dust was primarily associated with particles that were resuspended by localized winds and the transfer of construction vehicles as opposed to the decontamination and demolition operations (Supplementary Table S4)[28]. Furthermore, human activities such as the transportation of contaminants (removal of soil and radioactive waste) and land restoration might have caused some fluctuations in the ambient dose rate[19,28]. In the present study, our result also suggested that the fluctuations in ambient dose rate caused by human activities are accompanied by fluctuations in the detection rate of radiocesium. According to another report, weekly changes in vehicular traffic tends to affect the accumulation of airborne dust particles and radioactive materials resuspended in the air, thereby contributing to temporary variation in the concentration of radiocesium[29]. In addition, wind direction, wind speed, and other meteorological factors can also cause changes in radiocesium concentrations[27,30–32]. According to previous studies in Fukushima, the wind can affect the deposition level of ^{137}Cs, with high concentrations in the air associated with areas of high ^{137}Cs deposition[30]. Radiocesium resuspension and deposition can also be influenced by meteorological events such as rain out (washout), which can transfer radiocesium in the surface layer to the lower layer[27]. According to reports of the Chernobyl accident, a positive relationship was found between airborne radiocesium concentrations and wind speed[31,32]. In the present study, the results indicated that the detected radiocesium came not only from materials release from FDNPP accident but also from subsequent airborne radiocesium resuspended at certain locations during the study period.

The estimated annual effective doses for decontamination workers and residents of the decontamination area were lower than the recommended limit set by the Japanese government based on the recommendation of the International Commission on Radiological Protection[33–35] (Supplementary Tables S2 and S3, Figs. S2 and S3). Nevertheless, to control artificial radioactivity, avoid unnecessary radiation exposure, and alleviate radiation anxiety due to the FDNPP accident in these areas, environmental radioactivity monitoring and special education, including radiation safety for workers who engage in decontamination work and residents who will return to the SRRB, are necessary.

In the present study, changes in the ambient dose rate by season and weather were difficult to identify through a horizontal comparison based on car-borne surveys. Moreover, the detection rate of radiocesium in this study mainly comes from radiocesium deposited in the surface soils or asphalt of roads, trees, and plants, which is obviously lower than that of soil samples. However, the main artificial radionuclides derived from the FDNPP accident, such as ^{137}Cs, could be analyzed to sufficiently precise levels using high-purity germanium detectors. Therefore, the combination of radionuclide analysis of environmental samples such as soil and extensive monitoring via a car-borne survey could accurately evaluate the decontamination effects and external and internal exposure levels. These findings suggest that long-term follow-up monitoring is extremely important for the reconstruction of affected areas, including the SRRB, around the FDNPP.

Materials and methods

Survey location

The FDNPP (37°25′ N, 141°02′ E) is located on the boundary between Futaba town (37°25′ N, 141°02′ E) and Okuma town (37°25′ N, 141°02′ E) in Fukushima Prefecture on the east coast of Honshu Island, Japan. Both towns include DRZ and SRRB areas (Fig. 1)[4]. Further decontamination efforts have been continuing in the SRRB of Futaba town and Okuma town.

Survey of ambient dose rate and radiocesium detection

The ISF within the DRZ and SRRB areas (including the evacuation order lifted area) of Futaba town and Okuma town was surveyed using the Radi-probe car-borne survey system (Chiyoda Technology Corp., Tokyo, Japan) connected to a handheld radiation detector (HDS-101GN; Mirion Technologies, Inc., Japan) from October 2021 to November 2022 (10 times in the ISF, SRRB, and evacuation-over-lifted area of Futaba town and Okuma town)[36,37]. Radi-Probe is a data acquisition system for a car-borne survey. The system consists of a handheld radiation detector, a GPS receiver, a micro-camera, and a laptop personal computer (PC) that controls all devices[36]. The entire system is installed on the sedan car, with the handheld radiation detector was set on the front passenger seat about 1 m above the ground. The dose rate and the gamma-ray energy spectra obtained by the handheld radiation detector, tagged with the GPS position are continuously stored in the PC, which automatically captures position coordinates and a photo every 5 s in addition to spectral segments every 0.2 seconds[36,37]. The handheld radiation detector is a large thallium-doped cesium iodide scintillator with high sensitivity (typical 1400 cps per μSv/h for the ^{137}Cs source), and the measurable dose-rate range is 10 nSv/h–100 μSv/h, the measurable energy range gamma-ray is 30 keV–3 MeV using a multichannel analyzer with 512 channels[37]. The measured spectrum is internally converted to dose rate[36,37]. In other words, we measured gamma-ray directly by the standard method using the scintillator (conversion gamma-ray signal to electrical signals). The Radi-probe system shows the detected energy peaks of radiocesium registered in the detected net count values and their associated confidence (with levels 1–10 used as reference values)[19,38]. In other words, the detected rate of radiocesium was obtained qualitatively from the region of interest of the energy peaks of radiocesium (604 keV for ^{134}Cs and 662 keV for ^{137}Cs), which can be used to indicate the qualitatively surface deposition concentration of radiocesium, with values 1–10 used as reference confidence interval levels. Software installed on the PC has a graphical interface that can display gamma-ray energy spectra and a map with color-scaled ambient dose equivalent rates. Temporal variation of the ambient dose equivalent rate is also displayed on the graphical interface. Snapshots taken by the micro-camera in the front of the car are also displayed, which confirm the geographic environment and weather[36,37]. The calibration of Radi-probe system is carried out by Chiyoda Technol every 2 years. Additionally, we carried out the easy efficiency calibration by the standard radiation source (Japan Radioisotope Association, Tokyo, Japan) before each survey. Generally, the chassis and walls of a vehicle provide a shielding effect against external radiation; numerous other factors, such as the type of vehicle and the number of occupants, also affect this shielding factor[20]. Therefore, the shielding effect was calculated by measuring the interior and exterior of the vehicle in an open and flat area at a height of 1 m above the ground before each monitoring session. During the survey periods, the sedan car was driven at a constant speed by the same person, the shielding factors ranged from 1.19 to 1.84.

Effective dose

The effective dose through external exposure is calculated using the following formula[19]:

$$E_i = (D_{out} - D_{BG}) \cdot T \cdot R \tag{1}$$

$$E_w = \sum_{i=1}^{12} E_i \tag{2}$$

$$E = E_{out} + E_{in} \tag{3}$$

$$E_{out/in} = \left(D_{out/in} - D_{BG}\right) \cdot T \cdot F \cdot R \quad (4)$$

$$D_{in} = r \cdot D_{out} \quad (5)$$

where E_i is the estimated external effective dose (mSv/month by median), E_w the external effective dose for decontamination workers (mSv/year), E the external effective dose for residents who are going to return to the decontaminated area (mSv/year), $E_{out/in}$ the external effective dose for outdoor and indoor workers, $D_{out/in}$ the dose rate for a height of 1 m above ground outside and inside the house (μSv/h), D_{BG} 0.04 μSv/h, which was measured in the area of interest before the accident[39], T the work time (240 days × 8 h; the normal labor standard in Japan), F the occupancy factor (with 16 and 8 h [24 h/day] considered to represent the indoor and outdoor activities of daily living, respectively, based on the guideline of the Ministry of the Environment, Japan), R the age-dependent dose conversion coefficient for adults (0.6 corresponds to the effective dose for an adult), and r the deposited gamma location factor for a wooden house (0.4)[40].

Data analysis

All data followed a non-normal distribution. To compare differences among the measurement areas in the same period and the temporal variation within the same areas, the data were analyzed using the Mann–Whitney U and Kruskal–Wallis H tests.

Data availability

The datasets used and analyzed during the current study are available from the corresponding author upon reasonable request.

Received: 23 June 2023; Accepted: 12 December 2023
Published online: 18 December 2023

References

1. UNSCEAR. Sources, effects and risks of ionizing radiation: *United nations scientific committee on the effects of atomic radiation 2013 report,* I (2023, accessed 10 Mar 2023). (2013). https://www.unscear.org/unscear/uploads/documents/unscear-reports/UNSCEAR_2020_21_Report_Vol.II.pdf.
2. IAEA. *Environmental transfer of radionuclides in Japan following the accident at the Fukushima Daiichi Nuclear Power Plant.* IAEA-TECDOC-1927**,** IAEA, Vienna, (2020).
3. Nuclear Emergency Response Headquarters of Japanese Government. *Additional report of the Japanese Government to the IAEA—the accident at TEPCO's Fukushima Nuclear Power Stations (Second Report)* (2023, accessed 10 Mar 2023). https://www.iaea.org/sites/default/files/japanreport120911.pdf.
4. The Fukushima Prefecture. *Fukushima Revitalization Station: Transition of Evacuation Designated Zones* (2023, accessed 10 Mar 2023).. https://www.pref.fukushima.lg.jp/site/portal-english/en03-08.html.
5. International Atomic Energy Agency (IAEA). *The Fukushima Daiichi Accident* (2023, accessed 10 Mar 2023). http://www-pub.iaea.org/books/IAEABooks/10962/The-Fukushima-Daiichi-Accident.
6. Nuclear Regulation Authority, Japan. *Monitoring information of environmental radioactivity level* (2023, accessed 30 Sep 2023).. https://radioactivity.nsr.go.jp/en/.
7. Tokyo Electric Power Company *Radiation Dose measured at Monitoring Post of Fukushima Daiichi Nuclear Power Station* (2023, accessed 30 Sep 2023). https://www.tepco.co.jp/en/nu/fukushima-np/f1/index-e.html.
8. Ministry of the Environment of Japan. *Environmental Remediation: Decontamination* (2023, accessed 10 Mar 2023). http://josen.env.go.jp/en/decontamination/.
9. Ministry of the Environment of Japan. *Environmental remediation: Interim Storage Facility*(2023, accessed 10 Mar 2023). http://josen.env.go.jp/en/storage/.
10. Ministry of the Environment of Japan. *Annual Report on the Environment in Japan 2021, Chapter 4: Efforts for Reconstruction and Environmental Restoration from the Great East Japan Earthquake*(2023, accessed 10 Mar 2023). https://www.env.go.jp/content/900457471.pdf.
11. Ministry of the Environment of Japan. *Framework and Methods of Decontamination Projects*(2023, accessed 10 Mar 2023). http://josen.env.go.jp/en/policy_document/pdf/decontamination_projects_1902_03.pdf.
12. Ministry of the Environment of Japan. *Specific Reconstruction and Regeneration Base (Japanese)* (2023, accessed 10 Mar 2023). http://josen.env.go.jp/kyoten/index.html.
13. Oishi, K. *et al.* Risk perception of health risks associated with radiation exposure among residents of Okuma, Fukushima Prefecture. *Int. J. Environ. Res. Public Health* **18**, 13208 (2021).
14. Matsunaga, H. *et al.* Intention to return and perception of the health risk due to radiation exposure among residents in Tomioka Town, Fukushima Prefecture, stratified by gender and generation. *Disaster Med. Public Health Prep.* **16**, 206–213 (2022).
15. Ministry of the Environment of Japan. *Status of development of interim storage facilities* (2023, accessed 10 Mar 2023). http://josen.env.go.jp/plaza/info/data/pdf/data_2303_04.pdf#page=2.
16. Hiromitsu, S. *et al.* Design construction and monitoring of temporary storage facilities for removed contaminants. *Trans. Atom. Energy Soc. Jpn.* **12**, 1–12 (2013).
17. Japan Atomic Energy Agency. *Database for Radioactive Substance Monitoring Data* (2023, accessed 10 Mar 2023). https://emdb.jaea.go.jp/emdb/search.
18. Nuclear Regulation Authority. *Results of Airborne Monitoring in Fukushima Prefecture and neighboring prefectures and the Fourteenth Airborne Monitoring in the 80 km zone from the Fukushima Daiichi NPP* (2023, accessed 10 Mar 2023). https://radioactivity.nra.go.jp/en/contents/17000/16208/24/2022_17thAirborne%20monitoring%20press_english.pdf.
19. Cui, L. *et al.* Environmental remediation of the difficult-to-return zone in Tomioka Town, Fukushima Prefecture. *Sci. Rep.* **10**, 10165 (2020).
20. Matsuo, M. *et al.* Evaluation of environmental contamination and estimated radiation exposure dose rates among residents immediately after returning home to Tomioka Town, Fukushima Prefecture. *Int. J. Environ. Res. Public Health* **16**, 1481 (2019).
21. Yamaguchi, T. *et al.* Local level of radiation exposure doses due to radiocesium for returned residents in Tomioka Town, Fukushima Prefecture. *Radiat Prot Dosim.* **193**, 207–220 (2021).
22. Saito, K. *et al.* Summary of temporal changes in air dose rates and radionuclide deposition densities in the 80 km zone over five years after the Fukushima Nuclear Power Plant accident. *J. Environ. Radioact.* **210**, 105878 (2019).

23. Ministry of the Environment of Japan. *Decontamination projects for radioactive contamination discharged by Tokyo Electric Power Company Fukushima Daiichi Nuclear Power Station accident: Chapter 5: Effects, verification, and risk communication of decontamination* (2019, accessed 10 Mar 2023). http://josen.env.go.jp/en/policy_document/pdf/decontamination_projects_1902_05.pdf.
24. Shiroma, Y. *et al.* Changes of absorbed dose rate in air by car-borne survey in Namie Town, Fukushima Prefecture after the Fukushima Daiichi Nuclear Power Plant accident. *Radiat. Prot. Dosim.* **184**, 527–530 (2019).
25. Qian, W., Qian, W., Kang, H. S. & Lee, D. K. Distribution of seasonal rainfall in the East Asian monsoon region. *Theor. Appl. Climatol.* **73**, 151–168 (2002).
26. Tchorz-Trzeciakiewicz, D. E., Kozłowska, B. & Walencik-Łata, A. Seasonal variations of terrestrial gamma dose, natural radionuclides and human health. *Chemosphere* **310**, 136908 (2023).
27. Hosoda, M. *et al.* Evaluations of inventory and activity concentration of radiocesium in soil at a residential house 3 years afterthe Fukushima Nuclear accident. *Radiat. Prot. Dosim.* **184**, 518–522 (2019).
28. Taira, Y. *et al.* Assessment of localized and resuspended ^{137} Cs due to decontamination and demolition in the difficult-to-return zone of Tomioka town, Fukushima Prefecture. *Integr. Environ. Assess. Manag.* **18**, 1555–1563 (2022).
29. Akimoto, K. Annual and weekly cycles of radioactivity concentration observed in Fukushima City. *Health Phys.* **108**, 32–38 (2015).
30. Ochiai, S. *et al.* Temporal variation of post-accident atmospheric Cs in an evacuated area of Fukushima Prefecture: Size-dependent behaviors of Cs-bearing particles. *J. Environ. Radioact.* **165**, 131–139 (2016).
31. Wagenpfeil, F., Paretzke, H. G., Peres, J. M. & Tschiersch, J. Resuspension of coarse particles in the region of Chernobyl. *Atmos. Env.* **33**, 3313–3323 (1999).
32. Werner, H. Resuspension factors of 137Cs in Hannover after the Chernobyl accident. *J. Aerosol Sci.* **25**, 789–792 (1994).
33. Ministry of health, labour and welfare, Japan. *Ordinance on Prevention of Ionizing Radiation Hazards* (2023, accessed 10 Mar 2023) https://www.mhlw.go.jp/english/topics/2011eq/workers/ri/rl/rl_130708.pdf.
34. The International Commission on Radiological Protection (ICRP). In *The 2007 Recommendations of the International Commission on Radiological Protection* (2007).
35. The International Commission on Radiological Protection (ICRP). In *Application of the Commission's Recommendations to the Protection of People Living in Long-term Contaminated Areas after a Nuclear Accident or a Radiation Emergency* (2011).
36. Kobayashi, S. *et al.* Radioactive contamination mapping of northeastern and eastern Japan by a car-borne survey system. *RadiProbe. J. Environ. Radioact.* **139**, 281–293 (2015).
37. Mirion Technologies. *Template DMD-EN (windows.net)* (2023, accessed 30 Sep 2023) https://mirionprodstorage.blob.core.windows.net/prod-20220822/cms4_mirion/files/pdf/spec-sheets/spc-174-en-a_hds101g-gn.pdf?1645216852.
38. Varley, A. *et al.* Reconstructing the deposition environment and long-term fate of Chernobyl Cs-137 at the floodplain scale through mobile gamma spectrometry. *Environ. Pollut.* **240**, 191–199 (2018).
39. Ministry of the Environment of Japan. *Additional exposure doses after an accident (example of calculation)* (2023, accessed 30 Sep 2023). https://www.env.go.jp/en/chemi/rhm/basic-info/1st/02-04-11.html.
40. Ministry of the Environment of Japan. *Shielding and reduction coefficient* (2023, accessed 10 Mar 2023).https://www.env.go.jp/en/chemi/rhm/basic-info/1st/02-04-10.html.

Acknowledgements
We would like to thank all the study participants and the staffs of Futaba town, Okuma town, and Tomioka town for their cooperation.

Author contributions
Conceived and designed the observations: N.T. and Y.T.; performed the observations: M.L., Y.T., M.M., M.O., H.M., Y.K., and X.X.; analyzed the data: M.L. and Y.T.; wrote the paper: M.L. and Y.T. All authors approved the final version of the manuscript.

Funding
This work was supported by Research on the Health Effects of Radiation organized by the Ministry of the Environment, Japan.

Competing interests
The authors declare no competing interests.

Additional information
Supplementary Information The online version contains supplementary material available at https://doi.org/10.1038/s41598-023-49821-8.

Correspondence and requests for materials should be addressed to N.T.

Reprints and permissions information is available at www.nature.com/reprints.

Publisher's note Springer Nature remains neutral with regard to jurisdictional claims in published maps and institutional affiliations.

Journal of Radiation Research, 2025, pp. 1–3
https://doi.org/10.1093/jrr/rrae102

Comparative analysis of public concerns regarding treated water discharged from the Fukushima Daiichi Nuclear Power Station: perspectives before and after the initial release

Mengjie Liu, Hitomi Matsunaga*, Makiko Orita, Yuya Kashiwazaki, Xu Xiao and Noboru Takamura

Department of Global Health, Medicine and Welfare, Atomic Bomb Disease Institute, Nagasaki University Graduate School of Biomedical Sciences, 1-12-4 Sakamoto, Nagasaki City, Nagasaki Prefecture 852-8523, Japan
*Corresponding author. Department of Global Health, Medicine and Welfare, Atomic Bomb Disease Institute, Nagasaki University Graduate School of Biomedical Sciences, 1-12-4 Sakamoto, Nagasaki City, Nagasaki Prefecture 852-8523, Japan. Tel: +81-95-819-7171; Fax: +81-95-819-7172; Email: hmatsu@nagasaki-u.ac.jp
(Received 13 November 2024; revised 11 December 2024; editorial decision 19 December 2024)

To the Editors:

The 2011 Great East Japan Earthquake and tsunami triggered a major accident at the Fukushima Daiichi Nuclear Power Plant (FDNPP), leading to significant radioactive contamination due to damaged reactor cores [1]. Since the accident, seawater has been used to cool the reactor cores, and the resulting contaminated water containing radionuclides, such as cesium-137, strontium-90 and tritium, has been collected in tanks and stored on-site at the FDNPP. To treat the contaminated water, Tokyo Electric Power Company introduced the Advanced Liquid Treatment System (ALPS), which aims to remove most of the radionuclides in the water. Although the system can reduce the levels of radioactive substances in the contaminated water to some extent, it cannot completely remove tritium [2].

To address the accumulation of ALPS treated water stored at the FDNPP, the Japanese government announced on 13 April 2021, its plan to discharge the treated water into the ocean, and the discharge officially began on 24 August 2023 [3]. Although reports (e.g. IAEA guidelines) indicate that the discharge complies with international safety standards and the environmental impact is within controllable limits [2, 3], the initiative has faced strong opposition from neighboring countries, environmental organizations and fishery communities due to concerns about potential risks to marine ecosystems and human health [4, 5]. The release of treated water from the FDNPP has thus become a complex and sensitive issue, involving considerations of environmental protection, risk communication and public trust. Therefore, it is crucial for the government and experts to understand public attitudes, particularly those of Fukushima residents and evacuees, toward the discharge of treated water in order to conduct effective risk communication and build trust. This study aims to examine the changing trends in concern regarding treated water discharge among residents and evacuees living close to the FDNPP before and after the discharge plan.

We conducted surveys in November to December 2022 (before the discharge began) and December 2023 to January 2024 (after the discharge started) in the towns of Tomioka, Okuma and Futaba, which are close to FDNPP in the Hamadori area of Fukushima Prefecture. The questionnaire used in this study was adapted from previous research and the Fukushima Health Management Survey [6, 7]. It included demographic information (e.g. age, gender and current residence). Participants were asked to assess their concerns about discharge of treated water, and their risk perception of health effects and genetic effects. Additionally, mental health status was evaluated using the mental health dimension item of the validated Japanese version of the Short Form 8 (SF-8) scale. A score of 50 ± 10 (based on the average score for the general Japanese population) on the mental health dimension indicated good mental health. Eligible participants were those aged 20 or older who could receive the questionnaire from the municipal office. Two questionnaires were distributed to each household. After excluding responses with missing data, a total of 3414 responses were included in the analysis, with 1856 responses in 2022 and 1558 in 2023.

All study protocols were reviewed and approved by the Ethics Committee of the Nagasaki University Graduate School of Biomedical Sciences (approval numbers 21082702 and 23081805). Data analysis was conducted using IBM SPSS Statistics version 28 (IBM Corp., Armonk, NY, USA), with a P-value <0.05 considered statistically significant.

Table 1 shows the characteristics of the participants. The proportion of respondents concerned about treated water discharge

Table 1. Comparison of public concerns regarding treated water discharge from FDNPP between 2022 and 2023 (chi-square test results)

Variable	Reference	Study in 2022 N (%)	Study in 2023 N (%)	*P*-value
Age	<60	474 (26.1)	382 (24.9)	0.43
	≥60	1340 (73.9)	1150 (75.1)	
Gender	Male	921 (50.4)	861 (55.9)	0.001
	Female	906 (49.6)	678 (44.1)	
Residential status	Inside Fukushima	1342 (73.4)	1122 (73.7)	0.846
	Outside Fukushima	487 (26.6)	401 (26.3)	
Concerned about discharge of treated water	Yes	1108 (60.8)	648 (41.8)	<0.001
	No	715 (39.2)	901 (58.2)	
Anxiety regarding health effects	Yes	801 (44.0)	512 (33.3)	<0.001
	No	1019 (56.0)	1024 (66.7)	
Anxiety regarding genetic effects	Yes	898 (49.6)	563 (37.0)	<0.001
	No	913 (50.4)	959 (63.0)	
Mental health status	Poor	828 (45.7)	660 (42.8)	0.092
	Good	985 (54.3)	883 (57.2)	

Table 2. Logistic regression analysis of public concern regarding treated water discharged from the FDNPP in 2022 and 2023

Variable	Reference	Model 1		Model 2	
		OR	95% CI	OR	95% CI
Age	<60/≥60	0.921	0.784–1.083	0.921	0.783–1.083
Gender	Male/female	1.123	0.973–1.296	1.117	0.968–1.290
Concerned about discharge of treated water	Yes/no	0.495**	0.421–0.583	0.510**	0.432–0.601
Anxiety regarding health effects	Yes/no	0.911	0.770–1.079	–	–
Anxiety regarding genetic effects	Yes/no	–	–	0.852	0.721–1.007
Mental health status	Poor/good	1.058	0.913–1.225	1.071	0.925–1.240

Reference group: 2022 survey. Note: OR; odds ratio; CI; confidence interval.
** $P<0.001$.

significantly decreased from 60.8% in 2022 to 41.8% in 2023 ($P < 0.001$). Regarding health and genetic risks, 44% and 49.6% of respondents, respectively, expressed concerns in 2022 dropped significantly to 33.3% and 37% in 2023 ($P < 0.001$). We conducted a binary logistic regression analysis to compare the survey results from the Hamadori area between 2022 and 2023 (Table 2). Model 1 indicated that respondents in 2023 were significantly less likely to express concerns about the discharge of treated water compared to those in 2022, with an odds ratio (OR) of 0.495 (95% CI, 0.421–0.583, $P < 0.001$). Similarly, Model 2 yielded consistent results, with an OR of 0.510 (95% CI, 0.432–0.601, $P < 0.001$).

Overall, although residents still showed relatively high levels of concern about the discharge of treated water and their perceived risks of health and genetic effects, the present results indicate a significant decrease in residents' concerns regarding treated water discharges after the implementation of the discharge plan compared to the period before its initiation. We suggest that the reduction in concerns may be attributed to transparent communication between the government, experts and stakeholders, as well as the verification efforts by third-party organizations, such as the IAEA, which likely bolstered residents' trust [3]. Furthermore, the socio-economic recovery in fisheries and tourism appears to have offered additional reassurance to the local population [8].

These findings emphasize the need for ongoing, transparent and science-based communications, such as regular and large-scale lectures and meetings focused on the topic of health and genetic risks and radiation safety to maintain public trust. Continuous third-party verification and open engagement with affected communities are critical to mitigating reputational impacts and ensuring lasting confidence in radiation safety. Such ongoing dialogue and third-party oversight are essential not only for supporting the socio-economic recovery of the Fukushima region but also for fostering a collaborative environment for the safe, long-term decommissioning of the FDNPP.

ACKNOWLEDGEMENTS

The authors would like to thank all study participants and town staff.

CONFLICT OF INTEREST

The authors declare that they have no competing interests.

ETHICAL STATEMENT

This study was approved by the ethics committee of the Nagasaki University Graduate School of Biomedical Sciences (numbers 21082702 and 23081805).

REFERENCES

1. UNSCEAR. *Sources, Effects and Risks of Ionizing Radiation: United Nations Scientific Committee on the Effects of Atomic Radiation 2013 Report. I*. Vienna, Austria, 2013. https://www.unscear.org/unscear/uploads/documents/unscear-reports/UNSCEAR_2020_21_Report_Vol.II.pdf (20 October 2024, date last accessed).
2. Tokyo Electric Power Company. *Treated Water Portal Site*. Japan. https://www.tepco.co.jp/zh-cn/decommission/progress/watertreatment/oceanrelease/index-cn.html#process (20 October 2024, date last accessed).
3. International Atomic Energy Agency (IAEA). *Fukushima Daiichi Treated Water Release—Advanced Liquid Processing System (ALPS)*. Vienna, Austria. https://www.iaea.org/topics/response/fukushima-daiichi-nuclear-accident/fukushima-daiichi-alps-treated-water-discharge (20 October 2024, date last accessed).
4. Wang L, Li F. State duty to cooperate on the Fukushima nuclear contaminated water release. *Mar Policy* 2022;136:104878. https://doi.org/10.1016/j.marpol.2021.104878.
5. Mabon L, Kawabe M. Bring voices from the coast into the Fukushima treated water debate. *Proc Natl Acad Sci USA* 2022;119:e2205431119. https://doi.org/10.1073/pnas.2205431119.
6. Yasumura S, Hosoya M, Yamashita S *et al.* Study protocol for the Fukushima health management survey. *J Epidemiol* 2012;22:375–83. https://doi.org/10.2188/jea.JE20120105.
7. Hande V, Orita M, Matsunaga H *et al.* Thoughts, perceptions and concerns of coastal residents regarding the discharge of tritium-containing treated water from the Fukushima Daiichi Nuclear Power Plant into the Pacific Ocean. *BMC Public Health* 2023;23:2436. https://doi.org/10.1186/s12889-023-17349-1.
8. Fukushima Prefecture. *Fukushima Today, Steps for Reconstruction and Revitalization in Fukushima Prefecture*. Japan. https://www.pref.fukushima.lg.jp/uploaded/attachment/655993.pdf (20 October 2024, date last accessed).

Journal of Radiation Research, 2025, pp. 1–3
https://doi.org/10.1093/jrr/rraf003

Residents of the towns in which the Fukushima Daiichi nuclear station is located express more worries about reputational damage than about the discharge of treated water itself

Mengjie Liu[†], Hitomi Matsunaga[†,*], Makiko Orita, Yuya Kashiwazaki, Xu Xiao and Noboru Takamura

Department of Global Health, Medicine and Welfare, Atomic Bomb Disease Institute, Nagasaki University Graduate School of Biomedical Sciences, 1-12-4 Sakamoto, Nagasaki 852-8523, Japan

*Corresponding author. Department of Global Health, Medicine and Welfare, Atomic Bomb Disease Institute, Nagasaki University Graduate School of Biomedical Sciences. Email: hmatsu@nagasaki-u.ac.jp

[†]Mengjie Liu and Hitomi Matsunaga contributed equally to this work.

(Received 24 December 2024; revised 16 January 2025; editorial decision 22 January 2025)

To the Editor:

In August 2023, the regular discharge of treated water (DTW) from the Tokyo Electric Power Company's Fukushima Daiichi Nuclear Power Station (FDNPS) into the Pacific Ocean began. The Japanese government and the Tokyo Electric Power Company have conducted a series of dialogues and informed the public about this process, to enhance their understanding of the discharge protocol [1]. Furthermore, they have undertaken careful preparations, including the accumulation of scientific data regarding the environmental and human health implications of the discharge, and they have sought water-handling recommendations from the IAEA [2]. Nevertheless, public concerns persist [3].

The DTW site is located at the FDNPS, in Okuma and Futaba Towns. Immediately after the FDNPS accident, all residents were ordered to evacuate and forbidden to enter the towns without permission from the government. Although the evacuation orders for Okuma and Futaba Towns were partially lifted almost a decade later, in 2020 and 2022, respectively, the return rates for both towns have been very low, which is attributed to the varying consequences of the prolonged evacuation [4]. Moreover, residents of the towns have expressed deep-rooted concerns about radiation exposure and its health effects, including DTW [5–7].

Between November and December 2023, ∼3 months after the DTW's initiation, a questionnaire survey was conducted of all residents of Okuma and Futaba Towns aged 18 years and older who had a residence card at the time of the survey. The questionnaire was distributed and enclosed in public magazines to ∼4900 households in Okuma and 2600 households in Futaba. After excluding incomplete responses, 549 responses from Okuma and 419 from Futaba were deemed valid. The study protocol was approved by the Ethics Committee of the Nagasaki University Graduate School of Biomedical Sciences (Approval No. 23081805).

The survey results showed that 40.3% ($n = 390$) of respondents expressed concerns about DTW itself, whereas 68.2% ($n = 660$) were worried about reputational damage due to DTW (Table 1). Of all the reputational damage, the biggest worry was the impact on the fishing industry 76.6% ($n = 783$) by the multiple answers. Subsequent worries were related to its impact on commerce ($n = 330$, 32.3%), tourism ($n = 298$, 29.2%), their livelihood ($n = 74$, 7.2%), and other factors ($n = 106$, 10.4%). A regression model was calculated separately for current place of residence (Model 1) and respondents' intention to return (Model 2), because collinearity was confirmed (Table 2). The regression analysis results showed that, compared to males, females were more concerned about DTW (Model 1, odds ratio [OR]: 0.59, 95% confidence interval [CI]: 0.45–0.76, $P < 0.001$; Model 2, OR: 0.59, CI: 0.46–0.77, $P < 0.001$). Furthermore, compared to those aged <65 years, those aged ≥65 years were more worried about reputational damage caused by DTW (Model 1, OR: 1.40, CI: 1.05–1.87, $P < 0.05$; Model 2, OR: 1.40, CI: 1.05–1.87, $P < 0.05$). Notably, those who have not returned to the area were more concerned about DTW than those who have returned or who were living there (Model 2, OR: 2.46, CI: 1.05–5.73, $P < 0.05$). This result was similar to a previous study that showed people who were female or who had decided not to return tended to be more anxious about radiation exposure and its health effects following the nuclear accident [5, 6]. We found no statistical differences in worries about reputational damage depending on the

Table 1. Residents' concerns about DTW-related reputational damage

	Characteristic	Overall	Concerned about DTW		Concerns about reputational damage caused by DTW	
		n (%)	n (%)		n (%)	
		968 (100)	390 (40.3)	*P*-value	660 (68.2)	*P*-value
Sex	Male	536 (55.4)	185 (47.4)	<0.01	357 (54.1)	0.24
	Female	432 (44.6)	205 (52.6)		303 (45.9)	
Age (years)	< 65	355 (36.7)	144 (36.9)	0.89	258 (39.1)	0.02
	≥ 65	613 (63.3)	246 (63.1)		402 (60.9)	
Place of residence	Hamadori area;	487 (50.3)	191 (49.0)	0.63	325 (49.2)	0.44
	Pacific coast side	207 (21.4)	82 (21.0)		140 (21.2)	
	Inside Fukushima; not including Hamadori	274 (28.3)	117 (30.0)		195 (29.5)	
	Outside Fukushima					
Intention to return	Already returned or living in area	34 (3.5)	7 (1.8)	0.11	18 (2.7)	0.12
		126 (13.0)	53(13.6)		86 (13.0)	
	Want to return	253 (26.1)	107 (27.4)		183 (27.7)	
	Undecided	555 (57.3)	223 (57.2)		373 (56.5)	
	Do not want to return					

Note. Response: yes, Chi-square test, DTW: discharge of treated water

Table 2. Independent factors associated with anxiety and reputational damage related to DTW

		Concerned about DTW		Concerned about reputational damage due to DTW	
		Model 1 OR (95%Cl)	Model 2 OR (95% Cl)	Model 1 OR (95% Cl)	Model 2 OR (95% Cl)
Sex	Male/Female	0.59** (0.45–0.76)	0.59** (0.46–0.77)	0.87 (0.66–1.14)	0.88 (0.67–1.15)
Age (years)	< 65/≥ 65	0.99 (0.76–1.31)	1.01 (0.77–1.32)	1.40* (1.05–1.87)	1.40* (1.05–1.87)
Place of residence	Other/ Hamadori area; Pacific coast	1.06 (0.82–1.38)		1.16 (0.88–1.52)	
Intention to return	Other/ Already returned or living in area		2.46* (1.05–5.73)		1.97 (0.98–3.93)

Note. Reference; yes, logistic regression analysis, DTW: discharge of treated water, OR: odds ratio, Cl: confidence interval, $P < 0.05$*, $P < 0.01$**

respondents' current residential area or intention to return. In other words, the residents of the towns located near the FDNPS worried about reputational damage, regardless of whether they have decided to return or not, or where they live at present.

Compared with the timing of the initial DTW in 2023, the frequency of media coverage of DTW has decreased significantly over time. Impressively, the residents of the towns where the FDNPS is located clarified their decreasing perception of the risks to their health and genetic effects because of the DTW after the process started [7]. However, laypeople remain concerned, and these concerns might generate harmful rumors and misunderstandings about the DTW process, despite the inclusion of incredibly low levels of radionuclides in treated water [8]. Residents of the towns where the FDNPS is located were more worried about reputational damage than about DTW itself, including the health and environmental effects. This finding highlights the negative impact on society caused by insufficient or misleading information and the necessity of evaluating both domestic and international reactions to social and psychological consequences among the general population. It would be suggested that an important comparative analysis between the severity of social and psychological reactions in the population living near the FDNPS and the population that is not directly affected by these events but receives information about them only from the mass media.

It is essential to develop information to mitigate reputational damage related to DTW and develop human resources, both domestically and internationally, who can effectively communicate and disseminate information based on scientific evidence. In particular, both the health effects and how essential the DTW process is need to be better understood among those in medicine, the government, related fields, and the general public. Rumors are not only an issue of human rights but also cause real harm that generates economic losses [9]. Japan has experienced trade restrictions on seafood as a result of DTW, thus the government has a responsibility to restore the international trust and brand power of the Japanese seafood industry. Addressing the reputational damage of DTW will not only mitigate the anxiety experienced by victims of nuclear accidents but could also be an important means of preventing the deterioration of social trust among the global community.

PRESENTATION AT A CONFERENCE

No.

CONFLICT OF INTEREST

The authors declare that they have no competing interests.

REFERENCES

1. Cabinet Public Affairs Office, Cabinet Secretariat. *Japan's Efforts Related to ALPS Treated Water*. Japan. https://japan.kantei.go.jp/ongoingtopics/alps/index.html (22 December 2024, date last accessed).
2. International Atomic Energy Agency. *Comprehensive Report on the Safety Review of the ALPS—Treated Water at the Fukushima Daiichi Nuclear Power Station*. Japan. iaea_comprehensive_alps_report.pdf (22 December 2024, date last accessed).
3. Ministry of Economy, Trade and Industry. *Dialogue between Experts from Japan and China on the Discharge of ALPS Treated Water into the Sea*. Japan. https://www.meti.go.jp/english/press/2024/1219_002.html (22 December 2024, date last accessed).
4. Fukushima Prefectural Government. *Transition of the Evacuation-Designated Zones*. Japan. https://www.pref.fukushima.lg.jp/site/portal-english/en-m1-3.html (22 December 2024, date last accessed).
5. Oishi K, Orita M, Taira Y *et al.* Risk perception of health risks associated with radiation exposure among residents of Okuma, Fukushima prefecture. *IJERPH* 2021;18:13208. https://doi.org/10.3390/ijerph182413208.
6. Xiao X, Orita M, Kashiwazaki Y *et al.* Risk perception in long-term evacuees of Futaba town, Fukushima: a cross-sectional study reveals greater concerns outside the prefecture, 12 years after the accident. *JRR* 2024;65:549–54. https://doi.org/10.1093/jrr/rrae039.
7. Liu M, Matsunaga H, Orita M *et al.* Comparative analysis of public concerns regarding treated water discharged from the Fukushima Daiichi nuclear Power Station: perspectives before and after the initial release. *JRR* 2025;66:103–5. https://doi.org/10.1093/jrr/rrae102.
8. Hande V, Orita M, Matsunaga H *et al.* Thoughts, perceptions and concerns of coastal residents regarding the discharge of tritium-containing treated water from the Fukushima Daiichi nuclear power plant into the Pacific Ocean. *BMC Public Health* 2023;23:2436–6. https://doi.org/10.1186/s12889-023-17349-1.
9. The Japan Times. *Japan Announces New Fishing Industry Aid after China Ban*. Japan. https://www.japantimes.co.jp/news/2023/08/31/japan/politics/fukushima-water-fisheries/ (22 December 2024, date last accessed).

公益財団法人日中医学協会
TEL　03-5829-9123
FAX　03-3866-9080
〒101-0032 東京都千代田区岩本町 1-4-3
住泉KMビル6階
URL：https://www.jpcnma.or.jp/